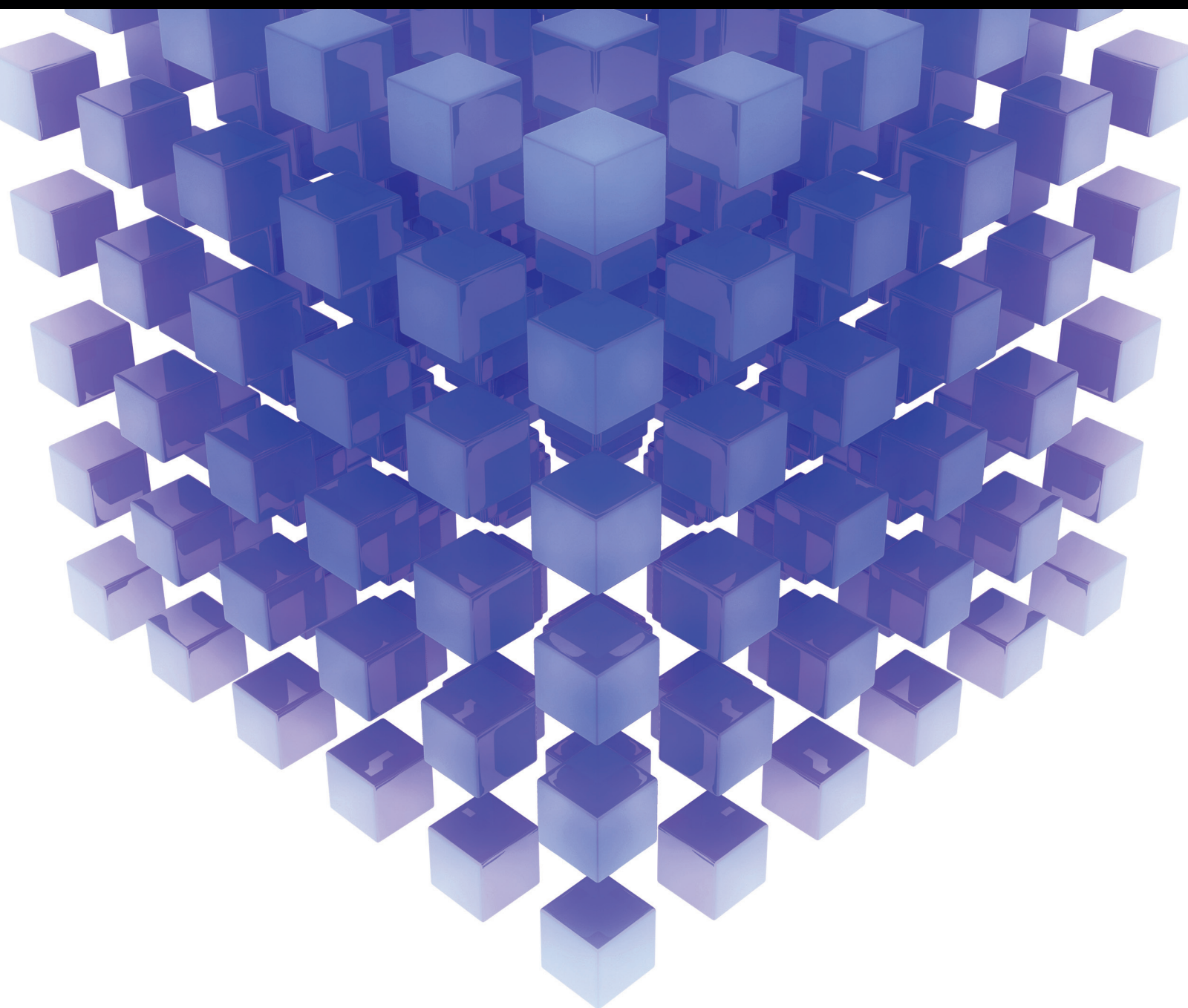


Mathematical Problems in Engineering

Biomechanical Constitutive Model Identification

Lead Guest Editor: Guillermo Rus

Guest Editors: Juan Melchor, Marie Muller, and Akhtar A. Khan





Biomechanical Constitutive Model Identification

Mathematical Problems in Engineering

Biomechanical Constitutive Model Identification

Lead Guest Editor: Guillermo Rus

Guest Editors: Juan Melchor, Marie Muller, and Akhtar A. Khan



Copyright © 2019 Hindawi. All rights reserved.

This is a special issue published in “Mathematical Problems in Engineering.” All articles are open access articles distributed under the Creative Commons Attribution License, which permits unrestricted use, distribution, and reproduction in any medium, provided the original work is properly cited.

Editorial Board

- Mohamed Abd El Aziz, Egypt
AITOUCHE Abdelouhab, France
Leonardo Acho, Spain
José A. Acosta, Spain
Daniela Addressi, Italy
Paolo Adesso, Italy
Claudia Adduce, Italy
Ramesh Agarwal, USA
Francesco Aggogeri, Italy
Juan C. Agüero, Australia
Ricardo Aguilar-Lopez, Mexico
Tarek Ahmed-Ali, France
Elias Aifantis, USA
Muhammad N. Akram, Norway
Guido Ala, Italy
Andrea Alaimo, Italy
Reza Alam, USA
Nicholas Alexander, UK
Salvatore Alfonzetti, Italy
Mohammad D. Aliyu, Canada
Juan A. Almendral, Spain
José Domingo Álvarez, Spain
Cláudio Alves, Portugal
J. P. Amezcua-Sanchez, Mexico
Lionel Amodeo, France
Sebastian Anita, Romania
Renata Archetti, Italy
Felice Arena, Italy
Sabri Arik, Turkey
Francesco Aristodemo, Italy
Fausto Arpino, Italy
Alessandro Arsie, USA
Edoardo Artioli, Italy
Fumihiko Ashida, Japan
Farhad Aslani, Australia
Mohsen Asle Zaeem, USA
Romain Aubry, USA
Matteo Aureli, USA
Richard I. Avery, USA
Viktor Avrutin, Germany
Francesco Aymerich, Italy
Sajad Azizi, Belgium
Michele Baccocchi, Italy
Seungik Baek, USA
Adil Bagirov, Australia
Khaled Bahlali, France
Laurent Bako, France
Pedro Balaguer, Spain
Stefan Balint, Romania
Ines Tejado Balsera, Spain
Alfonso Banos, Spain
Jerzy Baranowski, Poland
Roberto Baratti, Italy
Andrzej Bartoszewicz, Poland
David Bassir, France
Chiara Bedon, Italy
Azeddine Beghdadi, France
Denis Benasciutti, Italy
Ivano Benedetti, Italy
Rosa M. Benito, Spain
Elena Benvenuti, Italy
Giovanni Berselli, Italy
Giorgio Besagni, Italy
Michele Betti, Italy
Jean-Charles Beugnot, France
Pietro Bia, Italy
Carlo Bianca, France
Simone Bianco, Italy
Vincenzo Bianco, Italy
Vittorio Bianco, Italy
Gennaro N. Bifulco, Italy
David Bigaud, France
Antonio Bilotta, Italy
Paul Bogdan, USA
Guido Bolognesi, UK
Rodolfo Bontempo, Italy
Alberto Borboni, Italy
Paolo Boscariol, Italy
Daniela Boso, Italy
Guillermo Botella-Juan, Spain
Boulaïd Boulkroune, Belgium
Fabio Bovenga, Italy
Francesco Braghin, Italy
Ricardo Branco, Portugal
Maurizio Brocchini, Italy
Julien Bruchon, France
Matteo Bruggi, Italy
Michele Brun, Italy
Vasilis Burganos, Greece
Tito Busani, USA
Raquel Caballero-Águila, Spain
Filippo Cacace, Italy
Pierfrancesco Cacciola, UK
Salvatore Caddemi, Italy
Roberto Caldelli, Italy
Alberto Campagnolo, Italy
Eric Campos-Canton, Mexico
Marko Canadija, Croatia
Salvatore Cannella, Italy
Francesco Cannizzaro, Italy
Javier Cara, Spain
Ana Carpio, Spain
Caterina Casavola, Italy
Sara Casciati, Italy
Federica Caselli, Italy
Carmen Castillo, Spain
Inmaculada T. Castro, Spain
Miguel Castro, Portugal
Giuseppe Catalanotti, UK
Nicola Caterino, Italy
Alberto Cavallo, Italy
Gabriele Cazzulani, Italy
Luis Cea, Spain
Song Cen, China
Miguel Cerrolaza, Venezuela
M. Chadli, France
Gregory Chagnon, France
Ludovic Chamoin, France
Ching-Ter Chang, Taiwan
Qing Chang, USA
Michael J. Chappell, UK
Kacem Chehdi, France
Peter N. Cheimets, USA
Xinkai Chen, Japan
Luca Chiapponi, Italy
Francisco Chicano, Spain
Nicholas Chileshe, Australia
Adrian Chmielewski, Poland
Ioannis T. Christou, Greece
Hung-Yuan Chung, Taiwan
Simone Cinquemani, Italy
Roberto G. Citarella, Italy

Joaquim Ciurana, Spain
John D. Clayton, USA
Francesco Clementi, Italy
Piero Colajanni, Italy
Giuseppina Colicchio, Italy
Vassilios Constantoudis, Greece
Enrico Conte, Italy
Francesco Conte, Italy
Alessandro Contento, USA
Mario Cools, Belgium
Jean-Pierre Corriou, France
J.-C. Cortés, Spain
Carlo Cosentino, Italy
Paolo Crippa, Italy
Andrea Crivellini, Italy
Erik Cuevas, Mexico
Maria C. Cunha, Portugal
Peter Dabnichki, Australia
Luca D'Acierno, Italy
Weizhong Dai, USA
Andrea Dall'Asta, Italy
Purushothaman Damodaran, USA
Bhabani S. Dandapat, India
Farhang Daneshmand, Canada
Giuseppe D'Aniello, Italy
Sergey Dashkovskiy, Germany
Fabio De Angelis, Italy
Samuele De Bartolo, Italy
Abílio De Jesus, Portugal
Pietro De Lellis, Italy
Alessandro De Luca, Italy
Stefano de Miranda, Italy
Filippo de Monte, Italy
M. do Rosário de Pinho, Portugal
Michael Defoort, France
Alessandro Della Corte, Italy
Xavier Delorme, France
Laurent Dewasme, Belgium
Angelo Di Egidio, Italy
Roberta Di Pace, Italy
Ramón I. Diego, Spain
Yannis Dimakopoulos, Greece
Zhengtao Ding, UK
M. Djemai, France
Alexandre B. Dolgui, France
Georgios Dounias, Greece
Florent Duchaine, France
George S. Dulikravich, USA
Bogdan Dumitrescu, Romania
Horst Ecker, Austria
Saeed Eftekhar Azam, USA
Ahmed El Hajjaji, France
Antonio Elipe, Spain
Fouad Erchiqui, Canada
Anders Eriksson, Sweden
R. Emre Erkmen, Canada
G. Espinosa-Paredes, Mexico
Leandro F. F. Miguel, Brazil
Andrea L. Facci, Italy
Giacomo Falcucci, Italy
Giovanni Falsone, Italy
Hua Fan, China
Nicholas Fantuzzi, Italy
Yann Favennec, France
Fiorenzo A. Fazzolari, UK
Giuseppe Fedele, Italy
Roberto Fedele, Italy
Zhongyang Fei, China
Arturo J. Fernández, Spain
Jesus M. Fernandez Oro, Spain
Massimiliano Ferraioli, Italy
Massimiliano Ferrara, Italy
Francesco Ferrise, Italy
Eric Feulvarch, France
Barak Fishbain, Israel
S. Douwe Flapper, Netherlands
Thierry Floquet, France
Eric Florentin, France
Alessandro Formisano, Italy
Francesco Franco, Italy
Elisa Francomano, Italy
Tomonari Furukawa, USA
Juan C. G. Prada, Spain
Mohamed Gadala, Canada
Matteo Gaeta, Italy
Mauro Gaggero, Italy
Zoran Gajic, USA
Erez Gal, Israel
Jaime Gallardo-Alvarado, Mexico
Ugo Galvanetto, Italy
Akemi Gálvez, Spain
Rita Gamberini, Italy
Maria L. Gandarias, Spain
Arman Ganji, Canada
Zhiwei Gao, UK
Zhong-Ke Gao, China
Giovanni Garcea, Italy
Luis Rodolfo Garcia Carrillo, USA
Jose M. Garcia-Aznar, Spain
Akhil Garg, China
Harish Garg, India
Alessandro Gasparetto, Italy
Gianluca Gatti, Italy
Oleg V. Gendelman, Israel
Stylianos Georgantzinou, Greece
Fotios Georgiades, UK
Parviz Ghadimi, Iran
Mergen H. Ghayesh, Australia
Georgios I. Giannopoulos, Greece
Agathoklis Giaralis, UK
Pablo Gil, Spain
Anna M. Gil-Lafuente, Spain
Ivan Giorgio, Italy
Gaetano Giunta, Luxembourg
Alessio Gizzi, Italy
Jefferson L.M.A. Gomes, UK
Emilio Gómez-Déniz, Spain
Antonio M. Gonçalves de Lima, Brazil
David González, Spain
Chris Goodrich, USA
Rama S. R. Gorla, USA
Kannan Govindan, Denmark
Antoine Grall, France
George A. Gravvanis, Greece
Fabrizio Greco, Italy
David Greiner, Spain
Simonetta Grilli, Italy
Jason Gu, Canada
Federico Guarracino, Italy
Michele Guida, Italy
Zhaoxia Guo, China
José L. Guzmán, Spain
Quang Phuc Ha, Australia
Petr Hájek, Czech Republic
Weimin Han, USA
Zhen-Lai Han, China
Thomas Hanne, Switzerland
Mohammad A. Hariri-Ardebili, USA
Xiao-Qiao He, China
Nicolae Herisanu, Romania
Alfredo G. Hernández-Díaz, Spain

M.I. Herreros, Spain
Eckhard Hitzer, Japan
Paul Honeine, France
Jaromir Horacek, Czech Republic
Muneo Hori, Japan
András Horváth, Italy
S. Hassan Hosseinnia, Netherlands
Gordon Huang, Canada
Sajid Hussain, Canada
Asier Ibeas, Spain
Orest V. Iftime, Netherlands
Przemyslaw Ignaciuk, Poland
Giacomo Innocenti, Italy
Emilio Insfran Pelozo, Spain
Alessio Ishizaka, UK
Nazrul Islam, USA
Benoit Jung, France
Benjamin Ivorra, Spain
Payman Jalali, Finland
Mahdi Jalili, Australia
Łukasz Jankowski, Poland
Samuel N. Jator, USA
Juan C. Jauregui-Correa, Mexico
Reza Jazar, Australia
Khalide Jbilou, France
Piotr J0drzejowicz, Poland
Isabel S. Jesus, Portugal
Linni Jian, China
Bin Jiang, China
Zhongping Jiang, USA
Emilio Jiménez Macías, Spain
Ningde Jin, China
Xiaoliang Jin, USA
Liang Jing, Canada
Dylan F. Jones, UK
Palle E. Jorgensen, USA
Vyacheslav Kalashnikov, Mexico
Tamas Kalmar-Nagy, Hungary
Tomasz Kapitaniak, Poland
Julius Kaplunov, UK
Haranath Kar, India
Konstantinos Karamanos, Belgium
Krzysztof Kecik, Poland
Jean-Pierre Kenne, Canada
Ch. M. Khaliq, South Africa
Do Wan Kim, Republic of Korea
Nam-Il Kim, Republic of Korea
Jan Koci, Czech Republic
Ioannis Kostavelis, Greece
Sotiris B. Kotsiantis, Greece
Manfred Krafczyk, Germany
Frederic Kratz, France
Petr Krysl, USA
Krzysztof S. Kulpa, Poland
Shailesh I. Kundalwal, India
Jurgen Kurths, Germany
Cedrick A. K. Kwimiy, USA
Kyandoghere Kyamakya, Austria
Davide La Torre, Italy
Risto Lahdelma, Finland
Hak-Keung Lam, UK
Giovanni Lancioni, Italy
Jimmy Lauber, France
Antonino Laudani, Italy
Hervé Laurent, France
Aimé Lay-Ekuakille, Italy
Nicolas J. Leconte, France
Dimitri Lefebvre, France
Eric Lefevre, France
Marek Lefik, Poland
Yaguo Lei, China
Kauko Leiviskä, Finland
Thibault Lemaire, France
Roman Lewandowski, Poland
Chen-Feng Li, China
Jian Li, USA
Yang Li, China
Huchang Liao, China
En-Qiang Lin, USA
Zhiyun Lin, China
Peide Liu, China
Peter Liu, Taiwan
Wanquan Liu, Australia
Bonifacio Llamazares, Spain
Alessandro Lo Schiavo, Italy
Jean Jacques Loiseau, France
Francesco Lolli, Italy
Paolo Lonetti, Italy
Sandro Longo, Italy
António M. Lopes, Portugal
Sebastian López, Spain
Pablo Lopez-Crespo, Spain
Luis M. López-Ochoa, Spain
Ezequiel López-Rubio, Spain
Vassilios C. Loukopoulos, Greece
Jose A. Lozano-Galant, Spain
haiyan Lu, Australia
Gabriel Luque, Spain
Valentin Lychagin, Norway
Antonio Madeo, Italy
José María Maestre, Spain
Alessandro Magnani, Italy
Fazal M. Mahomed, South Africa
Noureddine Manamanni, France
Paolo Manfredi, Italy
Didier Maquin, France
Giuseppe Carlo Marano, Italy
Damijan Markovic, France
Francesco Marotti de Sciarra, Italy
Rui Cunha Marques, Portugal
Rodrigo Martinez-Bejar, Spain
Guiomar Martín-Herrán, Spain
Denizar Cruz Martins, Brazil
Benoit Marx, France
Elio Masciari, Italy
Franck Massa, France
Paolo Massioni, France
Alessandro Mauro, Italy
Fabio Mazza, Italy
Laura Mazzola, Italy
Driss Mehdi, France
Roderick Melnik, Canada
Pasquale Memmolo, Italy
Xiangyu Meng, USA
Jose Merodio, Spain
Alessio Merola, Italy
Mahmoud Mesbah, Iran
Luciano Mescia, Italy
Laurent Mevel, France
Mariusz Michta, Poland
Aki Mikkola, Finland
Giovanni Minafò, Italy
Hiroyuki Mino, Japan
Pablo Mira, Spain
Dimitrios Mitsotakis, New Zealand
Vito Mocella, Italy
Sara Montagna, Italy
Roberto Montanini, Italy
Francisco J. Montáns, Spain
Gisele Mophou, France
Rafael Morales, Spain

Marco Morandini, Italy
Javier Moreno-Valenzuela, Mexico
Simone Morganti, Italy
Caroline Mota, Brazil
Aziz Moukrim, France
Dimitris Mourtzis, Greece
Emiliano Mucchi, Italy
Josefa Mula, Spain
Jose J. Muñoz, Spain
Giuseppe Muscolino, Italy
Marco Mussetta, Italy
Hakim Naceur, France
Alessandro Naddeo, Italy
Hassane Naji, France
Mariko Nakano-Miyatake, Mexico
Keivan Navaie, UK
AMA Neves, Portugal
Luís C. Neves, UK
Dong Ngoduy, New Zealand
Nhon Nguyen-Thanh, Singapore
Tatsushi Nishi, Japan
Xesús Nogueira, Spain
Ben T. Nohara, Japan
Mohammed Nouari, France
Mustapha Nourelfath, Canada
Włodzimierz Ogryczak, Poland
Roger Ohayon, France
Krzysztof Okarma, Poland
Mitsuhiro Okayasu, Japan
Alberto Olivares, Spain
Enrique Onieva, Spain
Calogero Orlando, Italy
Alejandro Ortega-Moñux, Spain
Sergio Ortobelli, Italy
Naohisa Otsuka, Japan
Erika Ottaviano, Italy
Pawel Packo, Poland
Arturo Pagano, Italy
Alkis S. Paipetis, Greece
Roberto Palma, Spain
Alessandro Palmeri, UK
Pasquale Palumbo, Italy
Weifeng Pan, China
Jürgen Pannek, Germany
Elena Panteley, France
Achille Paolone, Italy
George A. Papakostas, Greece
Xosé M. Pardo, Spain
Vicente Parra-Vega, Mexico
Manuel Pastor, Spain
Petr Páta, Czech Republic
Pubudu N. Pathirana, Australia
Surajit Kumar Paul, India
Sitek PaweD, Poland
Luis Payá, Spain
Alexander Paz, Australia
Igor Pažanin, Croatia
Libor Pekař, Czech Republic
Francesco Pellicano, Italy
Marcello Pellicciari, Italy
Haipeng Peng, China
Mingshu Peng, China
Zhengbiao Peng, Australia
Zhi-ke Peng, China
Marzio Pennisi, Italy
Maria Patrizia Pera, Italy
Matjaz Perc, Slovenia
A. M. Bastos Pereira, Portugal
Ricardo Perera, Spain
Francesco Pesavento, Italy
Ivo Petras, Slovakia
Francesco Petrini, Italy
Lukasz Pieczonka, Poland
Dario Piga, Switzerland
Paulo M. Pimenta, Brazil
Antonina Pirrotta, Italy
Marco Pizzarelli, Italy
Vicent Pla, Spain
Javier Plaza, Spain
Kemal Polat, Turkey
Dragan Poljak, Croatia
Jorge Pomares, Spain
Sébastien Poncet, Canada
Volodymyr Ponomaryov, Mexico
Jean-Christophe Ponsart, France
Mauro Pontani, Italy
Cornelio Posadas-Castillo, Mexico
Francesc Pozo, Spain
Christopher Pretty, New Zealand
Luca Pugi, Italy
Krzysztof Puszynski, Poland
Giuseppe Quaranta, Italy
Vitomir Racic, Italy
Jose Ragot, France
Carlo Rainieri, Italy
Kumbakonam Ramamani Rajagopal, USA
Ali Ramazani, USA
Higinio Ramos, Spain
Alain Rassineux, France
S.S. Ravindran, USA
Alessandro Reali, Italy
Jose A. Reinoso, Spain
Oscar Reinoso, Spain
Carlo Renno, Italy
Fabrizio Renno, Italy
Nidhal Rezg, France
Ricardo Riaza, Spain
Francesco Riganti-Fulginei, Italy
Gerasimos Rigatos, Greece
Francesco Ripamonti, Italy
Jorge Rivera, Mexico
Eugenio Roanes-Lozano, Spain
Bruno G. M. Robert, France
Ana Maria A. C. Rocha, Portugal
José Rodellar, Spain
Luigi Rodino, Italy
Rosana Rodríguez López, Spain
Ignacio Rojas, Spain
Alessandra Romolo, Italy
Debasish Roy, India
Gianluigi Rozza, Italy
Jose de Jesus Rubio, Mexico
Rubén Ruiz, Spain
Antonio Ruiz-Cortes, Spain
Ivan D. Rukhlenko, Australia
Mazen Saad, France
Kishin Sadarangani, Spain
Andrés Sáez, Spain
Mehrddad Saif, Canada
John S. Sakellariou, Greece
Salvatore Salamone, USA
Vicente Salas, Spain
Jose Vicente Salcedo, Spain
Nunzio Salerno, Italy
Miguel A. Salido, Spain
Roque J. Saltarén, Spain
Alessandro Salvini, Italy
Sylwester Samborski, Poland
Ramon Sancibrian, Spain
Giuseppe Sanfilippo, Italy
José A. Sanz-Herrera, Spain

Nickolas S. Sapidis, Greece
Evangelos J. Sapountzakis, Greece
Luis Saucedo-Mora, Spain
Marcelo A. Savi, Brazil
Andrey V. Savkin, Australia
Roberta Sburlati, Italy
Gustavo Scaglia, Argentina
Thomas Schuster, Germany
Oliver Schütze, Mexico
Lotfi Senhadji, France
Junwon Seo, USA
Joan Serra-Sagrasta, Spain
Gerardo Severino, Italy
Ruben Sevilla, UK
Stefano Sfarra, Italy
Mohamed Shaat, UAE
Mostafa S. Shadloo, France
Leonid Shaikhet, Israel
Hassan M. Shanechi, USA
Bo Shen, Germany
Suzanne M. Shontz, USA
Babak Shotorban, USA
Zhan Shu, UK
Nuno Simões, Portugal
Christos H. Skiadas, Greece
Konstantina Skouri, Greece
Neale R. Smith, Mexico
Bogdan Smolka, Poland
Delfim Soares Jr., Brazil
Alba Sofi, Italy
Francesco Soldovieri, Italy
Raffaele Solimene, Italy
Jussi Sopenan, Finland
Marco Spadini, Italy
Bernardo Spagnolo, Italy
Paolo Spagnolo, Italy
Ruben Specogna, Italy
Vasilios Spitas, Greece
Sri Sridharan, USA
Ivanka Stamova, USA
RafaD StanisDawski, Poland
Florin Stoican, Romania
Salvatore Strano, Italy
Yakov Strelniker, Israel
Ning Sun, China
Qiuye Sun, China
Sergey A. Suslov, Australia
Thomas Svensson, Sweden
Andrzej Swierniak, Poland
Andras Szekrenyes, Hungary
Kumar K. Tamma, USA
Yang Tang, Germany
Hafez Tari, USA
Alessandro Tasora, Italy
Sergio Teggi, Italy
Ana C. Teodoro, Portugal
Alexander Timokha, Norway
Gisella Tomasini, Italy
Francesco Tornabene, Italy
Antonio Tornambe, Italy
Javier Martinez Torres, Spain
Mariano Torrisi, Italy
George Tsiatas, Greece
Antonios Tsourdos, UK
Federica Tubino, Italy
Nerio Tullini, Italy
Andrea Tundis, Italy
Emilio Turco, Italy
Ilhan Tuzcu, USA
Efstratios Tzirtzilakis, Greece
Filippo Ubertini, Italy
Francesco Ubertini, Italy
Mohammad Uddin, Australia
Hassan Ugail, UK
Giuseppe Vairo, Italy
Eusebio Valero, Spain
Pandian Vasant, Malaysia
Marcello Vasta, Italy
Carlos-Renato Vázquez, Mexico
Miguel E. Vázquez-Méndez, Spain
Josep Vehi, Spain
Martin Velasco Villa, Mexico
K. C. Veluvolu, Republic of Korea
Fons J. Verbeek, Netherlands
Franck J. Vernerey, USA
Georgios Veronis, USA
Vincenzo Vespi, Italy
Renato Vidoni, Italy
V. Vijayaraghavan, Australia
Anna Vila, Spain
Rafael J. Villanueva, Spain
Francisco R. Villatoro, Spain
Uchechukwu E. Vincent, UK
Gareth A. Vio, Australia
Francesca Vipiana, Italy
Stanislav Vitek, Czech Republic
Thuc P. Vo, UK
Jan Vorel, Czech Republic
Michael Vynnycky, Sweden
Hao Wang, USA
Liliang Wang, UK
Shuming Wang, China
Yongqi Wang, Germany
Roman Wan-Wendner, Austria
Jaroslaw Wąs, Poland
P.H. Wen, UK
Waldemar T. Wójcik, Poland
Changzhi Wu, China
Desheng D. Wu, Sweden
Yuqiang Wu, China
Michalis Xenos, Greece
Guangming Xie, China
Xue-Jun Xie, China
Gen Q. Xu, China
Hang Xu, China
Joseph J. Yame, France
Xinggang Yan, UK
Jixiang Yang, China
Mijia Yang, USA
Yongheng Yang, Denmark
Luis J. Yebra, Spain
Peng-Yeng Yin, Taiwan
Yuan Yuan, UK
Qin Yuming, China
Elena Zaitseva, Slovakia
Arkadiusz Zak, Poland
Daniel Zaldivar, Mexico
Francesco Zammori, Italy
Vittorio Zampoli, Italy
Rafal Zdunek, Poland
Ibrahim Zeid, USA
Hao Zhang, China
Haopeng Zhang, USA
Huaguang Zhang, China
Kai Zhang, China
Qingling Zhang, China
Xianming Zhang, Australia
Xuping Zhang, Denmark
Zhao Zhang, China
Yifan Zhao, UK
Jian G. Zhou, UK



Quanxin Zhu, China
Mustapha Zidi, France

Gaetano Zizzo, Italy
Zhixiang Zou, Germany

J. A. Fonseca de Oliveira Correia, Portugal

Contents

Biomechanical Constitutive Model Identification

Guillermo Rus , Juan Melchor , Marie Muller, and Akhtar A. Khan
Editorial (2 pages), Article ID 3607015, Volume 2019 (2019)

Identification of Viscoelastic Constitutive Parameters of a Cell Based on Fluid-Structure Coupled Finite Element Model and Experiment

Jun Qiu  and Fang-Fang Li 
Research Article (13 pages), Article ID 5868561, Volume 2019 (2019)

High-Resolution Strain Measurement for Biomechanical Parameters Assessment in Native and Decellularized Porcine Vessels

Juan Melchor , Juan M. Soto , Elena López-Ruiz , Javier Suarez , Gema Jiménez ,
Cristina Antich, Macarena Perán , Juan A. Marchal , and Guillermo Rus 
Research Article (14 pages), Article ID 2402606, Volume 2019 (2019)

Control Strategy and Experiments for Robot Assisted Craniomaxillofacial Surgery System

Tengfei Cui, Yonggui Wang , Xingguang Duan, and Xiaodong Ma
Research Article (12 pages), Article ID 4853046, Volume 2019 (2019)

Histobiomechanical Remodeling of the Cervix during Pregnancy: Proposed Framework

Jorge Torres , Inas Faris , and Antonio Callejas 
Research Article (11 pages), Article ID 5957432, Volume 2019 (2019)

Mapping Heterogeneous Elastic Property Distribution of Soft Tissues Using Harmonic Motion Data: A Theoretical Study

Yue Mei and Peng Yu 
Research Article (8 pages), Article ID 9131340, Volume 2018 (2019)

Effect of Contact Conditions of Torsional Wave Elastographic Probe on Human Cervix

G. Rus , M. Riveiro, and F. S. Molina
Research Article (6 pages), Article ID 6494758, Volume 2018 (2019)

Nonlinear Classical Elasticity Model for Materials with Fluid and Matrix Phases

Rafael Muñoz  and Juan Melchor 
Research Article (7 pages), Article ID 5049104, Volume 2018 (2019)

Steering Control Method for an Underactuated Unicycle Robot Based on Dynamic Model

Hongzhe Jin , Yang Zhang, Hui Zhang, Zhangxing Liu, Yubin Liu , Yanhe Zhu , and Jie Zhao 
Research Article (13 pages), Article ID 5240594, Volume 2018 (2019)

Extended Poroelasticity: An Analytical Solution and Its Application to p-Wave Propagation in Cervical Tissues

Roberto Palma  and Antonio M. Callejas
Research Article (6 pages), Article ID 5280141, Volume 2018 (2019)

Estimating the Relative Stiffness between a Hepatic Lesion and the Liver Parenchyma through Biomechanical Simulations of the Breathing Process

S. Martínez-Sanchis , M. J. Rupérez, E. Nadal , E. Pareja, S. Brugger, D. Borzacchiello ,
R. López-Andújar, and C. Monserrat
Research Article (10 pages), Article ID 5317324, Volume 2018 (2019)

Influence of the Temporomandibular Joint in the Estimation of Bone Density in the Mandible through a Bone Remodelling Model

Maria S. Commisso , Joaquín Ojeda, Juana Mayo, and Javier Martínez-Reina 
Research Article (14 pages), Article ID 7243696, Volume 2018 (2019)

Editorial

Biomechanical Constitutive Model Identification

Guillermo Rus ^{1,2,3} **Juan Melchor** ^{1,2,3} **Marie Muller**,⁴ and **Akhtar A. Khan**⁵

¹*Department of Structural Mechanics, University of Granada, Granada, 18071, Spain*

²*Instituto de Investigación Biosanitaria, ibs.GRANADA, Spain*

³*Excellence Research Unit "ModelingNature" (MNat), University of Granada, 18071, Spain*

⁴*Department of Mechanical and Aerospace Engineering, NC State University, NC, USA*

⁵*Center for Applied Computational Mathematics, Rochester Institute of Technology, NY, USA*

Correspondence should be addressed to Guillermo Rus; grus@ugr.es

Received 26 June 2019; Accepted 26 June 2019; Published 14 July 2019

Copyright © 2019 Guillermo Rus et al. This is an open access article distributed under the Creative Commons Attribution License, which permits unrestricted use, distribution, and reproduction in any medium, provided the original work is properly cited.

In biomechanics, reliable modeling and quantification of material parameters and the study of constitutive models and computational tools concerning experimental observations of living tissue are a rapidly expanding field of research. The primary reason for this interest is the ever-growing number of real-world applications such as cardiovascular, osteoarticular, reproductive, osteoarticular, and regenerative biomechanics. In summary, the capability of biomathematical models to realistically predict the various behavioral patterns observed in soft tissue is a longstanding challenging problem. To advance towards this quest, this special issue presents recent developments in the topics including soft tissue biomechanical models, applied, computational, or theoretical tissue mechanics continuum field theory, hyperelastic and viscoelastic quasi-incompressible transversely isotropic constitutive model formulation and identification, inverse problems, or biomechanical parameter identification problems.

The special issue contains eleven thoroughly reviewed research papers of high scientific merit. A summary of the key ideas of the included articles is as follows.

J. Qiu and F.-F. Li proposed a methodology to determine the viscoelastic parameters for a single cell combining flow chamber experiment and fluid-structure coupled finite element model. For the optimal parameters, they used the experimental observation to compare with the deformation response of the cell with different parameters in the finite element model. The developed framework was applied to osteocytes. J. Melchor et al. assessed the mechanical properties of two groups of porcine carotid blood vessels, namely,

native arteries and decellularized arteries. The biomechanical properties of both groups were determined by conducting uniaxial and circumferential tensile tests by using an ad hoc and lab-made device. T. Cui et al. developed a robot-assisted craniomaxillofacial surgery system and evaluated the feasibility and reliability of this robot system in phantom experiments. J. Torres et al. explored aspects of the remodeling of the cervix, which play a fundamental role in preventing preterm birth. The authors developed a framework where the variation of the histological properties is linked with the individual biomechanical evolution of the constituents, consequently providing the feasibility of a multiscale approach. Y. Mei and P. Yu focused on characterizing heterogeneous elastic property distribution of soft tissues which has direct implication in disease detection. They proposed an inverse approach to map the heterogeneous material property distribution of soft solids using harmonic motion data. Inspired by the challenges associated with characterizing the soft tissue mechanical functionality by current elastography techniques, G. Rus et al. proposed a mechanism to evaluate the robustness of the mechanical characterization of the cervix through the torsional wave elastography probe, specifically against some relevant contact conditions. R. Muñoz and J. Melchor presented a new classical nonlinear model proposing a constitutive equation that separates volumetric and deviatoric effects and compared the formulation to constitutive equations with Landau constants for weak elasticity and both types of related nonlinear constants. H. Jin et al. proposed a lateral balancing structure based on precession effect of double gyroscopes and its associated control strategy of the steering for an

underactuated unicycle robot. They provided numerical results to demonstrate the rationality of the lateral balance structure and the feasibility of the steering control method. R. Palma and A. M. Callejas presented a semianalytical solution based on Laplace transform to study the behavior of poroelastic materials in the context of the extended nonequilibrium thermodynamics. Utilizing the finite element simulation of the deformation that the liver undergoes during the breathing process, S. Martínez-Sanchis et al. developed a method to estimate, in vivo, the relative stiffness between a hepatic lesion and the liver parenchyma. M. S. Commisso et al. explored how the change in stress distributions affects the remodeling response of the mandible bone and showed the crucial effect of the temporomandibular joint on the stress distribution during the masticatory cycle.

Conflicts of Interest

The authors declare that they have no conflicts of interest.

Acknowledgments

Finally, we give our most sincere thanks to all the authors who have contributed to this special issue and to the collegial team of the coeditors that functioned very well together.

*Guillermo Rus
Juan Melchor
Marie Muller
Akhtar A. Khan*

Research Article

Identification of Viscoelastic Constitutive Parameters of a Cell Based on Fluid-Structure Coupled Finite Element Model and Experiment

Jun Qiu ^{1,2} and Fang-Fang Li ³

¹State Key Laboratory of Hydrosience & Engineering, Tsinghua University, Beijing 100084, China

²State Key Laboratory of Plateau Ecology and Agriculture, Qinghai University, Xining 810016, China

³College of Water Resources & Civil Engineering, China Agricultural University, Beijing 100083, China

Correspondence should be addressed to Fang-Fang Li; liff@cau.edu.cn

Received 20 December 2018; Revised 11 March 2019; Accepted 26 March 2019; Published 11 April 2019

Guest Editor: Juan Melchor

Copyright © 2019 Jun Qiu and Fang-Fang Li. This is an open access article distributed under the Creative Commons Attribution License, which permits unrestricted use, distribution, and reproduction in any medium, provided the original work is properly cited.

Although mechanical properties of a single cell as well as its mechanical response to stimulation are significant for mechanotransduction, it is difficult to quantitatively identify the viscoelasticity of a cell. This study proposes a methodology to determine the viscoelastic parameters for a single cell combining flow chamber experiment and fluid-structure coupled finite element model. The observation from the experiment is used to compare with the deformation response of the cell with different parameters in the finite element model with standard linear solid constitute model, which are adjusted until the two displacement response curves from the experiment and the simulation accord with each other, and then the corresponding combination of the viscoelastic parameters is determined to represent the viscoelasticity of the cell. The proposed methodology is applied on osteocytes in this study but can be generalized to other cells. The results indicate that both k_1 and k_2 of an osteocyte are in the order of several hundred Pa and η is in the order of kPa·s.

1. Introduction

Establishing and improving mechanical models of a cell is an active research field in biomechanics [1]. Various cellular mechanics models have been proposed, mainly including two categories: the models based on micro/nanostructure and the continuum cell models [1–3].

The models based on micro/nanostructure consider the cytoskeleton as the main structural component [2–9]. The mechanics of cytoskeleton of adherent cells were studied [3]. For suspended cells, such as red blood cells, a model of microhaemoglobin network [10, 11] was established to study the role of cell membrane and haemoglobin network in erythrocyte macromorphism.

On the other hand, the continuum methods regard a cell as continuums with determinate material properties. The parameters based on constitutive models of certain materials can be measured by experiments. Although these

models do not provide an in-depth study of the mechanics between biomolecules and bioions, the continuum methods are effective in understanding the overall mechanical properties of cells at the cellular level. Once the continuum mechanical model of a cell is established, the details of stress and strain distribution on the cell can be provided, which helps to understand the distribution and transmission of force between cytoskeleton and subcellular components. The cell mechanics models based on the continuum assumption [12] include solid model, mainly used for adherent cell research [13]; cortical coating droplet model, mainly used for suspension cell research [14]; structural damping model with power-law, mainly used for the study of dynamic properties of adherent cells [15]; biphasic model, mainly used for the study of muscle and skeletal cells [16]. Other cell mechanics models are refined based on these basic models.

In experiments, the cell size is between ten microns and dozens of microns, and the thickness of cell membrane is

between several nanometers and dozens of nanometers [13]. Conventional macromechanical loading methods and experimental techniques cannot be directly used in the study of cell mechanics. With the advancement of micromanipulation technology, many mechanical loading experimental methods for cultured cells *in vitro* have been proposed, and different types and functions of experimental devices have been developed to achieve quantitative study of the mechanical properties of cells, including micropipette aspiration [14, 17], unconfined cell compression [18], cyto-indentation [19], atomic force microscopy (AFM) [20, 21], magnetic bead rheometry [22], and optical traps [23]. In particular, many researchers have studied the adhesion and deformation of adherent cells under shear flow [24], for example, the shear effect of blood on endothelial cells *in vivo* [7] and the adhesion and debonding of cultured cells under shear stress [24]. The stress and deformation of a cell have direct impacts on the function and structure of the cell. Because of the extremely complex cytoskeleton network system inside the cell, the cell has the ability to deform actively and resist passive deformation. The mechanical properties of a cell are closely related to its structure and function. Viscoelasticity is an important part of in the research of cellular mechanical properties.

Osteocytes, mature bone cells embedded in mineralized bone matrix, are under dynamic shear fluid *in vivo* and exhibit significant viscoelastic behavior [25]. Abundant evidence has shown that osteocytes are the key mechanosensor cells that directly regulate bone-forming osteoblast and bone-removing osteoclast activities [26, 27]. Thus, osteocytes are critical to etiology and new treatments for osteoporosis [28].

In this study, the viscoelastic parameters of osteocytes are determined by a comparison between finite element model and experimental observation. A flow chamber experiment is carried out to record the behavior of osteocytes under shear flow, which is simulated by a fluid-structure interactive finite element model. Standard linear solid (SLS) model is used to describe the viscoelastic behavior of cells, the three parameters in which are determined by comparing the deformation of the cell under shear flow stress. Applying the methodology on three osteocytes, the three parameters of viscoelasticity are identified. The results show that both k_1 and k_2 are in the order of several hundred Pa and η is in the order of kPa·s.

2. Methodology

2.1. Flow Chamber Experiment. In cell flow chamber experiment, osteocytes adhere to the basal glass plate, which is placed in a square flow chamber, and a unidirectional flow of cell culture medium flows through the chamber. Osteocytes are deformed by fluid shear force, as shown in Figure 1(a).

The length of the flow chamber is 5 cm, which is three orders of magnitude larger than the cell scale. The height of the flow chamber is $550\ \mu\text{m}$ and the width is $700\ \mu\text{m}$. The size of osteocytes is around $10\ \mu\text{m}$.

It is generally believed that the shear stress of adherent cells in microvessels is $10\text{dyn}/\text{cm}^2$. Based on the theoretical analytical relationship between wall shear stress and flow

rate, the flow rate in a square cavity can be estimated. In the experiment in this study, the flow rate of $1.318\ \text{ml}/\text{min}$ is strictly controlled by using a microinjection pump, so as to control the shear force of flow field on cells.

In the cell shear flow experiment, the bottom and side deformations of the cells are obtained by a self-built quasi-three-dimensional microscopic imaging system, as illustrated in [29]. The microscopic images of the cell are recorded at 12 Hz frequency, and the displacement information of any point on the cell can be obtained by digital image correlation algorithm [29]. Figures 1(b) and 1(c) show the side images of the osteocyte before and after the deformation under shear stress.

2.2. 2D Fluid-Structure Coupled Finite Element Model.

Software ADINA developed by the research group led by K. J. Bathe in 1975 is a dynamic nonlinear finite element analysis software. ADINA has remarkable ability to solve fluid-structure interaction problems. In the process of fluid-solid coupling calculation, the fluid force is applied to the structure through the interface of fluid and solid, and the deformation of the structure affects the boundary conditions of the fluid in turn. When doing fluid-structure coupling calculation, the structure model and fluid model need to be built in ADINA structure module (ADINA Structures) and fluid module (ADINA CFD), respectively, and then the derived finite element input files from the two models are put into the ADINA fluid-structure coupling solver (ADINA-FSI) for calculation. Complex multifield coupled physical problems can be simulated and predicted by ADINA coupling solution, which is adopted in this study.

In order to verify the computational accuracy of the fluid-solid coupling calculation program and to provide an optimal grid size reference for 3D modeling, we studied the 2D model before establishing the 3D model.

2.2.1. Basic Assumptions of Finite Element Model. ① Osteocytes are regarded as homogeneous, isotropic, and nearly incompressible viscoelastic continuum.

② Active force produced by osteocytes under fluid shear is ignored; i.e., only the passive deformation of osteocytes is analyzed.

③ The hydrodynamic properties of water at room temperature are equivalent to those of the cell culture medium. Since the cell shear flow experiment is carried out in the laboratory and the experiment is executed within a few minutes, the influence of environmental temperature on the experiment is not considered.

2.2.2. 2D Finite Element Model of Cell Shear Flow Interaction.

The problem of flow in a square cross-section tube is the basis of the interaction of cell shear flow. The numerical simulation of the flow in a square cross-section tube needs to be realized firstly to study the interaction of cell shear flow. Within the laminar flow range, the fluid is assumed to be incompressible. The cross-section height of the square tube is H and the width is W . For steady laminar flow of incompressible fluid, the Navier-Stokes equation under unidirectional flow in a square cross-section tube is shown in [24]

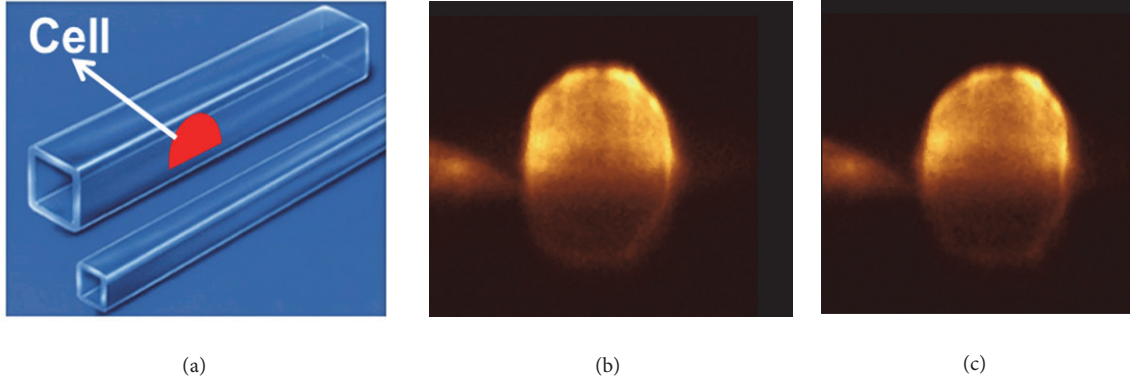


FIGURE 1: Cell flow chamber experiment. (a) Schematic diagram of flow chamber experiment; the side images of the osteocyte (b) before and (c) after the shear flow.

$$0 = -\frac{dP}{dx} + \mu \left(\frac{\partial^2 u_x}{\partial y^2} + \frac{\partial^2 u_x}{\partial z^2} \right) \quad (1)$$

where μ is the fluid viscous coefficient, P is the fluid pressure, u is the flow velocity, x is the dimension of the flow field direction, y is the direction of the height of the flow chamber, and z is the direction of the width of the flow chamber. The boundary conditions for this problem are shown in

$$\begin{aligned} u_x &= 0 \\ y &= \pm \frac{H}{2} \\ u_x &= 0 \\ z &= \pm \frac{w}{2} \end{aligned} \quad (2)$$

where H is the height of the flow chamber and w is the width of the flow chamber.

When the pressure gradient at the flow direction, the geometrical size of the square tube, and the viscous coefficient of the fluid in the tube are known, the distribution function of the velocity profile under the laminar flow state can be obtained as in

$$\begin{aligned} u_x &= \frac{1}{2\mu} \left(-\frac{dP}{dx} \right) \\ &\times \left\{ \left(\frac{H^2}{4} - z^2 \right) - \frac{8H^2}{\pi^3} \times \sum_{n=0}^{\infty} \frac{(-1)^n \cos[(2n+1)\pi z/H] \cosh[(2n+1)\pi y/H]}{(2n+1)^3 \cosh[(2n+1)\pi w/2H]} \right\} \end{aligned} \quad (3)$$

The wall shear stress t_w is as in

$$\begin{aligned} \tau_w &= -\mu \left. \frac{du_x}{dz} \right|_{z=-H/2} \\ &= -\frac{H}{2} \left(-\frac{dP}{dx} \right) \\ &\times \left\{ 1 - \frac{8}{\pi^2} \sum_{n=0}^{\infty} \frac{\cosh[(2n+1)\pi y/H]}{(2n+1)^2 \cosh[(2n+1)\pi w/2H]} \right\} \end{aligned} \quad (4)$$

The flow rate Q in the square section is as in

$$\begin{aligned} Q &= \frac{wH^3}{4\mu} \left(-\frac{dP}{dx} \right) \\ &\times \left\{ \frac{1}{3} - \frac{64H}{\pi^5 w} \sum_{n=0}^{\infty} \frac{\tanh[(2n+1)\pi w/2H]}{(2n+1)^5} \right\} \end{aligned} \quad (5)$$

In the 2D finite element model of tube flow, the tube thickness is $550 \mu\text{m}$ and the length is $1400 \mu\text{m}$. The wall nonslip boundary conditions are applied along the flow direction. The entrance boundary conditions are pressure $P=1 \text{ Pa}$, and the exit boundary conditions are free. Three mesh sizes are designed, including coarse meshes of $18.4 \mu\text{m}$, general meshes of $9.2 \mu\text{m}$, and fine meshes of $4.6 \mu\text{m}$.

Table 1 shows the convergence analysis results of 2D fluid meshes density. It can be seen that the solution of the 2D finite element model of tube flow converges to the theoretical solution by refining the mesh density. Even when the mesh density is small, the flow rate and velocity have high accuracy. Since the shear force is related to the first derivative of the flow rate, it is difficult to achieve high accuracy. Only refining the meshes can derive a more accurate shear force.

Comparing the analytical solutions and numerical solutions, it comes to a conclusion that the results of finite element analysis for such tube flow problems using ADINA software are reliable.

2.2.3. Convergence Analysis of 2D Fluid-Structure Coupled Finite Element Model. The fluid-structure coupling finite element model of 2D cell shear flow interaction is shown in Figure 2. In the flow chamber, the fluid in contact with cells is discretized by a fine mesh to keep the mesh size of the flow field in accordance with the cell mesh size. In this model, a cell is represented by a semicircle, and the bottom of the cell is completely fixed on the base of the flow chamber; i.e., cell debonding is out of consideration.

The cell and its adjacent fluids adopt three different mesh sizes: $0.4 \mu\text{m}$, $0.8 \mu\text{m}$, and $1.6 \mu\text{m}$. The responses of different mechanical variables with different mesh sizes are extracted, including the displacement of the cell's highest point along

TABLE 1: Convergence analysis of 2D fluid meshes density.

	Analytical solution	Coarse meshes		General meshes		Fine meshes	
		Numerical solution	Error	Numerical solution	Error	Numerical solution	Error
Max shear stress (Pa)	1.9643E-01	1.8990E-01	-3.32%	1.9320E-01	-1.64%	1.9480E-01	-0.83%
Max flow rate (mm/s)	2.0776E-02	2.0780E-02	0.02%	2.0780E-02	0.02%	2.0780E-02	0.02%
volume metric (mm ³ /s)	7.6179E-06	7.6094E-06	-0.11%	7.6158E-06	-0.03%	7.6174E-06	-0.01%

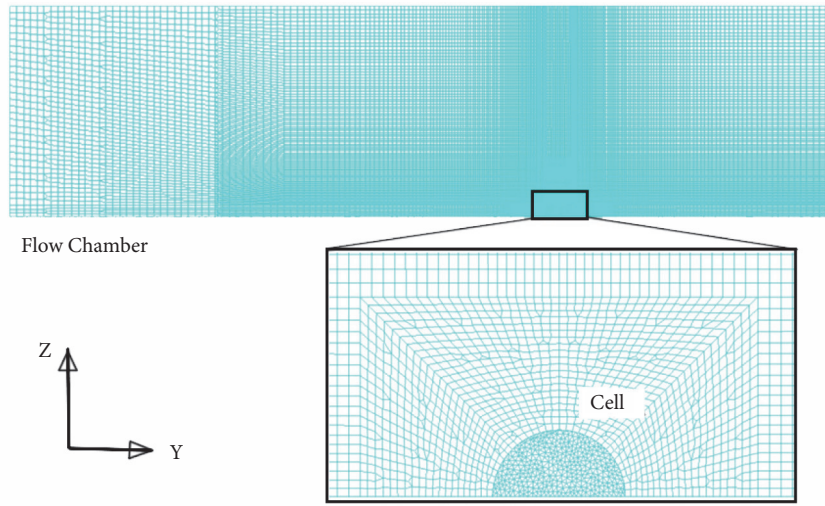


FIGURE 2: 2D fluid-structure coupled finite element model under share flow.

the flow field direction (y direction), the displacement of the cell's highest point along the flow field vertical direction (z direction), the positive pressure distribution along the cell surface, and the fluid shear stress distribution along the cell surface.

2.3. 3D Fluid-Structure Coupled Finite Element Model

2.3.1. Fluid Model. In the finite element simulation, the establishment of such full-scale model of the flow chamber requires enormous computational resources without necessity. The length of the flow chamber in the finite element model needs to be determined by theoretical deduction to ensure that, under certain boundary conditions, the fluid can achieve fully developed laminar flow in the chamber.

The Reynolds number Re is as in

$$Re = \frac{\rho v L}{\mu} \quad (6)$$

In the cell flow chamber experiment, the flow velocity v in the tube can be estimated by the cross-section area and flow rate of the square tube, and the width of the square tube can be taken as the characteristic size L , while the density of water ρ is constant. It can be estimated that the Reynolds number of

this flow problem is 30. Generally, laminar flow is recognized when the Reynolds number is less than 2100. For laminar flow, there is a prediction formula to estimate the entrance length L_ϵ required for the full development of the flow field, as shown in

$$\frac{L_\epsilon}{d} = 0.59 + 0.055Re \quad (7)$$

In this study, d is $550 \mu m$, and thus the length of the entrance needed for the full development of the flow field is $1400 \mu m$.

According to hydrodynamic experience, if the profile shape of velocity boundary condition applied at the entrance approximates the fully developed velocity profile, the velocity profile at the entrance can evolve to a fully developed velocity profile after a very short distance. It is of great significance to reduce the fluid field in the finite element model and thus to save computational resources and improve computational efficiency. The shape and size of the fully developed section can be obtained from the results of the finite element model of the tube flow with a length of $1400 \mu m$. Applying such fully developed velocity profile as a boundary condition to a shorter ($200 \mu m$) flow chamber model, a reliable fully developed flow field near the cell with a smaller computational model can be obtained.

The wall condition is applied around the square flow chamber; the pressure boundary condition (1400 μm flow chamber model) and the parabolic velocity boundary condition (200 μm flow chamber model) are applied at the entrance; and the free boundary is set at the exit.

When determining the fluid domain, the space occupied by cells needs to be removed. A fluid-structure coupling boundary condition is applied to the interface between fluid and cell.

2.3.2. Structure Model. Before establishing the final fluid-structure coupling finite element model based on 3D reconstructed cell configuration, a model based on hemispherical cell configuration is established to verify the validity of the model with simple geometric configuration.

Based on the fluid-structure coupling model of hemispherical cell configuration, the fluid domain is shown in Figure 3(a). The length of the square cross-section tube is 1400 μm . Wall shear conditions are applied around the tube, uniform velocity boundary conditions are applied at the entrance (57.06 mm/s), and free boundary conditions are applied at the exit. It is generally believed that the shear stress suffered by adherent cells in microvessels is 10 dyn/cm^2 , and then the flow rate in the tube can be estimated according to the theoretical analytical relationship between the wall shear force and the flow rate. The cell is fixed in the middle of the lower reaches of the whole tube. Transition mesh density technique is used to divide the spatial mesh of fluid domain. The mesh density near the cell is high, while the mesh density far from the cell is low. The viscosity of water at room temperature is regarded as the viscosity of the culture medium. The cell mesh and the fluid mesh near the cell are densified, as shown in Figure 3(b). The cell mesh size is 0.4 μm .

On the basis of the model above, the initial configuration of the cell is modified. The experimental data on the real osteocyte is applied to reconstruct 3D cell configuration, as illustrated in [30]. To improve computational efficiency and ensure computational accuracy, the length of the flow chamber is reduced to 200 μm . At the same time, the boundary condition of the velocity at flow chamber entrance is set as a paraboloid, the parameters of which are determined by the calculation results of the extracellular flow field velocity. In the fluid field, the area near the cell needs to be meshed more intensively. The area far from the cell can be divided into larger meshes. The meshes in the fluid domain near the cell can be divided into transitional meshes.

2.4. Viscoelastic Constitutive Model. Previous studies have shown that adherent cells present certain viscoelastic properties [22, 31–33]. The standard linear solid (SLS) can be used to describe the viscoelastic behavior of cells [34, 35], as shown in Figure 3(c).

There are three parameters in a SLS. Establishing the stress-strain relationship in time domain and applying the boundary conditions under stress relaxation conditions, the stress-strain relationship of viscoelastic materials in Laplace

space can be obtained by Laplace transformation, the simple expression of which is shown in

$$\frac{\sigma(t)}{\varepsilon_0} = E_{rel}(t) = k_1 + k_2 e^{(-t/\tau)}, \quad \tau = \frac{\eta}{k_2} \quad (8)$$

where E_{rel} is the relaxation modulus of the viscoelastic materials, $\sigma(t)$ is creep stress, and ε_0 is initial strain. It can be seen from the expression of relaxation modulus that, at the initial moment $t=0$, the elastic modulus is $k_1 + k_2$, which is called the instantaneous modulus, while when the time lasts for a long time, the second term of (8) becomes 0; i.e., the elastic modulus becomes k_1 , which is called the equilibrium modulus. The viscous coefficient and k_2 determine the relaxation response characteristic time of the viscoelastic materials together, which describes the evolution speed of viscoelastic materials from initial deformation to final equilibrium.

The viscoelastic material model in ADINA software is expressed by general viscoelastic constitutive relationship, as shown in

$$s_{ij}(t) = 2G(0) e_{ij}(t) + 2 \int_0^t e_{ij}(t-\tau) \frac{dG(\tau)}{d\tau} d\tau \quad (9)$$

$$\sigma_{kk}(t) = 3K(0) \varepsilon_{kk}(t) + 3 \int_0^t \varepsilon_{kk}(t-\tau) \frac{dK(\tau)}{d\tau} d\tau \quad (10)$$

Equation (9) and (10) show the relationship between shear stress and shear modulus, and the relationship between normal stress and bulk modulus, respectively. The shear modulus and bulk modulus are expressed in Prony series, respectively, as shown in

$$G(t) = G_\infty + \sum_{i=1}^{\eta_G} G_i e^{-\beta_i t} \quad (11)$$

$$K(t) = K_\infty + \sum_{i=1}^{\eta_K} K_i e^{-\gamma_i t} \quad (12)$$

The parameters in Prony series characterize the mechanical properties of viscoelastic materials. Assuming that cells are nearly incompressible materials, their bulk modulus can be regarded to be very large. Thus only the shear modulus of cells needs to be determined in the model, which can be magnified by several orders of magnitude to represent the bulk modulus of cells.

Retaining the constant term and the first exponential term of the shear stress in the form of Prony series, the first two forms of Prony series are the same as the viscoelastic material deduced before. Through the simple equivalence between parameters, the relationship between parameters in Prony series and those in SLS model can be easily found, as shown in

$$\begin{aligned} G_\infty &= \frac{1}{3} k_1 \\ G_1 &= \frac{1}{3} k_2 \\ \beta_1 &= \frac{1}{\tau} = \frac{k_2}{\eta} \end{aligned} \quad (13)$$

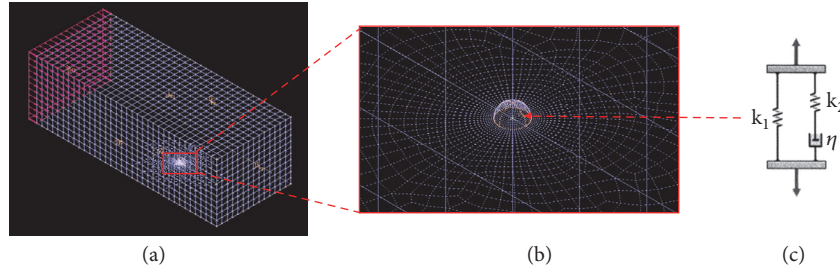


FIGURE 3: 3D fluid-structure coupled finite element model under share flow. (a) Fluid field of the fluid-structure coupled finite element model based on hemispherical cell; (b) meshing scheme of the fluid field near the cell; (c) standard linear solid (SLS) model.

To verify (13), the relaxation problem of viscoelastic materials under uniaxial tension is studied by theoretical and numerical methods, respectively. The theoretical solution is shown in

$$\sigma(t) = \varepsilon_0 \left(k_e + k_1 e^{-t/\tau} \right), \quad \tau = \frac{\eta}{k_1} \quad (14)$$

According to (13), a set of SLS parameters are transformed into parameters in Prony series and input into ADINA model. And for the same relaxation problem, the theoretical and numerical solutions are obtained, respectively, which are in good agreement as shown in Figure 4. Thus the relationship in (13) is valid.

2.5. Identification of Viscoelastic Parameters of a Cell. A fluid-structure coupled finite element model based on 3D cell configuration is established. Applying the same boundary conditions to the model as in the experiment and assigning certain values to the parameters of the cell viscoelastic model (k_1, k_2, η) , the mechanical response of an osteocyte under the selected material parameters can be calculated. If the mechanical response is the same as that of the cells measured in the experiment, the selected parameters can be considered to be able to characterize the mechanical properties of the osteocyte.

The overall framework of the method determining the viscoelastic parameters is shown in Figure 5. After establishing the fluid-structure coupling model for cell shear flow interaction, a set of estimated values of the three parameters osteocyte is given directly and then input into the finite element model for calculation. These parameters determine the 3D configuration of the cell under shear stress in the fluid-structure coupled finite element model. Meanwhile, the deformation process of cells under the fluid is observed by a self-built quasi-3D cell microscopic system, as illustrated in [29]. Quantitative data of cell deformation can be obtained by directly processing the cell images obtained in the experiment. Comparing the cell deformation configurations obtained from the finite element model based on the estimated values of three parameters with the experimental data, if they agree with each other well, the estimated values are taken as the viscoelastic parameters of the osteocyte, while if there is still a large gap between them, the viscoelastic coefficients will be reestimated until the proper values of the three parameters are determined.

Through literature research, we have known the general range of mechanical parameters of osteocytes, which is below 1kPa for suspended or partially adhered osteocytes [36, 37]. That is to say, we choose the initial value by prior knowledge.

After applying the methodology on three osteocytes, three viscoelastic parameters of each cell were obtained.

2.6. Calibration of Fluid-Structure Coupled Finite Element Model

2.6.1. Calibration of 2D Model. Table 2 shows the calculated values of the fluid-structure interaction model under three groups of meshing. It can be seen that shear stress and pressure depend more on the meshes than cell displacement. Such phenomenon is easy to understand in numerical calculation. Since stress is related to the first derivative of the flow velocity, the stress loses the first-order accuracy in the process of deriving the velocity. Therefore, it is necessary to study the influence of finer meshes on the shear stress and normal stress for the model.

As can be seen from Figure 6(a), the pressure distribution on the cell surface remains basically constant as the mesh size decreases to less than $0.4 \mu\text{m}$; i.e., the pressure response on the cell surface has reached a convergent solution.

As shown in Figure 6(b), the shear stress in the central part of the cell increases slightly and that in the bilateral part of the cell decreases slightly as the mesh size decreases from $1.6 \mu\text{m}$ to $0.1 \mu\text{m}$. When the cell size is less than $0.4 \mu\text{m}$, the distribution of shear stress does not change except for the small area at the top of the cell, which means that the shear stress on the cell surface basically converges. The distribution of shear stress at the top of cells has always been dependent on the scale of the mesh, which may be related to the inflection point of the wall boundary conditions. It is believed that it is no longer meaningful to reduce the mesh to capture the convergent solution of the shear stress. The stress and the corresponding deformation of the whole cell are concerned primarily, so it can be regarded that the shear stress distribution on the cell surface converges when the cell size is less than $0.4 \mu\text{m}$.

In Table 3, the stability of the fluid-structure interaction model in calculating the pressure and shear stress distribution along the cell surface with different mesh sizes ($0.1 \mu\text{m}$, $0.2 \mu\text{m}$, $0.4 \mu\text{m}$, $0.8 \mu\text{m}$, and $1.6 \mu\text{m}$) is summarized. The calculation shows that the shear stress is relatively dependent more on

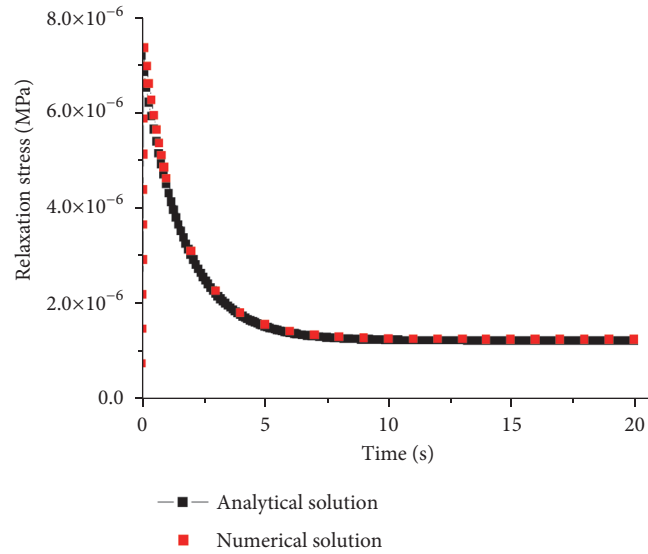


FIGURE 4: Comparison of theoretical and numerical solutions for stress relaxation problem.

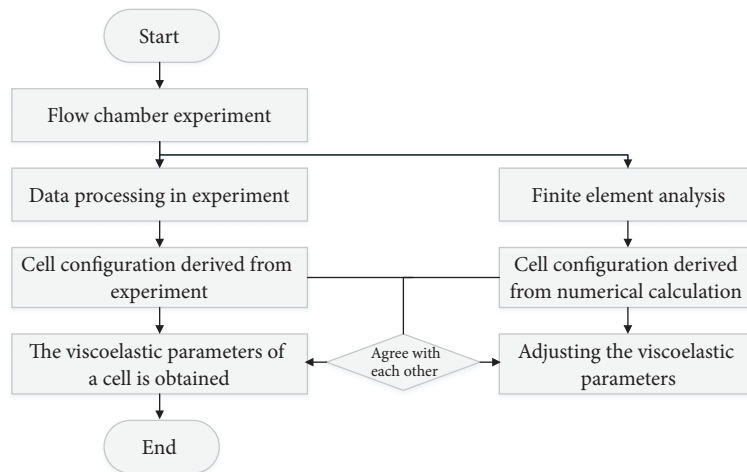


FIGURE 5: Framework of methodology to determine viscoelastic parameters of a cell.

the mesh, and its convergence rate is relatively slow with the decrease of the mesh size. In view of the whole cell deformation, rather than the local stress on cell surface, it can be concluded that when the mesh size is $0.4 \mu\text{m}$, the pressure and shear stress on cell surface converge.

2.6.2. Calibration of 3D Model. Inputting a set of three viscoelastic parameters of cell viscoelasticity into the fluid-structure coupling finite element model of cell shear flow interaction, the cell deformation information can be obtained, as shown in Figures 7(b)–7(g), in which colors represents the displacement information of cells along the direction of flow. The redder the color is, the larger the displacement is. It can be seen that the displacement at the top of the cell along the flow direction is the most significant, which is consistent with the experimental results.

The top area of the cell is chosen to represent the deformation of the whole cell configuration since it is the most obvious area of deformation and the displacement information here fully reflects the characteristics of the whole cell deformation. Figures 7(a) and 7(b) show the microscopic image of this area obtained in the experiment and the calculation results from the finite element model. Besides, the displacement of the cells along the flow direction is significant under the shear stress, while the displacement along the vertical direction of the flow field is small, so only the displacement of the cells along the flow direction is taken into account.

The relationship between the relaxation modulus of viscoelastic materials along the time is shown in (8).

In the following study of the three viscoelastic parameters of the cell, the range of the parameters found in previous

TABLE 2: Convergence analysis of fluid-structure interaction model of cell shear flow with three meshing methods.

	0.4 μm		0.8 μm		1.6 μm	
	Calculated Value	Calculated Value	Error*	Calculated Value	Error*	
Horizontal Displacement (μm)	0.0772	0.0753	-2.46%	0.0711	-5.58%	
Vertical Displacement (μm)	-0.0121	-0.012	-0.83%	-0.0119	-0.83%	
Shear Stress (Pa)	2.2	2.03	-7.73%	1.77	-12.81%	
Maximal Stress (Pa)	3.59	3.7	3.06%	3.86	4.32%	

Note: * refers to the relative error between the calculated value under the mesh density and that under the adjacent fine meshes; and all the physical quantities are from the highest point of the cell.

TABLE 3: Convergence analysis of fluid-structure interaction model of cell shear flow with 5 different mesh sizes.

	0.1 μm		0.2 μm		0.4 μm		0.8 μm		1.6 μm	
	Calculated Value	Calculated Value	Error*							
Shear Stress (Pa)	2.38	2.3	-3.36%	2.2	-4.35%	2.03	-7.73%	1.77	-12.81%	
Maximal Pressure (Pa)	3.56	3.58	0.56%	3.59	0.28%	3.7	3.06%	3.86	4.32%	

Note: * refers to the relative error between the calculated value under the mesh density and that under the adjacent fine meshes; and all the physical quantities are from the highest point of the cell.

studies are taken as [29, 38]. When adjusting k_1 , the other two parameters are kept constant, $k_2 = 600$ Pa and $\eta=1000$ Pa·s. The displacement at the top of the cell along the flow direction is shown in Figure 8(a). In the second half of the observed response curve, it can be found that k_1 significantly affects the response of the cell after equilibrium state, and k_1 slightly affects the initial deformation response at the starting point of the curve. Thus the equilibrium response of the cell can be reduced by increasing k_1 .

Adjusting the value of k_2 and keeping the other two parameters constant, $k_1=120$ Pa and $\eta=1000$ Pa·s, the displacement at the top of the cell along the flow direction is extracted, as shown in Figure 8(b). At the starting point of the response curve, it can be found that k_2 significantly affects the initial deformation response of the cell. From the second half of the response curve, it can be seen that k_2 basically does not affect the response of the cell after equilibrium state. Thus the initial deformation response can be reduced by increasing k_2 .

Adjusting the value of the viscosity coefficient η and keeping the other two parameters constant, $k_1=120$ Pa and $k_2=600$ Pa, the displacement at the top of the cell along the flow direction is extracted, as shown in Figure 8(c). At the starting point of the response curve, it can be found that η does not affect the initial deformation response of the cell. Then it can be observed that, with the increase of the viscosity coefficient η , the velocity of the cell which tends to equilibrium state slows down and the time needed to reach equilibrium is prolonged.

Through the study above, the effects of each parameter of the three viscoelastic parameters on the cell mechanical response under shear flow are understood, which helps to estimate the increment of each parameter according to the mechanical response of the cell and then to determine the optimal combination of the three viscoelastic parameters efficiently.

3. Results and Discussion

A specific osteocyte is selected to extract the displacement at the top area of the cell along the flow direction from the experimental results, as shown in Figure 9(a). The displacement response is typical as viscoelastic materials, which is also similar to the deformation response curve observed by other researchers [38].

According to previous reports on cell viscoelasticity, the first group of viscoelastic parameters called M1 is estimated firstly. The mechanical response of the cell represented by M1 in the fluid-structure coupled finite element model is shown in Figure 9(b). It can be seen that there is a certain gap between the mechanical response of the cell based on M1 and that of the cell in the experiment.

When estimating the viscoelastic parameters of the cell for the second and the third time, the values of k_1 and k_2 are reduced to a greater extent, and the value of η is increased slightly. Finally, the mechanical response of the cells represented by the selected viscoelastic parameter combination M3 is in good agreement with that of the cells in the experiment, as shown in Figure 9(c). Therefore, it is considered that the parameters of M3 represent the viscoelastic properties of the cell well, which are the viscoelastic parameters for the osteocyte numbered #01.

The process above shows the determination method for viscoelastic parameters of a particular cell. The actual process has undergone more iterations, and only three representative steps are presented here.

Even for the same kind of osteocyte, each osteocyte has different mechanical properties and responds differently to the same external mechanical stimuli. But interestingly, the adherent osteocytes show viscoelastic characteristics of delayed response to load. Figure 9(d) shows the response of three different osteocytes to the same fluid shear stress in

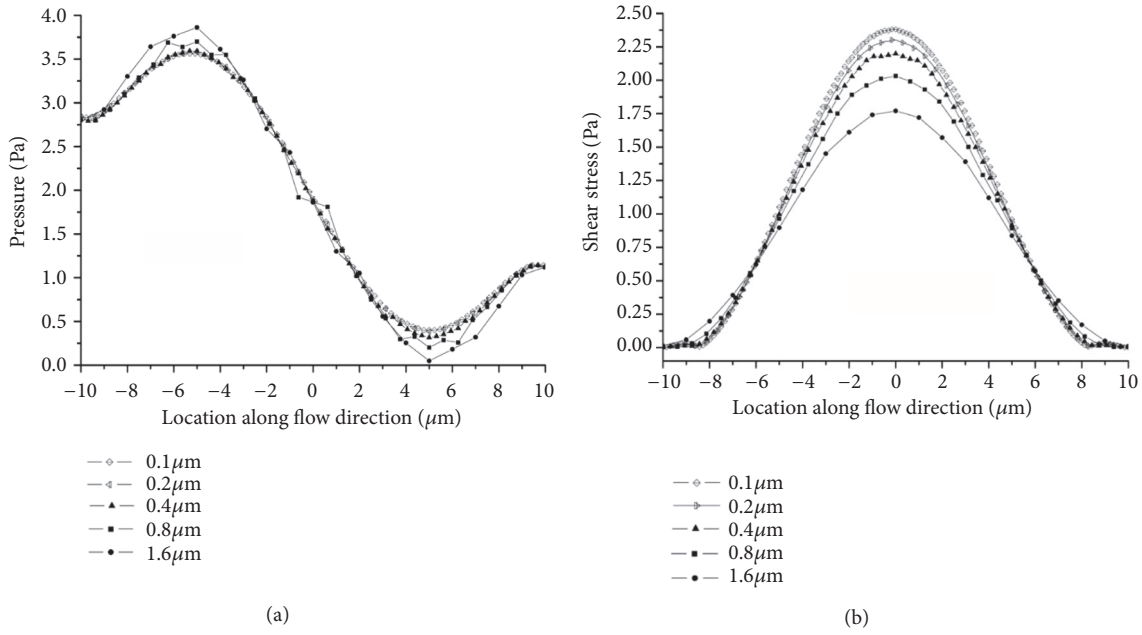


FIGURE 6: Convergence analysis of 5 different mesh sizes. (a) Pressure distribution on the cell surface; (b) shear stress distribution on the cell surface.

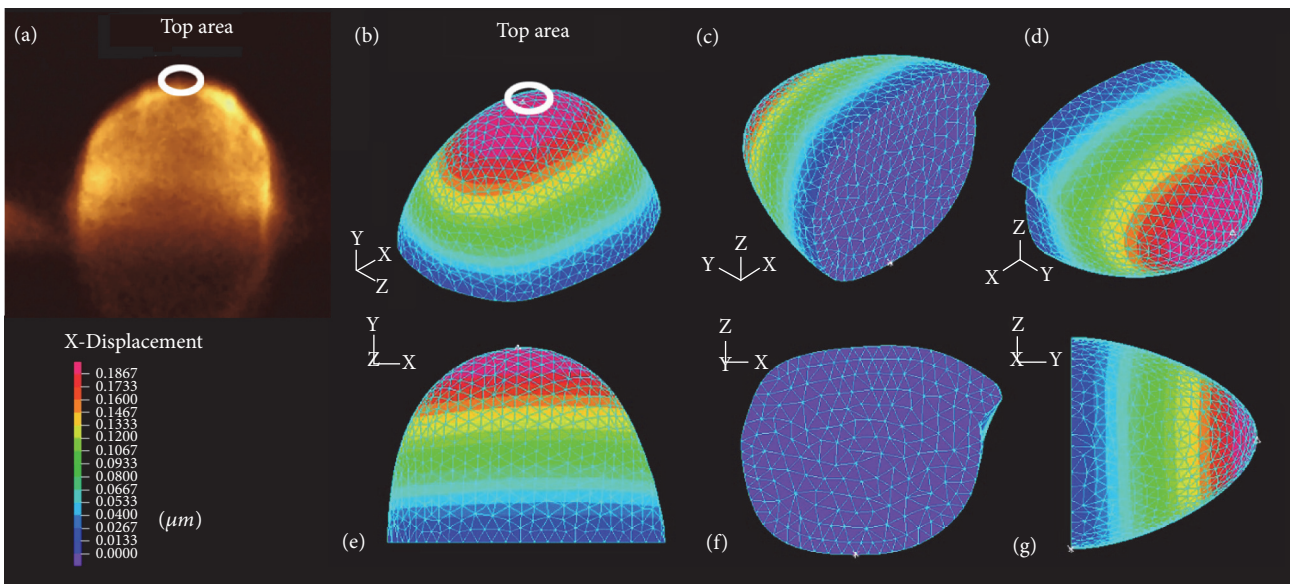


FIGURE 7: The deformation of the cell under shear stress in experiments (a) and in the fluid-structure coupling finite element model with different views (b~g).

the experiment, where the vertical coordinates of the curve indicate the displacement at the top area of the cell along the flow direction.

Three osteocytes are analyzed, and the final simulative and experimental results are shown in Figure 9(d). The identification results of the three parameters of viscoelasticity corresponding to these three osteocytes are shown in Table 4. Among the three parameters of osteocyte viscoelasticity, both k_1 and k_2 are in the order of several hundred Pa and η is in the order of $kPa \cdot s$.

Our results are consistent with previous understanding of osteocytes elastic parameters. Many scholars believe that the stiffness of suspended or partially adhered osteocytes is below $1kPa$, while that of fully adhered osteocytes is above $1kPa$ [36, 37]. The difference between our study and traditional studies on the mechanical properties of osteocytes is that we not only measured the elastic parameters, but also obtained the viscosity parameters of the cells. We believe that the viscosity parameters of cells might be an important indicator of cell mechanics and mechanotransduction.

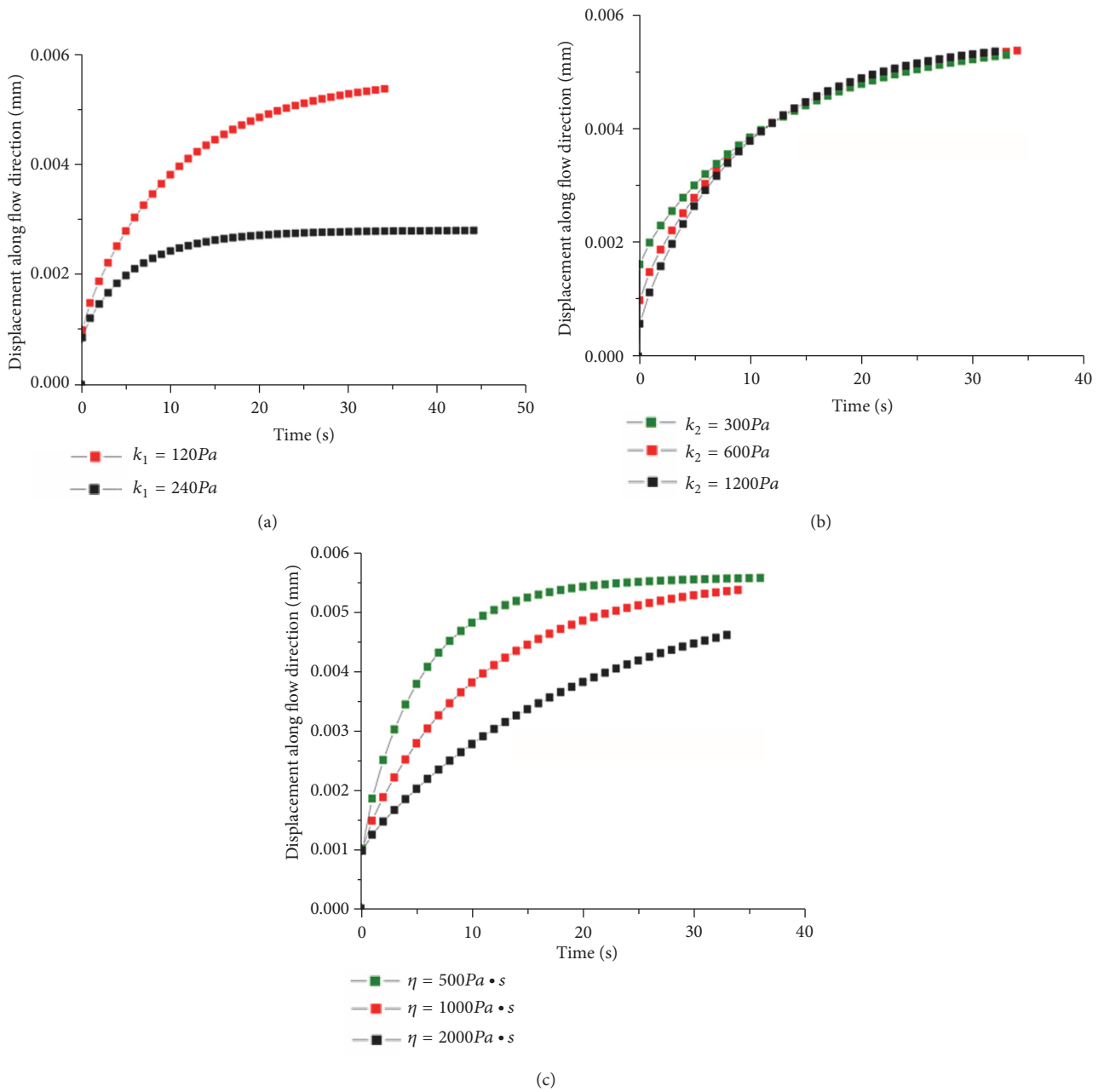


FIGURE 8: The influence of viscoelastic parameters on the cell mechanical response under fluid shear stress: (a) k_1 is changed; (b) k_2 is changed; (c) η is changed.

TABLE 4: Identification results of three viscoelastic parameters for osteocytes.

	Cell#01	Cell#02	Cell#03	Average (n=3)
k_1 (kPa)	0.11	0.17	0.18	0.15 ± 0.02
k_2 (kPa)	0.70	0.35	0.80	0.62 ± 0.14
η (kPa·s)	0.85	1.3	2.0	1.38 ± 0.33

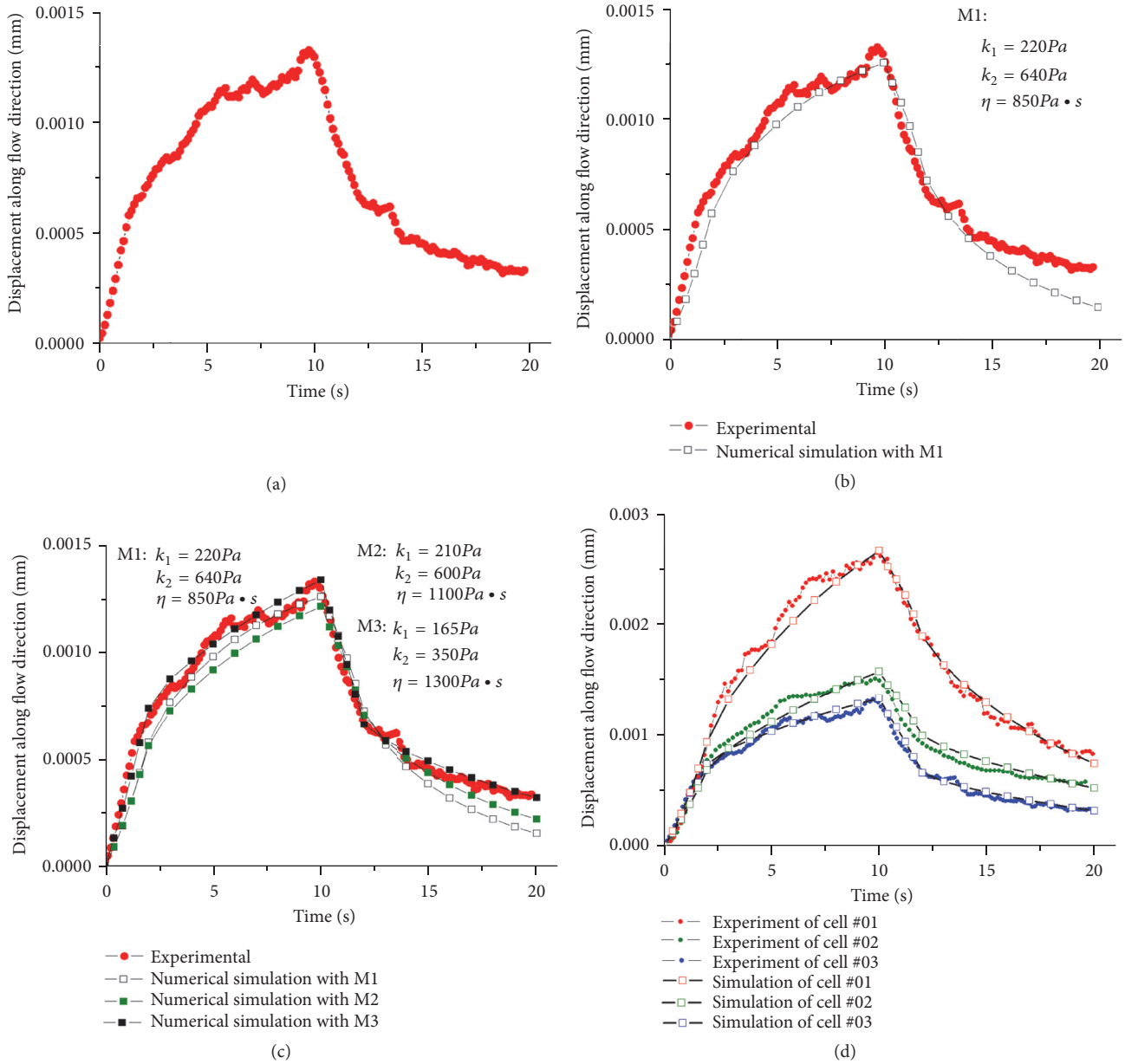


FIGURE 9: Comparison between the displace response of the cell in the fluid-structure coupled finite element model and those from the experimental results. (a) The displacement at the top area of the cell along the flow direction from the experimental results for #01 osteocyte; (b) using first group of viscoelastic parameters M1 for #01 osteocyte; (c) the process of three optimization iterations; M1, M2, and M3 are three groups of decision variables for #01 osteocyte; (d) comparison results for three different osteocytes (#01, #02, and #03).

Some scholars may wonder why a simpler linear viscoelastic constitutive model is chosen to study the viscoelastic behavior of cells here. When we carried out the research, we also tried different viscoelastic constitutive models to describe the cell mechanics properties. After going through lots of literatures, we decided to adopt a linear viscoelastic model with only three mechanical parameters, because the form of linear viscoelastic model is simple, the mechanical significance of each parameter is clear, and the three parameters can be measured through well design experiments one by one. Although more complex nonlinear viscoelastic

models may describe viscoelastic behavior more realistically, the corresponding meaning of each parameter is not easy to recognize, nor is it easy to determine the parameters through experiments. Therefore, we finally choose the linear viscoelastic constitutive model in this study.

Instead of using the current popular optimization algorithms, such as genetic algorithm, ant colony algorithm, and other global optimal algorithms, we adopted the basic idea of optimization to find the viscoelastic mechanical parameters of cells. The reasons come from three aspects. First, we have mastered the mechanical significance of the three parameters

in the linear viscoelastic model and can predict the changes in the mechanical behavior of cells caused by the changes in parameters. Secondly, through literature research, we have known the general range of mechanical parameters of osteocytes. We only need to search within this range, and the optimal solution found could be considered as the global optimal solution. Thirdly, the 3D fluid-solid coupling model requires a large amount of calculation, and optimization methods such as genetic algorithm and ant colony algorithm need tens of thousands of iterations to get better optimization results, so the calculation cost is too high. Based on the above three reasons, we choose the optimization algorithm based on manual judgment of optimization direction and step size in this paper.

4. Conclusion

A methodology to identify the viscoelasticity of a cell is proposed in this study. A flow chamber experiment is firstly carried out, and the deformation of the cell under shear flow is observed by a quasi-3D microscopy system. Meanwhile, a fluid-structure coupled finite element model is established using SLS assumption. The deformation of the cell simulated by the FE model is compared with the observation in the experiment. The three viscoelastic parameters are adjusted based on the comparison between the displace response of the cell in the fluid-structure coupled finite element model and that from the experimental results until the simulative and experimental results accord with each other, when the parameters in the FE model can be regarded to be able to represent the viscoelasticity of the cell. The methodology is applied on osteocytes, which have been hypothesized as mechanosensors in bone. The results indicate that both k_1 and k_2 of an osteocyte are in the order of several hundred Pa and η is in the order of kPa·s. The methodology proposed in this study can be generalized to identify the viscoelasticity of any other cells. The methodology for measuring the mechanical properties of cells developed in this paper should be developed towards the aspect of rapid and real-time measurement, which may contribute to the disease detection methods with cell mechanical parameters as indicators in the future.

Data Availability

The data used to support the findings of this study are available from the corresponding author upon request.

Conflicts of Interest

The authors declare that they have no conflicts of interest.

Acknowledgments

This research was supported by National Natural Science Foundation of China (Grants nos. 51879137, 91847302, and 11402136).

References

- [1] C. T. Lim, E. H. Zhou, and S. T. Quek, "Mechanical models for living cells - A review," *Journal of Biomechanics*, vol. 39, no. 2, pp. 195–216, 2006.
- [2] R. L. Satcher Jr. and C. F. Dewey Jr., "Theoretical estimates of mechanical properties of the endothelial cell cytoskeleton," *Biophysical Journal*, vol. 71, no. 1, pp. 109–118, 1996.
- [3] D. Stamenović and M. F. Coughlin, "The role of prestress and architecture of the cytoskeleton and deformability of cytoskeletal filaments in mechanics of adherent cells: A quantitative analysis," *Journal of Theoretical Biology*, vol. 201, no. 1, pp. 63–74, 1999.
- [4] U. G. Hofmann, C. Rotsch, W. J. Parak, and M. RadMacHer, "Investigating the cytoskeleton of chicken cardiocytes with the atomic force microscope," *Journal of Structural Biology*, vol. 119, no. 2, pp. 84–91, 1997.
- [5] P. Cañadas, V. M. Laurent, C. Oddou, D. Isabey, and S. Wendling, "A cellular tensegrity model to analyse the structural viscoelasticity of the cytoskeleton," *Journal of Theoretical Biology*, vol. 218, no. 2, pp. 155–173, 2002.
- [6] J. H.-C. Wang, "Substrate deformation determines actin cytoskeleton reorganization: A mathematical modeling and experimental study," *Journal of Theoretical Biology*, vol. 202, no. 1, pp. 33–41, 2000.
- [7] J. Pourati, A. Maniotis, D. Spiegel et al., "Is cytoskeletal tension a major determinant of cell deformability in adherent endothelial cells?" *American Journal of Physiology-Cell Physiology*, vol. 274, no. 5, pp. C1283–C1289, 1998.
- [8] N. Wang, I. M. Toli-Nørrelykke, J. Chen et al., "Cell prestress. I. Stiffness and prestress are closely associated in adherent contractile cells," *American Journal of Physiology-Cell Physiology*, vol. 282, no. 3, pp. 606–616, 2002.
- [9] D. Stamenović and D. E. Ingber, "Models of cytoskeletal mechanics of adherent cells," *Biomechanics and Modeling in Mechanobiology*, vol. 1, no. 1, pp. 95–108, 2002.
- [10] D. E. Discher, D. H. Boal, and S. K. Boey, "Simulations of the erythrocyte cytoskeleton at large deformation. II. Micropipette aspiration," *Biophysical Journal*, vol. 75, no. 3, pp. 1584–1597, 1998.
- [11] J. Li, M. Dao, C. T. Lim, and S. Suresh, "Spectrin-level modeling of the cytoskeleton and optical tweezers stretching of the erythrocyte," *Biophysical Journal*, vol. 88, no. 5, pp. 3707–3719, 2005.
- [12] M. A. Wozniak and C. S. Chen, "Mechanotransduction in development: a growing role for contractility," *Nature Reviews Molecular Cell Biology*, vol. 10, no. 1, pp. 34–43, 2009.
- [13] X. J. Fan, "Cell biomechanics," *Advances in Mechanics*, vol. 25, no. 2, pp. 197–208, 1995.
- [14] R. M. Hochmuth, "Micropipette aspiration of living cells," *Journal of Biomechanics*, vol. 33, no. 1, pp. 15–22, 2000.
- [15] B. Fabry, G. N. Maksym, J. P. Butler, M. Glogauer, D. Navajas, and J. J. Fredberg, "Scaling the microrheology of living cells," *Physical Review Letters*, vol. 87, no. 14, Article ID 148102, 2001.
- [16] V. C. Mow, S. C. Kuei, W. M. Lai, and C. G. Armstrong, "Biphasic creep and stress relaxation of articular cartilage in compression: theory and experiments," *Journal of Biomechanical Engineering*, vol. 102, no. 1, pp. 73–84, 1980.
- [17] F. P. T. Baaijens, W. R. Trickey, T. A. Laursen, and F. Guilak, "Large deformation finite element analysis of micropipette

- aspiration to determine the mechanical properties of the chondrocyte,” *Annals of Biomedical Engineering*, vol. 33, no. 4, pp. 494–501, 2005.
- [18] J. Z. Wu and W. Herzog, “Analysis of the mechanical behavior of chondrocytes in unconfined compression tests for cyclic loading,” *Journal of Biomechanics*, vol. 39, no. 4, pp. 603–616, 2006.
- [19] E. J. Koay, A. C. Shieh, and K. A. Athanasiou, “Creep indentation of single cells,” *Journal of Biomechanical Engineering*, vol. 125, no. 3, pp. 334–341, 2003.
- [20] E. M. Darling, S. Zauscher, and F. Guilak, “Viscoelastic properties of zonal articular chondrocytes measured by atomic force microscopy,” *Osteoarthritis and Cartilage*, vol. 14, no. 6, pp. 571–579, 2006.
- [21] V. Lulevich, T. Zink, H.-Y. Chen, F.-T. Liu, and G.-Y. Liu, “Cell mechanics using atomic force microscopy-based single-cell compression,” *Langmuir*, vol. 22, no. 19, pp. 8151–8155, 2006.
- [22] A. R. Bausch, F. Ziemann, A. A. Boulbitch, K. Jacobson, and E. Sackmann, “Local measurements of viscoelastic parameters of adherent cell surfaces by magnetic bead microrheometry,” *Biophysical Journal*, vol. 75, no. 4, pp. 2038–2049, 1998.
- [23] J. Guck, S. Schinkinger, B. Lincoln et al., “Optical deformability as an inherent cell marker for testing malignant transformation and metastatic competence,” *Biophysical Journal*, vol. 88, no. 5, pp. 3689–3698, 2005.
- [24] J. Cao, S. Usami, and C. Dong, “Development of a side-view chamber for studying cell-surface adhesion under flow conditions,” *Annals of Biomedical Engineering*, vol. 25, no. 3, pp. 573–580, 1997.
- [25] C. R. Jacobs, S. Temiyasathit, and A. B. Castillo, “Osteocyte mechanobiology and pericellular mechanics,” *Annual Review of Biomedical Engineering*, vol. 12, pp. 369–400, 2010.
- [26] L. F. Bonewald and M. L. Johnson, “Osteocytes, mechanosensing and Wnt signaling,” *Bone*, vol. 42, no. 4, pp. 606–615, 2008.
- [27] L. You, S. Temiyasathit, P. Lee et al., “Osteocytes as mechanosensors in the inhibition of bone resorption due to mechanical loading,” *Bone*, vol. 42, no. 1, pp. 172–179, 2008.
- [28] S. C. Manolagas, “Birth and death of bone cells: basic regulatory mechanisms and implications for the pathogenesis and treatment of osteoporosis,” *Endocrine Reviews*, vol. 21, no. 2, pp. 115–137, 2000.
- [29] A. D. Baik, X. L. Lu, J. Qiu et al., “Quasi-3D cytoskeletal dynamics of osteocytes under fluid flow,” *Biophysical Journal*, vol. 99, no. 9, pp. 2812–2820, 2010.
- [30] J. Qiu and F.-F. Li, “Mechanical behavior of an individual adherent MLO-Y4 osteocyte under shear flow,” *Biomechanics and Modeling in Mechanobiology*, vol. 16, no. 1, pp. 1–12, 2017.
- [31] S. Yamada, D. Wirtz, and S. C. Kuo, “Mechanics of living cells measured by laser tracking microrheology,” *Biophysical Journal*, vol. 78, no. 4, pp. 1736–1747, 2000.
- [32] E. Evans, N. Mohandas, and A. Leung, “Static and dynamic rigidities of normal and sickle erythrocytes. Major influence of cell hemoglobin concentration,” *The Journal of Clinical Investigation*, vol. 73, no. 2, pp. 477–488, 1984.
- [33] I. M. Ward and P. R. Pinnock, “The mechanical properties of solid polymers,” *British Journal of Applied Physics*, vol. 17, no. 1, pp. 3–32, 1966.
- [34] W. R. Trickey, G. M. Lee, and F. Guilak, “Viscoelastic properties of chondrocytes from normal and osteoarthritic human cartilage,” *Journal of Orthopaedic Research*, vol. 18, no. 6, pp. 891–898, 2000.
- [35] M. Sato, D. P. Theret, L. T. Wheeler, N. Ohshima, and R. M. Nerem, “Application of the micropipette technique to the measurement of cultured porcine aortic endothelial cell viscoelastic properties,” *Journal of Biomechanical Engineering*, vol. 112, no. 3, pp. 263–268, 1990.
- [36] S. Kuroshima, M. Kaku, T. Ishimoto, M. Sasaki, T. Nakano, and T. Sawase, “A paradigm shift for bone quality in dentistry: A literature review,” *Journal of Prosthodontic Research*, vol. 61, no. 4, pp. 353–362, 2017.
- [37] R. F. M. van Oers, H. Wang, and R. G. Bacabac, “Osteocyte shape and mechanical loading,” *Current Osteoporosis Reports*, vol. 13, no. 2, pp. 61–66, 2015.
- [38] R. Y. Kwon and C. R. Jacobs, “Time-dependent deformations in bone cells exposed to fluid flow in vitro: investigating the role of cellular deformation in fluid flow-induced signaling,” *Journal of Biomechanics*, vol. 40, no. 14, pp. 3162–3168, 2007.

Research Article

High-Resolution Strain Measurement for Biomechanical Parameters Assessment in Native and Decellularized Porcine Vessels

Juan Melchor ^{1,2,3}, Juan M. Soto ⁴, Elena López-Ruiz ^{2,3,5},
Javier Suarez ¹, Gema Jiménez ^{2,3,6,7}, Cristina Antich ^{6,7},
Macarena Perán ^{2,5}, Juan A. Marchal ^{2,3,6,7} and Guillermo Rus ^{1,2,3}

¹Department of Structural Mechanics, University of Granada, Granada 18071, Spain

²Instituto de Investigación Biosanitaria (ibs.GRANADA), Spain

³Excellence Research Unit “Modeling Nature” (MNat), University of Granada, 18071, Spain

⁴Department of Optics, Faculty of Physical Sciences, Complutense University of Madrid, Madrid 28040, Spain

⁵Department of Health Sciences, University of Jaén, Jaén, Spain

⁶Biopathology and Regenerative Medicine Institute (IBIMER), Centre for Biomedical Research, University of Granada, Granada, Spain

⁷Department of Human Anatomy and Embryology, Faculty of Medicine, University of Granada, Granada, Spain

Correspondence should be addressed to Juan Melchor; jmelchor@ugr.es

Received 19 December 2018; Revised 12 February 2019; Accepted 27 February 2019; Published 9 April 2019

Academic Editor: Gregory Chagnon

Copyright © 2019 Juan Melchor et al. This is an open access article distributed under the Creative Commons Attribution License, which permits unrestricted use, distribution, and reproduction in any medium, provided the original work is properly cited.

Decellularized vascular scaffolds are promising materials for vessel replacements. However, despite the natural origin of decellularized vessels, issues such as biomechanical incompatibility, immunogenicity risks, and the hazards of thrombus formation still need to be addressed. In this study, we assess the mechanical properties of two groups of porcine carotid blood vessels: (i) native arteries and (ii) decellularized arteries. The biomechanical properties of both groups ($n = 10$, sample size of each group) are determined by conducting uniaxial and circumferential tensile tests by using an ad hoc and lab-made device comprising a peristaltic pump that controls the load applied to the sample. This load is regularly incremented (8 grams per cycle with a pause of 20 seconds after each step) while keeping the vessels continuously hydrated. The strain is measured by an image cross-correlation technique applied on a high-resolution video. The mechanical testing analyses of the arteries revealed significant differences in burst pressure between the native (1345.08 ± 96.58 mbar) and decellularized (1067.79 ± 112.13 mbar) groups. Moreover, decellularized samples show a significantly lower maximum load at failure (15.78 ± 0.79 N) in comparison with native vessels (19.42 ± 0.80 N). Finally, the average ultimate circumferential tensile also changes between native (3.71 ± 0.37 MPa) and decellularized (2.93 ± 0.18 MPa) groups. This technique is able to measure the strain in the regime of large displacements and enables high-resolution image of the local strains, thus providing a valuable tool for characterizing several biomechanical parameters of the vessels also applicable to other soft tissue presenting hyperelastic behaviours.

1. Introduction

Arterial graft remains the primary therapy for patients with advanced cardiovascular disease. The ongoing need for arterial conduits is due to the poor clinical efficacy of existing synthetic grafts in small diameter artery applications around (~ 5 mm) [1, 2]. Besides, many patients with pathological arterial walls need an efficient replacement based on tissue

engineering procedures [3–5]. In particular, tissue engineering has been successfully applied to fabrication of printed-based matrices for developing useful implants [6, 7].

The arterial graft typically involves a decellularization procedure depending on the geometrical shape and the biomechanical properties of the required tissue [8]. Moreover, the process of acquiring native arteries and their decellularization requires a difficult methodology, not always

put into practice in an optimum manner. In this study, we explore the possibility of obtaining porcine decellularized arteries by applying an enzymatic digestion and detergent extraction procedure [1, 9, 10]. This process is able to provide implants to patients similarly to those made of synthetic materials, once the demanded biomechanical resistance is known. Some authors have also studied the fabrication of a hybrid tissue vascular graft by applying polymerized coatings on the outside of different aortic or carotid decellularized vessels, which significantly enhances their biomechanical behaviour [2, 11].

The outstanding role of assessing the biomechanical properties of biological specimens (in this case, different arteries) justifies the application of the mechanics of continuous media formalism. Particularly, it has been used to describe the results from several mechanical tensile tests aiming at retrieving the stiffness and elasticity of the samples. Typically, the mechanical characterization of the blood vessels has been obtained without taking into account the resolution of the displacements in axial or circumferential tests [12–14]. The error introduced by an inaccurate distance measurement is translated into significant misleading variations of the mechanical parameters. In this regard, we propose an image cross-correlation algorithm to improve the strain tracking experienced by the sample during the stress tests, thereby providing a high-resolution characterization of their mechanical parameters. The researchers that may introduce these mechanical concepts in the field of tissue engineering or clinical practice need this accurate characterization of the mechanical properties [15–17].

Soft tissues (such as blood vessels), understood as hyperelastic materials when subjected to uniaxial loads, are characterized by relevant shape changes as well as a strongly nonlinear response. Hyperelastic materials experience a great strain when a load is applied. Nevertheless, once the load is removed they return to a position very close to the initial one. On the other hand, when cyclical loads are applied to these materials, a considerable dissipation in the energy is exhibited as a response to the stress. The realization of this work has been based on the functions of the deformation energy suitable for soft tissues study developed by Holzapfel, Ogden, and Vito [18–21]. In this way, a semianalytical description of constitutive equations for soft tissues is explored and then it has been applied to develop a new technique for measuring the strain in mechanical tensile tests.

The remainder of the paper is organized as follows. Section 2 briefly describes the mechanical behaviour of the artery along with the derivation of its stress tensor. Next, Section 3 is devoted to the strain tensor. Then, Section 4 includes the experimental setup, the preparation of the biological samples, and the details of the statistical analysis performed in the experiment. Later, Section 5 describes the image cross-correlation algorithm proposed in this work for a better characterization of the sample mechanical properties. The following section includes the results from the mechanical tests along with the histological comparisons between native and decellularized vessels. Finally, Section 7 summarizes the main conclusions of the study and paves the way for future work.

2. Biomechanical Stress Tensor on Arteries Samples

The methodology applied for the mechanical characterization is based on the stress-strain curve analysis of the sample tested until failure. As later explained in Section 4.1, this curve is obtained by applying a loading stress to the sample and recording a process by a camera, therefore obtaining a 2D image for each load value applied to the specimen. For this purpose, Cauchy stress has been considered the most appropriate since it corresponds to the force or load divided by the area of the section of the sample as follows:

$$\sigma = \frac{N}{A}, \quad (1)$$

where σ is known as Cauchy stress, N is the applied force (in our experiments it corresponds to the load applied to the blood vessel in each measurement), and A is the area of the sample section. Consequently, σ is calculated by taken into consideration the geometry of the sample.

In particular, the porcine vessels exhibit the strain-stress curve displayed in Figure 1. In this representation, two different behaviour phases can occur depending on the amount of strain experimented by the sample, as explained in [22, 23]. Firstly, for low values of the strain a linear region exists in which the elastin composition prevails in the mechanical response of behaviour of the artery which is the collagen composition. By linear fitting of each region it is possible to obtain the value of Young's modulus that characterizes the elastin and collagen phases, respectively. Collagen Young's modulus is much larger than its elastin counterpart, thus implying a lower stiffness of the sample in this phase. Therefore, the collagen phase is chosen because in the elastin phase there are not enough significant points to approximate with reliability. Besides, this elastin phase is considered when the sample has less rigidity and the hyperelastic model is better fit with collagen region.

Moreover, it is also important to obtain the strength of the material (F_m) as the maximum load to failure, so that if the loading stress continues then the material breaks. Other relevant parameters are the ultimate tensile strength (UTS) defined as $S_r = F_m$ and the elongation under maximum load, as explained later. Furthermore, the true (or logarithmic) deformation $d\varepsilon$ is defined as the ratio between the increase in length (Δl) and the length of the sample (l) at any instant,

$$d\varepsilon = \frac{\Delta l}{l}, \quad (2)$$

The values of engineering ($d\varepsilon$) and logarithmic (s) deformations are related according to the following expression:

$$s = \ln \left(1 + \frac{\Delta l}{l_0} \right), \quad (3)$$

From the values (F , Δl) obtained in the mechanical test, one is able to plot the uniaxial component of tensors of Cauchy (σ) and the finite strain tensors (s) as displayed in Figure 1, thus obtaining its characteristic points (basically, the point in which the material suffers the mechanical failure and the point of the transition between elastin and collagen regions).

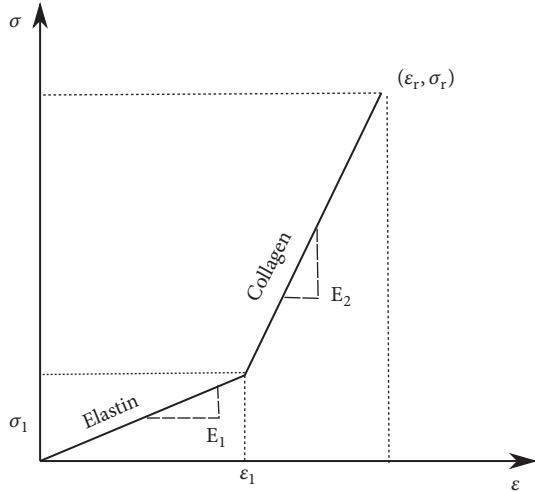


FIGURE 1: Theoretical stress-strain relationship for an elastic swine vessel reported by Garcia Herrera [22, 23]. Different Young's modulus values, E_1 and E_2 , characterize the regions in which the mechanical behaviour is dominated by elastin and collagen composition of the vessel, respectively. These regions are separated by a critical point of the curve of stress-strain (ϵ_1, σ_1) and the collagen phase ends abruptly when the failure of the material occurs (ϵ_r, σ_r) .

3. Biomechanical Strain Tensor Calculation on Arteries Samples

From the previous section we have derived an expression for the Cauchy stress that depends on the strain tensor. Let us now define two Cartesian directions, a and b (in our case the plane defined by ab corresponds to the XY plane, since the 2D image is recorded in the plane parallel to the force applied to the specimen). The plane ab is discretized by defining a 2D mesh within a region of interest (ROI, denoted as x) distributed along the aforementioned directions. Then, both the deformation gradient (F) and the Green-Lagrange axial deformation (S) are obtained to estimate the deformation of the specimen.

First, the deformation gradient of the region of interest in the direction a regarding the address b is a tensor given by

$$F_{ab} = \frac{\partial x_a}{\partial x_b^0}, \quad (4)$$

where in the previous expression the superscript 0 refers to the position at the initial instant of the experiment. F_{ab} is a Jacobian matrix or deformation gradient that acts as an operator transforming certain initial vectors (belonging to the environment of a point) from a reference configuration into the corresponding vectors in a final configuration. In this case, the initial state is when any deformation is applied to the sample whereas the ending state is measured after several successive deformations even leading to the failure of the material.

For the computational calculation, (4) must be discretized but this procedure is nontrivial. Since we move in a 2D plane,

one can define the four components in which Lagrangian notation is applied as

$$F_{11}^k(i, j) \approx \frac{x_1^k(i, j) - x_1^k(i, j+1)}{x_1^0(i, j) - x_1^0(i, j+1)}, \quad (5)$$

$$F_{12}^k(i, j) \approx \frac{x_1^k(i, j) - x_1^k(i, j+1)}{x_2^0(i+1, j) - x_2^0(i+1, j)}, \quad (6)$$

$$F_{21}^k(i, j) \approx \frac{x_2^k(i, j) - x_2^k(i, j+1)}{x_1^0(i, j) - x_1^0(i, j+1)}, \quad (7)$$

$$F_{22}^k(i, j) \approx \frac{x_2^k(i, j) - x_2^k(i+1, j)}{x_2^0(i, j) - x_2^0(i+1, j)}, \quad (8)$$

with i and j being the original coordinates representing the recorded ROI of the specimen (therefore, it is an immobile reference) and the superscript k denotes the video frame of the sequence of the experiment ($k = 0$ is the initial frame) since the stress σ is evaluated for each load increment in the tensile test. On the other hand, subscripts 1 and 2 denote, respectively, the X and Y Cartesian directions to which the deformation of the analyzed ROI points. Note that in this formulation the initial position of the specimen (superscript 0) has been defined as reference. These expressions justify the need for the application of an interpolation between frames k to facilitate the convergence. Note also that if the denominator reaches an extremely low value, then the value of F would be too large. To avoid this, the amount of load applied between consecutive video frames must be appropriate for linearly fitting the strain (and the deformation tensor components). Once the deformation gradient is computed, then Green-Lagrange strain can be derived as

$$\epsilon = \frac{1}{2} (FF^T - I) \quad (9)$$

in which I denotes the identity matrix and T superscript is the transposed matrix. Physically, the strain ϵ represents the quadratic difference between the lengths of deformed and nondeformed state; that is to say, this tensor measures the difference between the squares of differential surface elements in both cases.

By considering that our interest lies in the deformation in the direction in which the load is applied to the sample, then (9) is simplified to

$$e = \frac{\Delta l}{l_0} = \frac{l - l_0}{l_0}, \quad (10)$$

where e is the elongation at maximum load. For the particular case of a vessel sample let us assume that it has a thin wall; namely, its thickness is lower than one tenth of its length (see [24]). This approximation allows for the treatment of the wall as a surface and is subsequently using the Laplace-Young equation to estimate the circumferential stress created by an

internal pressure (burst pressure) in a thin-walled cylindrical pressure vessel as shown below

$$\begin{aligned} T_c &= \frac{Pr}{t} \longrightarrow \\ P &= \frac{2tT_c}{r}, \end{aligned} \quad (11)$$

where $T_c = N/A$ is the circumferential stress, P is the pressure, r is the radius, and t is the sample thickness. Note that double the thickness has been considered in (11) due to the form of adjusting the sample (ring) to the clamps, as further explained in Section 6.2.

4. Materials and Methods

4.1. Mechanical Testing. The theory of large strains has been applied for studying carotid vessels of swines as hyperelastic materials, in order to test their tensile strength and elongation at fracture. The samples have been grouped into two groups, native and decellularized arteries, further referred to as NA and DA, respectively. The main objective of this study is evaluating the impact of the arteries decellularization procedure on their mechanical properties. In particular, this analysis requires the following:

- (1) Stress rupture testing of each type of artery by calculating the maximum tensile load required for the fracture.
- (2) Computing the modulus of elasticity NA and DA vessels.
- (3) Extracting the hydrostatic pressure from arteries under circumferential tension.
- (4) Analyzing the relationship between the mechanical properties and histological analyses of vessels.

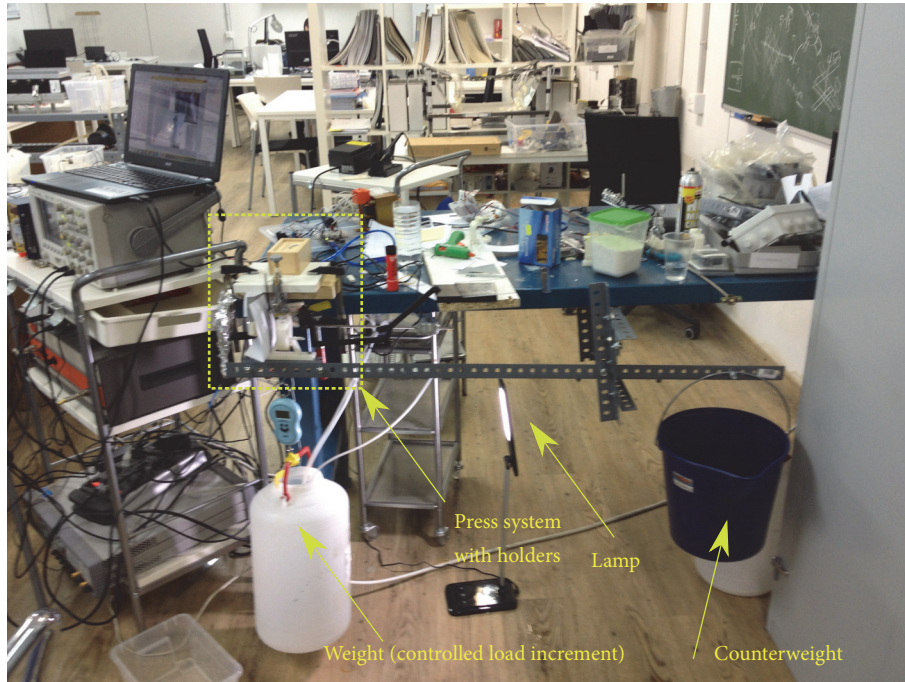
To carry out these goals, the strain-stress curve of each sample needs to be measured. With this purpose, the tensile-compression press included in Figure 2 has been arranged for the mechanical test of the samples. In particular, it includes the bars that support the entire setup, a water container to apply a load to the vessel and another bucket filled with water acting as a counterweight. The press, as indicated in Figures 2 and 3(a), consists of two clamps fabricated in epoxy resin for favoring the fastening of the arteries. The vessel sample remains fixed by means of PLA-printed holders (see Figure 3(b)) that prevent the artery from torsion and other undesired movement.

A peristaltic pump (controlled by an Arduino microcontroller) is used to increase the load gradually at 8 grams increments, while keeping the vessels continuously hydrated. After each load step, a pause of 20 seconds has been set in order to stabilize the system and avoid undesired rheological phenomena or oscillations that may hinder the tracking. It is worth pointing out that such a small load increment has been chosen because when the motion between consecutive frames is excessively large, a nonlinear regime of movement may occur.

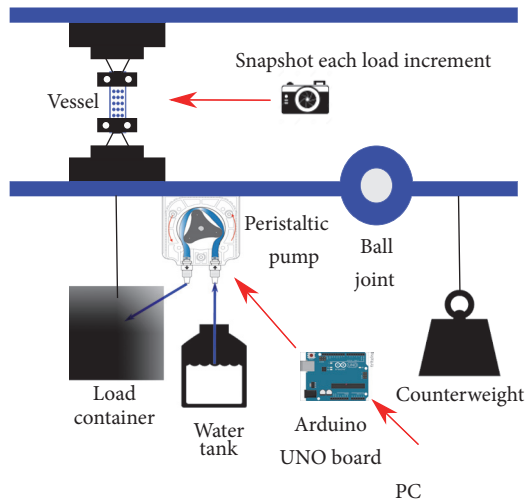
Then, the deformation has been measured by recording a high-resolution video and obtaining the displacements from the recorded images as previously reported [2, 25, 26]. In particular, we apply a cross-correlation image algorithm that is described thoroughly in Section 5 for strain measurement. This video is triggered at the beginning of pumping and custom image capture software is used to record at a rate of 1 frame per load increment until the sample breakdown. A conventional camera (IPEVO Ziggi-HD High Definition USB CDVU-04IP model, 5 Mpix, 1280×720 resolution) has been used to acquire the image sequence in the parallel plane with respect to the surface in which the deformation tensor is measured. Finally, it is worth underlining that the preparation of the experiment is essential and includes some basic steps:

- (i) By engraving the vessel with a speckle or random dot pattern the monitorization of the strain of different regions of the sample is facilitated. Taking into account the fact that the strain is measured by using a cross-correlation technique (as explained in Section 5), if more details are added to the vessel then this algorithm works better as more characteristic points can be followed with the tracking procedure. The analysis of an image sequence based on correlation works better if some details of the sample changes during the experiment, as this operation highlights the morphological differences that have occurred. As the surface of the sample is flat and without any striking feature, the staining is mandatory if a reliable strain assessment is needed. In this case, acrylic black paint has been used to apply the pattern over the sample and then the sample is dried out a few minutes.
- (ii) A uniform background and illumination throughout the entire experiment help to maintain an optimum contrast in the recorded image
- (iii) The arteries must be kept continuously hydrated to maintain their mechanical properties, for instance, by spraying them with PBS during the mechanical test. Thanks to the waterproof capability of the acrylic paint, once the artery is stained the pattern is not removed with the PBS, thus providing an enduring marking of the sample.
- (iv) All the blood vessels are cut with the same mold (see Figure 3(c)) for tailoring them and maintain similar dimensions, thus controlling the area of the minimum section where each one break.

4.2. Tissue Harvest and Preparation. Porcine carotid arteries are obtained from a slaughterhouse and transported to the laboratory stored in cold PBS with 1% penicillin/streptomycin. Immediately after arrival, carotid arteries are cleaned to remove the excess of connective and adventitial tissues. Next, the carotid arteries are rinsed in sterile PBS and cut into segments of 3-5 cm in length and 3-4 mm in diameter. Finally, they were immediately frozen in PBS at -80°C for later use; it has been previously shown that the freeze-and-defrost process does not significantly affect artery mechanics [26–28]. At the time of testing, specimens were



(a)



(b)



(c)

FIGURE 2: (a) Press setup comprising clips and fasteners for holding the sample attached to several weights and counterweights for controlling the applied load. The data are sent to a computer and processed with MATLAB. (b) Schematic representation of the whole measurement system. The artery suffers an increasing load and the process is registered by a camera. (c) Placement of the sample into the clamps to undertake the uniaxial tensile experiment.

thawed in a 37°C water bath and tested within 1 h of thawing [29].

4.3. Decellularization Process. The decellularization process of carotid tissue samples is performed as previously described [2] using enzymatic digestion and detergent extraction. Carotid arteries were immersed in deionized water for 24 h at 4°C followed by treatment with 0.05% Trypsin with 0.02% EDTA (Sigma Aldrich, St. Louis, MO, USA) for 1 h at 37°C. After a short rinse in PBS to remove trypsin excess,

the samples are treated with a solution of 2% Triton X-100 and 0.8% ammonium hydroxide (Sigma) in deionized water for 72 h at 4°C. This solution has been changed every 24 h. After the decellularization, samples were washed in deionized water three times, for 24 h each, to remove chemical residues. All these steps of the preparation are carried out under continuous shaking except trypsin incubation.

4.4. Histological and Immunofluorescence Analyses. Samples were fixed in 4% paraformaldehyde, embedded in paraffin in

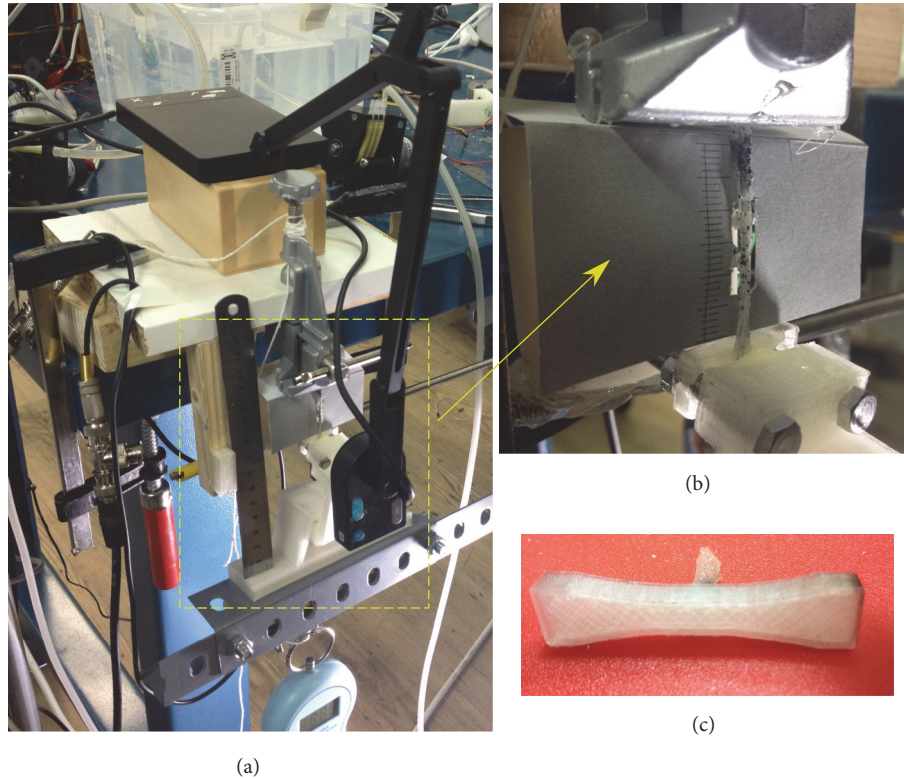


FIGURE 3: (a) Close-up view of the camera attached to the press setup for performing the tracking of the motion. (b) Vessel sample placed in the press during a test. Note that a random speckle pattern has been impressed over it to ease the strain tracking with the image cross-correlation algorithm. (c) Mold printed in 3D with polylactic acid (PLA) to maintain the dimensions of the samples.

an automatic tissue processor (TP1020, Leica, Germany), cut into 5 mm sections, and stained with Hematoxylin and Eosin (H&E) and Masson's Trichrome as previously reported [30]. Images are acquired with an inverted microscope (Nikon H550s, USA).

4.5. Scanning Electron Microscopy (SEM). Arteries are washed twice with 0.1 M cacodylate buffer (Sigma) and fixed with 2.5% (w/v) glutaraldehyde in 0.1 M cacodylate buffer (pH 7.4; Poly-sciences, Warrington, PA) for 4 h at 4°C. Thereafter, samples are rinsed several times with sodium cacodylate buffer. After fixation, samples are postfixed with 1% w/v osmium tetroxide for 1 h RT, dehydrated stepwise with ethanol (50%, 70%, 90% and 100%, 15 min each), critical point dried in CO₂, and gold coated by sputtering. Finally, the images are examined by using a FEI Quanta 400 scanning electron microscope (Oregon, USA).

4.6. Statistical Analysis. Each experiment has been conducted with 10 samples. Results are presented as mean \pm standard deviation (SD). A Student's t-test is used to test the significance level between specific cases. The results are considered significantly different at p-values $p < 0.05$ (*) and $p < 0.01$ (**).

5. Image Cross-Correlation Algorithm for Strain Tracking

Traditionally, obtaining precise strain measurements during uniaxial tensile testing can be performed by clamping a strain gauge to the sample. Nevertheless, here we aim at obtaining a contactless strain measurement, whereby we need laser extensometers or a recording of digital images series and then applying a digital image correlation software; see [31, 32]. The most conventional correlation algorithms monitor the positions of two parallel markers during the experiment (for instance, comparing an intensity profile along the tensile direction), and hence the strain of the sample can be calculated. According to previous works [32], one of the main difficulties for strain assessment based on correlation occurs when the deformed area of the sample is large to hinder the matching of consecutive images. In this regard, our protocol of measurement is robust thanks to the speckle engraving of the sample.

As previously explained in Section 4.1 and sketched in Figure 2(b), a press system has been designed for conducting different mechanical test over the vessel samples. Note that it is important to choose an appropriate distance for recording so that the failure of the sample occurs far from the edges of the image and at the same time make the most of the camera field of view. Moreover, for obtaining a good calibration for

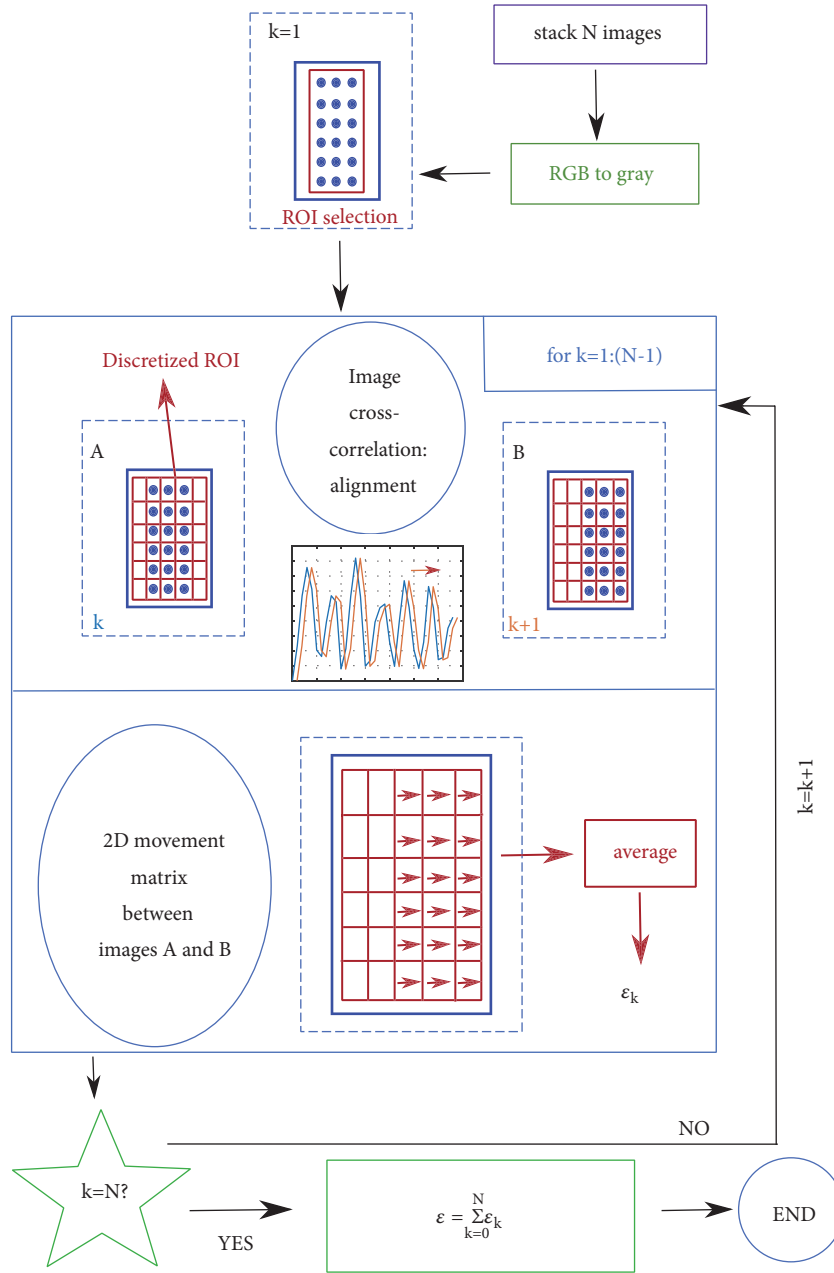


FIGURE 4: Flowchart summarizing the algorithm of cross-correlation for finding the strain from an image sequence.

the measurement of the strains, the pixel size of the camera and its resolution must be taken into account or, alternatively, an object of known dimensions can be included in the recorded field of view. In this way, it is possible to correlate the measurement in pixels registered by the camera and the real distances. After the acquisition of this image sequence, a tracking algorithm based on image cross-correlation is applied sequentially between each consecutive pair of frames of the sequence. This algorithm, also summarized in the flowchart from the Figure 4, follows these steps:

- (1) We start with a sequence of N input images that contains a recording of all the experiment. If they are

in RGB color (as in our case), they are firstly converted to grayscale.

- (2) A ROI or mask is defined in the first frame of the sequence so that all the images outside this mask are ignored. Typically, this ROI is the middle area of the vessel in order to circumvent unwanted border effects. For this ROI the movement is approximated by a piecewise linear function.
- (3) A discretization is applied to transform the ROI into an array of discrete blocks, so that the number of characteristic points is reduced. The tracking algorithm is applied to each of these blocks instead of applying it

pixel by pixel, for alleviating its computational cost. Note that the number of blocks should be optimized by taking into account both the camera resolution and the amount of strain experienced by the sample. For instance, if the block-size is extremely small then the ROI will contain too many blocks, thus producing an increase in computation time. Moreover, these tiny blocks are more prone to noise problems. Conversely, the discretization with a small number of large blocks is expected to hinder the most subtle movements. Furthermore, the largest the strain is experienced by the sample, the more the blocks are needed to monitor the process while minimizing in the measured distances. Consequently, there is a trade-off between the computational cost and the precision of the tracking algorithm. In this case, a rectangular discretization mesh has been chosen with blocks of 8 pixels in width by 16 pixels in height.

- (4) Between each pair of consecutive frames, hereinafter referred to as A (the first image) and B (the second one), the motion of each block of the discretized ROI is measured by finding the peak of cross-correlation between A and B. We compute the maximum of image cross-correlation (xcorr) to obtain the motion (strain) that have occurred within every discretization block of the block between A and B. One can obtain the 2D strain as follows:

$$\varepsilon(x_1^k, x_2^k) = \max [\text{xcorr}(\text{image}_k, \text{image}_{k+1})] \quad (12)$$

In this way, the best matching between the two images is found. It is important to highlight that, as the images are bidimensional (2D), the correlation is also evaluated in the 2D plane. It is worth remarking that the speckle pattern impressed in the artery helps out with tracking as it enhances the number of features to be trailed unless an undesired torsion movement occurs. Nevertheless, the two clamps that hold the sample edges prevent this torsion from happening.

- (5) Taking into consideration the fact that throughout our experiments only uniaxial tests (e.g., along x_1 axis) have been performed, then the strain in that direction prevails over the torsion movement (along x_2 axis). Consequently, by averaging the 2D motion of all the blocks one obtains the mean strain suffered by the sample under test for the k -image of the sequence, denoted as

$$\varepsilon_k = \text{mean} [\varepsilon(x_1^k, x_2^k)]. \quad (13)$$

- (6) Now we proceed with the following pair of images of the sequence. The initial ROI is updated for taking into account the mean movement (ε_k) experienced by the sample in the previous pair of frames. The steps ((3)-(5)) are repeated until reaching the end of the recorded sequence.

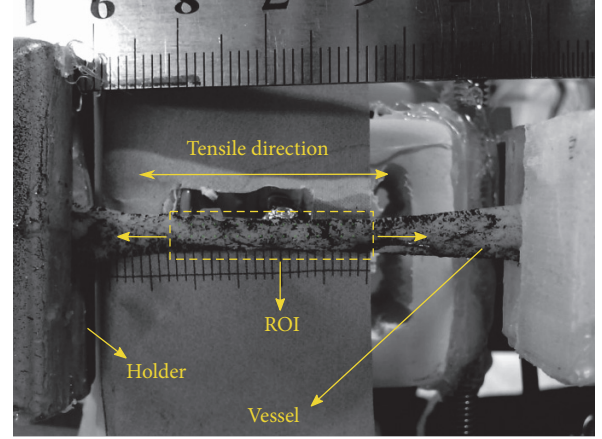


FIGURE 5: Example of vessel attached to two holders that secure it during the uniaxial tensile experiment, thus avoiding undesired torsion movement. The region of interest (ROI) has been delimited by a dashed yellow line.

- (7) We compute the global strain along all the experiment by adding all the strain between consecutive images:

$$\varepsilon = \sum_{K=1}^{N-1} \varepsilon_k \quad (14)$$

Thanks to this image correlation algorithm different mechanical tests have been conducted and monitored, namely, uniaxial test (explained in Section 6.1) and circumferential tensile stress test (Section 6.2).

6. Results and Discussion

6.1. Uniaxial Testing. For uniaxial testing, the sample is placed as shown in Figure 5 and stretched with the experimental setup from Figure 2. From this framework it is possible to obtain a 2D strain, but the movement along the direction in which the load is applied has a prevailing effect (as demonstrated in the experiment sequences displayed in Figures 6 and 7). Consequently, only this direction is considered for the analysis. In this way, the strain-stress curve of the samples is obtained (see an example for two arteries, one of each group, in Figure 8(a)). Next, Young's modulus has been extracted as the slope of its linear region (see Figure 8(b)). We recall that this linear region is associated with the collagen content of the sample. In particular, from Figure 8(a) the expected value for Young's modulus is 4.31 ± 0.25 MPa for the decellularized sample and 3.11 ± 0.15 MPa for the native one. After computing this stress-strain curve for $n = 10$ samples in each category, we obtain the results included in Figure 8(b): 4.98 ± 0.67 MPa for the decellularized versus 3.53 ± 0.56 MPa for the native specimens. These values are in good agreement with the usual blood vessels range of Young's modulus [10, 13, 26]. The value of Young' modulus slightly changes when a conventional correlation algorithm based on the tracking of two parallel markers is used. These markers are placed in both edges of the vessel along the direction in

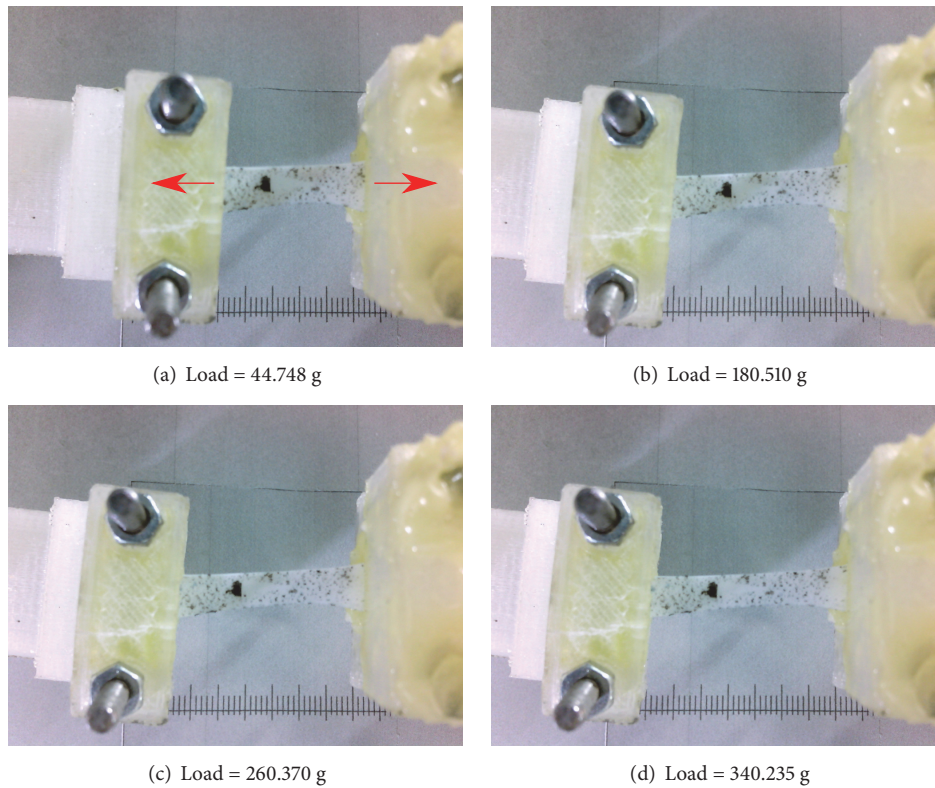


FIGURE 6: Four different frames from a recording of a uniaxial tensile test in a decellularized vessel with an increasing load. The sample is stretched in the direction marked with red arrows, and the strain tracking is enhanced thanks to the speckle pattern applied to the sample.

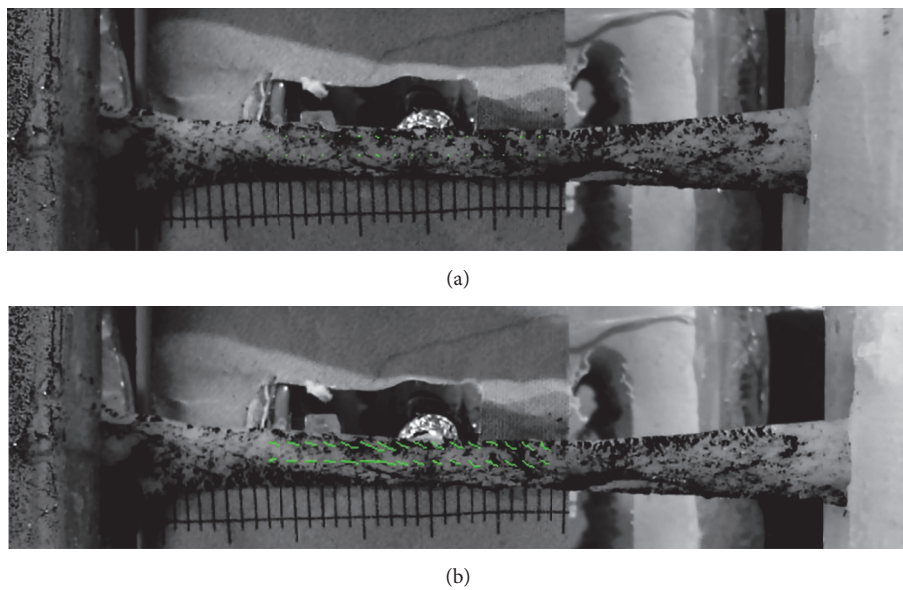


FIGURE 7: Two different frames showing the typical output of the tracking algorithm for uniaxial tensile test over an artery. Green dots represent the center of each block in the discretized ROI and the green line represents the movement in regard to the first frame of the recorded sequence. The reader is further referred to the video Visualization 1 in Supplementary Materials to see the whole tracking sequence.

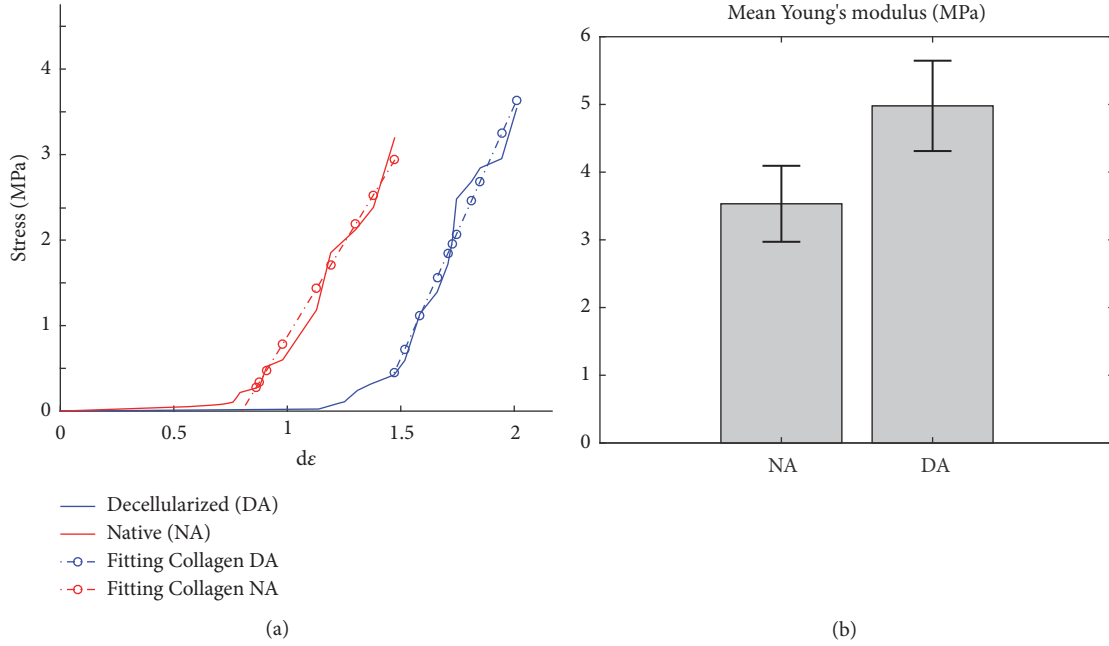


FIGURE 8: (a) Experimental stress-strain relationship for elastic swine vessels, along with the linear fitting of the curve along the collagen region. (b) Young modulus for each group of vessels (represented as mean \pm -SD, (**) $p < 0.01$).

which the load is applied. With this procedure one reaches a value of 4.47 ± 0.82 MPa for decellularized and 3.46 ± 0.75 for native vessels, respectively. The underestimation of Young's modulus is probably due to the deformation experienced by the sample, hence obstructing the tracking of the strain. The artery warped not only along the longitudinal direction, as expected in a uniaxial test, but also in the traverse direction. Moreover, by averaging several 2D blocks of the sample instead of only using 1D intensity profile correlation-based matching we obtain a more accurate measurement, as the small undesired and unavoidable torsion of the sample along the traverse direction has also been taken into account. The deformation maps have been also analyzed for native and decellularized arteries at several elongation ratios (see Figure 9). An initial cross-section of $20 \text{ mm} \times 5 \text{ mm}$ has been considered for all the vessels.

Indeed, there exist relevant changes (p -values of $p < 0.01$ in Student's T- test) between both groups. Therefore, it could be interpreted as the procedure of decellularization has a remarkable impact on elasticity.

6.2. Ring Testing. Ultimate tensile strength, maximum load and burst pressure has been determined for ring sections of arteries ($n = 10$ samples in each group), in order to test the circumferential stress. The ring sections are prepared as explained in Section 4.2 and mounted on custom-made holders. Each sample is tested by applying an increasing load until failure. The diameter, width, thickness, and length of each sample used for the calculations aforementioned in Section 2 are measured with a high-precision slide caliper. The sample displacement is determined by the image correlation algorithm and, in this case, the speckle pattern is

engraved in the transverse wall of the ring. We must underline that the mean radius of the ring samples has been used for calculations because it represents the distance to the neutral axis or centroid.

The burst pressure of the samples is calculated from their maximum load to failure. We recall that twice the sample thickness has been considered as defined in (11). The ring is arranged wrapping the two clamps and is stretched along a certain direction in which there is a double layer of vessel; thus the effective thickness is twice that of the ring. The radial stress is calculated and converted to millibars by considering the load, the mean radius and the circumferential UTS [9, 24, 33]. In comparison with the uniaxial test, the circumferential mechanical properties are significantly different due to different disposal of vessel fibers along longitudinal and circumferential directions.

The mechanical testing revealed significant differences between NA and DA rings. As summarized in Figure 10, there exist relevant dissimilarities between the mean burst pressure of the native arteries (1345.08 ± 96.58 mbar) and the decellularized group (1067.79 ± 112.13 mbar). Furthermore, there also exist differences regarding the maximum load that each type of artery can stand: the native stands 19.42 ± 0.80 N whereas the decellularized is able to withstand a lower value (15.78 ± 0.79 N). Finally, the circumferential UTS is also different, with an expected value of 3.71 ± 0.37 [MPa] within the native group while in the decellularized this value decreases (2.93 ± 0.18 [MPa]).

6.3. Histological Characterization of Native and Decellularized Arteries. As explained in Section 4.2, the samples are first

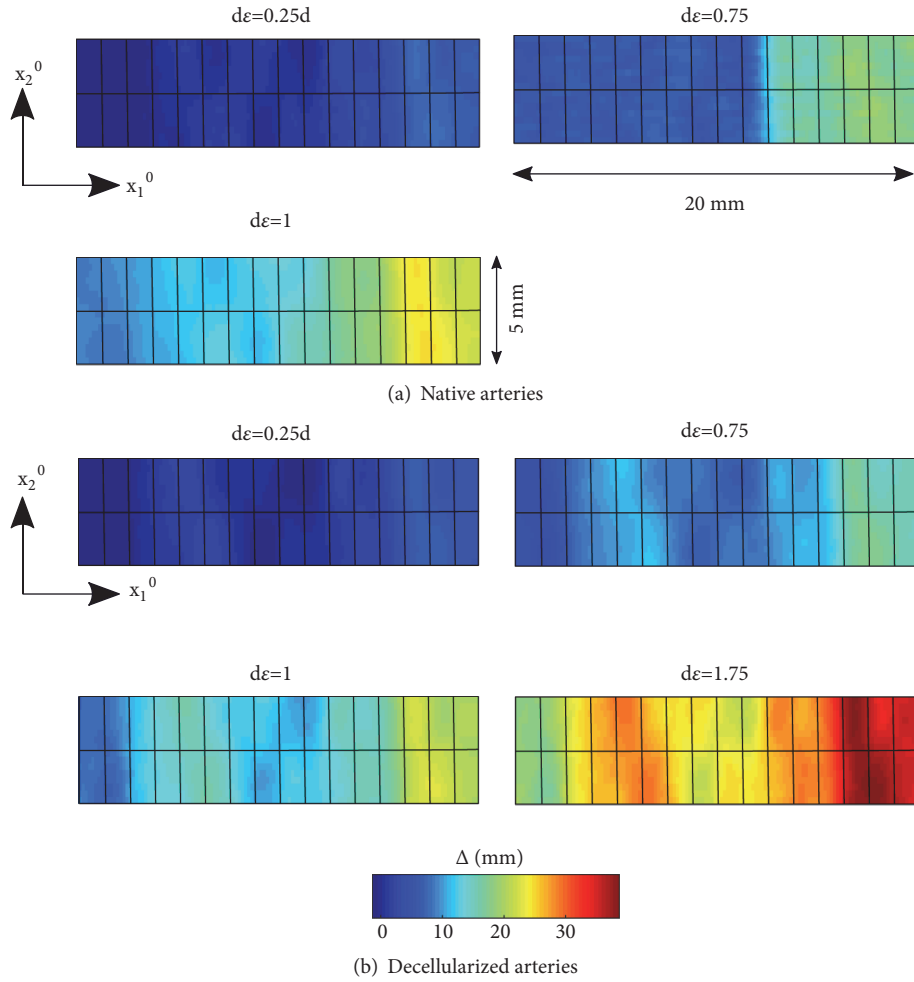


FIGURE 9: Deformation maps for a native (a) and decellularized (b) vessel, evaluated at different elongation ratios. An initial rectangular cross-section of $20 \text{ mm} \times 5 \text{ mm}$ has been considered in all cases. The rectangular grid accounts for the discretization mesh applied for the tracking algorithm.

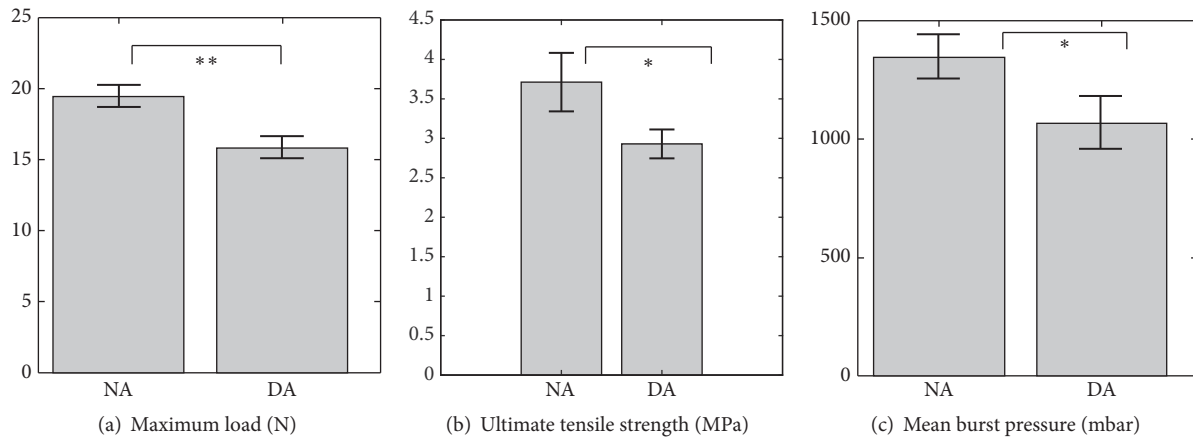


FIGURE 10: Comparison between the mechanical parameters of native (NA) and decellularized (DA) arteries in the circumferential stress test, including the load (a), ultimate tensile strength (b), and hydrostatic burst pressure (c) from annular portions (rings) of samples. All the results are represented as mean±SD, (*) $p < 0.05$ and (**) $p < 0.01$.

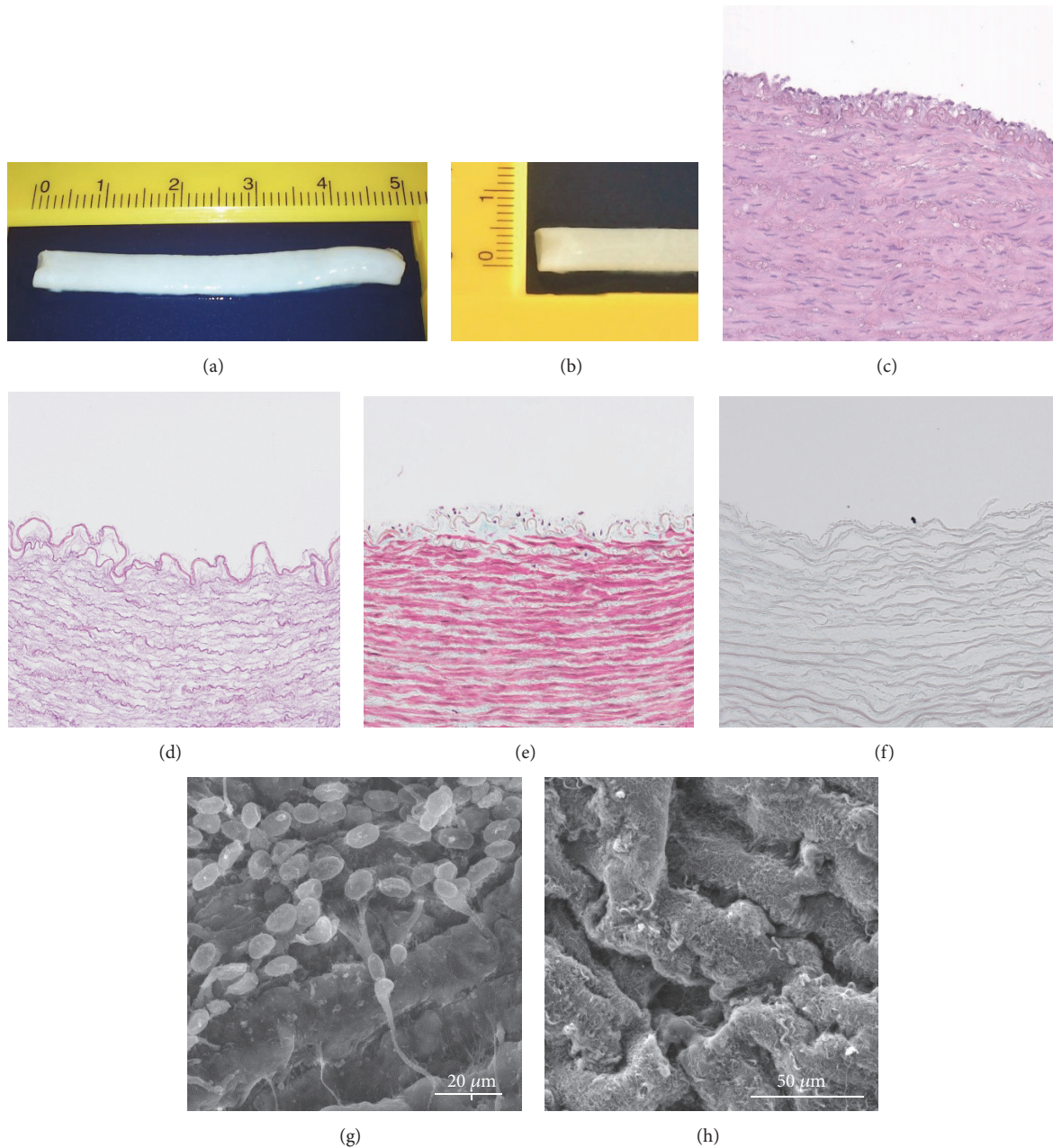


FIGURE 11: Characterization of porcine carotid arterial tissue before and after decellularization. (a,b) Macroscopic images of decellularized left common porcine carotid artery (artery length ~ 50 mm; inner diameter ~ 4 mm). Histology of porcine arteries: (c, e) native arteries and (d, f) decellularized arteries. (c) H&E staining of native arteries. (d) H&E staining of decellularized arteries showing complete removal of vascular cells. (e) Masson's Trichrome staining of native arteries. (f) Masson's Trichrome staining of decellularized artery showing collagens fibers and no cells (20x magnification). SEM micrographs of the luminal surface: (g) native arteries and (h) decellularized arteries; scale bar indicates $20 \mu\text{m}$ and $50 \mu\text{m}$, respectively.

prepared and cut (see Figures 11(a) and 11(b)). Then, histological analyses and scanning electron microscopy (SEM) are performed on artery samples to demonstrate the efficacy of the decellularization process in native carotid arteries. Complete removal of vascular cells is confirmed by H&E and Masson's Trichrome staining after the decellularization procedure (Figures 11(d) and 11(f)) when compared with native arteries (Figures 11(c) and 11(e)). Native arteries showed

high density of cells embedded in collagen fibers (stained turquoise) (Figure 11(e)), while no cells were detected in the decellularized arteries (Figures 11(d) and 11(f)). In addition, the characteristic concentric layers of elastin (stained pink) and collagen fibers of native arteries remained intact at decellularized arteries showing the same circumferential orientation and a well preserved ECM (Figures 11(d) and 11(f)). SEM analyses were used to further confirm the removal of the cells

at the luminal surface and demonstrated that decellularized arteries retain the basic extracellular microstructure (Figures 11(g) and 11(h)).

7. Conclusions

In order to provide quality criteria for natural and bio-engineered arteries, different traction mechanical tests have been carried out for two types of blood vessels, native and decellularized. The mechanical properties have been analyzed which are the UTS, Young's modulus, maximum load at failure, and burst pressure. To assess these parameters, several intermediate physical measurements of the vessel samples have been measured such as radial stress, radius, thickness, width, and length. The stress-strain curves are also computed based on an image cross-correlation algorithm developed in-house, combined with a laboratory-prototyped tensile testing machine designed for this purpose.

Strain at failure is seen to increase after decellularization due to cell removal and increased collagen fiber mobility along with the uncrimping of collagen fibers. After decellularization the collagen matrix remains, but other cellular proteins are removed. Therefore, the amount of collagen tends to increase as a percentage of dry weight after decellularization. Then, the increase in stiffness in terms of elastic modulus in the decellularized arteries may be due to the decrease in the cell layer, leaving only a hardening collagen layer (shown in Figure 11). Note that the results are interesting for future experiments or biomedical applications in which different coatings are tested to reinforce the strength of the arteries.

Several studies have shown structural alterations that could be related to changes in mechanical properties. Though the intention of most decellularization procedures is to effectively remove all the cells and nuclear components while minimize disruption to the ECM, the removal of cells can lead to changes to native ECM structure [29]. Moreover, depending on the decellularization method some studies have demonstrated alterations of the ECM structure and thus in the mechanical properties, being SDS and Triton X-100 based protocols more suitable for maintaining the major structure of the elastin and collagen network in the ECM [34].

In summary, this technique is able to measure the strain in the regime of large displacements and enables high-resolution image of the local strains. Thus, it provides a valuable tool for characterizing several biomechanical parameters of the vessels (Young's modulus, stress-strain curve, etc.) and also other hyperelastic materials through uniaxial (or biaxial) tension test. Finally, it is worth pointing out that with image cross-correlation algorithm it is possible to obtain a two-dimensional strain map, from which the heterogeneity and several components of the strain tensor can be reconstructed from a single measurement. In this way, it provides a 2D tracking of the mechanical properties variations; hence a deeper insight of the stress test is obtained.

Data Availability

The data used to support the findings of this study are available from the corresponding author upon request.

Conflicts of Interest

The authors declare that there are no conflicts of interest regarding the publication of this paper.

Acknowledgments

This research was supported by the Ministry of Education [DPI2014-51870-R, DPI2017-85359-R, UNGR15-CE-3664, and PII6/00339], Junta de Andalucía [PIN-0030-2017, PIN-0379, CTS-6568, and PI-0107-2017 Projects], and University of Granada [PP2017-PIP2019]. Ministerio de Economía y Competitividad is also acknowledged for funding the project [TEC2014-57394-P] and MNA Scientific Unit of Excellence (UCE.PP2017.03).

Supplementary Materials

Visualization 1: tracking algorithm for uniaxial tensile test until failure applied in an artery. Green dots represent the center of each block in the discretized ROI and the green line represents the movement apropos of the first frame of the recorded sequence. A pause of 20 seconds has been set between the acquisitions of consecutive frames. (*Supplementary Materials*)

References

- [1] C. Quint, Y. Kondo, R. J. Manson, J. H. Lawson, A. Dardik, and L. E. Niklason, "Decellularized tissue-engineered blood vessel as an arterial conduit," *Proceedings of the National Academy of Sciences of the United States of America*, vol. 108, no. 22, pp. 9214–9219, 2011.
- [2] E. López-Ruiz, S. Venkateswaran, M. Perán et al., "Poly(ethylmethacrylate-co-diethylaminoethyl acrylate) coating improves endothelial re-population, bio-mechanical and anti-thrombogenic properties of decellularized carotid arteries for blood vessel replacement," *Scientific Reports*, vol. 7, no. 1, 2017.
- [3] A. Carpentier, J. L. Guermonprez, A. Deloche, C. Frechette, and C. DuBost, "The aorta-to-coronary radial artery bypass graft: a technique avoiding pathological changes in grafts," *The Annals of Thoracic Surgery*, vol. 16, no. 2, pp. 111–121, 1973.
- [4] L. R. Caplan, "Lacunar infarction and small vessel disease: pathology and pathophysiology," *Journal of Stroke*, vol. 17, no. 1, p. 2, 2015.
- [5] F. M. van der Valk, S. L. Verweij, K. A. Zwinderman et al., "Thresholds for arterial wall inflammation quantified by 18F-FDG PET imaging," *JACC: Cardiovascular Imaging*, vol. 9, no. 10, pp. 1198–1207, 2016.
- [6] L. Iop and G. Gerosa, "Guided tissue regeneration in heart valve replacement: from preclinical research to first-in-human trials," *BioMed Research International*, vol. 2015, Article ID 432901, 13 pages, 2015.
- [7] A. Keable, K. Fenna, H. M. Yuen et al., "Deposition of amyloid β in the walls of human leptomeningeal arteries in relation to perivascular drainage pathways in cerebral amyloid angiopathy," *Biochimica et Biophysica Acta (BBA) - Molecular Basis of Disease*, vol. 1862, no. 5, pp. 1037–1046, 2016.
- [8] S. L. Dahl, C. Rhim, Y. C. Song, and L. E. Niklason, "Mechanical properties and compositions of tissue engineered and native

- arteries,” *Annals of Biomedical Engineering*, vol. 35, no. 3, pp. 348–355, 2007.
- [9] Y. Zhao, S. Zhang, J. Zhou et al., “The development of a tissue-engineered artery using decellularized scaffold and autologous ovine mesenchymal stem cells,” *Biomaterials*, vol. 31, no. 2, pp. 296–307, 2010.
- [10] Y. M. Ju, J. S. Choi, A. Atala, J. J. Yoo, and S. J. Lee, “Bilayered scaffold for engineering cellularized blood vessels,” *Biomaterials*, vol. 31, no. 15, pp. 4313–4321, 2010.
- [11] W. Gong, D. Lei, S. Li et al., “Hybrid small-diameter vascular grafts: Anti-expansion effect of electrospun poly ϵ -caprolactone on heparin-coated decellularized matrices,” *Biomaterials*, vol. 76, pp. 359–370, 2016.
- [12] Y.-C. Fung, *Biomechanics*, Springer, 1990.
- [13] J. D. Enderle and J. D. Bronzino, *Introduction to Biomedical Engineering*, Academic Press, 2012.
- [14] F. A. Duck, *Physical Properties of Tissues: A Comprehensive Reference Book*, Academic Press, 2013.
- [15] A. N. Natali, E. L. Carniel, P. G. Pavan, P. Dario, and I. Izzo, “Hyperelastic models for the analysis of soft tissue mechanics: definition of constitutive parameters,” in *Proceedings of the Biomedical Robotics and Biomechatronics, BioRob 2006*, pp. 188–191, IEEE, 2006.
- [16] E. J. Weinberg and M. R. Kaazempur-Mofrad, “A large-strain finite element formulation for biological tissues with application to mitral valve leaflet tissue mechanics,” *Journal of Biomechanics*, vol. 39, no. 8, pp. 1557–1561, 2006.
- [17] J. M. Deneweth, S. G. McLean, and E. M. Arruda, “Evaluation of hyperelastic models for the non-linear and non-uniform high strain-rate mechanics of tibial cartilage,” *Journal of Biomechanics*, vol. 46, no. 10, pp. 1604–1610, 2013.
- [18] G. A. Holzapfel, T. C. Gasser, and R. W. Ogden, “A new constitutive framework for arterial wall mechanics and a comparative study of material models,” *Journal of Elasticity*, vol. 61, no. 1–3, pp. 1–48, 2000.
- [19] G. A. Holzapfel, “Determination of material models for arterial walls from uniaxial extension tests and histological structure,” *Journal of Theoretical Biology*, vol. 238, no. 2, pp. 290–302, 2006.
- [20] G. A. Holzapfel and R. W. Ogden, “Constitutive modelling of arteries,” *Proceedings of the Royal Society A Mathematical, Physical and Engineering Sciences*, vol. 466, no. 2118, pp. 1551–1597, 2010.
- [21] R. P. Vito and S. A. Dixon, “Blood vessel constitutive models—1995–2002,” *Annual Review of Biomedical Engineering*, vol. 5, no. 1, pp. 413–439, 2003.
- [22] C. M. García-Herrera, D. J. Celentano, M. A. Cruchaga et al., “Mechanical characterisation of the human thoracic descending aorta: experiments and modelling,” *Computer Methods in Biomechanics and Biomedical Engineering*, vol. 15, no. 2, pp. 185–193, 2012.
- [23] C. M. García-Herrera, D. J. Celentano, and M. A. Cruchaga, “Bending and pressurisation test of the human aortic arch: experiments, modelling and simulation of a patient-specific case,” *Computer Methods in Biomechanics and Biomedical Engineering*, vol. 16, no. 8, pp. 830–839, 2013.
- [24] K. Schmidt-Nielsen, *Animal Physiology: Adaptation and Environment*, Cambridge University Press, 1997.
- [25] V. Alastrué, E. Peña, M. Martínez, and M. Doblaré, “Experimental study and constitutive modelling of the passive mechanical properties of the ovine infrarenal vena cava tissue,” *Journal of Biomechanics*, vol. 41, no. 14, pp. 3038–3045, 2008.
- [26] W. Sheridan, G. Duffy, and B. Murphy, “Mechanical characterization of a customized decellularized scaffold for vascular tissue engineering,” *Journal of the Mechanical Behavior of Biomedical Materials*, vol. 8, pp. 58–70, 2012.
- [27] M. Chow and Y. Zhang, “Changes in the mechanical and biochemical properties of aortic tissue due to cold storage,” *Journal of Surgical Research*, vol. 171, no. 2, pp. 434–442, 2011.
- [28] B. D. Stemper, N. Yoganandan, M. R. Stineman, T. A. Gennarelli, J. L. Baisden, and F. A. Pintar, “Mechanics of fresh, refrigerated, and frozen arterial tissue,” *Journal of Surgical Research*, vol. 139, no. 2, pp. 236–242, 2007.
- [29] C. Williams, J. Liao, E. Joyce et al., “Altered structural and mechanical properties in decellularized rabbit carotid arteries,” *Acta Biomaterialia*, vol. 5, no. 4, pp. 993–1005, 2009.
- [30] G. Jiménez, E. López-Ruiz, W. Kwiatkowski et al., “Activin A/BMP2 chimera AB235 drives efficient redifferentiation of long term cultured autologous chondrocytes,” *Scientific Reports*, vol. 5, Article ID 16400, 2015.
- [31] M. Jerabek, Z. Major, and R. Lang, “Strain determination of polymeric materials using digital image correlation,” *Polymer Testing*, vol. 29, no. 3, pp. 407–416, 2010.
- [32] P. Hung and A. S. Voloshin, “In-plane strain measurement by digital image correlation,” *Journal of the Brazilian Society of Mechanical Sciences and Engineering*, vol. 25, no. 3, 2003.
- [33] R. E. Shadwick, “Mechanical design in arteries,” *Journal of Experimental Biology*, vol. 202, no. 23, pp. 3305–3313, 1999.
- [34] Y. Zou and Y. Zhang, “Mechanical evaluation of decellularized porcine thoracic aorta,” *Journal of Surgical Research*, vol. 175, no. 2, pp. 359–368, 2012.

Research Article

Control Strategy and Experiments for Robot Assisted Craniomaxillofacial Surgery System

Tengfei Cui,¹ Yonggui Wang ,¹ Xingguang Duan,¹ and Xiaodong Ma²

¹Beijing Advanced Innovation Center for Intelligent Robots and Systems, School of Mechatronic Engineering, Beijing Institute of Technology 5 Nandajie, Zhongguancun, Haidian, Beijing 100081, China

²The General Hospital of the People's Liberation Army, China

Correspondence should be addressed to Yonggui Wang; wangyg1025@163.com

Received 10 December 2018; Revised 10 February 2019; Accepted 7 March 2019; Published 27 March 2019

Guest Editor: Marie Muller

Copyright © 2019 Tengfei Cui et al. This is an open access article distributed under the Creative Commons Attribution License, which permits unrestricted use, distribution, and reproduction in any medium, provided the original work is properly cited.

Since the intricate anatomical structure of the craniomaxillofacial region and the limitation of surgical field and instrument, the current surgery is extremely of high risk and difficult to implement. The puncturing operations for biopsy, ablation, and brachytherapy have become vital method for disease diagnosis and treatment. Therefore, a craniomaxillofacial surgery robot system was developed to achieve accurate positioning of the puncture needle and automatic surgical operation. Master-slave control and “kinematic + optics” hybrid automatic motion control based on navigation system, which is proposed in order to improve the needle positioning accuracy, were implemented for different processes of the operation. In addition, the kinematic simulation, kinematic parameters identification, positioning accuracy experiment (0.56 ± 0.21 mm), and phantom experiments (1.42 ± 0.33 mm, 1.62 ± 0.26 mm, and 1.41 ± 0.30 mm for biopsy, radiofrequency, and brachytherapy of phantom experiments) were conducted to verify the feasibility of the hybrid automatic control method and evaluate the function of the surgical robot system.

1. Introduction

With the development of modern medical technology and the application of new technology in clinical practice, robot-assisted surgery is widely used as supportive tool for diagnosis, operation planning, and treatment in surgical intervention. Robot assisted puncture surgery is being increasingly accepted as an alternative treatment for cancer patients for surgery, especially in biopsy, thermal coagulation, and brachytherapy [1–3]. This way benefits patients with advantages of functional saving, symptomatic palliation, and local disease control. The puncture surgeries for craniomaxillofacial region usually are performed by doctors, relying on plentiful clinical experience or various image navigation devices. The intricacy anatomic structure, the extremely irregular shape, and evident personalized feature in maxillofacial surgery bring great challenge to surgical operation [4]. In craniomaxillofacial lesions, especially recurrent maxillofacial cancer, although some experienced surgeon performing the procedure could reduce the potential risks and have some functional results by using commercialized surgery

navigation system [5], such as BrainLab, intraoperative accurate puncture is still difficult for many doctors because of the complex tissue structure and requirements of high accuracy puncture.

Minimally invasive surgical procedures in craniomaxillofacial regions involve tumor biopsy, radioactive seeds brachytherapy, and radiofrequency thermal coagulation. Maxillofacial tumor, especially in skull base region, is one of the most common diseases and early diagnosis is important for treatment. With advance of minimally invasive surgery, needle biopsy has become a widely used method for early diagnosis. Radioactive seeds brachytherapy is well suited for skull base tumor because, unlike traditional radiotherapy, it does not use very high dose rates and is less likely to harm critical organs. At present the procedures of brachytherapy are associated with exposure to radiation. Radiofrequency thermal coagulation faces many challenges including deep oval foramen, long puncture path, complex anatomy, and high precision requirements. Surgeon manually locates the skin entry site of needle, adjusts the angulation of the needle, and negotiates the obstruction during the puncture. These

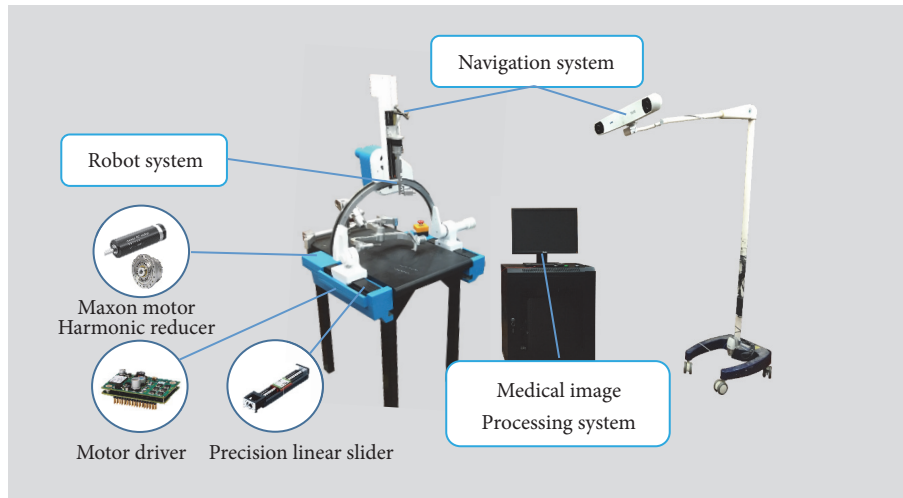


FIGURE 1: The presentation of robot assisted craniomaxillofacial surgery system.

can be great technical challenges for doctors. Needle puncture accuracy affects surgical treatment effect and may cause harm to the patient. Although technical assistance methods have been provided for needle puncture surgery, including conventional CT guide [6], individual template assistance, and image navigation [7], accurate needle placement still depends largely to a great extent on the surgeon's experience and hand-eye-mind coordination.

Surgical robots assisted craniomaxillofacial surgeries have developed rapidly nowadays, and advanced control technology and computer advantages greatly improve the maxillofacial surgery, especially the complex anatomical structure. The integration of imaging and robotic technology as "the third hand and eye" of the surgeon can be greatly taken advantage of robotic operation, improve needle displacement accuracy, and automatically perform the needle operation. The robot technology is widely known as an important instrument in the maxillofacial surgery because of its increasing advantages, such as high accuracy, stability, and flexibility of control. In 1994 Kavanagh [8] used the image-guided Robodoc robotic system for the first time in preclinical trials in the field of oral and maxillofacial surgery on the sacrum. In 1998 an interactive surgical robot system OTTO for craniomaxillofacial, which was installed on a surgical ceiling, was introduced by Lueth and Hein for drilling or cutting [9]. Genden et al. used Da Vinci robot to complete 9 cases of postoperative repair and reconstruction of tumors [10]. In 2010 Selber conducted a series of studies on the reconstruction of oropharyngeal defect by using Da Vinci surgical robot, including 1 case of free forearm flap, 2 cases of free anterolateral thigh flap, and 1 case of facial artery myomucosal flaps [11]. Theodossy et al. [12] and Omar et al. [13] used robotic arms (FARO arms) to simulate orthognathic surgery in model surgery. Chen Liming et al. [14] combined the Yaskawa MOTOMAN SV3X robot with optical navigation in Japan to simulate the craniofacial deformity on the human skull. Boesecke et al. [15] simulated 48 robotic-assisted implant placements that can accurately locate the

position, direction, and depth of preoperatively designed implants and assist doctors in the preparation of implant nests. Sun et al. [16] used a 6-degree-of-freedom Mitsubishi robot to perform automated dental implantation. The results showed that the registration accuracy was (1.42 ± 0.7) mm, indicating the feasibility of robot-assisted implant surgery. The RobaCKa robot system was developed by University of Karlsruhe (TH) and University of Heidelberg for craniofacial surgical osteotomy [17]. Kawana et al. [18] developed a remote controlled haptic drilling robot for oral and maxillofacial system. In addition, craniomaxillofacial surgery assisted robots have conducted extensive research in tumor treatment and other surgeries [19–22].

In radioactive tumor brachytherapy surgery, radioactive seeds implantation can adversely affect the operator's health and the potential ill effects of radiation cannot be ignored [23–28]. The robot assisted puncture system could provide great convenience for doctor once it can automatically perform needle puncture, radioactive seeds delivery and keep the doctor at a safe distance from the radioactive seeds. At the same time, the doctor can visualize the procedure of needle puncture in real time and display it in the medical image system [29]. By comparing preoperative planning and postoperative images, the robot assisted surgery system could verify the operation effectiveness. So we have developed a robot assisted craniomaxillofacial surgery system and evaluated the feasibility and reliability of this robot system in phantom experiments.

2. System Overview

According to the function of the surgical robot system, the robot assisted craniomaxillofacial surgery system as shown in Figure 1 could be divided into three subsystems, including robot subsystem, navigation subsystem, and medical image processing subsystem.

Robot subsystem comprises a positioning mechanism for needle displacement and three end effectors for tumor

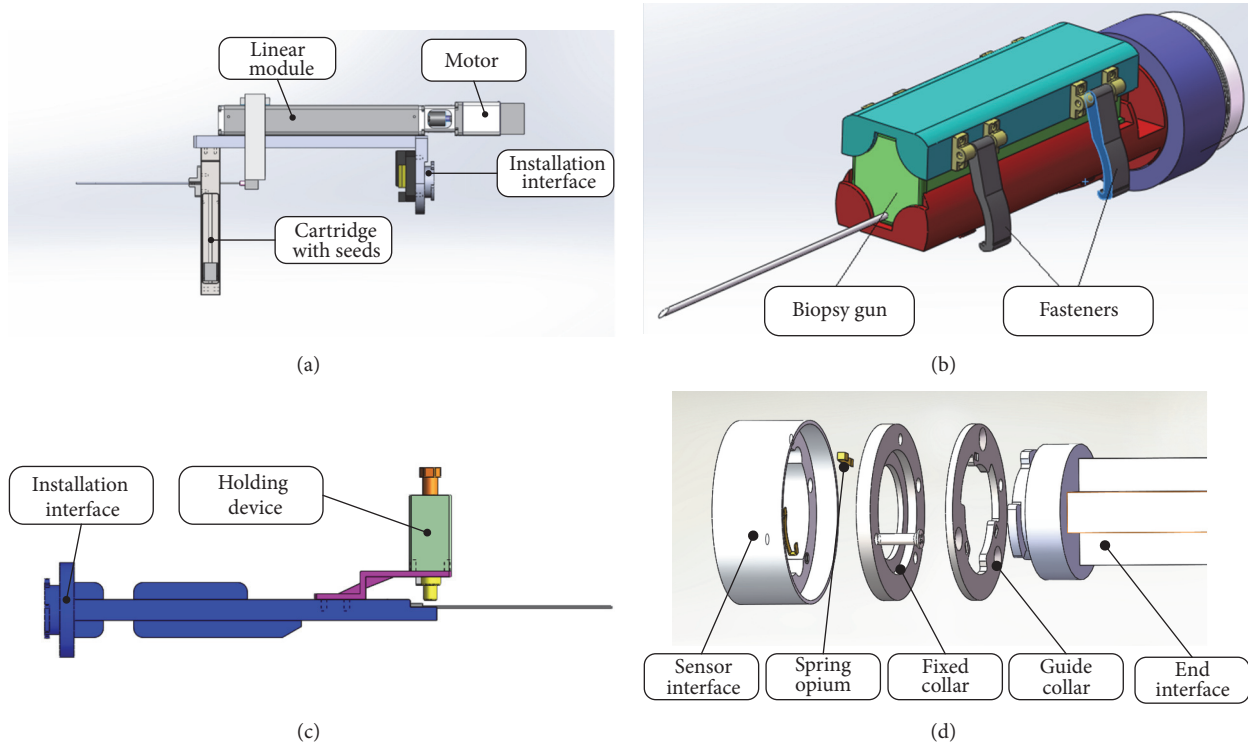


FIGURE 2: (a) Robot end effector for brachytherapy surgery; (b) end effector for biopsy surgery with clinical biopsy gun; (c) end effector for radiofrequency surgery with fast locking mechanism; (d) general interface explosion diagram.

biopsy, radioactive tumor brachytherapy, and radiofrequency thermal coagulation (Figure 1). In brief, the technical specifications of the robot system are as follows: (1) this weight is 15 kg, portable and remotely controlled, easy to be fixed to the operating table; (2) 5 degrees of freedom (DOFs) robot is used, with 3 DOFs for rotational motion, 1DOF for translational motion, and 1 DOF for surgical end effector operation. Rotating joint DOF consists of maxon motor and harmonic reducer; prismatic joint includes motor and precision linear slider. (3) Three operations correspond to three different surgical end effectors, and the universal interface at the robot fifth joint mounts quickly the end effectors to the robot with high accuracy. (4) Bus control system based on CANopen protocol completes robot joint control. (5) A 6-dimension force sensor (3813A SRI, Sunrise Instruments, Nanning, China) is fixed between the fifth joint and the end effector.

According to operation requirements, three end effectors (Figure 2) are designed, quickly installed, and disassembled to the robot end joint through the universal interface. In addition, the end effector for brachytherapy containing a cartridge with radioactive seeds was connected by a clamping slot connection, which facilitated easy removal and sterilization.

Navigation subsystem (Figure 3) realizes the registrations of various workspaces, obtained the transformational relationships between any robot workspaces, and provides real-time intraoperative navigation for surgery. An optical tracking system (Polaris, Northern Digital Inc., Waterloo, Canada) with 0.35 mm positioning accuracy and 20 Hz update rate

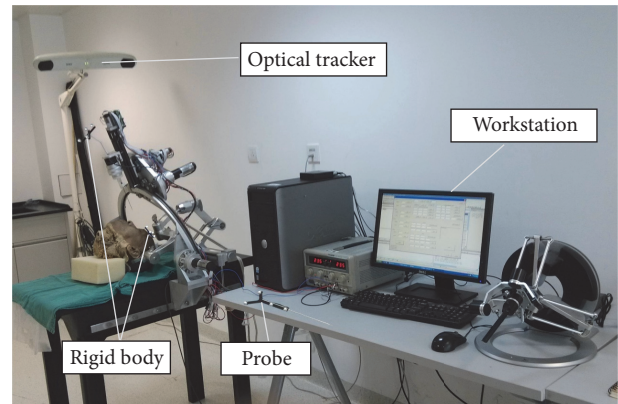


FIGURE 3: The presentation of navigation subsystem.

is focused that consisted of an optical tracker, one passive four-marker probe, and two passive four-marker rigid bodies. Two passive rigid bodies are fixed on the robot end effector and patient's head. In the surgical robot space navigation and positioning system, two important functions are surgical registration and intraoperative real-time tracking navigation. The optical tracker as measurement tool tracks the positions and orientations of probes and rigid bodies in real time.

Medical image processing subsystem includes the following features: 3D volume rendering of medical images, surgical scene control, 2D and 3D image segmentation, puncture

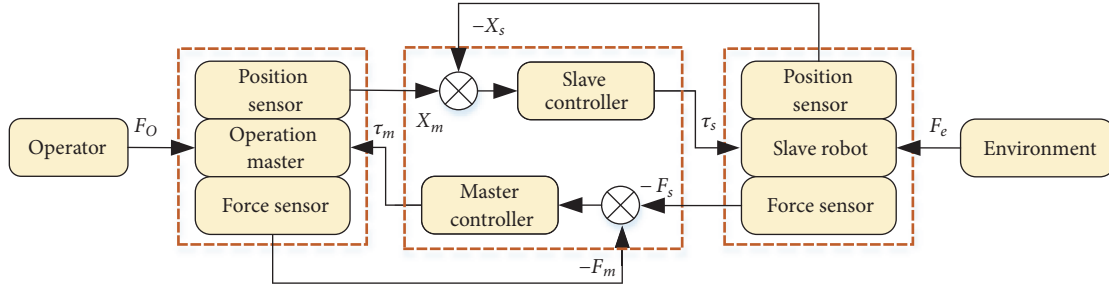


FIGURE 4: The control strategy of double-end force/position feedback.

path information processing, puncture path recommendation, postoperative verification, and evaluation. In addition, combining optical navigation system, real-time display of puncture needles in the image processing subsystem is displayed.

3. Control Strategy

In order to be convenient to the doctor's operation and reduce the learning time in which doctors operate surgical robot, the control system of surgical robot is designed from the perspective of human-computer interaction and operation procedure and is divided into two parts, automatic control for fine adjustment and master-slave control for passive positioning. Master-slave control mainly moves puncture needle from the starting point to the vicinity of entry point and remotely implants radioactive seeds. In master-slave mode, the robot's movement follows the doctor's hand, avoids collision with the patient's body, and positions the operation needle in the vicinity of the entry point [30, 31]. In automatic control mode, the robot achieves the precise positioning of the target point and completes the puncture process. The robot control hardware design mainly includes drive module (maxon motor and ACK-055-06 control driver of Copley, USA), CAN communication card (CAN-PCI-02 Copley), six-dimensional force sensor (3813A SRI, Sunrise Instruments, Nanning, China), and hardware circuit modules.

3.1. Master-Slave Control. The goal of the master-slave control is to obtain high transparency and provide good maneuverability. In the master-slave mode, the puncture needle could be controlled from current position to the vicinity of the entry point. The method is a more convenient operation, especially in the radioactive tumor brachytherapy surgery; this reduces the radiation received during the procedure. The doctor could complete radioactive tumor brachytherapy surgery by using remote operation. The master device (6 DOFs, omega.6 haptic device, Force Dimension, Switzerland) provides decoupling of translational and rotational motions, enabling gravity compensation, etc., and the slave device is the surgical robot. The doctor views the target and current pose of the puncture needle in real time, observes the movement of the robot, and prevents the puncture needle from interfering with the obstacle such as skull, fixed bracket,

or surgical instruments in the surrounding environment. The control strategy of double-end force/position feedback is used and has a good dynamic response, as shown in Figure 4.

The dynamic equation of the master could be expressed as follows:

$$\begin{aligned} F_o - \tau_m &= M_m s^2 X_m + B_m s X_m + K_m X_m \\ \tau_m &= K_f (F_m - F_s) \end{aligned} \quad (1)$$

where M_m , B_m , and K_m are the inertia, damping coefficient, and stiffness matrix of master device. F_m and F_s are the force values monitored from the master and slave force sensor. τ_m is the driving force of the master device. F_o is the force applied by the operator to the master device. X_m is the displacement vector. K_f is the force gain matrix. The dynamic equation of the slave could be displayed.

$$\begin{aligned} \tau_s - F_e &= M_s s^2 X_s + B_s s X_s + K_s X_s \\ \tau_s &= K_a (X_m - X_s) + K_v (X_m - X_s) \\ &\quad + K_p (X_m - X_s) \end{aligned} \quad (2)$$

where K_a , K_v , and K_p are the acceleration, speed, and position gain matrix of the slave. The dynamic equation and control strategy of the environmental could be expressed.

$$\begin{aligned} F_e &= - (M_e s^2 X_e + B_e s X_e + K_e X_e) \\ X_e &= -X_s \end{aligned} \quad (3)$$

M_e , B_e , and K_e , respectively, represent the inertia, damping coefficient, and stiffness matrix of the tissue environment. X_e is the position vector of the contact tissue environment. A constant transmission delay in the communication channel is considered. In the master-slave control strategy, the integral separation PID control algorithm is adapted and improves the speed response in stages. The method is that when the deviation is more than a given deviation, PID control is used to avoid overshooting and ensure the system's response speed. When the deviation is less than a given threshold, PID control is used to ensure the control accuracy. The method is to

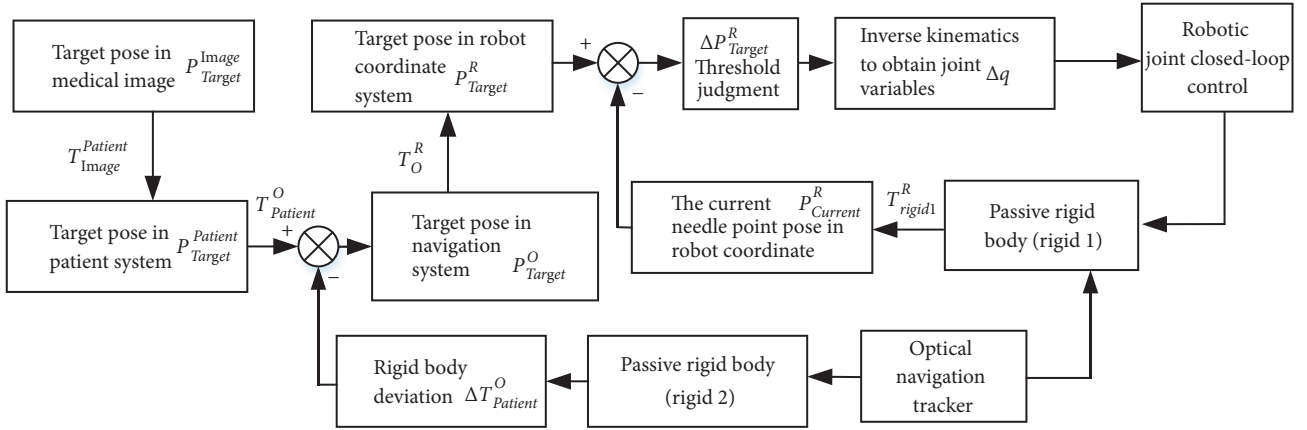


FIGURE 5: Robot navigation control system block diagram based on optical navigation.

multiply the integral term by a coefficient, and the value of the coefficient is 0 or 1 depending on the deviation.

$$u(k) = K_p e(k) + \beta \frac{T}{T_I} \sum_{j=0}^k e(j) + \frac{T_D}{T} [e(k) - e(k-1)] \quad (4)$$

$$\beta = \begin{cases} 1 & |e(k)| \leq \varepsilon \\ 0 & |e(k)| > \varepsilon \end{cases} \quad (5)$$

Through analyzing the control method of the PID method and combining the master-slave control algorithm, accurate and rapid control of the master-slave operation could be realized.

3.2. "Kinematics + Optics" Hybrid Automatic Motion Control.

Once the robot needle reaches the vicinity of the entry point during the execution of the surgery, the automatic motion control is chosen by doctor from the master-slave control. By the surgical planning software, the target pose of the puncture entry point is transmitted to the robot system and navigation system. The positioning accuracy of robot could be affected by the kinematics calculation, mechanical transmission, servo control, etc. In order to improve the positioning accuracy of the robot, the "kinematics + optics" hybrid motion control method is proposed. The robot inversely solves each joint movement angle through the inverse kinematic, and the target pose is converted into the navigation system through spatial registration relationships. The robot, which moves to the target point according to the operation plan, realizes accurate motion through the closed loop control of the joint encoder. Meanwhile, the pose quaternions from navigation system are used for pose correction. The pose needle and patient could be tracked and compensated in real time to ensure the accuracy of the puncture.

The robot automatic control system block diagram is shown in Figure 5. Firstly, the target point in the medical image system is converted into the real patient coordinate system. The navigation system is used to locate the position

of the patient in real time by the passive rigid body fixed to the patient, so as to compensate the deviation caused by the movement of patient. After the target pose is transmitted to surgical robot coordinate system, the robot moves to the target point by comparing with the real-time pose of the puncture needle tip as so to achieve accurate positioning of the target point.

The robot automatic control system includes two closed-loop controls; one is the servo control of the robot body system, that is single-joint servo control, and the other is global closed-loop control based on optical navigation. In robot automatic control, the global closed-loop control is achieved by real time acquisitions of optical navigation. P_{Target}^{Image} is the target pose in the medical image coordinate system. By the conversion relationship between the patient coordinate system and the image coordinate system, the target pose in the patient coordinate system can be obtained.

$$P_{Target}^{Patient} = T_{Image}^{Patient} P_{Target}^{Image} \quad (6)$$

The target point is converted from patient coordinate system to the optical navigation coordinate system, and the conversion relationship between the two coordinate systems has been determined in the spatial registration. Due to movements of the patient or optical navigation tracker during surgical operation, the transfer relationship is compensated through real-time navigation tracking. The target point in the navigation coordinate system P_{Target}^O is represented.

$$P_{Target}^O = (T_{Image}^O + \Delta T_{Image}^O) P_{Target}^{Image} \quad (7)$$

Before the robot moves to target point, the target position and orientation of robot will be transformed from navigation coordinate system to robot coordinate system. Also due to the movement of the robot or optical navigation the transfer relationship between them is compensated through real-time navigation tracking. Since the passive navigation rigid is installed at the end effector of the robot and the robot transfer relationship is based on the robot base coordinate system,

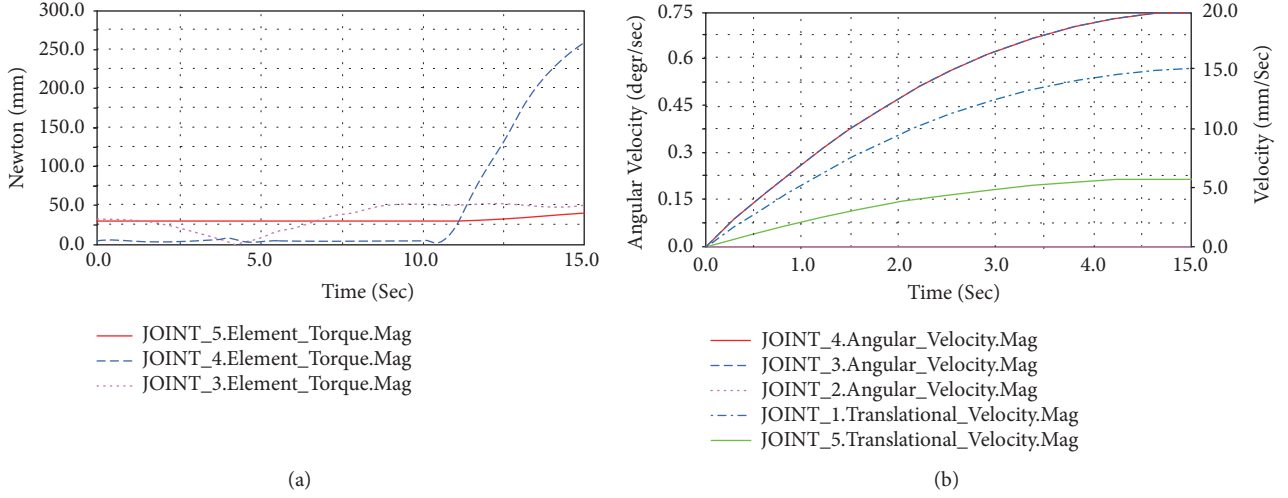


FIGURE 6: When the motion trajectory was given, the variation curve of force, velocity of the robotic joint could be obtained. The curves of three rotary joint driving forces (a) help to the drive unit selection; the variation curves of joint speed ensure the robotic flexible movement.

the robot joint angle values are determined by the inverse kinematics so that the deviation between the robot coordinate system and navigation coordinate system could be calculated. ΔT_O^R is the compensation parameter matrix, and the target point in robot base coordinate system could be listed.

$$P_{\text{Target}}^R = (T_O^R + \Delta T_O^R) P_{\text{Target}}^O \quad (8)$$

Through inverse kinematics calculation, the target point can be converted into the joint vectors of robot to control the robot motion. The position information of current puncture point in navigation coordinate system can be obtained by the real-time tracking of passive rigid body. The pose of current puncture point is converted to the robot coordinate system, and the closed-loop control can be achieved by comparing with the target pose in robot base coordinate system. $\Delta \bar{P}_{\text{Target}}^R$ is deviation between the current pose information of puncture point and the target pose in robot base coordinate system. The deviation can be adjusted by PID controller:

$$\begin{aligned} \Delta \bar{P}_{\text{Target}}^R &= K_p [\Delta P_{\text{Target}}^R(k) - \Delta P_{\text{Target}}^R(k-1)] \\ &+ K_I \Delta P_{\text{Target}}^R(k) + K_D [\Delta P_{\text{Target}}^R(k) \\ &- 2\Delta P_{\text{Target}}^R(k-1) + \Delta P_{\text{Target}}^R(k-2)] \end{aligned} \quad (9)$$

$$\bar{P}_{B\text{Target}(k)}^R = \bar{P}_{B\text{Target}(k-1)}^R + \Delta \bar{P}_{B\text{Target}(k)}^R \quad (10)$$

where K_p is the proportional gain, K_I is the integral gain, K_D is the derivative gain, k is the sampling sequence, and $k = 0, 1, 2, \dots, n$. $\Delta \bar{P}_{\text{Target}}^R$ is the increment of deviation at the k sampling time. $\bar{P}_{B\text{Target}(k)}^R$ is the output of the PID controller at the k sampling time. The optimal deviation is obtained by adjusting the gain parameters of PID controller. Thus, the joint angles can be calculated by inverse kinematics to control the robot to reach the target position.

4. Simulation and Experiments

4.1. Kinematic Simulation. The simulation aims to express the process of robot running and then ensures the velocity and acceleration of motion joints in the process of continuous motion. The method of simulation is analyzing mechanical property to single component with application of Newtonian mechanics, establishing the relationship of force and velocity under certain restraint condition. Once setting the robot and the motion trajectory, the postprocessor module of Adams could be used to analyze robot joint force and velocity as shown in Figure 6. It is significant to optimize the structure and hardware selection of robot.

4.2. D-H Parameter Identification. According to the correction of the D-H parameter model of the robot, there are certain errors in the parameters of the robot due to the factors such as processing, assembly, and environments. The geometric method and fitting method are adopted for the D-H parameter identification. The zero position of robot is determined by geometric method and the initial kinematics D-H parameter of the robot is given. Then, the D-H parameters are corrected by using the fitting method. The parameter identification for measuring tool uses FARO measuring arm (FARO Edge, FRAO Technology, Inc.).

The FRAO measuring arm is fixed near the surgical robot to ensure that the measuring points could cover the operating space of the surgical robot. The origin positions of each joint coordinate system of the robot kinematic model are obtained by fitting spatial point sets. The method is to control each joint of robot to move to different positions and to obtain the coordinates of the marker points on the end effector using the probe of the FARO measurement arm at each position. The corresponding joint axis directions are calculated by fitting these measurement points. Then the initial D-H parameters could be got by the corresponding joint coordinate origins positions.

TABLE 1: The D-H parameter identification results.

Joint	α_i (o)	d_i /(mm)	a_i /(mm)	θ_i (°)	Range
1	90.75	d_1	-0.08	0.052	-200~200 mm
2	0.02	0.04	0.13	θ_2	-80°~50°
3	-0.06	0.021	403.26	θ_3	-60°~60°
4	-89.53	-0.10	0.074	θ_4	-70°~70°
5	0.09	d_4	-0.06	0.04	0~200 mm

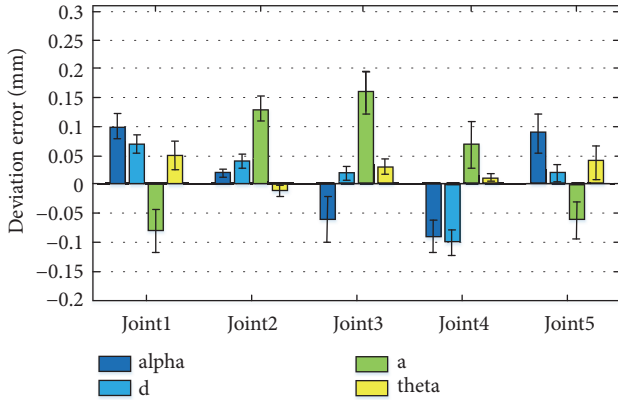


FIGURE 7: The identification errors of each joint's D-H parameters. 20 points were selected as a group to solve D-H identification parameters and 5 trials were performed to obtain the mean and standard deviation.

The deviation of the transformation matrix of the robot link is the difference between the actual transformation matrix ${}^jT_i^R$ and the nominal transformation matrix ${}^jT_i^N$.

$$\begin{aligned}
 d\left({}^jT_i^N\right) &= {}^jT_i^N - jT_i^R \\
 &= \frac{\partial {}^jT_i^N}{\partial \theta_i} \delta \theta_i + \frac{\partial {}^jT_i^N}{\partial d_i} \delta d_i + \frac{\partial {}^jT_i^N}{\partial a_i} \delta a_i \\
 &\quad + \frac{\partial {}^jT_i^N}{\partial \alpha_i} \delta \alpha_i
 \end{aligned} \quad (11)$$

A certain threshold of the deviation between the theoretical pose value and the actual pose value in the measurement coordinate system is set. Once the threshold satisfies the conditions, the parameter deviation vector could be obtained. 20 point coordinates in the measurement coordinate system and the corresponding joint angles are recorded. The iterative least squares method is used to obtain the deviation of the joint coordinate system parameters. 5 trials for each of 20 points were performed and averaged in Figure 7. The correction value of the D-H parameters is calculated in Table 1.

4.3. *Positioning Accuracy Experiments.* Robot positioning accuracy experiments are the verification of the controlled

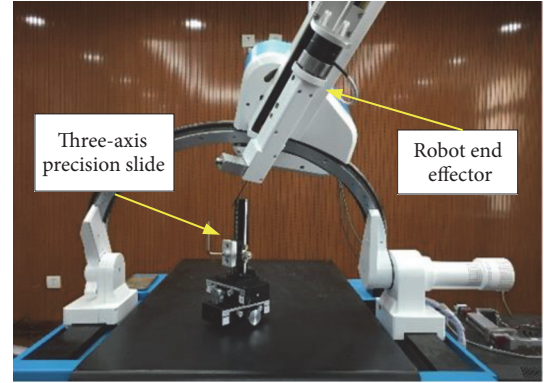


FIGURE 8: The positioning error experiments based on open-loop control and hybrid automatic control.

positioning of the surgical robot system. These have been implemented in open-loop robot control mode and “kinematics + optics” hybrid control mode based on navigation system. The feasibility of “kinematics + optics” hybrid automatic motion control could be verified. In order to calculate the influence of errors such as 3D medical image reconstruction and registration algorithm, the target point coordinates are obtained directly by using the passive probe of the optical navigation in the experiment. The three-axis precision slide (K301-30LMS-4 Suruga Seiki Co., Ltd., Accuracy 0.1mm) is used as the measurement tool as shown in Figure 8. The predetermined target positions coordinates are recorded by the optical measuring probe from the end point of the three-axis precision slide.

In the positioning accuracy experiment of open-loop robot control mode, the angle differences of each joint are calculated by analyzing the pose deviation between the target position and the current position. Then the robot reaches the target point through the motor servo control. The positioning error of open-loop control mode could be calculated by comparing Euclidean distance between the position of the needle tip and the target point.

In the positioning accuracy experiment of hybrid control mode, the passive rigid body is fixed at the end-effector of robot. The optical tracker is placed in a representative location to achieve the best positioning effect. The “kinematics + optics” hybrid motion control method is applied to the motion control of robot. The needle tip of robot is controlled to move to predetermined target positions, and

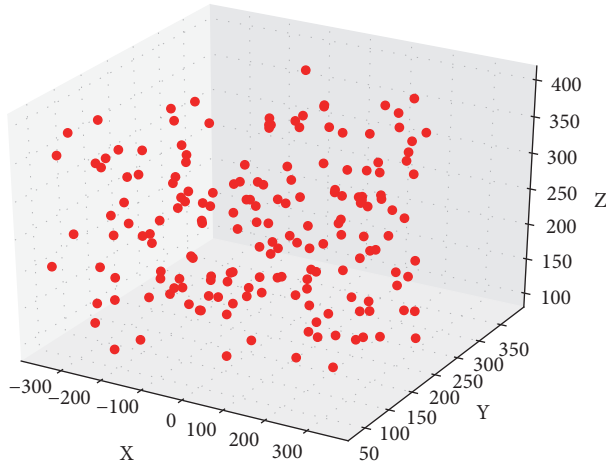


FIGURE 9: Test point distribution map in the workspace.

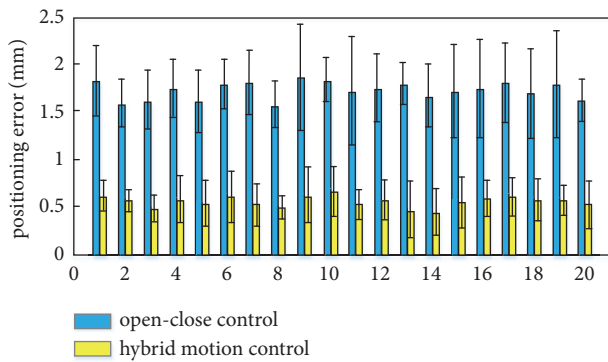


FIGURE 10: Comparing the positioning error between open-loop mode and hybrid motion control mode; each bar shows the mean and standard deviation of 10 trails for each of 20 preset location points.

its coordinates are recorded by the three-axis precision slide simultaneously. Then the positioning error of robot based on “kinematics + optics” hybrid motion control method can be obtained. In order to ensure the accuracy of the operation in actual operation, the maximum speed is operated at a distance of 3 cm from the target point. Within 3 cm from the target point, the needle point speed is controlled to be less than 0.02 m/s.

In order to ensure the effectiveness of the robot operation in the workspace, we randomly grabbed 200 points in the workspace in Figure 9 and divided them into 10 groups, 20 points in each group. Control the puncture needle from the same starting position to the target position in open-loop and “kinematic + optics” hybrid motion control mode in each group.

Figure 10 shows the positioning error for each of 20 preset points, when performing the experiments in open-loop control mode and hybrid motion control mode. The 10 trials were implemented to verify two control modes. The positioning error of open-close control mode is $1.73 \pm$



FIGURE 11: The setup of phantom experiments of biopsy, radiofrequency, and brachytherapy, including navigation system, control station, surgical robot, and phantom.

0.46 mm, while the hybrid mode control is 0.56 ± 0.21 mm. The reason is mainly the repetitive error of robot installation, robot D-H parameter error, registration error, etc. The hybrid motion control could reduce the impact of above error on the experimental results.

4.4. Phantom Experiments of Biopsy, Radiofrequency, and Brachytherapy. In order to verify the error of the robot-assisted puncture surgery system, the phantom experiments of biopsy, radiofrequency, and brachytherapy were conducted as shown in Figure 11. The skin was simulated by plasticine and the puncture target made with meat balls was buried inside the phantom. For different operations, the corresponding end effector was chosen. In the brachytherapy phantom experiment, the stainless steel wires of 1 mm diameter and 5 mm length were used instead of radioactive seeds to avoid radiation to the operators. All experiments were performed in the department of oral and maxillofacial surgery (Peking University School and Hospital of Stomatology). The study was approved by the local ethics committee.

The preoperative planning coordinates and postoperative seeds position were aligned by matrix transformation after image fusion, using the ICP algorithm. The total error was defined as the Euclidean distance calculated by the offsets of the coordinates. 30 trails of biopsy phantom experiments were performed and the mean placement error was 1.42 ± 0.33 mm. In the radiofrequency thermal coagulation phantom experiment, the mean placement error corresponding to 20 groups was 1.62 ± 0.26 mm. In the radioactive tumor brachytherapy phantom experiment, a total of 100 seeds were deposited by the robot system. The mean placement error was 1.41 ± 0.30 mm in phantom experiments ($p < 0.005$). The results of experiments were shown in Figure 12.

The cause of the errors includes the following: the layer spacing of the CT device, the 3D reconstruction image algorithm, the registration algorithm, robot control positioning error, and needle deformation. From the experiments data, the reason that the error of radiofrequency experiment is more than biopsy and brachytherapy is the longer puncture depths. The effect of brachytherapy experiment is analysis by the treatment planning system and shows that the radioactive dose map deviation is less than 1%, which is a reasonable seeds implantation as shown in Figure 13.

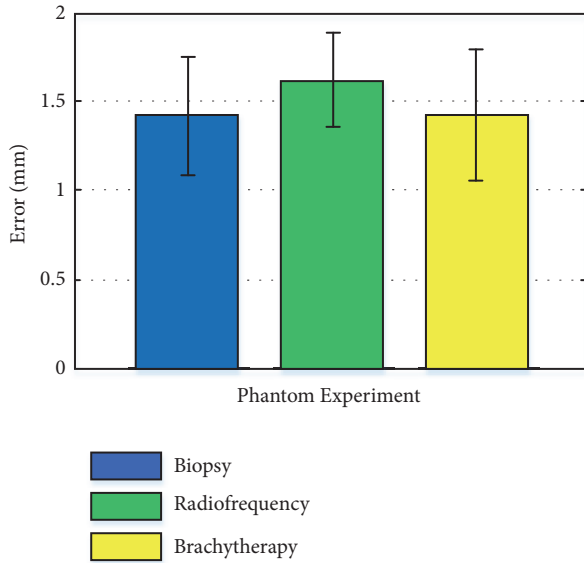


FIGURE 12: The accuracy of phantom experiments of biopsy, radiofrequency, and brachytherapy.

5. Conclusions and Discussion

This paper presents a robot assisted craniomaxillofacial surgery system through the analysis of surgical requirements. Motion performance analysis was conducted to validate the flexibility and feasibility of robot system. The hybrid automatic control for active fine adjustment and master-slave control for passive positioning were designed to build robot control system. In addition, the kinematic simulation and D-H parameter identification experiments were conducted to verify robotic precise manipulation. Positioning accuracy and phantom experiments of biopsy, radiofrequency, and brachytherapy demonstrate that the robot assisted surgery system could have accurate puncture effect.

From the perspective of human development and clinical application, laparoscopic robots, orthopedic robots, vascular interventional robots, and targeted puncturing robots are several important directions. The positioning of the puncture needle is achieved relying on the high precision and stability of the robot [32, 33]. Its application scope includes neurosurgery, craniomaxillofacial puncture, lung, liver, and other organs' percutaneous puncture. Robot-assisted puncture surgery systems are generally composed of surgical robots, medical image planning and processing, and surgical navigation systems, which are, respectively, "hand", "brain," and "eye" of the entire system. In order to provide doctors with a wider vision field and simplify surgical procedures, the surgical robots that are visualized, of lightweight, and easy to integrate with CT/MR devices have begun extensive research. Some puncture robot systems have been commercialized and completed a series of clinical operations in specific areas. At present, commercialized puncture robot systems such as the MAXIO robot system (Perfint Healthcare Pvt. Ltd) are placed near to the CT bed and are controlled to move to the target

point through the surgical planning. In addition, there are ROSA from Medtech in France [34], Renaissance from Mazor Robotics in the United States, Pathfinder from Pathfinder Technologies [35], NeuroMate robotics from Renishaw in UK [36], B-Rob from ISYS Medizintechnik GmbH [37], etc. These systems have already demonstrated certain clinical effects.

In our positioning accuracy experiments, the navigation probe was used to specify the target point. The robot positioning error is analyzed by comparing the specified target point and the actual position of the needle tip. The coordinates of the two measuring points must be in the same coordinate system. It is difficult to measure the coordinates of the puncture tip using an optical navigation probe. So the three-axis precision slide (K301-30LMS-4 Suruga Seiki Co., Ltd., Accuracy 0.1 mm) is chosen to measure coordinates. In order to facilitate the measurement of the coordinates of the needle tip of the puncture needle, a cylindrical rod with a cross section pit is connected to the end of the three-axis precision slide. 20 points, whose positions could be measured by precision slides, are selected for positioning accuracy experiments as much as possible into the robot's entire workspace. The 10 trials were implemented to verify two control modes. The positioning error of open-close control mode is 1.73 ± 0.46 mm, while the hybrid mode control is 0.56 ± 0.21 mm. The reason is that the repeated positioning errors in robotic installation beds are variable, and the registration error between robot and navigation system is also present. The "kinematic + optical" hybrid motion control method utilizes the characteristics of optical navigation real time closed-loop control and kinematics to achieve closed-loop robot control.

In phantom experiments, different materials have been used to simulate soft tissue, with most studies using gels and polyvinyl chloride, which cannot really simulate the complexity of the tissues of the maxillofacial region. During the surgical procedure, the surgical end effectors are replaced as required. If the universal interface generates increased error when replacing the surgical actuator, the surgical robot puncture needle needs to be recalibrated. Therefore, the error experiment about replacing the robot end effector was conducted. The average value of replacing error of the biopsy end effector is 0.307 mm, and the standard deviation is 0.157 mm. The radiofrequency end effector is 0.348 mm and the standard deviation is 0.238 mm. The brachytherapy is 0.164 mm and the standard deviation is 0.091 mm. The phantom experiment study had some drawbacks, as neither plasticine nor meat balls used as targets exhibit significant anisotropism or simulate the complex behavior of soft tissues. The skin was simulated by plasticine and the puncture target was made with meat balls. Compared with the puncture accuracy experiments, the puncture errors caused by the phantom experiments mainly include the following: the layer spacing of imaging equipment, the 3D reconstruction image algorithm, the registration algorithm, the robot control positioning error, and puncture needle deformation caused by plasticine [38]. In addition to the phantom experiment, we also carried out cadaveric experiment on this prototype. The surgical robot finished the needle placement and automatic

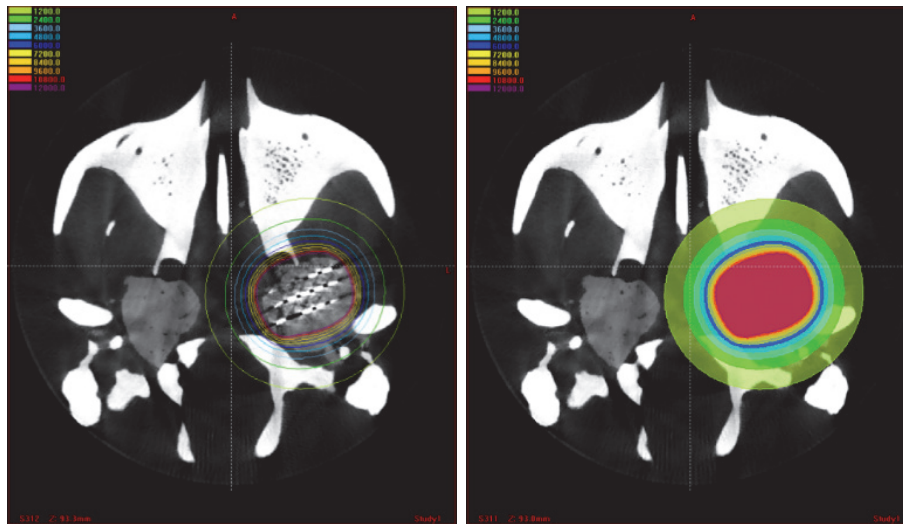


FIGURE 13: The analysis of the radioactive does map deviation.

puncture. In the cadaveric experiment, the average error of biopsy puncture is 2.58 mm, the standard deviation is 0.61 mm, and the tissue can be taken in the biopsy gun for each puncture. The average error of radiofrequency thermal coagulation surgery is 3.17 ± 0.94 mm; one of the 20 experiments failed to pass through the foramen ovale. The average error of the brachytherapy is 2.83 ± 0.50 mm; the TPS system analysis shows that the radioactive dose topographic map deviation was less than 5%.

The needle deformation is an important challenge for robot assisted puncture. The most commonly used oblique tip puncture needles in clinical practice are nickel-titanium alloy materials, which have high elasticity. In the process of soft tissue puncture, there is a needle deflection due to the asymmetry of the needle tip. A reasonable explanation is that needle deflection was primarily responsible for needle displacement with simulated tissue or real tissue, as has been reported in previous studies [39, 40]. Although the hybrid motion control guarantees robot motion accuracy to 0.8mm, the performance of needles, which are vulnerable to be bendable, can bring external errors. At present, the deformation of the puncture needle caused by the soft tissue and the physiological movement of the human body becomes a bottleneck for the robot to achieve high precision puncture positioning. As the puncture needle advances in soft tissue, it receives various resistances from the soft tissue. For oblique flexible needle, the relationship between puncture force and needle deformation is studied to obtain the interaction mechanism, which can make the puncture process accurate, controllable, and safe.

For the difficulty of needle deflection, we carried out the theory and experimental study of needle deflection based on force perception as shown in Figure 14. The 18G and 20G flexible oblique-tip needles were used to puncture the phantom at different speeds. The camera took the puncture process and the puncture depth was 120 mm to analyze the difficulty of needle deflection. The flexible oblique-tip needle

is used so that the needle deflection can be presented more easily. The soft tissue phantom should be able to simulate good viscoelastic soft tissue characteristics. The phantom used in this puncture experiment was prepared by mixing gelatin powder with water in a certain proportion and refrigerating in a refrigerator at 4°C for 12 hours. Since the gel is prone to water loss and hardening, the experiment must be completed within 1 hour after being taken out from refrigerator.

Analysis of experimental results shows that the finer the puncture needle is, the larger the needle deflection is. By recording the puncture force, the theoretical model is used to analyze the offset of the flexible oblique-tip needle. The offset of the needle in the acquired image is compared with the theoretical analysis; the measured error is less than 1 mm. This work is still under study; experiments on multilayer soft tissue phantoms are continuing to be performed.

Although many efforts have been made to model needle insertion forces, it has so far not been possible to correctly predict needle tissue interactions because of the variability of the soft tissue properties. Interventions with rotating needles are a considerable alternative to provide highly beneficial accuracy in relative studies [41, 42] and we will take this into consideration when studying the next work. In the future, some functions need to be optimized in order to improve the system performance. More phantom and clinical experiments should be done to improve and evaluate the robot system.

Data Availability

All data used to support the findings of this study are available from the corresponding author upon request.

Conflicts of Interest

The authors declare that there are no conflicts of interest regarding the publication of this paper.

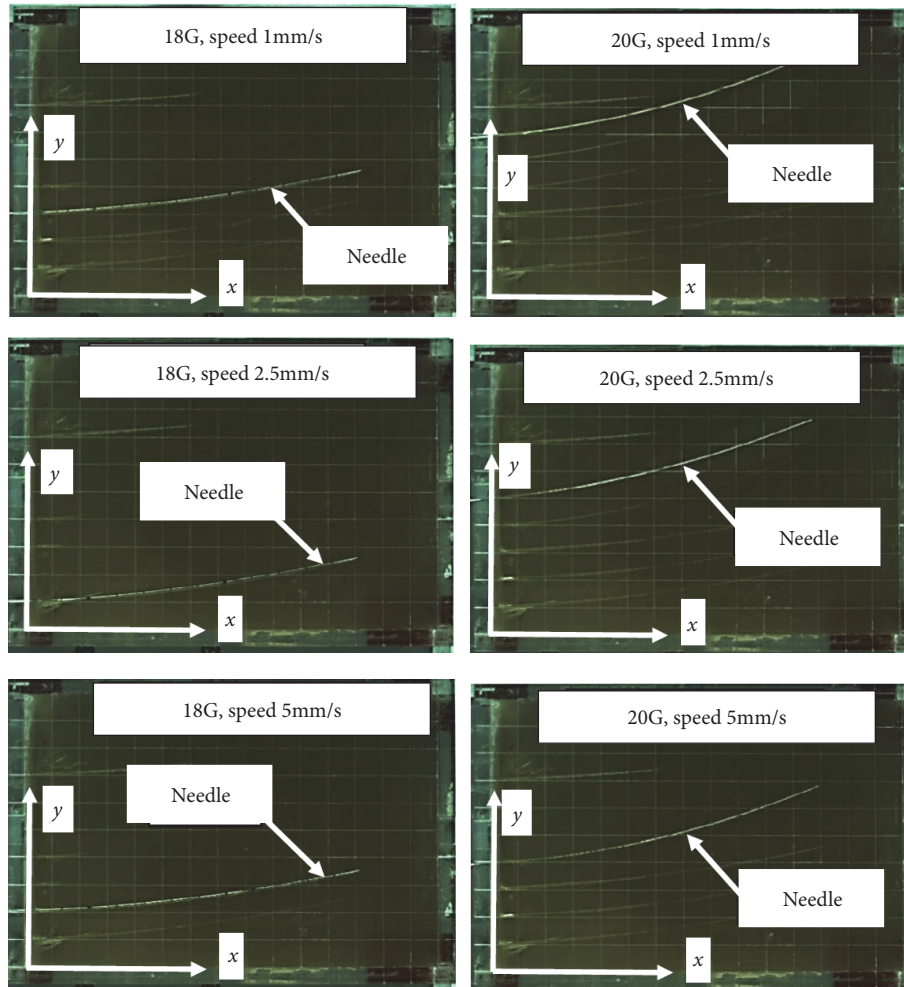


FIGURE 14: The experiment of needle deflection.

Acknowledgments

This research was supported by the National Key R&D Program of China (Grant No. 2017YFB1304302), China Postdoctoral Science Foundation funded project (Grant No. 2018M641216), and National Natural Science Foundation of China (Grant No. 61673064).

References

- [1] B. S. Peters, P. R. Armijo, C. Krause, S. A. Choudhury, and D. Oleynikov, "Review of emerging surgical robotic technology," *Surgical Endoscopy*, vol. 32, no. 4, pp. 1636–1655, 2018.
- [2] L. Yu, X. Chen, and A. Margalit, "Robot-assisted vs freehand pedicle screw fixation in spin surgery – a systematic review and a meta-analysis of comparative study," *International Journal of Medical Robotics and Computer Assisted Surgery*, vol. 14, article 1892, 2018.
- [3] D. P. Losey, C. G. McDonald, E. Battaglia, and M. K. O'Malley, "A review of intent detection, arbitration, and communication aspects of shared control for physical human-robot interaction," *Applied Mechanics Reviews*, vol. 70, 2018.
- [4] M. Hagio, K. Ishizaki, M. Ryu, T. Nomura, N. Takano, and K. Sakurai, "Maxillofacial prosthetic treatment factors affecting oral health-related quality of life after surgery for patients with oral cancer," *Journal of Prosthetic Dentistry*, vol. 119, no. 4, pp. 663–670, 2018.
- [5] H. Boyes, J. Brraclough, and R. Ratansl, "Structured review of the patient-reported outcome instruments used in clinical trials in head and neck surgery," *British Journal of Oral and Maxillofacial Surgery*, vol. 56, pp. 161–167, 2018.
- [6] Y. L. Jiang, N. Meng, J. J. Wang et al., "CT-guided iodine-125 seed permanent implantation for recurrent head and neck cancers," *Radiation Oncology*, vol. 5, article 68, 2010.
- [7] R. Krempien, S. Hassfeld, J. Kozak et al., "Frameless image guidance improves accuracy in three-dimensional interstitial brachytherapy needle placement," *International Journal of Radiation Oncology, Biology, and Physics*, vol. 60, no. 5, pp. 1645–1651, 2004.
- [8] K. T. Kavanagh, "Applications of image-directed robotics in otolaryngologic surgery," *The Laryngoscope*, vol. 104, no. 3, pp. 283–293, 1994.
- [9] T. C. Lueth, A. Hein, J. Albrecht et al., "A surgical robot system for maxillofacial surgery," in *Proceedings of the 24th Annual Conference of the Industrial Electronics Society, IECON '98*, vol. 4, pp. 2470–2475, IEEE, August 1998.
- [10] E. M. Genden, S. Desai, and C.-K. Sung, "Transoral robotic surgery for the management of head and neck cancer: a

- preliminary experience,” *Head and Neck*, vol. 31, no. 3, pp. 283–289, 2009.
- [11] J. C. Selber, “Transoral robotic reconstruction of oropharyngeal defects: a case series,” *Plastic and Reconstructive Surgery*, vol. 126, no. 6, pp. 1978–1987, 2010.
 - [12] T. Theodossy and M. A. Bamber, “Model surgery with a passive robot arm for orthognathic surgery planning,” *Journal of Oral and Maxillofacial Surgery*, vol. 61, no. 11, pp. 1310–1317, 2003.
 - [13] E. A. Z. Omar and M. A. Bamber, “Orthognathic model surgery by using of a passive Robot Arm,” *The Saudi Dental Journal*, vol. 22, no. 2, pp. 47–55, 2010.
 - [14] L. M. Chen, N. Luan, S. L. Zhang et al., “Research on the application of multi DOF robot on orthognathic navigation surgery,” *Mach Electron*, vol. 4, pp. 57–60, 2010.
 - [15] R. Boesecke, J. Brief, J. Raczkowski et al., “Robot assistant for dental implantology,” in *Proceedings of the International Conference on Medical Image Computing and Computer-Assisted Intervention*, pp. 1302–1303, Springer, Berlin, Germany, 2001.
 - [16] X. Sun, F. D. McKenzie, S. Bawab, J. Li, Y. Yoon, and J.-K. Huang, “Automated dental implantation using image-guided robotics: registration results,” *International Journal for Computer Assisted Radiology and Surgery*, vol. 6, no. 5, pp. 627–634, 2011.
 - [17] D. Engel, W. Korb, J. Raczkowski, S. Hassfeld, and H. Woern, “Location decision for a robot milling complex trajectories in craniofacial surgery,” in *Proceedings of the 17th International Congress and Exhibition of Computer Assisted Radiology and Surgery*, 2003.
 - [18] H. Kawana, S. Usuda, K. Yu, T. Nakagawa, and K. Ohnishi, “A remote controlled haptic drilling robot for oral and maxillofacial surgery,” *International Journal of Oral and Maxillofacial Surgery*, vol. 46, article 207, 2017.
 - [19] L. Lin, Y. Shi, A. Tan et al., “Mandibular angle split osteotomy based on a novel augmented reality navigation using specialized robot-assisted arms - A feasibility study,” *Journal of Cranio-Maxillo-Facial Surgery*, vol. 44, no. 2, pp. 215–223, 2016.
 - [20] X. Kong, X. Duan, and Y. Wang, “An integrated system for planning, navigation and robotic assistance for mandible reconstruction surgery,” *Intelligent Service Robotics*, vol. 9, no. 2, pp. 113–121, 2016.
 - [21] N. Nadjmi, “Transoral robotic cleft palate surgery (TORCS),” *The Cleft Palate-Craniofacial Journal*, vol. 44, pp. 114–115, 2015.
 - [22] K. Ohnishi, K. Yu, T. Nakagawa, and H. Kawana, “Automatic stop system for avoiding over cut in implant surgery using haptic drilling robot,” *Journal of Oral and Maxillofacial Surgery*, vol. 72, article 61, 2014.
 - [23] M. Wierzbicka, A. Bartochowska, V. Strnad et al., “The role of brachytherapy in the treatment of squamous cell carcinoma of the head and neck,” *European Archives of Oto-Rhino-Laryngology*, vol. 273, no. 2, pp. 269–276, 2016.
 - [24] M.-W. Huang, J.-G. Zhang, L. Zheng, S.-M. Liu, and G.-Y. Yu, “Accuracy evaluation of a 3D-printed individual template for needle guidance in head and neck brachytherapy,” *Journal of Radiation Research*, vol. 57, no. 6, pp. 662–667, 2016.
 - [25] T. Popescu, A. C. Kacsó, D. Pisla, and G. Kacsó, “Brachytherapy next generation: Robotic systems,” *Journal of Contemporary Brachytherapy*, vol. 7, no. 6, pp. 510–514, 2015.
 - [26] J. Kettenbach and G. Kronreif, “Robotic systems for percutaneous needle-guided interventions,” *Minimally Invasive Therapy & Allied Technologies*, vol. 24, no. 1, pp. 45–53, 2015.
 - [27] R. Seifabadi, F. Aalamifar, I. Iordachita, and G. Fichtinger, “Toward teleoperated needle steering under continuous MRI guidance for prostate percutaneous interventions,” *The International Journal of Medical Robotics and Computer Assisted Surgery*, vol. 12, no. 3, pp. 355–369, 2016.
 - [28] K. Cleary, S. Lim, C. Jun et al., “Robotically assisted long bone biopsy under MRI imaging: workflow and preclinical study,” *Academic Radiology*, vol. 25, no. 1, pp. 74–81, 2018.
 - [29] Z. Du, W. Wang, Z. Yan, W. Dong, and W. Wang, “Variable admittance control based on fuzzy reinforcement learning for minimally invasive surgery manipulator,” *Sensors*, vol. 17, pp. 844–859, 2017.
 - [30] F. Oscari, R. Oboe, O. A. D. Albasini, S. Masiero, and G. Rosati, “Design and construction of a bilateral haptic system for the remote assessment of the stiffness and range of motion of the hand,” *Sensors*, vol. 16, article 1633, 2016.
 - [31] S. Zhang, S. Guo, B. Gao, H. Hirata, and H. Ishihara, “Design of a novel telerehabilitation system with a force-sensing mechanism,” *Sensors*, vol. 15, no. 5, pp. 11511–11527, 2015.
 - [32] M. Bowthorpe, M. Tavakoli, H. Becher, and R. Howe, “Smith predictor-based robot control for ultrasound-guided teleoperated beating-heart surgery,” *IEEE Journal of Biomedical and Health Informatics*, vol. 18, no. 1, pp. 157–166, 2014.
 - [33] J. Dong, L. Zhang, L. Yu et al., “Puncture locating for laparoscopic robot in minimally invasive surgery,” in *Proceedings of the International Symposium on Intelligent Information Technology Application*, pp. 658–662, December 2008.
 - [34] J. Gonzalez-Martinez, S. Vadera, J. Mullin et al., “Robot-assisted stereotactic laser ablation in medically intractable epilepsy: operative technique,” *Neurosurgery*, vol. 10, pp. 167–172, 2014.
 - [35] G. Deacon, A. Harwood, J. Holdback et al., “The pathfinder image-guided surgical robot,” *Proceedings of The Institution of Mechanical Engineers Part H*, vol. 224, no. 5, pp. 691–713, 2010.
 - [36] D. Von Langsdorff, P. Paquis, and D. Fontaine, “In vivo measurement of the frame-based application accuracy of the Neuromate neurosurgical robot,” *Journal of Neurosurgery*, vol. 122, no. 1, pp. 191–194, 2015.
 - [37] J. Kettenbach, L. Kara, G. Toporek, M. Fuerst, and G. Kronreif, “A robotic needle-positioning and guidance system for CT-guided puncture: ex vivo results,” *Minimally Invasive Therapy and Allied Technologies*, vol. 23, no. 5, pp. 271–278, 2014.
 - [38] Q. Duan, Z. Du, H. Yu, Y. Wang, and W. Dong, “Error analysis and experimental study of a Bi-planar parallel mechanism in a pedicle screw robot system,” *Sensors*, vol. 16, pp. 2022–2036, 2016.
 - [39] G. Li, H. Su, W. Shang et al., “A fully actuated robotic assistant for MRI guided prostate biopsy and brachytherapy,” *Proceeding of SPIE-the International Society*, vol. 8671, no. 3, article 867117, 2013.
 - [40] G. Wan, Z. Wei, L. Gardi, D. B. Downey, and A. Fenster, “Brachytherapy needle deflection evaluation and correction,” *Medical Physics*, vol. 32, no. 4, pp. 902–909, 2005.
 - [41] B. L. Davies, S. J. Harris, and E. Dibble, “Brachytherapy - an example of a urological minimally invasive robotic procedure,” *The International Journal of Medical Robotics and Computer Assisted Surgery*, vol. 1, pp. 88–96, 2004.
 - [42] M. A. Meltsner, N. J. Ferrier, and B. R. Thomadsen, “Observations on rotating needle insertions using a brachytherapy robot,” *Physics in Medicine and Biology*, vol. 52, no. 19, pp. 6027–6037, 2007.

Research Article

Histobiomechanical Remodeling of the Cervix during Pregnancy: Proposed Framework

Jorge Torres ¹, Inas Faris ^{1,2} and Antonio Callejas ^{1,2}

¹Department of Structural Mechanics, University of Granada, 18071, Spain

²Biosanitary Research Institute, Granada 18016, Spain

Correspondence should be addressed to Jorge Torres; geresez@ugr.es

Received 14 September 2018; Accepted 12 February 2019; Published 27 February 2019

Guest Editor: Marie Muller

Copyright © 2019 Jorge Torres et al. This is an open access article distributed under the Creative Commons Attribution License, which permits unrestricted use, distribution, and reproduction in any medium, provided the original work is properly cited.

Pregnancy involves a gradual change in tissue consistency, where, as gestational age increases a drop in stiffness is noticeable. The extracellular matrix (ECM) of the cervix whose behavior is controlled by the collagen structure is reconfigured, due to hormonal and protein related factors that degraded it. There is an increase in cellular and water content. The collagen maintains a stable percentage, although the synthesis-solubility interaction causes a transformation in the network increasing its diameter and waviness, which destabilizes the mechanical integrity. Further understanding of the remodeling of the cervix becomes a key element in the progress against preterm birth. However, since the woman is in a very delicate state, the available information is scattered. The aim is to provide a framework where the variation of the histological properties is linked with the individual biomechanical evolution of the constituents; therefore a multiscale approach to the problem can be made. The results of different authors were reviewed to obtain values of each component depending on the gestational age, and then they were combined with the mechanical development of each variable obtained from the outputs of numerical simulations of another author. An additive function is proposed, in which the mechanical contribution of each constituent is added to a reference value established for a nonpregnant state. Results show how biochemistry models the mechanical behavior of the tissue through the histology and morphology of the ECM.

1. Introduction

The anatomical function of the cervix is to serve as a gatekeeper during pregnancy, separating the fetus from the outside. Gestation is a delicate process where there is often lack of information. The possibility of obtaining samples of cervical tissue at any time is solely limited to scientific and at risk cases, which is preventing an adequate breakthrough in the characterization of the etiology of the cervix. This is now an urgent problem in the case of premature birth, the first cause of infant mortality in children under five years of age [1, 2]. It remains a major clinical challenge for obstetricians due to the difficulty in its prevention; likewise, some techniques used (such as cerclage and progesterone), while encouraging, present some limitations [3, 4].

It is well known that from the moment a woman gets pregnant biological transformations occur, coming from the combination of the growing pressures exerted by the fetus and biochemical processes, all of which involve the

remodeling of the cervical tissue. This implies changes in the morphology of the tissue to the point of altering mechanical properties [5]. The cervical stroma, which is the part that has a connective role, has a composition that consists of a collection of macromolecules necessary for pregnancy and to produce muscle functions [6]. Additionally, there is a set of molecules embedded in an extracellular matrix (ECM), which provides structural support to the cells. Collagen fibers are its main constituent, which form a cross-linked network intertwined with the protein elastin, with both being surrounded by a viscous substance of glycosaminoglycans (GAGs) and water [7]. Collagen provides tensile strength and firmness through its hierarchical composition, made of small fibers comprising a bundle [8]. Furthermore, its waviness confers anisotropy and heterogeneity to the tissue. With these components, a viscoelastic behavior is exhibited, with great deformations and relaxations. In low stress elastin acts as a spring returning quickly to its state [9]. GAGs, due to their viscous character, under compression serve as dampers [10]. The water modifies

TABLE 1: Stroma evolution during gestation. Percentages refer to dry tissue, except for water and dry tissue, which are in relation to the total.

Constituents	Nonpregnant	Content (%)			Reference
		Early	Late	Postpartum	
Water	78	75	83	76	[35]
Dry tissue	22	25	17	24	-
Collagen content	71	-	78	-	[11]
Collagen solubility	17	75	76	88	[34]
Elastin	1.33	-	0.73	-	[51]
GAGs	1.6	-	2.6	1.2	[24]
Cells	8	-	15	-	[6]

the mechanical relations in the cervix entering a state of unbalance, disorganizing the components [11]. Therefore, the ECM ensures the integrity of the tissue during gestation.

The remodeling process is a progressive transformation of the appearance of the tissue that is translated into four phases which are superimposed as they occur until birth, namely, softening, ripening, dilation, and postpartum [12]. There exist a series of factors, mainly hormonal and protein related, that promote an inflammatory state [13] that degrades the ECM and enhance tissue distensibility. The mechanical response during gestation is a decrease in stiffness, which is governed by the structure of collagen. There is a reduction of cross-linking between fibers; besides, the distinctive arrangement of the fibers changes, from being aligned to curling [14].

As can be inferred from the above, the morphology of the cervix during pregnancy is a complicated subject to study, where the greater information collected comes from the moments before and after delivery. Experimental data of the morphological and biochemical characteristics at the microscopic level is essential to monitor trends and to be able to program specific actions since the mechanical properties at the macroscopic level of the tissue are related to them [5, 15]. Notwithstanding, the complex structure of the cervix hinders the analysis of individual changes in each component, whose behavior is interrelated.

Hence, the main objective of this work is to provide a first approach in a temporal prediction of the stiffness evolution of the cervix, where the contribution of each constituent will be highlighted. To get here, an histobiomechanical framework that materializes in a curve of stiffness versus gestational age is built. Besides, the relationships established between biochemistry and histology will be shown.

2. Materials and Methods

Histological transformations in the tissue are responsible for variations in consistency. As a starting point, the basis of this study is on the multiscale approach proposed by Peralta [16], which indicates the interconnections between components, which allows filling gaps in knowledge. In order to study the mechanisms that govern internal processes of the remodeling, a three-step procedure is proposed: (1) to fit curves for the chosen values of the content of the fundamental constituents of the cervical stroma derived from the literature, (2) to adapt the results of Peralta et al. [15] where they computed a numerical relationship between histological

and morphological changes and the tissue elasticity, and (3) to combine the previous results. It is suggested that the process is inverted, beginning from the mechanical contribution of each independent element to end with a real evolution of the whole set.

2.1. Content of the Components and Fitting. Since each person is different, whether by obstetrical or medical history, the values chosen to represent each component should be representative of the important variations recorded. Selection criteria are proposed based on existing information: (i) It must follow the behavior recorded by most studies. Some measures deviate much from the general trend and remain isolated as cases without validation by other sources. (ii) The biochemical analysis that has been used for measuring is crucial. First of all, the result should be in dry weight, because large variations are registered when working with wet weight [17]. Secondly, the assay should be standardized to contrast it with other sources. (iii) Sufficient data should be available. Many studies have evaluated the content of some components only at one point in pregnancy, usually at the beginning, so that evolution of these cannot be envisaged.

Selected data are summarized in Table 1. The gestation age corresponds to 0 weeks in nonpregnant, 12 weeks in early, 38 weeks in late, and 42 weeks in postpartum phase.

The chosen values are fitted to time evolution curves with the intent to relate the gestational age to absolute values (%) of each ECM component. Many different mathematical models for growth can be useful [18], which can vary in flexibility and number of parameters needed. For example, the development of many organisms is represented by logistic curves [19] while cell growth is represented with exponential models [20]. In these situations, nonlinear modeling stands as a tool able to estimate characteristic parameters, which could establish a more reliable link between gestational age and component content. By convention, a balance between variance and bias is always sought. However, due to the scarcity of data that has been mentioned, a good fit is desired, prioritizing the bias and discarding the variance. The curves can be fitted to the data using nonlinear least squares. This procedure is conducted by a Levenberg-Marquardt algorithm [21].

The following content describes the temporal evolution of each ECM component and its characteristics.

2.1.1. Collagen. In terms of dry weight, the collagen content remains practically constant. This has not been measured

by many researchers, as it is a rigorous process. It is fitted to a logistic curve (see (1)) that simulates how the increase of collagen at first is important to then stagnate due to the interaction solubility-synthesis that will be discussed later.

$$\frac{dC}{dt} = C(k - \delta) \quad (1)$$

where C is the collagen content in function of the time, k is the growth rate, and δ is the steepness of the inflection zone, related to the rate of synthesis of new collagen.

It is expected that as collagen turnover increases, a synthesis-degradation process will be appreciated, affecting the morphology [22] and reducing the mechanical strength. The cervical fibroblasts secrete tropocollagen that self-assembles into fibrils, and then they aggregate to form a collagen fiber [23]. It is believed that as solubility increases (on account of proteases, collagenases, lysyl oxidase, etc.), the synthesis process is repeated more frequently, which means that by not having enough time to be properly disposed of, the collagen is created in new directions and increases disorganization [24]. These newly synthesized fibrils are combined with each other, losing their combined strength due to weaker cross-links, thus favoring degradation [25]. In short, the faster this synthesis is, the greater solubility will be observed, becoming a feedback process.

A crystallization-like system is proposed for synthesis representation. The formation of a new crystal starts with a nucleation process [26], a thermodynamical phase that is dependent on the solute concentration. Heterogeneous primary nucleation occurs when there is an increase in crystal synthesis due to interaction with other particles, which catalyzes this process by providing sustenance.

$$\frac{dS}{dt} = L + k \cdot t^n \quad (2)$$

Equation (2) is expressed in terms of tissue remodeling, with S being the synthesis rate, L the value at time 0, k the growth rate, and n an empirical exponent from crystallization trials.

As discussed above, the interaction solubility-synthesis is key to understand the loss of tensile strength, since the concentration of collagen does not seem to vary significantly and therefore could not be the cause of the changes. This is perceived as a nutritional intake, where the created collagen is destroyed, but when synthesis exceeds degradation, a saturation environment is reached. To represent this, a Morgan-Mercer-Flodin sigmoidal model is suggested (see (3)).

$$S_o = \gamma - \frac{\gamma - \alpha}{1 + (kt)^\delta} \quad (3)$$

where S_o is the solubility rate, γ is the saturation value, α is the initial nonpregnant value, k is the growth rate, and δ is the point where degradation exceeds collagen creation.

Following the synthetic model created by Peralta et al. [15] (outlined in the following section), the morphology of the collagen fibers can be described using three parameters: diameter, interfibrillar space, and waviness. The range of

variation in diameter and interfibrillar space increases with gestation [27, 28], and thus it is expected to evolve in a linear fashion (see (4)):

$$\frac{dD}{dt} = k \quad (4)$$

with D being the value over time and k the slope of the function (the evolution ratio).

Pinheiro et al. [29] examined the evolution of collagen waviness in the pubic joint of pregnant mice, which resembles the behavior of connective tissues in humans. They measure the crimp angle and length directly on the electron micrograph confirming a decrease in angle and consequently an increase in length. The fibers were arrays of parallel fibrils relatively straight at the beginning. As gestation progressed, the fibers were thicker due to the deposition that packed them together, following a wavy course. When the tensile forces become palpable near delivery, this poorly bonded set of fibers tends to easily stretch and separate, leaving fibrils alone, paving the way to complete remodeling. It is hypothesized that, given that it is a fast process, the fibrils do not have time to bond properly which is causing increasing disorganization. By means of the model of Cacho et al. [30] a beta distribution of the crimp is assumed. They generate a data set randomly distributed within a range in the X axis, so that each associated point on the Y and Z axes was distributed with a zero mean normal. With this conditioning, the data are considered as Gaussian white noise, so that its probability density function (PDF) is only characterized by the variance σ^2 .

Three distributions are conceived, ranging according to the phases of early, mid, and late pregnancy. Equation (5) presents the distribution and its parameters:

$$\begin{aligned} \beta(a, b) &= \frac{x^{a-1} (x-1)^{b-1}}{B(a, b)} \\ B(a, b) &= \frac{\Gamma(a) \Gamma(b)}{\Gamma(a+b)} \\ a &= \left(\frac{1-\mu}{\sigma^2} - \frac{1}{\mu} \right) \mu^2 \\ b &= a \left(\frac{1}{\mu} - 1 \right) \end{aligned} \quad (5)$$

where $B()$ is the beta function, a normalization constant to ensure that the total probability integrates to 1, and $\Gamma()$ is the gamma function. The shape parameters of the distribution (a, b) configure its scale and position. This output will give references about the fitting parameters and the behavior of the waviness.

Taking into account the interaction solubility-synthesis and the values of the probability distribution, a similar evolution is anticipated. This is reflected in a logistical function (see (6)).

$$\frac{dW}{dt} = W(k - \delta) \quad (6)$$

where $W(t)$ is the collagen waviness in function of the time, k is the growth rate, and δ is the steepness of the inflection zone, where solubility overcomes synthesis.

2.1.2. Water. The interstitial fluid controls the stiffness response of the tissue. It presents a similar development to hyaluronic acid (HA) that affects collagen organization [31]. When the content increases before delivery, about 5%, it enters a state of nonequilibrium, which reduces the elasticity. As can be observed in Table 1, hydration follows a cyclic behavior represented in

$$\frac{d^2 H(t)}{dt^2} + H(t) = 0 \quad (7)$$

where $H(t)$ is the hydration content in function of time.

2.1.3. Cells. In general terms, there is an increase in vascularization. In the nonpregnant state, there are approximately 8 to 10 % of fibroblast, epithelial, and smooth muscle cells. Near delivery there is an enormous increment of cells due to the proinflammatory state [10]; as a result, an exponential growth rate characterizes the phenomena (see (8)), although at some point in the postpartum this will be limited by the return of the nonpregnant state.

$$A \left(\frac{dC}{dt} - kC \right) = 0 \quad (8)$$

where $C(t)$ is the content of the cell in function of time, A the initial value, and k the growth rate.

2.1.4. GAGs. As a whole, they show a very rapid and abrupt evolution when it comes to labor, which can be divided into two phases and then fitted to an exponential model; see

$$G(t) = ae^{bt} + ce^{dt} \quad (9)$$

where $G(t)$ is the GAGs content in function of time, a and c are the initial values, and b and d are the growth rates.

2.2. Contribution to the Stiffness of the Constituents. This section summarizes the results of the work of Peralta et al. [15]. The greatest difficulty in this study came from the individual description of each component. To tackle this, a numerical model that relates the architectural changes in the microscale to the propagation of shear waves was proposed. This made it possible to obtain quantitative information, in elastic terms of the shear modulus.

The effect of each constituent was studied independently, i.e., not affecting the behavior of the whole; when a content varied, reference values were set. The reference configuration for the model (see Table 2) was established at typical values of the nonpregnant state; for that reason any change in content over time impacted on the computed mechanical properties.

They proposed different models of analysis, and here the one that has the fibers arranged longitudinally and perpendicular to the propagation is adapted. The election is based on a recent study by [32], where pregnant samples were analyzed to find that the cervix section is mostly composed

TABLE 2: Reference input values of the model. Source: [15].

Fiber diameter	5 μm
Interfibrillar space	1 μm
Fiber waviness (sd)	15 μm
Fiber fraction	20%
Hydration	80%
GAGs	1.5%
Cells	8%

of circumferential collagen, which is the direction that will determine the behavior before dilation. The rest is exhibited in a radial form. Nevertheless, this implies that if only the effect of one profile is taken into account, erroneous conclusions can be reached, because waviness configures the network in a random way. So it is proposed to implement a probability density based on directionality within a circle, similar to a normal distribution. This method will be adopted for obtaining the reference value of the stiffness of the cervical tissue and for the final contribution of the waviness. It is estimated that the greatest contribution of waviness comes from the perpendicular profile; however, the parallel profile helps in setting up the network due to the crimping of the fibers. The contribution of this profile is calculated with a Von Mises distribution (10); its density function for the angle x is

$$f(x) = G_n \frac{x}{\pi/2} + G_p \frac{\pi/2 - 2}{\pi/2} \frac{e^{k \cdot \cos(x-\mu)}}{2\pi I_0(k)} \quad (10)$$

with G_n and G_p being the elastic contribution of the perpendicular and parallel profile, respectively, μ where the distribution is clustered, k a dispersion measure that concentrates the points in μ , and I_0 the modified Bessel function of order 0. Following this, the cumulative density function (11) is computed in the interval $0 - \pi/2$.

$$F(x) = \int_0^{\pi/2} f(x) dx \quad (11)$$

Regarding the behavior of the components, several differences between this work and Table 1 can be found. The concentration of collagen is progressively reduced in the numerical model, which became effective by decreasing its mechanical contribution; however, there is a slight increase. This decision does not affect this work, as the stress and the constant synthesis of immature fibers underwent by the collagen network are causing the loss of tensile strength. On the other hand, GAGs content has been informed to increase until labor and then quickly drop. Nonetheless, the synthetic model considered that GAGs decrease for the beginning, which means that fewer particles were formed between collagen and less disorganization can be appreciated. For this reason, it is considered that there is no effective change in the consistency by this component.

The final results are fitted with polynomial functions in order to get an interpolation that collects all the values from the range. The most relevant properties of the model considered are fiber diameter, fiber waviness, hydration,

and cells. Since interfibrillar space and diameter are linked characteristics, they have a joint contribution represented as a single variable. Although GAGs have been found to have no appreciable effect on stiffness, they are known to alter the mechanical structure of the tissue [10, 33]. This is probably due to the fact that GAGs affect other components, mainly collagen, so that its action is indirect, and therefore its independent variation in concentration could not quantify a physical interaction with other elements.

2.3. Gestational Age against Cervical Stiffness. The last step is to combine these two previous results to create a curve that relates gestational age to cervix stiffness. Growth curves (gestational age dependent variables) are entered into the outcome of numerical simulations (mechanical development of each variable). Once implemented, each component will contribute to the consistency, either by adding to or subtracting from the reference value set for the nonpregnant state; therefore it works in relative terms. The influence on the reference value can be represented as an analogy of a Taylor series, as in (12).

$$G(D, W, H, C) = G(ref) + \Delta G(Dia) + \Delta G(Wav) + \Delta G(Wat) + \Delta G(Cel) \quad (12)$$

$G(D, W, H, C)$ represents the final contribution of the elements considered, $G(ref)$ is the reference value, and $\Delta G(Dia)$, $\Delta G(Wav)$, $\Delta G(Wat)$, and $\Delta G(Cel)$ are the relative inputs of the diameter and waviness of the collagen, water, and cells, respectively.

3. Results and Discussion

First of all, the chosen data will be examined for each component; readers are referred to Table 1. Next, the solution of the differential equations and the parameters obtained in the nonlinear fittings and curves will be shown. Second, the stiffness curves of the synthetic model of each variable are adopted through polynomial fittings and the reference stiffness value is obtained. Finally, the relative contribution of each component is taken and a complete model of the cervical mechanical evolution is provided.

The latest data recorded for the collagen content was made by Myers et al. [11], where there is a small increase in collagen content, reflected in (13). Results are displayed in Figure 1.

$$C(t) = \alpha + \frac{\gamma - \alpha}{1 + e^{(k-t)/\delta}} \quad (13)$$

In the first few weeks the rate of solubility shows a very large increase, and then it stabilizes and stagnates near the end (see Figure 2). This behavior can be modeled with the data registered by Uldbjerg et al. [34].

The interaction solubility-synthesis configures the ratio of synthesis. There must be a balance to preserve the structural integrity, and so, synthesis is opposed to solubility action with similar values (see Figure 3).

The data for the diameter and interfibrillar space were taken from the model of Peralta et al. [15]. As the other components of the ECM develop, they will affect the morphology

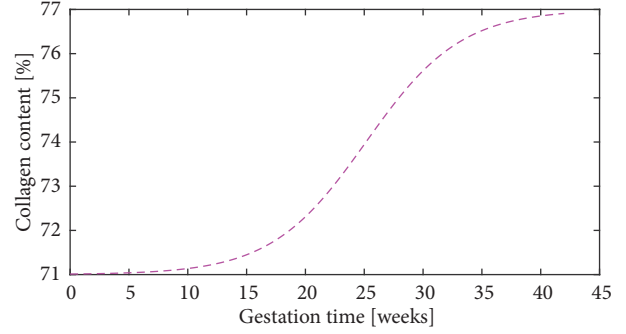


FIGURE 1: Collagen content evolution during pregnancy, with α being the initial value and γ the maximum content. Parameters: $k=25.15$, $\delta=4.035$, $\alpha=71$, and $\gamma=77$.

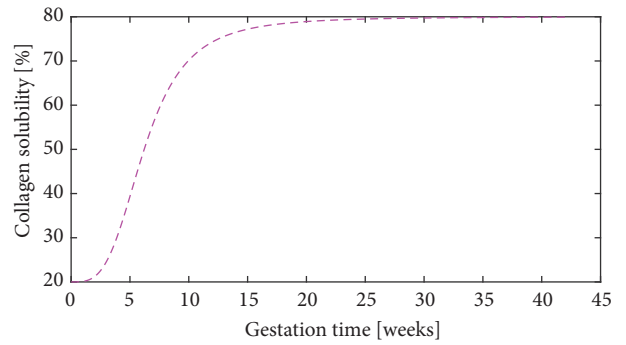


FIGURE 2: Collagen solubility evolution during pregnancy. Parameters: $k=0.161$, $\delta=3.42$, $\alpha=20$, and $\gamma=80$.

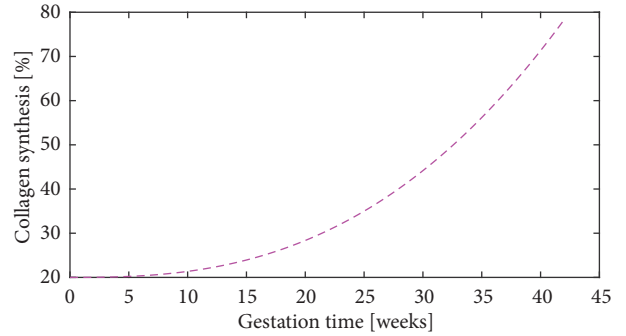


FIGURE 3: Collagen synthesis evolution during pregnancy. Parameters: $L=20$, $k=0.003281$, $n=2.618$.

of the collagen; in this case, it is assumed in a linear fashion (see Figure 4). The range for the diameter is established in (5, 10) μm and for the interspace in (1, 4) μm . The models for diameter and space are illustrated in (14), respectively.

$$\begin{aligned} F_d &= 0.119t + 5 \\ I_d &= 0.0714t + 1 \end{aligned} \quad (14)$$

In the case of waviness, the fibers increase its crimping in agreement with the synthesis of collagen. The range of the variance σ^2 for the beta distribution has been restricted to 5-45 μm . It has been quantified from the fiber fraction with

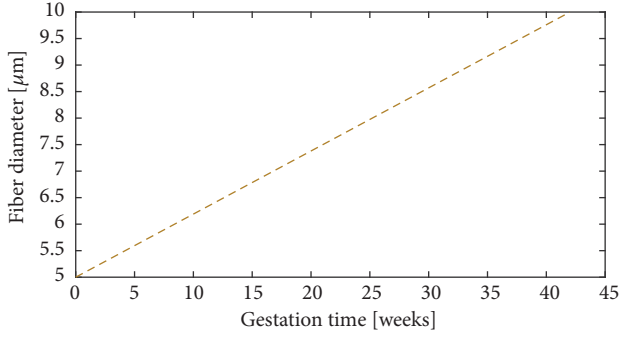
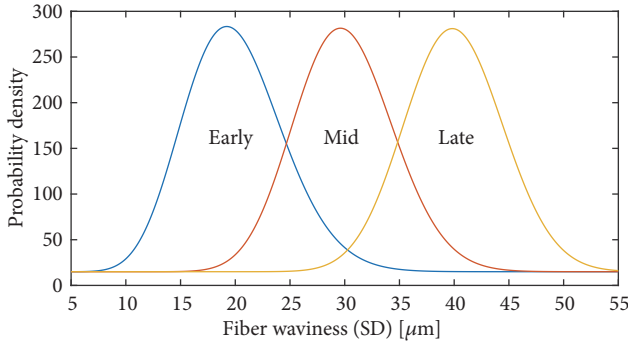


FIGURE 4: Collagen diameter evolution during pregnancy.

FIGURE 5: Waviness probability density function. Parameters: for early ($a=15.8$; $b=63.2$), for mid ($a=31.2$; $b=72.8$), and for late phase ($a=47.6$; $b=71.4$).

respect to the total ECM and the morphology observed in microscope images [16]. Since the β distribution is restricted to (0-1), it is possible to shift and scale the output through (15).

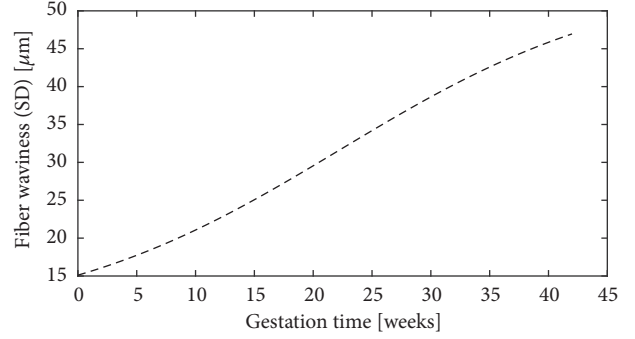
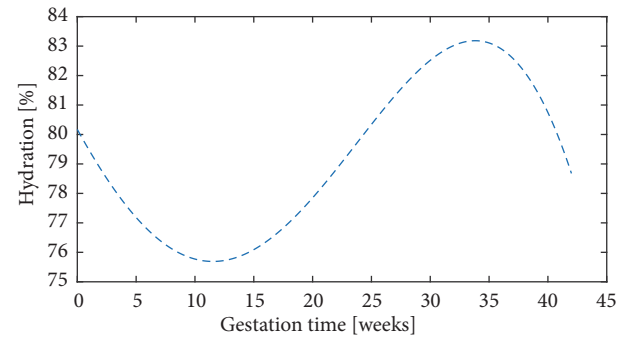
$$5 + (45 - 5) \cdot \beta(pdf) \quad (15)$$

The shape parameters of the distribution are computed according to the phase of pregnancy, where it is assumed that the mean (μ) of the early phase is $15 \mu\text{m}$, for the mid phase $25 \mu\text{m}$, and for the late phase $35 \mu\text{m}$, with a variance (σ^2) for all of $0.002 \mu\text{m}^2$. These values once calculated are presented in Figure 5, along with their probability density. The results allow estimating key evolutionary points in the waviness. There is a minimum around $8 \mu\text{m}$ and a maximum around $55 \mu\text{m}$. In early phase the most probable value is approximately $20 \mu\text{m}$, in mid phase is $30 \mu\text{m}$, and in late phase is $40 \mu\text{m}$.

Due to their reliance on collagen synthesis, a similar evolution is expected for waviness, starting with cautious crimping and then undertaking a remarkable increase, reaching a value that could not be higher. Equation (16) is the logistic function solution. Figure 6 represents the estimated curve with its parameters.

$$W(t) = \alpha + \frac{\gamma - \alpha}{1 + e^{(k-t)/\delta}} \quad (16)$$

Some authors have measured the water content in the cervix, to conclude that there is an increase of 5%. However, only a few were able to complete the data in all the stages

FIGURE 6: Fiber waviness evolution during pregnancy. α is the lower crimping value and γ the maximum waviness reached. Parameters: $k=22.26$, $\delta=12.42$, $\alpha=8.5$, and $\gamma=54.8$.FIGURE 7: Water content evolution during pregnancy. Parameters: $a_1=712.3$; $a_2=636.7$; $b_1=0.05475$; $b_2=0.0587$; $c_1=0.705$; $c_2=3.788$.

of pregnancy. Anderson et al. [35] obtained a sinusoidal relationship, that is translated into (17), where a_i is the amplitude of the change, b_i the frequency according to the stage of pregnancy, and c_i the phase that indicates the initial percentage. In Figure 7 the transformation is visualized.

$$H(t) = a_1 \sin(b_1 t + c_1) + a_2 \sin(b_2 t + c_2) \quad (17)$$

The cell proliferation is based on the protection and preparation for the last phase of pregnancy, where there are a number of chain reactions that affect the hormones responsible for pregnancy. Due to this, an exponential evolution (see (18)) is presented, via the data of Oxlund et al. [6]. Figure 8 shows the output.

$$C(t) = Ae^{kt} \quad (18)$$

The last constituent studied is GAGs. They have a strong relationship with collagen morphology and water content. Therefore, they begin with gradual growth, to reach birth and fall exponentially (see Figure 9). The data of Shimizu et al. [24] is faithful to this description.

In the next point, the reference mechanical value of the cervix has been calculated. It comes from the conjunction of the profiles of the numerical model and the distribution of Von Mises. The module G for the perpendicular profile is 14 kPa and for the parallel is 166 kPa . The distribution is clustered in $\mu=\pi/2$ and $k=2$. The computed value after using the cumulative distribution function is 31 kPa .

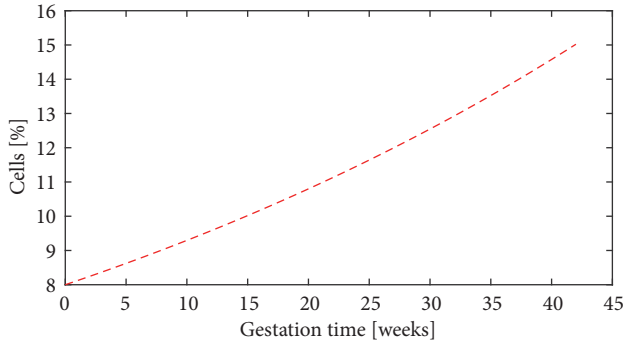


FIGURE 8: Cells content evolution during pregnancy. Parameters: $A=8$; $k=0.015$.

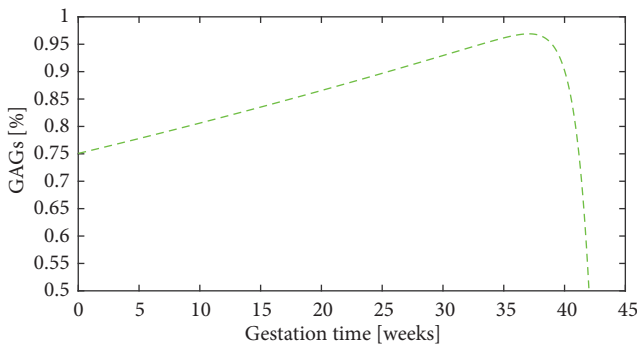


FIGURE 9: GAGs content evolution during pregnancy. Parameters: $a=-3.3 \cdot 10^{-16}$; $b=0.8326$; $c=0.7507$; $d=0.007117$.

The response of the diameter and waviness of collagen, water, and cells, which are the elements considered for the final model, are adapted with polynomial fittings. Figure 10 displays the adaptation.

The combination of both results, introducing the temporal evolution in the mechanical contribution and subtracting the initial value given to each constituent, is presented in Figure 11. It is emphasized that the collagen morphology is mainly responsible for decay in stiffness. Hydration has no appreciable effect due to its scale a priori, while cells increase their production and counteract the loss of distensibility caused by collagen.

The final model is displayed in Figure 12. The central value is 31 kPa, and then terms of the relative contribution of each component are added to simulate a complete function. At first, the drop in stiffness is noticeable. By week 25, the synthesis-solubility interaction of collagen stabilizes and this is when cell recruitment becomes palpable, balancing the mechanical integrity of cervical tissue.

Several authors have conducted feasibility studies regarding the use of shear wave elastography on pregnant women. They are based on the SSI technique [36] that is able to quantify the shear wave speed (SWS). Once this speed (C_s) is computed and under the assumption of a purely elastic and incompressible medium the shear modulus (μ) can be described as $\mu = \rho C_s^2$, with ρ being the density of the tissue. Bearing this in mind, the range of values stemming from

this final model are consistent with the study of Peralta et al. [37]. On the other hand, in the works of Muller et al. and Hernandez-Andrade et al. [38, 39], although they obtained a narrower and smaller value range, they observed a similar trend; from the first weeks there is a notable decrease in the stiffness that in mid pregnancy softens. For its part, in a recent study of Carlson et al. [40] using a prototype of shear waves, they noted that stiffness is reduced by half from the first to the third trimester, with values close to those of this work.

Furthermore, this elastic transformation of the cervix can be assimilated with the remodeling that is experienced in the different phases of pregnancy.

Cervical softening is the first and longest phase that commonly starts in the first month. At this moment it begins a slowly increasing turnover of ECM components, which shows a decline in resistance, associated with unordered collagen fibers, elastic tension, increased water content, and proteoglycans [41]. In the nonpregnant cervix the epithelial cells are scant; however, during pregnancy the hormone relaxin is implicated in their proliferation when the synthesis of some prostaglandins (PGs) begins to be noticed and the cytokine interleukin-8 (IL-8) appears [42]. From this moment the cells are configured as the main support to the structural integrity. They secrete mucus plug [43], a physical barrier against infections, as well as a proliferation of fibroblasts. Yet, due to regulation in the ECM, the collagen fibers begin to lose strength in their state of creation and assembly, where the matricellular proteins thrombospondin 2 (THBS2) and tenascin C (TnC) modify the collagen architecture [28]. This is reflected in the first 25 weeks of the graph.

Cervical ripening begins a few weeks before delivery and is characterized by rapid changes in the cervix, where integrity is being lost in order to prepare for the delivery. There is a marked increase in the synthesis of proteoglycans, collagen, and hyaluronic acid (HA), a hydrophilic glycosaminoglycan, which interacts with epithelium cells and proteoglycans as versican. HA is in a large molecular weight form that has been said to favor tissue hydration, resulting in a viscoelastic material, which unbalances the structure of the collagen network, dispersing and reducing its mechanical resistance due to increasing collagen solubility [44, 45]. The cervical epithelium continues to provide a mucosal barrier against infection while regulating steroid hormones to provide a rich estrogen environment. In order to initiate this phase, it is necessary that the activity of progesterone decays, since it has been proven that introducing its inhibitors during softening cause it to reach maturation sooner [46], proving that progesterone is a factor that maintains pregnancy. The loss of this hormone helps the estrogen to reach its receptors, facilitating the activation of ripening.

At term there must be a dilation of the cervix, which is preceded by biochemical changes caused by a new hormonal regulation, contractions of the myometrium, and the tension of the fetal protrusion, triggering the maximal loss of tensile strength. This process involves the infiltration of leukocytes, PGs, proteases, and collagenases into the ECM [13]. The protective mucus plug is expelled; in addition, it comes to a phase of effacement where the cervix narrows its walls and shortens, to reach 10 cm in diameter. The activity of

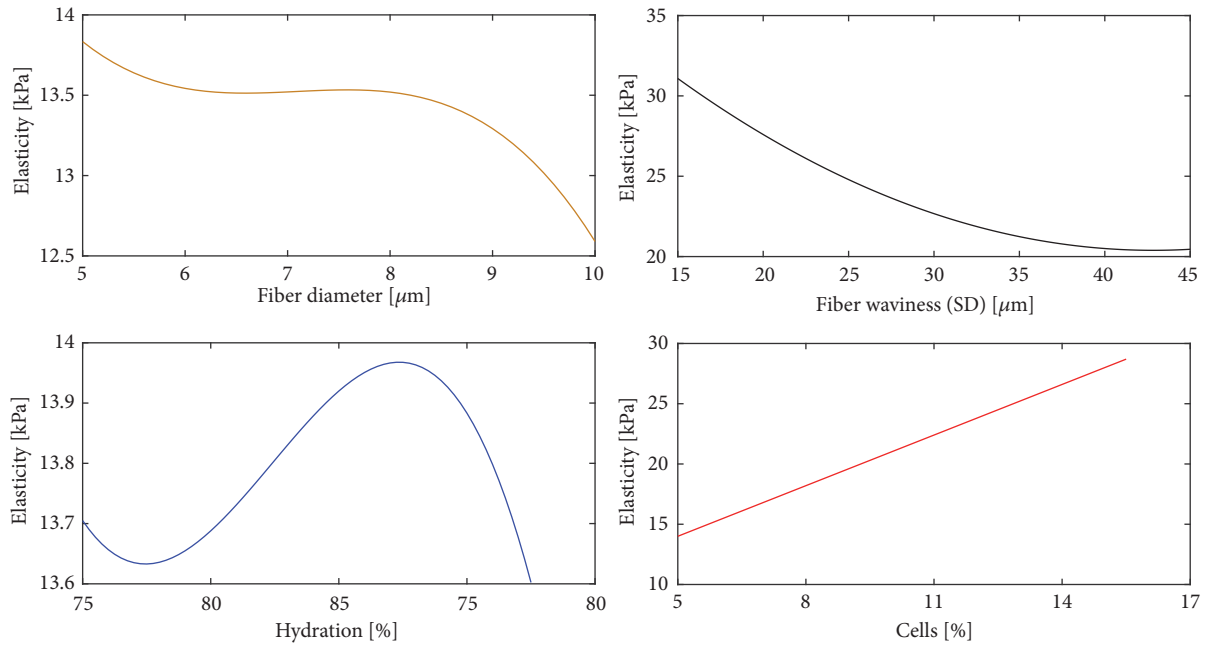


FIGURE 10: Content of each component versus elasticity. Polynomials of degree three were used for diameter and hydration, degree two for waviness, and degree one for cells.

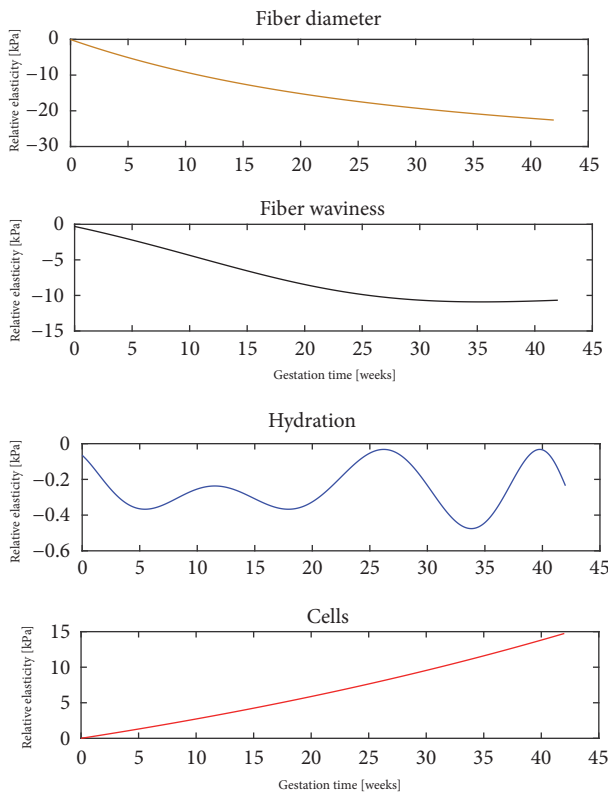


FIGURE 11: Content of each component versus elasticity. The polynomial degree for diameter and hydration is three, for waviness is two, and for cell is one.

the enzyme hyaluronidase is increased, breaking down HA bonds and promoting a shorter duration of labor by cause of loss of cervical mechanical strength [47]. It has been

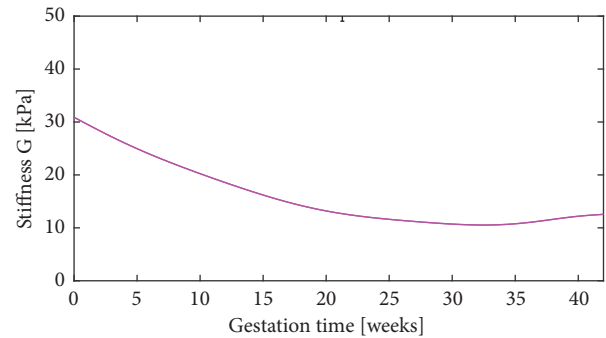


FIGURE 12: Evolute biomechanical model of the cervix.

proven that PGs have a crucial function in the late term. The application of exogenous PGs increased collagen solubility and altered ECM components, imitating cervical ripening and dilation effects. Notwithstanding, the prostaglandins PGE2 and PGF2 do not increase its content which has left a gap as to its operation, even introducing a progesterone inhibitor induced ripening, but no rise in PGs was registered [48, 49]. To complete pregnancy it is necessary that the female reproductive system is transformed from a static formation to an active one with the coordination of its components. This coordination will lead to the final contractions that are transmitted through gap junctions. The fetus intervenes through the placenta, which creates different hormones. This is reflected in changes in progesterone-estrogen ratio, upregulation of oxytocin, PGs, and the decrease of nitric oxide (NO). The previous phases (ripening and dilation) can be grouped from week 25 to week 38. The stiffness drop is no longer so marked. On the one hand, collagen continues to lose its structure, but on the other hand, cells

together with hormonal activity mean the infiltration of many components.

The postpartum phase, the uterine involution, is meant to recover the tensile strength of the tissue, to avoid environmental contamination and to prepare for ensuing pregnancies. An increase in leukocyte cells allows the renewal of tissue functionality, breaking down components causing weakness and disorganization of the ECM through the secretion of the enzyme protease. On the other side, there is an upregulation of synthesis of ECM constituents to return to a nonpregnant state [50] and loss of tissue hydration. The last stretch of the plot is remarkable for being the only one in which stiffness begins to rise.

This flow explains and validates decisions on both the content of components and their evolution.

This work has certain limitations. The resulting curve was achieved through values from a simulation, which does not necessarily have to be correct. With real values, the curve would be more reliable and optimized. The fit models have been chosen for convenience to simulate the behavior explained, so that some parameters are not clearly defined. The advantage of studying the components individually becomes a constraint as soft tissue remodeling is usually approached from the perspective of mixing theory. There is a mass balance where the constituents make a continuous exchange of percentages of properties. In the work of Myers et al. [52] it is proposed to adopt the tissue composition as state variables that mathematically describe the state of a dynamic system. In the future, this model can be used to build a continuum biomechanical framework.

4. Conclusions

A framework of histobiomechanical properties of the cervical stroma is proposed. A literature review was carried out to explore the contributions of several authors, and then nonordinary developments have been identified. In the case of hydration there is a cyclical tendency, probably related to the feeding of the fetus and eventually when water breaks. GAGs decrease exponentially when delivery arrives. It may be thought that it is due to the increase in mucus plug that somewhat dissolves the polysaccharides of GAGs, allowing a hyperstretching of cervical tissue by removing most of its viscosity. The rest of the constituents follow an increasing trend, either logistically for collagen or exponentially for cells. This was combined with the outputs of a numerical model to build a function that relates gestational age to stiffness. The spatial medium generated is based on increasing the diameter and waviness of collagen fibers along with hydration and cellular content.

Hormones have been identified as the most active elements of pregnancy. The role of oxytocin, PGs, and progesterone as triggers of the whole process should always be kept in mind. More detailed monitoring of these variables can lead to improvements. The combination of cells and the proteolysis of enzyme plays a key role near childbirth. They degrade collagen while trying to maintain the integrity of an increasingly unstable structure. Thus biochemistry is able to control histology.

The viscous part of the model is irrelevant, being more sensitive to modifications in the microstructure than to the ECM content. This has shown that there is a drop in elasticity during pregnancy represented by a function with histological parameters. It can be seen that everything leads to collagen, which is why it has become the most studied component in this study. In a more general view, it is proposed to study the behavior of collagen in specimens in the absence of other constituents.

Data Availability

The data used to support the findings of this study are available from the corresponding author upon request.

Conflicts of Interest

The authors declare that there are no conflicts of interest regarding the publication of this paper.

Acknowledgments

This research was supported by the Ministry of Education [DPI2017-83859-R, DPI2014-51870-R, DPI2010-17065, and UNGR15-CE-3664], Ministry of Health [DTS15/00093 and PI16/00339, PI-0107-2017, PIN-0030-2017], Junta de Andalucía [PI1-CTS-8089], and the European Social Fund (youth employment initiative) projects.

References

- [1] T. Moore, E. M. Hennessy, J. Myles et al., "Neurological and developmental outcome in extremely preterm children born in England in 1995 and 2006: the EPICure studies," *British Medical Journal*, vol. 345, no. 7886, Article ID e7961, 2012.
- [2] H. Blencowe, S. Cousens, D. Chou et al., "Born too Soon: the global epidemiology of 15 million preterm births," *Reproductive Health*, vol. 10, no. 1, article S2, 2013.
- [3] M. S. To, Z. Alfirevic, V. C. F. Heath et al., "Cervical cerclage for prevention of preterm delivery in women with short cervix: Randomised controlled trial," *The Lancet*, vol. 363, no. 9424, pp. 1849–1853, 2004.
- [4] C. A. Crowther, P. Ashwood, A. J. McPhee et al., "Vaginal progesterone pessaries for pregnant women with a previous preterm birth to prevent neonatal respiratory distress syndrome (the PROGRESS Study): A multicentre, randomised, placebo-controlled trial," *PLoS Medicine*, vol. 14, no. 9, Article ID e1002390, 2017.
- [5] K. M. Myers, H. Feltovich, E. Mazza et al., "The mechanical role of the cervix in pregnancy," *Journal of Biomechanics*, vol. 48, no. 9, pp. 1511–1523, 2015.
- [6] B. S. Oxlund, G. Ørtoft, A. Brüel et al., "Collagen concentration and biomechanical properties of samples from the lower uterine cervix in relation to age and parity in non-pregnant women," *Reproductive Biology and Endocrinology*, vol. 8, no. 1, p. 82, 2010.
- [7] P. C. Leppert, "Anatomy and physiology of cervical ripening," *Clinical Obstetrics and Gynecology*, vol. 38, no. 2, pp. 267–279, 1995.

- [8] M. P. E. Wenger, L. Bozec, M. A. Horton, and P. Mesquidaz, "Mechanical properties of collagen fibrils," *Biophysical Journal*, vol. 93, no. 4, pp. 1255–1263, 2007.
- [9] P. C. Leppert, S. Keller, J. Cerreta, Y. Hosannah, and I. Mandl, "The content of elastin in the uterine cervix," *Archives of Biochemistry and Biophysics*, vol. 222, no. 1, pp. 53–58, 1983.
- [10] Y. Akgul, R. Holt, M. Mummert, A. Word, and M. Mahendroo, "Dynamic changes in cervical glycosaminoglycan composition during normal pregnancy and preterm birth," *Endocrinology*, vol. 153, no. 7, pp. 3493–3503, 2012.
- [11] K. M. Myers, A. P. Paskaleva, M. House, and S. Socrate, "Mechanical and biochemical properties of human cervical tissue," *Acta Biomaterialia*, vol. 4, no. 1, pp. 104–116, 2008.
- [12] B. Timmons, M. Akins, and M. Mahendroo, "Cervical remodeling during pregnancy and parturition," *Trends in Endocrinology & Metabolism*, vol. 21, no. 6, pp. 353–361, 2010.
- [13] R. Word, X. Li, M. Hnat, and K. Carrick, "Dynamics of cervical remodeling during pregnancy and parturition: mechanisms and current concepts," *Seminars in Reproductive Medicine*, vol. 25, no. 1, pp. 069–079, 2007.
- [14] H. Feltovich, T. J. Hall, and V. Berghella, "Beyond cervical length: Emerging technologies for assessing the pregnant cervix," *American Journal of Obstetrics & Gynecology*, vol. 207, no. 5, pp. 345–354, 2012.
- [15] L. Peralta, G. Rus, N. Bochud, and F. S. Molina, "Mechanical assessment of cervical remodelling in pregnancy: Insight from a synthetic model," *Journal of Biomechanics*, vol. 48, no. 9, pp. 1557–1565, 2015.
- [16] P. Pereira and L. María, "Feasibility of using ultrasonic shear waves to assess cervical remodelling during the gestation period," 2018, <http://digibug.ugr.es/handle/10481/50941>.
- [17] M. House, D. L. Kaplan, and S. Socrate, "Relationships between mechanical properties and extracellular matrix constituents of the cervical stroma during pregnancy," *Seminars in Perinatology*, vol. 33, no. 5, pp. 300–307, 2009.
- [18] P. Ghisletta, E. Cantoni, and N. Jacot, "Nonlinear growth curve models," in *Proceedings of the International Conference on Dependent Data in Social Sciences Research Forms, Issues, and Methods of Analysis*, pp. 47–66, Springer, December 2013.
- [19] A. Tsoularis and J. Wallace, "Analysis of logistic growth models," *Mathematical Biosciences*, vol. 179, no. 1, pp. 21–55, 2002.
- [20] S. Cooper, "Distinguishing between linear and exponential cell growth during the division cycle: Single-cell studies, cell-culture studies, and the object of cell-cycle research," *Theoretical Biology and Medical Modelling*, vol. 3, no. 1, p. 10, 2006.
- [21] J. J. Moré, "The Levenberg-Marquardt algorithm: implementation and theory," in *Numerical Analysis*, pp. 105–116, Springer, Berlin, Germany, 1978.
- [22] A. J. Fosang, C. J. Handley, V. Santer, D. A. Lowther, and G. D. Thornburn, "Pregnancy-related changes in the connective tissue of the ovine cervix," *Biology of Reproduction*, vol. 30, no. 5, pp. 1223–1235, 1984.
- [23] E. G. Canty and K. E. Kadler, "Procollagen trafficking, processing and fibrillogenesis," *Journal of Cell Science*, vol. 118, no. 7, pp. 1341–1353, 2005.
- [24] K. Myers, S. Socrate, D. Tzeranis, and M. House, "Changes in the biochemical constituents and morphologic appearance of the human cervical stroma during pregnancy," *European Journal of Obstetrics & Gynecology and Reproductive Biology*, vol. 144, no. 1, pp. S82–S89, 2009.
- [25] A. K. Williamson, A. C. Chen, K. Masuda, E. J.-M. A. Thonar, and R. L. Sah, "Tensile mechanical properties of bovine articular cartilage: Variations with growth and relationships to collagen network components," *Journal of Orthopaedic Research*, vol. 21, no. 5, pp. 872–880, 2003.
- [26] N. S. Tavare, *Industrial Crystallization: Process Simulation Analysis and Design*, Springer Science & Business Media, 2013.
- [27] M. Mahendroo, "Cervical remodeling in term and preterm birth: Insights from an animal model," *Reproduction*, vol. 143, no. 4, pp. 429–438, 2012.
- [28] M. L. Akins, K. Luby-Phelps, R. A. Bank, and M. Mahendroo, "Cervical softening during pregnancy: Regulated changes in collagen cross-linking and composition of matricellular proteins in the mouse," *Biology of Reproduction*, vol. 84, no. 5, pp. 1053–1062, 2011.
- [29] M. C. Pinheiro, S. G. Moraes, C. N. Battlehner, E. G. Caldini, O. M. S. Toledo, and P. P. Joazeiro, "Histochemical and ultrastructural study of collagen fibers in mouse pubic symphysis during late pregnancy," *Micron*, vol. 35, no. 8, pp. 685–693, 2004.
- [30] F. Cacho, P. J. Elbischger, J. F. Rodríguez, M. Doblaré, and G. A. Holzapfel, "A constitutive model for fibrous tissues considering collagen fiber crimp," *International Journal of Non-Linear Mechanics*, vol. 42, no. 2, pp. 391–402, 2007.
- [31] S. Jorge, S. Chang, J. J. Barzilai, P. Leppert, and J. H. Segars, "Mechanical signaling in reproductive tissues: Mechanisms and importance," *Reproductive Sciences*, vol. 21, no. 9, pp. 1093–1107, 2014.
- [32] Y. Gan, W. Yao, K. M. Myers, J. Y. Vink, R. J. Wapner, and C. P. Hendon, "Analyzing three-dimensional ultrastructure of human cervical tissue using optical coherence tomography," *Biomedical Optics Express*, vol. 6, no. 4, pp. 1090–1108, 2015.
- [33] G. B. de Oliveira, A. M. do Vale, A. C. dos Santos, C. E. B. de Moura, H. A. D. O. Rocha, and M. F. de Oliveira, "Composition and significance of glycosaminoglycans in the uterus and placenta of mammals," *Brazilian Archives of Biology and Technology*, vol. 58, no. 4, pp. 512–520, 2015.
- [34] N. Ulbjerg, G. Ekman, A. Malmström, K. Olsson, and U. Ulmsten, "Ripening of the human uterine cervix related to changes in collagen, glycosaminoglycans, and collagenolytic activity," *American Journal of Obstetrics & Gynecology*, vol. 147, no. 6, pp. 662–666, 1983.
- [35] J. Anderson, N. Brown, M. S. Mahendroo, and J. Reese, "Utilization of different aquaporin water channels in the mouse cervix during pregnancy and parturition and in models of preterm and delayed cervical ripening," *Endocrinology*, vol. 147, no. 1, pp. 130–140, 2006.
- [36] J. Bercoff, M. Tanter, and M. Fink, "Supersonic shear imaging: a new technique for soft tissue elasticity mapping," *IEEE Transactions on Ultrasonics, Ferroelectrics and Frequency Control*, vol. 51, no. 4, pp. 396–409, 2004.
- [37] L. Peralta, F. S. Molina, J. Melchor et al., "Transient elastography to assess the cervical ripening during pregnancy: a preliminary study," *European Journal of Ultrasound*, vol. 38, no. 4, pp. 395–402, 2017.
- [38] M. Muller, D. Ait-Belkacem, M. Hessabi et al., "Assessment of the cervix in pregnant women using shear wave elastography: a feasibility study," *Ultrasound in Medicine & Biology*, vol. 41, no. 11, pp. 2789–2797, 2015.
- [39] E. Hernandez-Andrade, A. Auriol-Garibay, M. Garcia et al., "Effect of depth on shear-wave elastography estimated in the internal and external cervical os during pregnancy," *Journal of Perinatal Medicine*, vol. 42, no. 5, pp. 549–557, 2014.

- [40] L. C. Carlson, T. J. Hall, I. M. Rosado-Mendez et al., "Detection of changes in cervical softness using shear wave speed in early versus late pregnancy: An in vivo cross-sectional study," *Ultrasound in Medicine & Biology*, vol. 44, no. 3, pp. 515–521, 2018.
- [41] S. Y. Yu, C. A. Tozzi, J. Babiarz, and P. C. Leppert, "Collagen changes in rat cervix in pregnancy—polarized light microscopic and electron microscopic studies," *Proceedings of the Society for Experimental Biology and Medicine*, vol. 209, no. 4, pp. 360–368, 1995.
- [42] C. G. Barclay, J. E. Brennand, R. W. Kelly, and A. A. Calder, "Interleukin-8 production by the human cervix," *American Journal of Obstetrics & Gynecology*, vol. 169, no. 3, pp. 625–632, 1993.
- [43] O. D. Sherwood, "Relaxin's physiological roles and other diverse actions," *Endocrine Reviews*, vol. 25, no. 2, pp. 205–234, 2004.
- [44] M. Obara, H. Hirano, M. Ogawa et al., "Changes in molecular weight of hyaluronan and hyaluronidase activity in uterine cervical mucus in cervical ripening," *Acta Obstetrica et Gynecologica Scandinavica*, vol. 80, no. 6, pp. 492–496, 2001.
- [45] E. E. Maradny, N. Kanayama, H. Kobayashi et al., "The role of hyaluronic acid as a mediator and regulator of cervical ripening," *Human Reproduction*, vol. 12, no. 5, pp. 1080–1088, 1997.
- [46] C. L. Elliott, J. E. Brennand, and A. A. Calder, "The effects of mifepristone on cervical ripening and labor induction in primigravidae," *Obstetrics & Gynecology*, vol. 92, no. 5, pp. 804–809, 1998.
- [47] B. D. Byers, E. Bytautiene, M. M. Costantine et al., "Hyaluronidase modifies the biomechanical properties of the rat cervix and shortens the duration of labor independent of myometrial contractility," *American Journal of Obstetrics & Gynecology*, vol. 203, no. 6, p. 596.e1, 2010.
- [48] N. C. W. Hill and I. Z. Mackenzie, "2308 second trimester terminations using extra-amniotic or intra-amniotic prostaglandin E2: an analysis of efficacy and complications," *BJOG: An International Journal of Obstetrics & Gynaecology*, vol. 96, no. 12, pp. 1424–1431, 1989.
- [49] A. Rådestad, N. J. Christensen, and L. Strömberg, "Induced cervical ripening with mifepristone in first trimester abortion. A double-blind randomized biomechanical study," *Contraception*, vol. 38, no. 3, pp. 301–312, 1988.
- [50] U. B. Knudsen, N. Uldbjerg, T. Rechberger, and K. Fredens, "Eosinophils in human cervical ripening," *European Journal of Obstetrics & Gynecology and Reproductive Biology*, vol. 72, no. 2, pp. 165–168, 1997.
- [51] G. Godeau, D. Rotten, C. Gavignet, M. C. Colin, and A. M. Robert, "Evolution of the elastic network at the cervix of the uterus during and after pregnancy," *Biology of the Cell*, vol. 60, no. 1, 1987.
- [52] K. Myers and G. A. Ateshian, "Interstitial growth and remodeling of biological tissues: Tissue composition as state variables," *Journal of the Mechanical Behavior of Biomedical Materials*, vol. 29, pp. 544–556, 2014.

Research Article

Mapping Heterogeneous Elastic Property Distribution of Soft Tissues Using Harmonic Motion Data: A Theoretical Study

Yue Mei^{1,2} and Peng Yu ^{1,3}

¹College of Civil Engineering and Architecture, Key Laboratory of Disaster Prevention and Structural Safety of Ministry of Education, Guangxi Key Laboratory of Disaster Prevention and Structural Safety, Guangxi University, Nanning, 530004, China

²Zienkiewicz Centre for Computational Engineering, Swansea University, Swansea, SA1 8EN, UK

³Institute of Mechanics and Advanced Materials, School of Engineering, Cardiff University, Cardiff, CF24 3AA, UK

Correspondence should be addressed to Peng Yu; glpengyu@gmail.com

Received 29 August 2018; Revised 25 November 2018; Accepted 11 December 2018; Published 31 December 2018

Academic Editor: Guillermo Rus

Copyright © 2018 Yue Mei and Peng Yu. This is an open access article distributed under the Creative Commons Attribution License, which permits unrestricted use, distribution, and reproduction in any medium, provided the original work is properly cited.

Characterizing heterogeneous elastic property distribution of soft tissues is of great importance in disease detection. In this paper, we investigate an inverse approach to map the heterogeneous material property distribution of soft solids using harmonic motion data. To examine the feasibility of this approach, a number of numerical examples are presented. We observe that the shear modulus distribution is recovered well using harmonic motion measurements. Compared to the static inverse approach, the proposed dynamic inverse method improves the quality of the recovered shear modulus distribution significantly. We also study the influence of the uncertainty in the driving frequency on the reconstruction results and observe that the influence is not very significant in recovering the shape of the inclusion. The proposed inverse algorithm has potential to be a promising tool to diagnose diseases in clinical medicine.

1. Introduction

Mechanical signal or response has a long history of being used for health assessment and disease detection. For instance, more than 2000 years ago, Chinese developed a pulse diagnosis where physicians assessed patients' health conditions based on their wrist-pulse [1, 2] since alteration of the frequency, amplitude, etc. of the wrist-pulse was highly correlated to the pathologic changes. With the fast development of mechanical techniques, a large number of mechanical based medical devices including ultrasonography have been invented and widely used in healthcare institutions. In particular, the development of imaging modalities [3, 4] provides us with the availability to measure the deformation and motion of tissues and organs inside our body. With the full-field measured data of the region of interest, we are capable of mapping the heterogeneous mechanical property distribution of soft tissues. Since many diseases such as cancerous diseases [5, 6] and cardiovascular diseases [7, 8] induce the alteration of mechanical properties of associated

tissues, mapping heterogeneous mechanical behavior might be useful for the disease detection.

With the accurate imaging data, identifying nonhomogeneous material property distribution requires solving an inverse problem. Due to its ill-posed nature, it is very difficult to solve the inverse problem. There are many methods to solve the inverse problem such as direct approaches [9–12] and statistical approaches [13]. A prevalent approach is to regularize the problem and pose the inverse problem to be a constrained minimization problem [11, 14–16]. To improve the computational efficiency of solving the inverse problem using an iterative inverse algorithm, the adjoint method has been proposed. This approach has been widely applied to map both linear [17, 18] and nonlinear [19, 20] elastic property distributions of soft tissues utilizing measured displacement fields in the quasi-static case.

In this paper, we will generalize the regularized inverse approach into dynamic cases. We assume the tissue or biological organ is subjected to harmonic motion, solve the inverse problem in the frequency domain, and map the linear elastic

property distribution using harmonic motion data. This paper is organized as follows: In **Methods**, we will discuss the mathematical details of the proposed approach and a number of numerical examples will be presented in **Results**. We will discuss the proposed method and associated results in Discussion and paper closure will be in **Conclusions**.

2. Methods

The wave equation for harmonic motion in the frequency domain is written as

$$\begin{aligned} \nabla \sigma + \rho \omega^2 \mathbf{u} &= 0 \quad \text{on } \Omega \\ \mathbf{u} &= \mathbf{u}_0 \quad \text{on } \Gamma_u \\ \sigma \cdot \mathbf{n} &= \mathbf{t}_0 \quad \text{on } \Gamma_t, \end{aligned} \quad (1)$$

where \mathbf{u} and σ denote the displacement vector and stress tensor, respectively. ρ and ω represent the mass density and angular frequency, respectively. In addition, the vectors \mathbf{u}_0 and \mathbf{t}_0 are the boundary conditions at $\Gamma_u \cup \Gamma_t$. In this paper, the solid is assumed to be an incompressible, linear elastic and in the state of plane stress; thus the stress-strain relation is

$$\sigma_{ij} = 2\mu \varepsilon_{ij} + 2\mu \varepsilon_{kk} \delta_{ij}, \quad (2)$$

where μ is shear modulus and ε_{ij} is the strain. For a known shear modulus distribution, the displacement field can be acquired by solving a forward problem using the finite element method (FEM), leading to the following discretized equations:

$$\mathbf{K}(\mu) \mathbf{u} + \mathbf{M} \mathbf{u} = \mathbf{f}, \quad (3)$$

where \mathbf{K} and \mathbf{M} are the stiffness matrix and mass matrix, respectively. Meanwhile, \mathbf{u} and \mathbf{f} are the displacement and force vectors, respectively. Since FEM has been widely used for solving equations of motion, for brevity, we do not intend to discuss here.

The inverse problem is solved by an optimization approach where an objective function π is minimized in the L2 norm:

$$\pi = \frac{1}{2} \|\mathbf{W}(\mathbf{u}(\mu) - \mathbf{u}^{meas})\|_0^2 + \frac{1}{2} \alpha \text{Reg}(\mu), \quad (4)$$

where \mathbf{u}^{meas} and $\mathbf{u}(\mu)$ are the nodal measured and computed displacements, respectively. The computed displacement field is obtained by solving the forward problem at the current estimated shear modulus distribution. The shape function \mathbf{W} represents the approximation from the continuous displacement field to the associated discretized field. The second term in (4) is the regularization term. In this paper, we employ the total variation diminishing (TVD) regularization term ($\text{Reg}(\mu) = \int_{\Omega} \sqrt{(\nabla \mu)^2 + c^2} d\Omega$, where c is a small constant and is set to 10^{-2} in order to avoid the singularity when computing the derivative of the regularization term with respect to shear moduli). α is the regularization factor to control the contribution of the regularization term to the

objective function. A smaller α leads to strong distortion of reconstruction, while a larger value will oversmooth the final results. In this paper, the optimal regularization factor is visually determined. To be specific, we start with a very large regularization, keep solving the inverse problem with a decreasing regularization factor, and then observe the shear modulus reconstructions. This optimal regularization factor will be determined when the reconstruction of the background starts oscillation. The same strategy has also been utilized in [17–21].

The inverse problem is solved by a quasi-Newton approach, the L-BFGS (limited-Broyden–Fletcher–Goldfarb–Shanno) method, which requires the objective function value and its spatial gradient with respect to shear moduli. The gradient of the objective function can be calculated as follows:

$$\frac{\partial \pi}{\partial \mu_j} = \left\langle \mathbf{W}(\mathbf{u} - \mathbf{u}^{meas}), \mathbf{W} \frac{\partial \mathbf{u}}{\partial \mu_j} \right\rangle + \frac{1}{2} \alpha \frac{\partial \text{Reg}(\mu_j)}{\partial \mu_j}, \quad (5)$$

where j represents the global node number. $\langle \cdot, \cdot \rangle$ denotes the inner product. Differentiating (3) with respect to the nodal shear modulus μ_j yields

$$\frac{\partial \mathbf{u}}{\partial \mu_j} = -(\mathbf{K} + \mathbf{M})^{-1} \frac{\partial \mathbf{K}}{\partial \mu_j} \mathbf{u}. \quad (6)$$

Substituting (6) into (5) leads to

$$\begin{aligned} \frac{\partial \pi}{\partial \mu_j} &= \left\langle \mathbf{W}(\mathbf{u} - \mathbf{u}^{meas}), -\mathbf{W}(\mathbf{K} + \mathbf{M})^{-1} \frac{\partial \mathbf{K}}{\partial \mu_j} \mathbf{u} \right\rangle \\ &+ \frac{1}{2} \alpha \frac{\partial \text{Reg}(\mu_j)}{\partial \mu_j}. \end{aligned} \quad (7)$$

This straightforward approach to evaluate the gradient is computationally intensive; thus the adjoint method is adopted to calculate the gradient in a highly efficient way [21]. More specifically, if we rewrite (7) by taking advantage of the definition of a transpose, the following equation can be obtained:

$$\begin{aligned} \frac{\partial \pi}{\partial \mu_j} &= \left\langle -(\mathbf{K} + \mathbf{M})^{-T} \mathbf{W}^T \mathbf{W}(\mathbf{u} - \mathbf{u}^{meas}), \frac{\partial \mathbf{K}}{\partial \mu_j} \mathbf{u} \right\rangle \\ &+ \frac{1}{2} \alpha \frac{\partial \text{Reg}(\mu_j)}{\partial \mu_j}. \end{aligned} \quad (8)$$

Accordingly, the adjoint equation can be acquired:

$$-(\mathbf{K} + \mathbf{M})^T \mathbf{D} = \mathbf{W}^T \mathbf{W}(\mathbf{u} - \mathbf{u}^{meas}). \quad (9)$$

If we solve the adjoint equation for the vector \mathbf{D} , the gradient can be expressed as

$$\frac{\partial \pi}{\partial \mu_j} = \left\langle \mathbf{D}, \frac{\partial \mathbf{K}}{\partial \mu_j} \mathbf{u} \right\rangle + \frac{1}{2} \alpha \frac{\partial \text{Reg}(\mu_j)}{\partial \mu_j}. \quad (10)$$

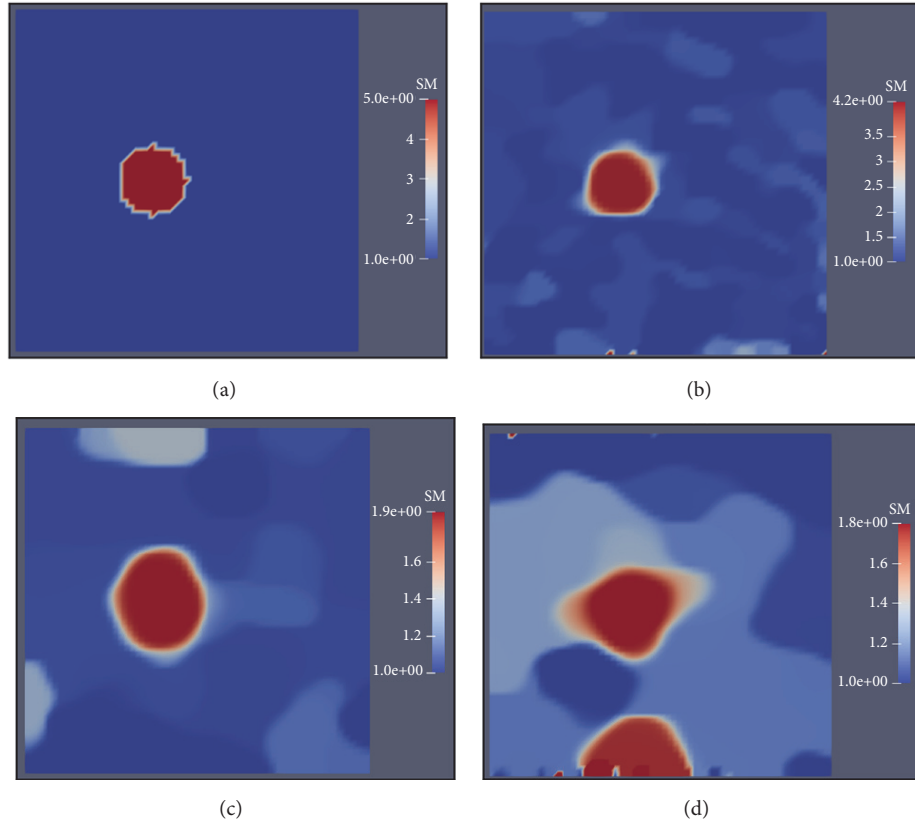


FIGURE 1: (a) The target shear modulus distribution; ((b)–(d)) the reconstructed shear modulus distributions in the presence of 3%, 5%, and 10% noise, respectively. In this case, the driving frequency is 0Hz (the static case).

Thus, we merely need to solve two forward problems at every minimization iteration using the adjoint method. The inverse solver will terminate when one of the two following stop criteria is satisfied: (1) the difference between the objective function values at the current and last minimization iterations is smaller than the machine precision; (2) the norm of the gradient of the objective function with respect to shear moduli is smaller than the machine precision.

The in-house inverse algorithm is implemented by Fortran and parallelized by openMP. For the L-BFGS algorithm, we adopt an open source L-BFGS subroutine developed by [22, 23]. In this work, we will primarily test the inverse algorithms; thus measured data obtained by simulation will be employed in numerical examples, assuming the material property distribution is known. We then use the simulated data to solve the inverse problem and compare the reconstructed shear modulus distribution with the target values. To mimic real data, we add up to 10% white Gaussian noise into the simulated data, and the noise level is defined as

$$\text{noise} = \frac{\sqrt{\sum_{i=1}^n (u_i^{\text{meas}} - u_i^{\text{exact}})^2}}{\sqrt{\sum_{i=1}^n (u_i^{\text{exact}})^2}} \times 100\%, \quad (11)$$

where n is the total number of displacement data. u_i^{meas} and u_i^{exact} are the measured displacement and noise-free displacement, respectively.

3. Results

In this section, we will present numerical examples where the geometric model is shown in Figure 1(a). More specifically, a circular inclusion with a shear modulus value of 500Pa is embedded in the $1 \times 1 \text{cm}^2$ square background with a shear modulus value of 100Pa. The radius of the inclusion is 0.1cm. The square model is discretized by 3600 bilinear elements. In respect of the boundary conditions, we fully fix the bottom edge and apply 1% shear deformation on the top edge. When solving the inverse problem, the initial guess of shear modulus distribution is homogeneous throughout the problem domain and the initial shear modulus value is 10Pa. In addition, we restrict the search domain of the shear modulus of every node to interval $[10, 3000] \text{Pa}$.

As seen in Figure 1, when the noise level is low (3%), the shear modulus distribution is recovered with very good quality, since both the value and shape of the shear modulus of the inclusion are close to the target. With the increase of noise level, the reconstruction becomes worse (see Figures 1(b)–1(d)). In particular, when the noise level reaches 10%, the mapped inclusion is distorted and a strong artifact is observed on the background in Figure 1(d). We also investigate the sensitivity of the regularization factors to the reconstructed shear modulus distribution (see Figure 2). We observe that, for a very small regularization factor ($\alpha = 10^{-10}$ in Figure 2(b)), the reconstructed shear modulus distribution oscillates

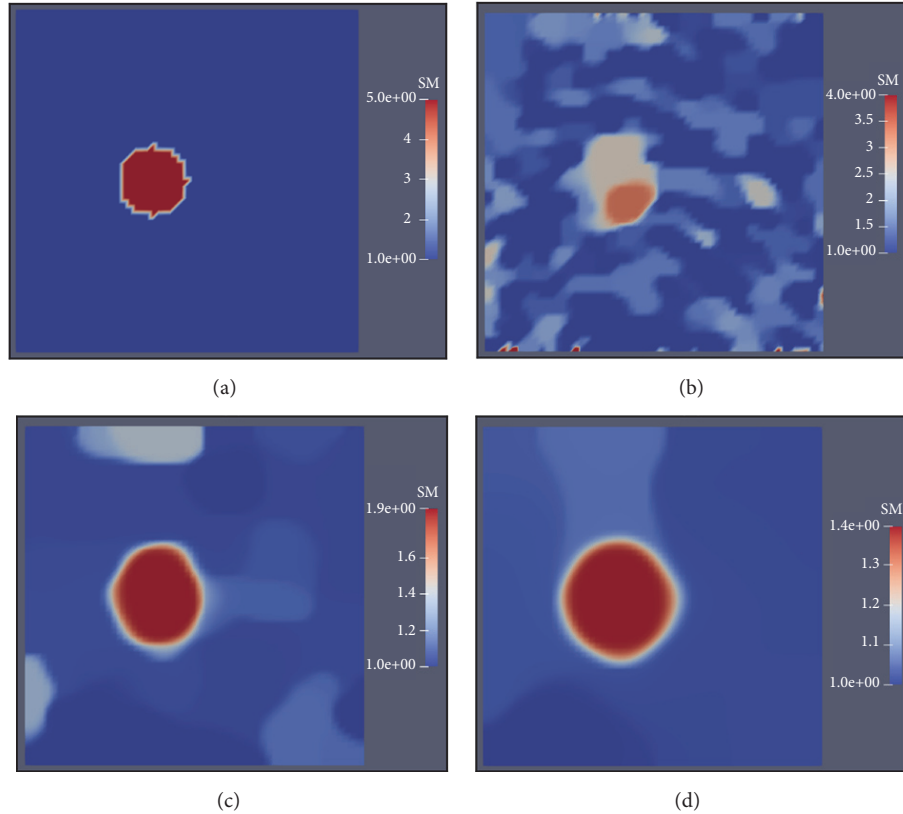


FIGURE 2: (a) The target shear modulus distribution; ((b)–(d)) the reconstructed shear modulus distributions in the presence of 5% noise with regularization factors of 10^{-10} , 10^{-9} , and 5×10^{-9} , respectively. In this case, the driving frequency is 0Hz (the static case).

significantly. For a very large regularization factor ($\alpha = 5 \times 10^{-9}$ in Figure 2(d)), the shear modulus distribution of the background is very smooth. Meanwhile, the inclusion can be recovered successfully but becomes much larger than the target. Thus, the optimal regularization factor should be selected between them as shown in Figure 2(c).

For a relative low driving frequency (Figure 3), we find that the inclusion is also recovered well in the case of low noise level (3% noise). However, compared to the static case (see Figure 1(b)), both the shape and value of the inclusion are slightly worse mapped. Besides, though increasing noise level will deteriorate the mapped shear modulus distribution, the quality of reconstructed results in this dynamic case is slightly better than the static case (compare Figures 1(c) and 1(d) and Figures 3(c) and 3(d)). For higher driving frequencies of 20Hz and 40Hz (Figures 4 and 5), we observe that the inclusion is well recovered for noise levels up to 5%. Even with 10% noise level, the inclusion is recovered well without too many artifacts. Comparing the reconstructed results for varying driving frequencies, we also observe that the driving frequency of 40Hz yields the best reconstruction results.

We also study the effect of the uncertainty in the driving frequency on the reconstructed results. In Figures 6 and 7, we also add noise to the driving frequency in solving the inverse problem. We discover that the decrease of driving frequency reduces the value of the mapped inclusion (see Figure 6) but also reduces the artifact of the background

simultaneously. The shape of the mapped inclusion seems to remain the same level for different driving frequencies. When we raise the driving frequency (Figure 7), it is clear that the value of the shear modulus of the mapped inclusion rises but the background experiences a stronger oscillation than that using the exact driving frequency.

4. Discussion

This paper presents the regularized inverse approach to map the heterogeneous elastic property distribution of the soft solids using harmonic motion data. It took 5000-10000 iterations for convergence to solve the inverse problem in this paper. We compared the reconstructed results when the driving frequencies are 0Hz (static case), 2Hz, 20Hz, and 40Hz, respectively. We also varied the initial guess of the shear modulus from 10Pa to 1000Pa and acquired very similar reconstructed shear modulus distribution. We notice that using static data is capable of mapping the elastic property distribution well with a low noise level. However, for higher noise level, the dynamic data yields better reconstruction results. Thereby, this is one of the advantages of utilizing dynamic measurement. Another merit of using harmonic motion data is that we can quantitatively determine the shear modulus distribution merely using displacement measurements. This is impossible for the static case owing to the homogeneity of the equilibrium equations. Thereby,

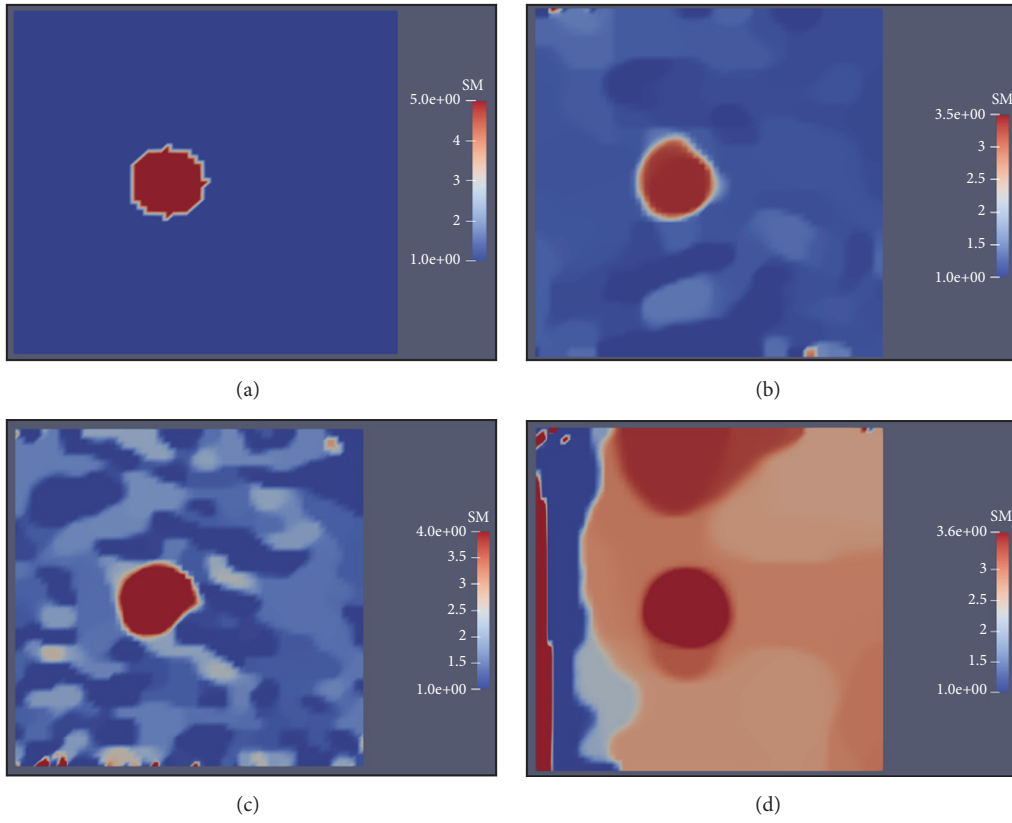


FIGURE 3: (a) The target shear modulus distribution; ((b)–(d)) the reconstructed shear modulus distributions in the presence of 3%, 5%, and 10% noise, respectively. In this case, the driving frequency is 2Hz.

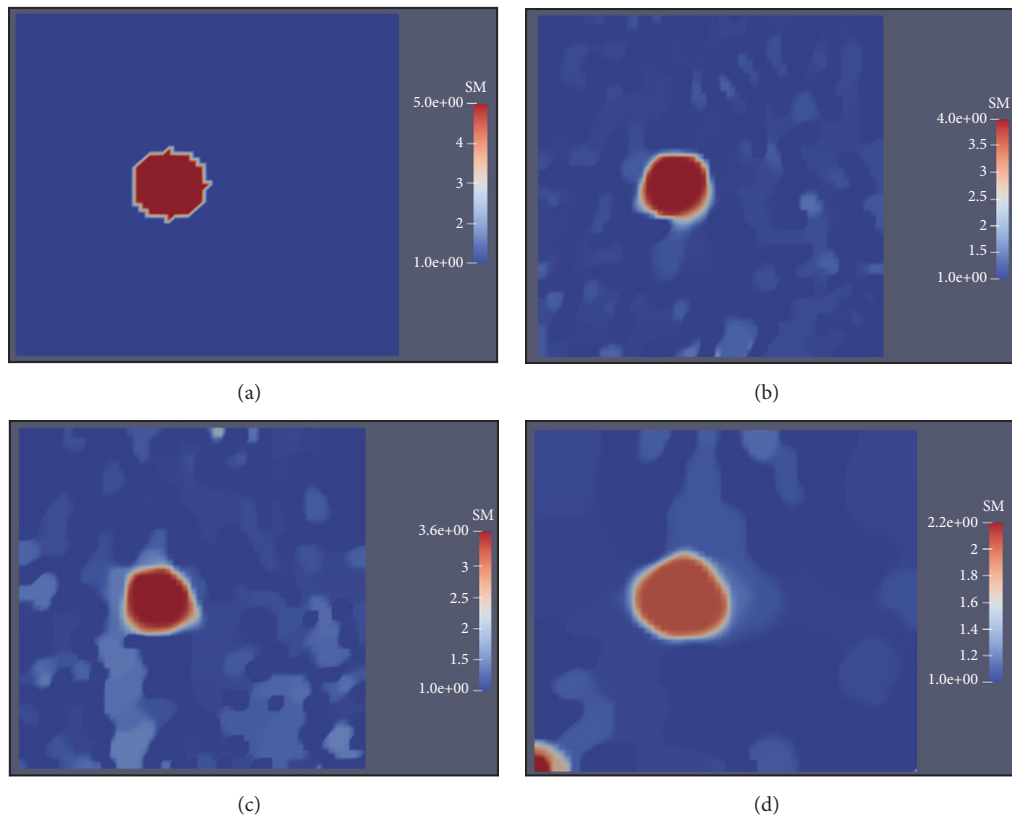


FIGURE 4: (a) The target shear modulus distribution; ((b)–(d)) the reconstructed shear modulus distributions in the presence of 3%, 5%, and 10% noise, respectively. In this case, the driving frequency is 20Hz.

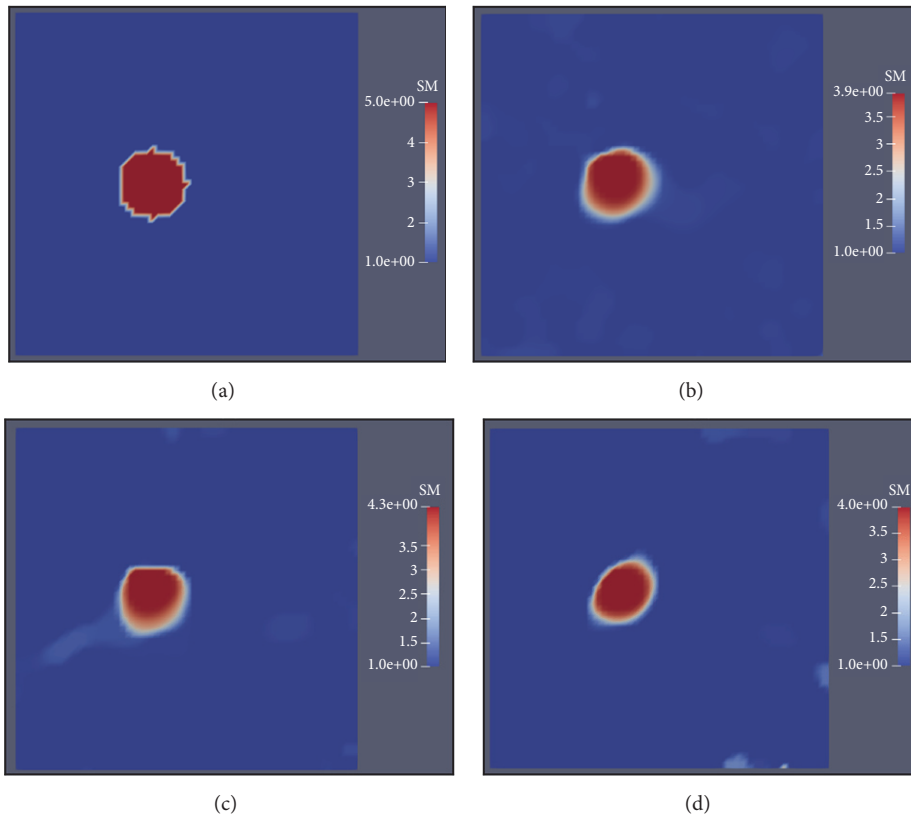


FIGURE 5: (a) The target shear modulus distribution; ((b)–(d)) the reconstructed shear modulus distributions when the driving frequency increases by 3%, 5%, and 10%, respectively. In this case, the exact driving frequency is 40Hz.

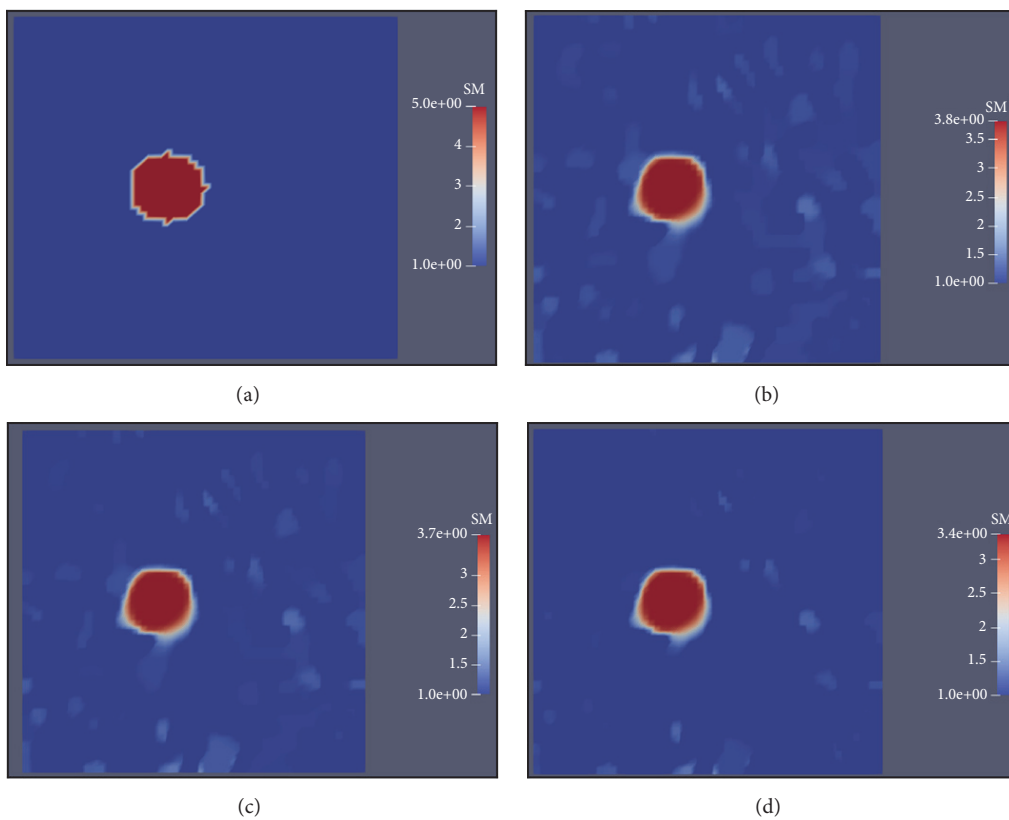


FIGURE 6: (a) The target shear modulus distribution; ((b)–(d)) the reconstructed shear modulus distributions when the driving frequency decreases by 3%, 5%, and 10% in the inverse problem, respectively. In this case, the exact driving frequency is 20Hz and noise level is 3%.

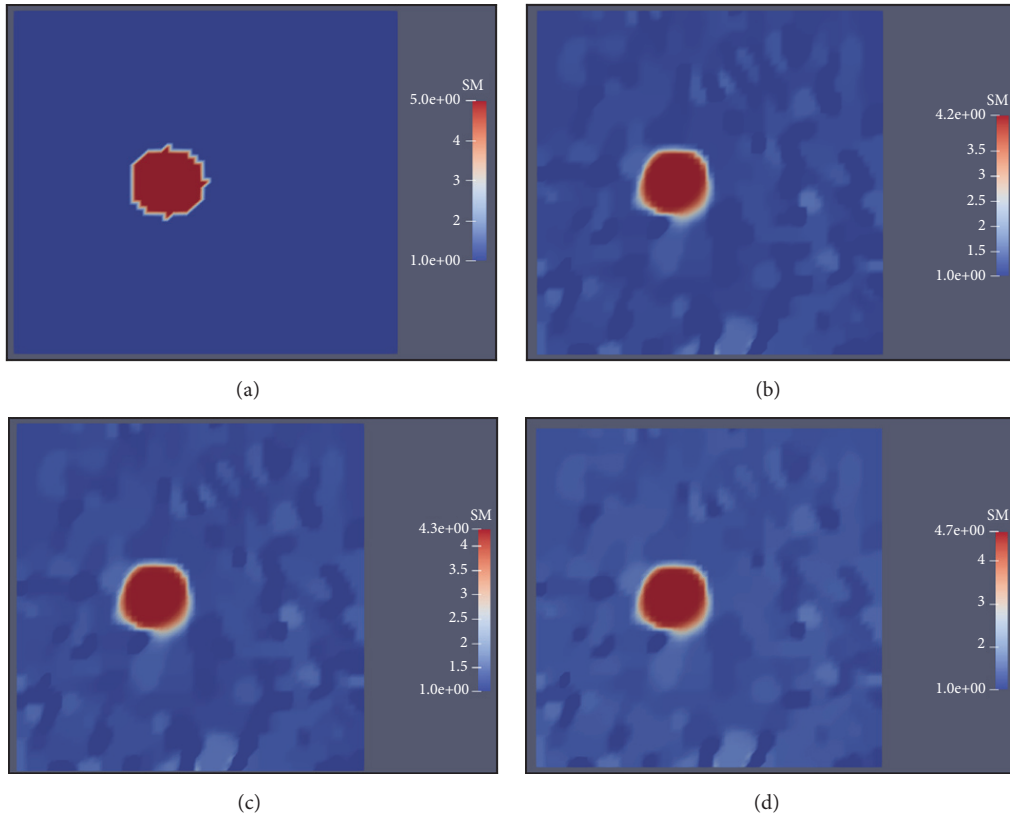


FIGURE 7: (a) The target shear modulus distribution; ((b)–(d)) the reconstructed shear modulus distributions when the driving frequency increases by 3%, 5%, and 10% in the inverse problem, respectively. In this case, the exact driving frequency is 20Hz and noise level is 3%.

we must know nonzero force or traction information, or shear modulus values in a certain subregion for the static case. Otherwise, the shear modulus distribution can only be determined relatively up to a multiplicative factor. This has been well studied in [18]. We also learn that the uncertainty in the driving frequency might not necessarily reduce the quality of reconstructed results. However, the reason behind this remains an open question. Though we merely test the plane stress case in this paper, the proposed approach can be easily generalized to 2D plane strain and 3D cases. Besides, the experimental data should be utilized to test the feasibility of the proposed method. In this paper, we reveal that using harmonic data is capable of yielding higher quality of reconstruction even with very high noise level. Further, the error in driving frequency does not decrease the reconstruction quality significantly. Therefore, this analysis is of great significance in applying the approach to the practical cases.

5. Conclusions

In this paper, we study the feasibility of characterizing the nonhomogeneous elastic modulus distribution utilizing full-field harmonic motion data. We test several numerical cases and observe that this approach is capable of mapping the elastic property distribution well even with high noise levels. We also investigate how the uncertainty in the driving frequency affects the reconstruction of the shear modulus distribution.

We realize that the uncertainty in the driving frequency might not reduce the quality of reconstruction results.

Data Availability

The data used to support the findings of this study are available from the corresponding author upon request.

Conflicts of Interest

The authors declare that there are no conflicts of interest regarding the publication of this paper.

Acknowledgments

Peng Yu thanks the support from China Scholarship Council (201406150089).

References

- [1] S. Li, *Pulse diagnosis*, Paradigm Publications, 1985.
- [2] Bob. Flaws, *The secret of Chinese pulse diagnosis*, Blue Poppy Enterprises, Inc., 1995.
- [3] L. Dong, P. Wijesinghe, J. T. Dantuono et al., “Quantitative compression optical coherence elastography as an inverse elasticity problem,” *IEEE Journal of Selected Topics in Quantum Electronics*, vol. 22, no. 3, pp. 277–287, 2016.

- [4] Z. Liu, C. Huang, and J. Luo, "A systematic investigation of lateral estimation using various interpolation approaches in conventional ultrasound imaging," *IEEE Transactions on Ultrasonics, Ferroelectrics, and Frequency Control*, vol. 64, no. 8, pp. 1149–1160, 2017.
- [5] P. Wellman, R. D. Howe, E. Dalton, and K. A. Kern, "Breast tissue stiffness in compression is correlated to histological diagnosis," Technical Report, 1-15, Harvard BioRobotics Laboratory, 1999.
- [6] T. Liu, O. A. Babaniyi, T. J. Hall, P. E. Barbone, and A. A. Oberai, "Noninvasive in-vivo quantification of mechanical heterogeneity of invasive breast carcinomas," *PLoS One*, vol. 10, no. 7, 2015.
- [7] M. S. Richards and M. M. Doyley, "Investigating the impact of spatial priors on the performance of model-based IVUS elastography," *Physics in Medicine and Biology*, vol. 56, no. 22, pp. 7223–7246, 2011.
- [8] M. S. Richards, R. Perucchio, and M. M. Doyley, "Visualizing the Stress Distribution With in Vascular Tissues Using Intravascular Ultrasound Elastography: A Preliminary Investigation," *Ultrasound in Medicine & Biology*, vol. 41, no. 6, pp. 1616–1631, 2015.
- [9] R. Sinkus, J. Lorenzen, D. Schrader, M. Lorenzen, M. Dargatz, and D. Holz, "High-resolution tensor MR elastography for breast tumour detection," *Physics in Medicine and Biology*, vol. 45, no. 6, pp. 1649–1664, 2000.
- [10] I. Sack, B. Beierbach, U. Hamhaber, D. Klatt, and J. Braun, "Non-invasive measurement of brain viscoelasticity using magnetic resonance elastography," *NMR in Biomedicine: An International Journal Devoted to the Development and Application of Magnetic Resonance In vivo*, vol. 21, no. 3, pp. 265–271, 2008.
- [11] M. M. Doyley, "Model-based elastography: a survey of approaches to the inverse elasticity problem," *Physics in Medicine and Biology*, vol. 57, no. 3, pp. R35–R73, 2012.
- [12] E. E. W. Van Houten, M. M. Doyley, F. E. Kennedy, J. B. Weaver, and K. D. Paulsen, "Initial in vivo experience with steady-state subzone-based MR elastography of the human breast," *Journal of Magnetic Resonance Imaging*, vol. 17, no. 1, pp. 72–85, 2003.
- [13] E. E. W. Van Houten, K. D. Paulsen, M. I. Miga, F. E. Kennedy, and J. B. Weaver, "An overlapping subzone technique for MR-based elastic property reconstruction," *Magnetic Resonance in Medicine: An Official Journal of the International Society for Magnetic Resonance in Medicine*, vol. 42, no. 4, pp. 779–786, 1999.
- [14] E. E. W. Van Houten, M. M. Doyley, F. E. Kennedy, K. D. Paulsen, and J. B. Weaver, "A three-parameter mechanical property reconstruction method for MR-based elastic property imaging," *IEEE Transactions on Medical Imaging*, vol. 24, no. 3, pp. 311–324, 2005.
- [15] H. Eskandari, S. E. Salcudean, R. Rohling, and J. Ohayon, "Viscoelastic characterization of soft tissue from dynamic finite element models," *Physics in Medicine and Biology*, vol. 53, no. 22, pp. 6569–6590, 2008.
- [16] H. Eskandari, S. E. Salcudean, R. Rohling, and I. Bell, "Real-time solution of the finite element inverse problem of viscoelasticity," *Inverse Problems*, vol. 27, no. 8, Article ID 085002, 2011.
- [17] Y. Mei, S. Kuznetsov, and S. Goenezen, "Reduced Boundary Sensitivity and Improved Contrast of the Regularized Inverse Problem Solution in Elasticity," *Journal of Applied Mechanics*, vol. 83, no. 3, Article ID 031001, 2016.
- [18] Y. Mei, M. Tajderi, and S. Goenezen, "Regularizing Biomechanical Maps for Partially Known Material Properties," *International Journal of Applied Mechanics*, vol. 9, no. 2, Article ID 1750020, 2017.
- [19] S. Lalitha Sridhar, Y. Mei, and S. Goenezen, "Improving the sensitivity to map nonlinear parameters for hyperelastic problems," *Computer Methods in Applied Mechanics and Engineering*, vol. 331, pp. 474–491, 2018.
- [20] S. Goenezen, P. Barbone, and A. A. Oberai, "Solution of the nonlinear elasticity imaging inverse problem: The incompressible case," *Computer Methods Applied Mechanics and Engineering*, vol. 200, no. 13-16, pp. 1406–1420, 2011.
- [21] A. A. Oberai, N. H. Gokhale, M. M. Doyley, and J. C. Bamber, "Evaluation of the adjoint equation based algorithm for elasticity imaging," *Physics in Medicine and Biology*, vol. 49, no. 13, pp. 2955–2974, 2004.
- [22] C. Zhu, R. H. Boyd, P. Lu, and J. Nocedal, *L-BFGS-B: FORTRAN Subroutines for Large-Scale Bound-Constrained Optimization*, Northwestern University Department of Electrical Engineering, 1994.
- [23] C. Zhu, R. H. Byrd, P. Lu, and J. Nocedal, "L-BFGS-B: a limited memory FORTRAN code for solving bound constrained optimization problems," Technical Report No. NAM-11, EECS Department, Northwestern University, Evanston, 1994.

Research Article

Effect of Contact Conditions of Torsional Wave Elastographic Probe on Human Cervix

G. Rus , M. Riveiro, and F. S. Molina

Ultrasonics Group TEP-959, Biomechanics Group TEC-12 of the Biosanitary Research Institute IBS, MNat Excellence Scientific Unit UCE.PP2017.03, NDE Lab, Department of Structural Mechanics, University of Granada, Spain

Correspondence should be addressed to G. Rus; grus@ugr.es

Received 14 September 2018; Revised 1 November 2018; Accepted 18 November 2018; Published 29 November 2018

Academic Editor: Alessandro Lo Schiavo

Copyright © 2018 G. Rus et al. This is an open access article distributed under the Creative Commons Attribution License, which permits unrestricted use, distribution, and reproduction in any medium, provided the original work is properly cited.

There is a challenge in characterizing the soft tissue mechanical functionality in cylindrical geometries by current elastography techniques applied to small organs. Torsional waves are a type of shear elastic waves that propagate through soft tissue radially and in depth in a curled geometry, ideally suited to explore structures such as the cervix. Here, a sensor based on a novel arrangement of concentric sandwiches of piezo- and electromechanical elements is prototyped and tested to quantitatively assess stiffness in human cervix. The purpose is to determine the robustness of a torsional wave elastography (TWE) sensor prototype to quantify cervical stiffness, as a first step to validate a reliable measurement protocol using TWE. An array of tests designed to validate a set of hypothesis about the contact conditions were performed on up to 3 different nonpregnant voluntary women. The mechanical properties were reconstructed from the recorded TWE signals, and the outcomes were statistically analyzed to validate the contact condition hypothesis. The results suggest that, although future tests need to be performed to fully assess the repeatability and quality of the measurements, some characteristics of the measurement protocol become clear; in particular: (1) the use of speculum is recommended since it not only stabilizes the measurements, but also corrects and stabilizes the orientation of the cervical neck, and allows to visually verify the positioning and alignment of the probe, while not significantly increasing discomfort to women during this test; (2) the use of lubricant gel has no significant effect on the measurement quality; (3) 1cm off-centering from external cervical os is not acceptable; (4) a range of applied force between 500-2000 N does not significantly vary measurement signal quality, but the reconstructed value of the shear modulus does vary, probably due to its constitutive nonlinearity; (5) breathing movements affects measurements, but short duration of TWE pulse (0.3 s) allows to take measurements in apnea.

1. Introduction

The structural microarchitecture of soft tissue is recently catching attention among the biomechanics community, and it is gaining interest for clinical diagnosis in a broad spectrum of medical specialties, since quantitative measurement of cervical elasticity by shear waves in vivo constitutes a new diagnostic principle that only recently is being proposed [1–5]. This concept is first being applied to early diagnosing birth and labor disorders, such as premature ripening of the cervix, delivery induction failures, etc.

In the last years, elastography has been proposed by many authors to evaluate cervical stiffness/softness [1–3, 6, 7], as there is no clinical tool for the quantitative and objective assessment of the cervical biomechanical state during pregnancy [4]. The World Health Organization (WHO) estimates

that in 2017 approximately 15 million babies will be born preterm (< 37 weeks of gestation), this is, a rate above 1 in 10 newborns [8]. Worldwide, complications of preterm birth have supplanted pneumonia as the primary cause of child mortality for children under five years of age [8, 9]. The problem is not isolated to the developing countries, as preterm birth rates are rising in most countries in Europe [10]. While some progress is being made in identifying cultural and/or socioeconomic risk factors of preterm birth, there is a considerable proportion of unpredictable spontaneous preterm delivery, and the biology of cervical ripening that leads to birth remains poorly understood.

To objectively quantify cervical stiffness, a TWE sensor prototype was designed, prototyped and was the object of the present test for measurement robustness. Unlike commercial elastography, torsional wave is shear elastic waves

that propagate through soft tissue radially and in depth in a curled geometry, perfectly suited to the small size and specific cylindrical shape of the cervix, which challenge ARFI-based elastography [11]. The TWE sensor is based on a novel arrangement of concentric sandwiches of piezo- and electromechanical elements, which enables the precise interrogation of soft tissue mechanical functionality in cylindrical geometries.

The purpose of this work is to evaluate the robustness of the mechanical characterization of the cervix through the TWE probe, specifically against some relevant contact conditions. By robustness we define the maintenance of measurement signals quality and consistency against variations in a set of examination procedures and errors during the application of the clinical probe operation. The specific objectives are

- (O1) To verify the positioning, orientation and alignment of the probe respect to the cervix.
- (O2) To determine the need of speculum.
- (O3) To determine the need of lubricant gel.
- (O4) To validate the robustness against probe cervical os off-centering.
- (O5) To analyze the effect of probe applied force on the cervix within a soft force range.

To this end, an array of tests designed to validate a set of hypothesis about the contact conditions were performed on up to 3 different nonpregnant voluntary women. The mechanical properties were reconstructed from the recorded TWE signals, and the outcomes were statistically analyzed to validate the contact condition hypothesis.

2. Methods

The endovaginal examination with the TWE probe was simultaneously guided by an abdominal sagittal ecography to assess cervical alignment to endocervical canal (to analyze objective O1), and to confirm the probe position on the cervix using or not speculum (to analyze objective O2). The probe was positioned in contact with the cervical lips, centered at the os. The torsional waves propagate in depth and radially interrogating the compound dermal, internal stromatic connective tissue, therefore not excluding mucus, epithelium, and crypts, which are a priori expected to be a potential explanation for measurement complications to be tested. An examination series was performed with and without lubricant gel on the probe (to analyze objective O3). Measurements in external cervical os against other regions of the cervix (anterior, posterior and lateral lips) were obtained (to analyze objective O4). The operators applied first a normal force and second a soft force on the cervix, in a range of 500-2000 N (equivalent to 50-200 g). A training for the operator was required to apply a uniform force, within an error of subjective perception around $\pm 20\%$ which was estimated through testing probe force in a balance (to analyze objective O5). The variation between measurements taken at the start and the end of the examination protocol in each woman was calculated. The protocol sequence was repeated twice by each



FIGURE 1: In-lab designed and prototype torsional wave elastography probe.

operator. Breathing and postural movements of the subjects were recorded during measurement.

2.1. Torsional Wave Elastography. Elastography was performed using an in-lab designed and prototyped probe capable of generating, receiving and analysing torsional waves free of spurious compression waves, as well as sensing them at safe radiation energies. The proof of concept device (Figure 1) is composed of three parts; sensor, generation/receiver electronic system, and the interface software. The proposed sensor concept is based on (1) a transmitting disc with a sandwich design combining piezoceramic or electromechanical elements to control impedance and inertia, resonant frequency and energy transmission to reduce dilatational waves, and a Faraday shield to control electronic cross-talk. The receiving part consists of a (2) crown ring sandwich with a converse design to the transmitter, encapsulated in (3) a casing with geometrical and material selection to control the mechanical cross-talk. This configuration eliminates the masking p-waves that systematically arise at the boundaries of the regular contact or comb transducers. Further technical details are processing for reconstruction of mechanical parameters are covered by patents [12–14] and previous publications by the authors [15, 16]. From the reconstructed shear wave velocity c_s , it is possible to compute a shear elasticity under the assumption of a purely elastic and incompressible medium, for which the shear modulus μ can be written as

$$\mu = \rho c_s^2 \quad (1)$$

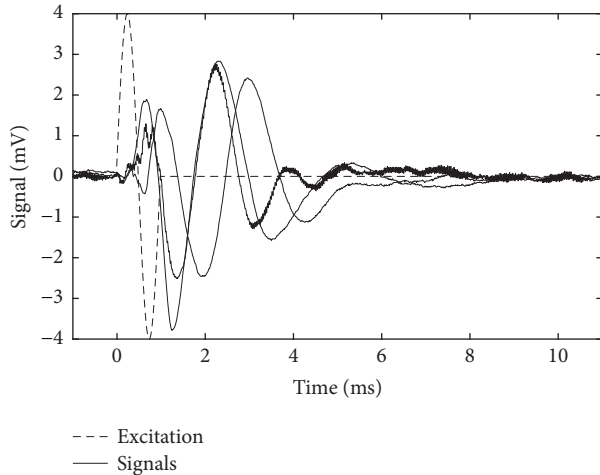


FIGURE 2: Illustrative example of three transmitted and received 1kHz signals.

where ρ is the density of the medium. In order to describe soft tissue elasticity, the usual parameter is Young's modulus, $E = \mu(3\lambda + 2\mu)/(\lambda + \mu)$. In macroscopic and homogeneous media λ is $10^4 \sim 10^6$ times larger than μ , thus a good and an usual approximation of E is: $E = 3\mu$. Thus, Young's modulus can then deduced from the shear wave velocity as

$$E = 3\rho c_s^2 \quad (2)$$

The propagated torsional wave is a burst configured as a 1-cycle sinusoid of frequency f between 0.5 and 1.5 kHz with $10\times$ averaging. An example of the transmitted and received signal is shown in Figure 2.

2.2. Settings and Ethical Issues. The study was conducted in the Fetal Medicine Unit at the University Hospital Complex of Granada, Spain, in March 2017. The prototype of the probe and the analysis of the data were performed at the Non-Destructive Laboratory (University of Granada). The study was designed according to the Declaration of Helsinki, with the approval of the 'Comité de Ética de la Investigación Biomédica de Granada, the Comité de Ética de la Universidad de Granada,' and the 'Comisión de Ética e Investigación Sanitaria del Hospital Universitario San Cecilio de Granada.'

2.3. Population. Eligible participants were non-pregnant, >18 years old women. Exclusion criteria were cervical surgery (e.g., conization), premalignant or malignant cervical changes, and menopause. All the eligible women agreed to participate and gave written informed consent. Datasets were anonymized.

2.4. Outcome Measures. The outcomes to compare the set of measurements in the protocol were cervical stiffness (G), estimated through the velocity of signal, and signal quality (Q).

2.5. Statistical Analysis. To compare the effects of using a speculum, a lubricant gel, a range of pressure, and the probe

off-centering from cervical os on the measurements, the ANOVA test was used. Stiffness was normalized to a reference subject (A) within women. The p-values for all hypothesis were 2-sided and a statistical significance was considered at $p < 0.05$. Data were analysed using the MATLAB [17], particularly packages `ttest2` and `anova1` [18].

3. Results

A total of 3 women aged 27-39 years were recruited for examination through TWE technique. They were one primiparous, one multiparous, and one nulliparous woman. Obstetrical formulae of term-birth/preterm-birth (< 37 weeks)/Abortus/Living children (TPAL) were T1P0A2L1, T2P0AIL2, and T0P0A0L0, respectively.

The measurements protocol through TWE probe could not be totally applied in some of the participants. A time interval of 30 minutes was considered to test variation between outcomes of measurements from the start to the end of the protocol application in one woman.

ANOVA analysis results for the tested hypothesis are shown in Table 1 and illustrated in Figure 3, including the specification of the hypothesis to be tested, the number N of patients, and the number of operators. p-value and t-stat are provided, as well as the summary of the reconstructed stiffness modulus G and the quality estimate Q .

The limitation of the small population (3 women) theoretically increases the risk of type-II error, but due to the multiplicity of measurements taken intraoperator and, as the p-values indicate, most of the hypotheses are tested with statistical significance, overcoming the limitation for the goals of this study. In the next studies, a larger population will be required for inter-operator repeatability and other tests.

4. Conclusions

The statistical analysis of the tested hypothesis about the contact conditions allow us to draw a number of conclusions, detailed below, which provide initial hints of the measurement protocol to be applied by the clinician to operate the present TWE probe. However, further hypothesis needs to be tested, which are the goal of a future work, to assess the feasibility of objectively quantifying cervical stiffness through a TWE sensor prototype with repeatability and reliability, upon a measurement protocol to be designed.

- (i) The use of speculum is recommended during TWE examination since it corrects and stabilizes the orientation of the cervical neck, and allows to visually verify the positioning and alignment of the probe, as supported with simultaneous abdominal echography. Although the use of speculum becomes a training requirement for the operator, the speculum does not significantly increase discomfort to women during this test.
- (ii) The use of lubricant gel has no significant effect on the measurement quality, and it is therefore proposed to be optional.

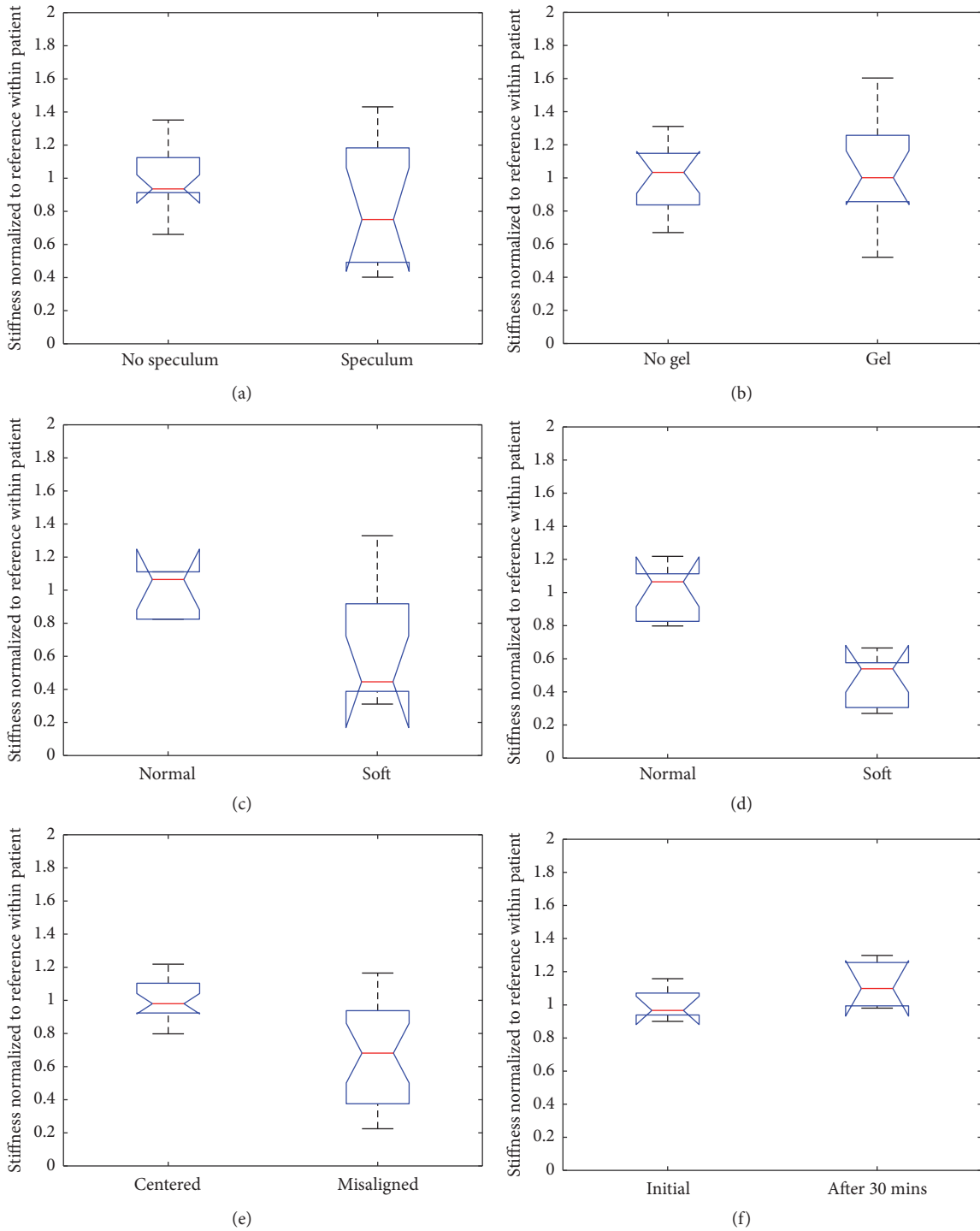


FIGURE 3: ANOVA box plots for testing each hypothesis indicated on the left vertical axis.

- (iii) A threshold of 1cm off-centering from external cervical os divides measurements into stable or unstable and therefore repeatable or non-repeatable. Therefore, such a misalignment is not acceptable.
- (iv) A range of applied force between 500-2000 N does not significantly vary measurement signal quality.

However, the reconstructed value of the shear modulus does vary, probably due to the constitutive nonlinearity of the tissue.

- (v) Breathing movements affects measurements, but short duration of TWE pulse (0.3 s) allows us to take measurements in apnea.

- (vi) Larger sample-size studies using a validated measurement protocol with a concordance test to assess inter-operator and intraoperator repeatability are needed in further research.

Data Availability

The data used to support the findings of this study have not been made available because it is part of the intellectual property of the company Innitius (www.innitius.com), partly covered by patent pending.

Conflicts of Interest

The authors are members of the company Innitius (<https://www.innitius.com>), which is in charge of the technical development of the probe used in the contribution.

Acknowledgments

The authors are grateful to Pilar Carretero, Andrea Pazos, and the volunteering patients for their collaborations. This research was supported by the Ministry of Education DPI2017-83859- R, DPI2014-51870- R, DPI2010-17065, and UNGR15-CE- 3664, Ministry of Health DTS15/00093 and PI16/00339, PI-0107- 2017, and PIN-0030- 2017, and Junta de Andaluca PI1-CTS- 8089 projects.

References

- [1] M. Swiatkowska-Freund and K. Preis, "Elastography of the uterine cervix: Implications for success of induction of labor," *Ultrasound in Obstetrics & Gynecology*, vol. 38, no. 1, pp. 52–56, 2011.
- [2] S. Pereira, A. P. Frick, L. C. Poon, A. Zamprakou, and K. H. Nicolaides, "Successful induction of labor: Prediction by preinduction cervical length, angle of progression and cervical elastography," *Ultrasound in Obstetrics & Gynecology*, vol. 44, no. 4, pp. 468–475, 2014.
- [3] S. Wozniak, P. Czuczwar, P. Szkodziak, P. Milart, E. Wozniakowska, and T. Paszkowski, "Elastography in predicting preterm delivery in asymptomatic, low-risk women: A prospective observational study," *BMC Pregnancy and Childbirth*, vol. 14, no. 1, 2014.
- [4] H. Feltovich, T. J. Hall, and V. Berghella, "Beyond cervical length: Emerging technologies for assessing the pregnant cervix," *American Journal of Obstetrics & Gynecology*, vol. 207, no. 5, pp. 345–354, 2012.
- [5] L. C. Carlson, H. Feltovich, M. L. Palmeri, J. J. Dahl, A. Munoz del Rio, and T. J. Hall, "Estimation of shear wave speed in the human uterine cervix," *Ultrasound in Obstetrics & Gynecology*, vol. 43, no. 4, pp. 452–458, 2014.
- [6] M. R. Khalil, P. Thorsen, and N. Uldbjerg, "Cervical ultrasound elastography may hold potential to predict risk of preterm birth," *Danish Medical Journal*, vol. 60, no. 1, 2013.
- [7] K. Köbbing, A. Fruscalzo, K. Hammer et al., "Quantitative Elastography of the uterine cervix as a predictor of preterm delivery," *Journal of Perinatology*, vol. 34, no. 10, pp. 774–780, 2014.
- [8] WHO, "March of dimes, the partnership for maternal, newborn & child health, and save the children. 2012. born too soon," in *The Global Action Report on Preterm Birth*, C. P. Howson, M. V. Kinney, and J. E. Lawn, Eds., Geneva, 2012.
- [9] WHO. Fact sheet - preterm birth. *Magnetic Resonance in Medicine*, 2016.
- [10] J. Zeitlin et al., "Wideband mr elastography for viscoelasticity model identification," *International J. of Obstetrics and Gynecol.*, vol. 120, pp. 1356–1365, 2013.
- [11] L. Peralta, F. S. Molina, J. Melchor et al., "Transient Elastography to Assess the Cervical Ripening during Pregnancy: A Preliminary Study," *Ultraschall in der Medizin / European Journal of Ultrasound (UiM/EJU)*, vol. 38, no. 4, pp. 395–402, 2017.
- [12] G. Rus, "Procedimiento de obtención de datos sobre la elasticidad de materiales empleando ondas de torsión, 14," PCT/ES2017/070065, 2016.
- [13] G. Rus, "Dispositivo emisor de ondas ultrasónicas de torsión y transductor que lo comprende, 16," PCT/ES2016/070540, 2015.
- [14] G. Rus, "Transductor ultrasónico de torsión para diagnóstico tisular, 14," PCT/ES2012/070380, Article ID 070380, p. S2012, 2011.
- [15] J. Melchor and G. Rus, "Torsional ultrasonic transducer computational design optimization," *Ultrasonics*, vol. 54, no. 7, pp. 1950–1962, 2014.
- [16] A. Callejas, A. Gomez, J. Melchor et al., "Performance study of a torsional wave sensor and cervical tissue characterization," *Sensors*, vol. 17, no. 9, 2017.
- [17] The Mathworks, Inc., Natick, Massachusetts. MATLAB version 8.5.0.197613 (R2015a), 2015.
- [18] R. V. Hogg and J. Ledolter, *Engineering Statistics*, New York: MacMillan, 1987, Engineering Statistics.

Research Article

Nonlinear Classical Elasticity Model for Materials with Fluid and Matrix Phases

Rafael Muñoz ^{1,2} and Juan Melchor ^{2,3,4}

¹Department of Civil Engineering, University of Granada, Granada 18071, Spain

²NDE Lab., Department of Structural Mechanics, University of Granada, Granada 18071, Spain

³Biosanitary Research Institute, Granada 18071, Spain

⁴MNat Scientific Unit of Excellence, University of Granada, Granada, Spain

Correspondence should be addressed to Rafael Muñoz; rmb@ugr.es

Received 14 September 2018; Accepted 1 November 2018; Published 27 November 2018

Academic Editor: John D. Clayton

Copyright © 2018 Rafael Muñoz and Juan Melchor. This is an open access article distributed under the Creative Commons Attribution License, which permits unrestricted use, distribution, and reproduction in any medium, provided the original work is properly cited.

Materials with fluid and matrix phases present different acoustic responses in each phase. While longitudinal waves propagate in both phases, shear waves do it only through the solid matrix. Longitudinal waves are mainly described by volumetric propagation and shear waves by deviatoric processes. In the case of nonlinear propagation cross effects occur between both components. This paper presents a new classical nonlinear model proposing a constitutive equation that separates volumetric and deviatoric effects. Four nonlinear constants of third order are defined. The formulation is compared to constitutive equations with Landau constants for weakly elasticity and both types of nonlinear constants related. Some reinterpretation of the Landau's constants arises in terms of parallel or cross nonlinear effects between volumetric and deviatoric components.

1. Introduction

The study of the coefficients of acoustic nonlinearity has recently been recovered again [1–6]. The classical nonlinear behavior of a material can be characterized using different parameters: first-second nonlinear parameters, Landau and Murnaghan constants, and stiffness matrices of second and third order [7–9]. An example of this interest could be the advances in early damage detection [10–13] of materials with complex structures in Nondestructive Evaluation field, allowing new paradigms that explore the connection between the micromechanical scales.

On the mathematical description of nonlinear effects, it is important to separate the geometrical nonlinearity from the material-dependent constitutive nonlinearity. The nonlinear analysis is based on Taylor series expansions of the strain energy, where the Landau [14] and Murnaghan [15] coefficients surge and only account for the material-dependent constitutive nonlinearity. The dynamic problem and its wave equation deduction bring several calculations that introduce geometrical nonlinearities. The first one arises when the stress tensor is calculated from the strain energy

expansion, where several operations involving the deformation gradient tensor generate new nonlinear terms (see (13), terms that are independent of Landau constants). The second, the kinematic relations add the well-known cross derivative term of the displacements, which is independent on the material nonlinear behavior.

The understanding of the nonlinear constants meaning (Landau, Murnaghan, β , δ , or stiffness coefficients) turns tough, and their interpretation does not appear as straight forward as it could seem. Probably, the most intuitive interpretation comes from the first nonlinear parameter β and the Finite Amplitude technique [16], where the parameter is a measurement of the growth on the second harmonic amplitude with distance. However, this parameter must be further carefully interpreted, since different definitions of them can be found in literature while nomenclature is maintained the same [10, 17]. As some examples in this vain, first and second nonlinear parameters (β and δ), defined directly as wave equation coefficients [18], usually accounts for both geometrical and constitutive nonlinearity. There are simplifications on some developments that define only constitutive versions

of the coefficients β and δ , directly applying a Taylor series expansion on the stress as a function of strain that are used for unidimensional plane wave propagation cases and neglecting geometrical nonlinearity [19, 20]. Anyway, all these theoretical proposals have definitely contributed to understand the main nonlinear experimental phenomena. But new approaches can better interpret different situations and open new visions.

This paper proposes deepening on the study of classical nonlinear acoustics, proposing a new mathematical formulation with the aim of presenting a different classical nonlinear equation. It splits the general first-order nonlinearity (usually measured by β or by Landau's constants) into four specific nonlinear phenomena (measured with four new nonlinear constants), due to the interaction of the deviatoric and volumetric components of the deformation and stress tensors. This paradigm turns specially useful to explain shear wave nonlinear propagation in materials constituted by two phases, as solid fibers embedded in a quasi-fluid matrix. This is the case of soft tissues, where the propagation of shear waves in the liquid phase can be neglected against that occurring in the solid structure.

Nonlinear first- and second-order constants are usually referred to the nonlinear order of the terms in the wave equation, or in other cases at the constitutive equation, while other nonlinear constants are referred to the order of the Taylor series expansion of the Energy, like Landau constants as third order. As the new four nonlinear constants are compared to Landau constants in this paper, they will be referred as third-order nonlinear constants.

The concept would be scalable to the third and higher harmonics [21–23]. Non-classical nonlinear effects are not considered at the moment, in order to ease the analysis, and viscosity, just partially, but they could be considered in future works, since they could be noteworthy in some cases. The connection of these new four nonlinear constants with the Landau third-order elasticity constants is also explored.

2. Methods

The general method of this paper is the deduction of the nonlinear wave equation, where the new proposed constitutive equation is the starting point.

$$\sigma_{ij} = \sigma_{ij}(v, D_{ij}) \quad (1)$$

where v and D_{ij} are the volumetric and deviatoric parts of the deformation tensor ε_{ij} . This equation defines the new four β nonlinear constants. The constitutive equation is transformed into $\sigma_{ij} = \sigma_{ij}(\varepsilon_{ij})$ and compared with the similar expression given by Landau formulation for weakly elasticity to relate the four β constants to Landau nonlinear constants.

Finally, the nonlinear equation of motion as a function of the new parameters is deduced,

$$\rho \ddot{u}_i = \sigma_{ij,j} \quad (2)$$

2.1. Theoretical Preliminars. The dynamic elastic problem comprises the momentum balance equation, compatibility

TABLE 1: List of variables.

Quantity	Symbol	Units
Displacement	u_i	m
Stress	σ_{ij}	Pa
Strain	ε_{ij}	-
Space	x_i	m
Time	t	s
Lamé constants	λ, μ	Pa
Density	ρ	kg/m ³
Kinematic viscosity	$\gamma = \frac{\eta}{\rho}$	s ⁻¹

equations, and the kinematic relationships. For wave propagation (body forces neglected), the first and third equations would be

$$\rho \ddot{u}_i + \gamma \rho \dot{u}_i = \sigma_{ij,j} \quad (3)$$

$$\varepsilon_{ij} = \frac{1}{2} (u_{i,j} + u_{j,i} + u_{k,i} u_{k,j}) \quad (4)$$

where Table 1 shows the symbols of the magnitudes.

The compatibility equations can be considered separating them into linear, viscous, and nonlinear stress components, σ_{ij}^L , σ_{ij}^V , and σ_{ij}^{NL} .

$$\sigma_{ij} = \sigma_{ij}^L + \sigma_{ij}^V + \sigma_{ij}^{NL} \quad (5)$$

The nonlinear term can be deduced, following a similar concept of series expansion put forth by Landau [24, 25], where the volumetric and deviatoric decomposition of the stress tensor was considered, and only the volumetric part was detailed in terms of the nonlinear parameter β , in the following expression:

$$-p = -3Kv + 9K\beta v^2 - 3\eta^v \dot{v}. \quad (6)$$

where p and v are the volumetric components of the stress and deformation tensors, respectively, so that

$$\sigma_{ij} = \underbrace{-p\delta_{ij}}_{\text{volumetric}} + \underbrace{\tau_{ij}}_{\text{deviatoric}}, \quad p = -\frac{1}{3}\sigma_{kk} \quad (7)$$

$$\varepsilon_{ij} = -v\delta_{ij} + D_{ij}, \quad v = -\frac{1}{3}\varepsilon_{kk} \quad (8)$$

with τ_{ij} and D_{ij} being the deviatoric parts of the stress and strain tensors.

2.2. *Proposal of a New Constitutive Equation.* However, a more generalized constitutive relationship can be hypothesized using a combination of four of nonlinear parameters of third-order β that may explain a different scenario of calculations. These combinations could be expanded as exploring the whole set of combinations by quadratic terms as follows:

$$\sigma_{ij} = \underbrace{\frac{-3Kv\delta_{ij}}{\text{pressure}} + \frac{2\mu D_{ij}}{\text{shear}}}_{\sigma_{ij}^L(\text{Linear})} + \underbrace{\frac{-3\eta^v v\delta_{ij}}{\text{pressure}} + \frac{2\eta \dot{D}_{ij}}{\text{shear}}}_{\sigma_{ij}^V(\text{Viscous})} \quad (9)$$

$$+ \underbrace{\frac{+9K\beta^{vp} v^2 \delta_{ij} + 9K\beta^{dp} D_{kp} D_{pk} \delta_{ij}}{\text{pressure}} + \frac{4\mu\beta^{ds} D_{ik} D_{kj} + 4\mu\beta^{cs} v D_{ij}}{\text{shear}}}_{\sigma_{ij}^{NL}(\text{Nonlinear})}$$

The constants K and μ accompanying nonlinear parameters have been chosen in accordance with (6), as the quadratic power expansion. Four nonlinear parameters of third order (third, in terms of Energy expansion) have been defined and their terms can be interpreted, as follows:

- (i) Term with β^{vp} : nonlinear volumetric stress generated from the behavior of the volumetric component of the deformation
- (ii) Term with β^{dp} : nonlinear volumetric stress generated from the behavior of the deviatoric component of the deformation
- (iii) Term with β^{ds} : nonlinear stress generated from the behavior of the deviatoric component of the deformation
- (iv) Term with β^{cs} : nonlinear deviatoric stress generated from the interaction between the volumetric and deviatoric components of the deformation

To complete all possible combinations of quadratic terms, there are two additional combinations which have been removed, since the deviatoric trace D_{kk} is always null.

- (i) A term with $vD_{kk}\delta_{ij}$: it would be a nonlinear volumetric stress generated from the volumetric part of the deformation
- (ii) A term with $D_{kk}^2\delta_{ij}$: with similar interpretation than the previous one

This expression of the stress presents a similar structure to the expression of the stress with Third-Order Elastic Constants in the Landau form (\mathcal{A} , \mathcal{B} , \mathcal{C}), shown below in (13), so it will be considered later to obtain the differential equation in a parallel deduction.

Notwithstanding, there is another interesting expression fully separating the nonlinear volumetric and deviatoric components of the stress. The stress term with β^{ds} is dependent on the square $D_{ik}D_{kj}$ of the deviatoric component of the deformation D_{ij} and can be split into a volumetric and deviatoric part

$$D_{ik}D_{kj} = \frac{1}{3}D_{pk}D_{kp}\delta_{ij} + d_{ij} \quad (10)$$

$$d_{ij} = \text{deviatoric} [D_{ik}D_{kj}] \quad (11)$$

Thus,

$$\sigma_{ij} = \underbrace{\frac{-3Kv\delta_{ij}}{\text{pressure}} + \frac{2\mu D_{ij}}{\text{shear}}}_{\sigma_{ij}^L(\text{Linear})} + \underbrace{\frac{-3\eta^v v\delta_{ij}}{\text{pressure}} + \frac{2\eta \dot{D}_{ij}}{\text{shear}}}_{\sigma_{ij}^V(\text{Viscous})} \quad (12)$$

$$+ \underbrace{\frac{+9K\beta^{vp} v^2 \delta_{ij} + (9K\beta^{dp} + 4\mu\beta^{ds})D_{kp}D_{pk}\delta_{ij}}{\text{pressure}} + \frac{4\mu\beta^{ds}d_{ij} + 4\mu\beta^{cs}vD_{ij}}{\text{shear}}}_{\sigma_{ij}^{NL}(\text{Nonlinear})}$$

2.3. *Relationship to Formulations with Landau Constants.* As aforementioned, a quite similar expression of the Cauchy stress tensor can be found as a function of the Landau constants and the deformation tensor, for weakly elasticity:

$$\sigma_{ij} = \underbrace{\lambda \delta_{ij} \varepsilon_{kk} + 2\mu \varepsilon_{ij}}_{\sigma_{ij}^L} + \underbrace{2\eta \dot{\varepsilon}_{ij} - \frac{2}{3}\eta \delta_{ij} \dot{\varepsilon}_{kk} + \eta^v \delta_{ij} \dot{\varepsilon}_{kk}}_{\sigma_{ij}^V} \quad (13)$$

$$+ \underbrace{(\mathcal{A} + 4\mu) \varepsilon_{ik} \varepsilon_{kj} + \mathcal{B} \varepsilon_{kp} \varepsilon_{pk} \delta_{ij} + 2 \left(\mathcal{B} + K - \frac{5}{3}\mu \right) \varepsilon_{kk} \varepsilon_{ij} + \left(\mathcal{C} - K + \frac{2}{3}\mu \right) \varepsilon_{kk}^2 \delta_{ij}}_{\sigma_{ij}^{NL}}$$

In order to obtain the relationship between the Landau constants and the new four nonlinear parameters β , (13) is separated into volumetric and deviatoric components:

$$\varepsilon_{ij} = -v\delta_{ij} + D_{ij} \quad (14)$$

$$\varepsilon_{kk} = -v\delta_{kk} + D_{kk} = -3v \quad (15)$$

$$\varepsilon_{ik} = -v\delta_{ik} + D_{ik} \quad (16)$$

$$\varepsilon_{kj} = -v\delta_{kj} + D_{kj} \quad (17)$$

$$\varepsilon_{ik} \varepsilon_{kj} = v^2 \delta_{ik} \delta_{kj} - v D_{ik} \delta_{kj} - v D_{kj} \delta_{ik} + D_{ik} D_{kj} \quad (18)$$

$$\varepsilon_{kp} = -v\delta_{kp} + D_{kp} \quad (19)$$

$$\varepsilon_{pk} = -v\delta_{pk} + D_{pk} \quad (20)$$

$$\varepsilon_{pk} \varepsilon_{kp} = v^2 \delta_{pk} \delta_{kp} - v D_{pk} \delta_{kp} - v D_{kp} \delta_{pk} + D_{pk} D_{kp} \quad (21)$$

$$\varepsilon_{kk}^2 = 9v^2 \quad (22)$$

The nonlinear terms of (13) result in the following expressions:

$$\begin{aligned} & (\mathcal{A} + 4\mu) \varepsilon_{ik} \varepsilon_{kj} \\ &= (\mathcal{A} + 4\mu) (v^2 \delta_{ik} \delta_{kj} - \nu D_{ik} \delta_{kj} - \nu \delta_{ik} D_{kj} + D_{ik} D_{kj}) \end{aligned} \quad (23)$$

$$\mathcal{B} \varepsilon_{kp} \varepsilon_{pk} \delta_{ij} = \mathcal{B} (3v^2 + D_{kp} D_{pk}) \delta_{ij} \quad (24)$$

$$\begin{aligned} & 2 \left(\mathcal{B} + K - \frac{5}{3} \mu \right) \varepsilon_{kk} \varepsilon_{ij} \\ &= 2 \left(\mathcal{B} + K - \frac{5}{3} \mu \right) (3v^2 \delta_{ij} - 3\nu D_{ij}) \end{aligned} \quad (25)$$

$$\left(C - K + \frac{2}{3} \right) \varepsilon_{kk}^2 \delta_{ij} = \left(C - K + \frac{2}{3} \mu \right) 9v^2 \delta_{ij} \quad (26)$$

The above analysis is also valid by combining the nonlinear part of the stress with ν and D_{ij} in the constitutive equation,

$$\begin{aligned} \sigma_{ij}^{NL} &= (\mathcal{A} + 9\mathcal{B} + 9\mathcal{C} - 3K) v^2 \delta_{ij} + \mathcal{B} D_{kp} D_{pk} \delta_{ij} \\ &+ (\mathcal{A} + 4\mu) D_{ik} D_{kj} \\ &+ (-2\mathcal{A} + 6\mathcal{B} - 6K + 2\mu) \nu D_{ij} \end{aligned} \quad (27)$$

Comparing this expression with (9),

$$\beta^{vp} = \frac{\mathcal{A} + 9\mathcal{B} + 9\mathcal{C} - 3K}{9K} \quad (28)$$

$$\beta^{dp} = \frac{\mathcal{B}}{9K} \quad (29)$$

$$\beta^{ds} = \frac{\mathcal{A} + 4\mu}{4\mu} \quad (30)$$

$$\beta^{cs} = \frac{-2\mathcal{A} - 6\mathcal{B} - 6K + 2\mu}{4\mu} \quad (31)$$

$$\mathcal{A} = 4\mu (\beta^{ds} - 1) \quad (32)$$

$$\mathcal{B} = 9K \beta^{dp} \quad (33)$$

$$\mathcal{C} = K \beta^{vp} - \frac{4}{9} \mu \beta^{ds} - 9K \beta^{dp} + \frac{1}{3} K \quad (34)$$

For the viscous components, it is shown that the establish definition in (6) matches Landau's one:

$$2\eta \dot{\varepsilon}_{ij} = 2\eta (-\nu \delta_{ij} + \dot{D}_{ij}) \quad (35)$$

$$-\frac{2}{3} \eta \dot{\varepsilon}_{kk} \delta_{ij} = 2\eta \nu \delta_{ij} \quad (36)$$

$$\eta^v \dot{\varepsilon}_{kk} \delta_{ij} = -3\eta^v \nu \delta_{ij} \quad (37)$$

$$\sigma_{ij}^v = -3\eta^v \nu \delta_{ij} + 2\eta \dot{D}_{ij} \quad (38)$$

2.4. Differential Wave Equation. Adopting the acoustic nonlinear constitutive equation presented in (9), in terms of

deviatoric a volumetric parts of the deformation, it is possible to obtain the three dimensional nonlinear equation of motion in terms of the new four parameters β . Previously, the kinematic relations must be introduced in the constitutive equation.

$$\varepsilon_{ij} = \frac{1}{2} \left(\frac{\partial u_i}{\partial x_j} + \frac{\partial u_j}{\partial x_i} + \frac{\partial u_k}{\partial u_i} \frac{\partial u_k}{\partial u_j} \right) \quad (39)$$

The wave equation is,

$$\begin{aligned} \rho \frac{\partial^2 u_i}{\partial t^2} &= K \left(\frac{\partial^2 u_k}{\partial x_k \partial x_i} + \frac{\partial u_l}{\partial x_k} \frac{\partial^2 u_l}{\partial x_k \partial x_i} \right) \\ &+ \mu \left(\frac{\partial^2 u_i}{\partial x_j^2} + \frac{\partial^2 u_j}{\partial x_i \partial x_j} + \frac{\partial^2 u_k}{\partial x_j^2} \frac{\partial u_k}{\partial x_i} + \frac{\partial^2 u_k}{\partial x_i \partial x_j} \frac{\partial u_k}{\partial x_j} \right. \\ &\quad \left. - \frac{2}{3} \left(\frac{\partial^2 u_k}{\partial x_k \partial x_i} + \frac{\partial u_l}{\partial x_k} \frac{\partial^2 u_l}{\partial x_k \partial x_i} \right) \right) \\ &+ 2K \beta^{vp} \left(\frac{\partial^2 u_k}{\partial x_k \partial x_i} \frac{\partial u_l}{\partial x_l} \right) \\ &+ 9K \beta^{dp} \left(\frac{1}{2} \left(\frac{\partial^2 u_l}{\partial x_k \partial x_i} \frac{\partial u_l}{\partial x_k} + \frac{\partial^2 u_k}{\partial x_i \partial x_l} \frac{\partial u_k}{\partial x_l} \right) \right. \\ &\quad \left. + \frac{\partial^2 u_l}{\partial x_k \partial x_i} \frac{\partial u_k}{\partial x_l} + \frac{\partial^2 u_k}{\partial x_i \partial x_l} \frac{\partial u_l}{\partial x_k} \right) - \frac{2}{3} \frac{\partial^2 u_k}{\partial x_k \partial x_i} \frac{\partial u_l}{\partial x_l} \Big) \\ &+ 4\mu \beta^{ds} \left(\frac{1}{4} \left(\frac{\partial^2 u_i}{\partial x_k \partial x_j} \frac{\partial u_k}{\partial x_j} + \frac{\partial^2 u_k}{\partial x_i \partial x_j} \frac{\partial u_k}{\partial x_j} \right) \right. \\ &\quad \left. + \frac{\partial^2 u_i}{\partial x_k \partial x_j} \frac{\partial u_j}{\partial x_k} + \frac{\partial^2 u_k}{\partial x_i \partial x_j} \frac{\partial u_j}{\partial x_k} \right) \Big) \\ &+ 4\mu \beta^{ds} \left(\frac{1}{4} \left(\frac{\partial^2 u_k}{\partial x_j \partial x_j} \frac{\partial u_i}{\partial x_k} + \frac{\partial^2 u_j}{\partial x_k \partial x_j} \frac{\partial u_i}{\partial x_k} \right) \right. \\ &\quad \left. + \frac{\partial^2 u_k}{\partial x_j \partial x_j} \frac{\partial u_k}{\partial x_i} + \frac{\partial^2 u_j}{\partial x_k \partial x_j} \frac{\partial u_k}{\partial x_i} \right) \Big) \\ &+ 4\mu \beta^{ds} \left(-\frac{1}{3} \left(\frac{\partial^2 u_k}{\partial x_k \partial x_j} \frac{\partial u_i}{\partial x_j} + \frac{\partial^2 u_k}{\partial x_k \partial x_j} \frac{\partial u_j}{\partial x_i} \right) \right. \\ &\quad \left. + \frac{\partial^2 u_i}{\partial x_j^2} \frac{\partial u_k}{\partial x_k} + \frac{\partial^2 u_j}{\partial x_i \partial x_j} \frac{\partial u_k}{\partial x_k} \right) + \frac{2}{9} \frac{\partial^2 u_k}{\partial x_k \partial x_i} \frac{\partial u_l}{\partial x_l} \Big) \\ &+ 4\mu \beta^{ds} \left(-\frac{1}{6} \left(\frac{\partial^2 u_l}{\partial x_k \partial x_i} \frac{\partial u_l}{\partial x_k} + \frac{\partial^2 u_k}{\partial x_l \partial x_i} \frac{\partial u_k}{\partial x_l} \right) \right. \end{aligned}$$

$$\begin{aligned}
 & + \frac{\partial^2 u_l}{\partial x_k \partial x_i} \frac{\partial u_k}{\partial x_l} + \frac{\partial^2 u_k}{\partial x_l \partial x_i} \frac{\partial u_l}{\partial x_k} \Big) + \frac{2}{9} \frac{\partial^2 u_k}{\partial x_k \partial x_i} \frac{\partial u_l}{\partial x_l} \Big) \\
 & + 4\mu\beta^{cs} \left(-\frac{1}{6} \left(\frac{\partial^2 u_k}{\partial x_k \partial x_j} \frac{\partial u_i}{\partial x_j} + \frac{\partial^2 u_k}{\partial x_k \partial x_j} \frac{\partial u_j}{\partial x_i} \right) \right. \\
 & \left. + \frac{\partial^2 u_i}{\partial x_j^2} \frac{\partial u_k}{\partial x_k} + \frac{\partial^2 u_j}{\partial x_i \partial x_j} \frac{\partial u_k}{\partial x_k} \right) + \frac{2}{9} \frac{\partial^2 u_k}{\partial x_k \partial x_i} \frac{\partial u_l}{\partial x_l} \Big)
 \end{aligned} \quad (40)$$

where, as it was defined, K is the Bulk modulus, μ is the shear modulus, ρ is the density, and β^{vp} , β^{dp} , β^{ds} , and β^{cs} are the four nonlinear parameters of third order already explained in the constitutive expression.

3. Discussion

Considering the new nonlinear constitutive equation (12), it can be applied to the case of a pure plane horizontal shear

$$\begin{aligned}
 \sigma_{ij} = & \underbrace{K\varepsilon_{11}\delta_{ij} + 2\mu \begin{bmatrix} \frac{2}{3}\varepsilon_{11} & 0 & 0 \\ 0 & -\frac{1}{3}\varepsilon_{11} & 0 \\ 0 & 0 & -\frac{1}{3}\varepsilon_{11} \end{bmatrix}}_{\text{linear}} \\
 & + \underbrace{\left(K\beta^{vp} + 6K\beta^{dp} + 4\mu\beta^{cs} \right) \varepsilon_{11}^2 \delta_{ij} + 4\mu \left(\beta^{ds} - \beta^{cs} \right) \begin{bmatrix} \frac{2}{9}\varepsilon_{11}^2 & 0 & 0 \\ 0 & -\frac{1}{9}\varepsilon_{11}^2 & 0 \\ 0 & 0 & -\frac{1}{9}\varepsilon_{11}^2 \end{bmatrix}}_{\text{nonlinear}},
 \end{aligned} \quad (42)$$

where now the four nonlinear coefficients must be considered, indicating the existence of all kind of cross and parallel effects, although pure volumetric plus deviatoric nonlinear stress components are the result, allowing the separation of both nonlinear components.

Landau constants only account for the constitutive nonlinear behavior of the material, expressed in all the nonlinear terms of (13) that include \mathcal{A} , \mathcal{B} and \mathcal{C} . As mentioned above, there are several additional nonlinear terms in this expression without these constants, but with K and μ . They represent the geometrical nonlinearity originated in the geometrical transformation from the Piola tensor P_{ij} as a function of the strain energy U to get the Cauchy stress tensor.

$$P_{ij} = \frac{\partial U}{\partial F_{ij}} = F_{ij} \frac{\partial U}{\partial \varepsilon_{ij}} \quad (43)$$

wave. Disregarding the viscous term, the deformation tensor ε_{ij} will have all components null but ε_{12} , yielding $D_{ij} = \varepsilon_{ij}$, $v = -(1/3)\varepsilon_{kk} = 0$, and $D_{kp}D_{pk} = 2\varepsilon_{12}^2$,

$$\begin{aligned}
 \sigma_{ij} = & \underbrace{\begin{bmatrix} 0 & 2\mu\varepsilon_{12} & 0 \\ 2\mu\varepsilon_{12} & 0 & 0 \\ 0 & 0 & 0 \end{bmatrix}}_{\text{linear}} \\
 & + \underbrace{\begin{bmatrix} (9K\beta^{dp} + 4\mu\beta^{cs})\varepsilon_{12}^2 & 0 & 0 \\ 0 & (9K\beta^{dp} + 4\mu\beta^{cs})\varepsilon_{12}^2 & 0 \\ 0 & 0 & 9K\beta^{dp}2\varepsilon_{12}^2 \end{bmatrix}}_{\text{nonlinear}}
 \end{aligned} \quad (41)$$

In this case, the linear part of the stress continues with the same shear structure while the nonlinear part is a diagonal matrix meaning that there exists a volumetric component in it that would contribute to posterior volumetric deformations. Only two constants survive reducing the mathematical complexity for shear waves.

If it is a compressional wave in the x_1 direction, with $\varepsilon_{ij} = 0 \forall ij \neq 11$,

$$\sigma_{ij} = \frac{1}{\det(F)} P_{ij} F_{ji} \quad (44)$$

$$\sigma_{ij} = \frac{1}{\det(F)} F_{ij} \frac{\partial U}{\partial \varepsilon_{ij}} F_{ji} \quad (45)$$

It must be noted that the four new β constants would include constitutive and geometrical effects, with the exception of β^{dp} that is only of constitutive nature (see (29) and (28), (30), and (31)).

Considering the relations among the four new β parameters and Landau constants in (32), (33), (34), (28), (29), (30), and (31), some conclusions can be extracted.

- (i) As the Landau constant \mathcal{B} is only dependent on β^{dp} (see (33)), \mathcal{B} is a measure of the intensity on the cross effect from the deviatoric deformation into a nonlinear volumetric stress.

- (ii) As the Landau constant \mathcal{A} is only dependent on β^{ds} (see (32)), \mathcal{A} is a measure of the intensity on the nonlinear effect from the deviatoric deformation into the stress, which can be split into both volumetric and deviatoric parts (see (12)).
- (iii) As the Landau constant \mathcal{E} is only dependent on β^{vp} (see (34)), \mathcal{E} is the only one that measures the intensity on the nonlinear effect from the volumetric deformation into the volumetric component of the stress.
- (iv) As expected, β^{cs} is linearly dependent on β^{ds} and β^{dp} :

$$\beta^{cs} = -2\beta^{ds} - \frac{27K}{2\mu}\beta^{dp} - \frac{1}{2} - \frac{3K}{2\mu} \quad (46)$$

4. Conclusions

A new approach is proposed in the field of nonlinear acoustics introducing the volumetric and deviatoric separation in deformation and stress. The relevance of this expression is directly linked to the possibility of separating longitudinal and shear waves and selecting the responses of interest. Additional interpretations on the Landau constants are deduced in terms of the cross and parallel effects between volumetric and deviatoric components.

Data Availability

No data were used to support this study.

Conflicts of Interest

The authors declare that there are no conflicts of interest regarding the publication of this article.

Acknowledgments

This research was supported by the Ministry of Education [Grant nos. DPI2014-51870-R, DPI2017-85359-R, and UNGRI5-CE-3664], Ministry of Health [DTSI5/00093 and PII6/00339], Junta de Andalucía [PIN-0030-2017 and PI-0107-2017 projects], and University of Granada [PP2017-PIP2019].

References

- [1] M. F. Hamilton and D. T. Blackstock, *Nonlinear Acoustics*, vol. 237, Academic Press, San Diego, Calif, USA, 1998.
- [2] D. D. Muir, *One-Sided Ultrasonic Determination of Third Order Elastic Constants Using Angle-Beam Acoustoelasticity Measurements [Dissertation thesis]*, Georgia Institute of Technology, 2009.
- [3] C. Pantea, C. F. Osterhoudt, and D. N. Sinha, "Determination of acoustical nonlinear parameter β of water using the finite amplitude method," *Ultrasonics*, vol. 53, no. 5, pp. 1012–1019, 2013.
- [4] C. Trarieux, S. Callé, H. Moreschi, G. Renaud, and M. Defontaine, "Modeling nonlinear viscoelasticity in dynamic acoustoelasticity," *Applied Physics Letters*, vol. 105, no. 26, Article ID 264103, 2014.
- [5] J. Melchor, L. Peralta, G. Rus, N. Saffari, and J. Soto, "Single-transmitter setup on nonlinear mixing to measure acoustic nonlinearity of first order," in *Proceedings of the 6th European Symposium on Ultrasonic Characterization of Bone (ESUCB '15)*, pp. 1–4, IEEE, 2015.
- [6] R. Munoz, G. Rus, N. Bochud et al., "Nonlinear ultrasonics for early damage detection," *Emerging Design Solutions in Structural Health Monitoring Systems*, p. 171, 2015.
- [7] N. Antonin, M. Bentahar, V. Tournat et al., "Nonlinear acoustic characterization of micro-damaged materials through higher harmonic resonance analysis," *NDT & E International*, vol. 45, no. 1, pp. 1–8, 2012.
- [8] Y. Jiang, G.-Y. Li, L.-X. Qian et al., "Characterization of the nonlinear elastic properties of soft tissues using the supersonic shear imaging (SSI) technique: Inverse method, ex vivo and in vivo experiments," *Medical Image Analysis*, vol. 20, no. 1, pp. 97–111, 2015.
- [9] M. McGovern and H. Reis, "Linear and nonlinear ultrasonic characterization of limestone," in *Proceedings of the SPIE Smart Structures and Materials & Nondestructive Evaluation and Health Monitoring*, p. 94381A, San Diego, Calif, USA.
- [10] R. Munoz, J. C. Ruano, G. Rus et al., "Nonlinear ultrasonics for early damage detection," *Emerging Design Solutions in Structural Health Monitoring Systems*, pp. 171–206, 2015.
- [11] K. E. A. Van Den Abeele, W. Desadeleer, G. De Schutter, and M. Wevers, "Active and passive monitoring of the early hydration process in concrete using linear and nonlinear acoustics," *Cement and Concrete Research*, vol. 39, no. 5, pp. 426–432, 2009.
- [12] J. Kim and J. Lee, "A micromechanical model for nonlinear acoustic properties of interfaces between solids," *Journal of Applied Physics*, vol. 101, no. 4, Article ID 043501, 2007.
- [13] S. S. Kessler, S. M. Spearing, and C. Soutis, "Damage detection in composite materials using Lamb wave methods," *Smart Materials & Structures*, vol. 11, no. 2, pp. 269–278, 2002.
- [14] L. D. Landau and E. M. Lifshitz, "Theory of elasticity," in *Course of Theoretical Physics*, vol. 7, 1986.
- [15] F. D. Murnaghan, *Finite Deformation of an Elastic Solid*, Chapman & Hall, London, UK, 1951.
- [16] M. A. Breazeale and D. O. Thompson, "Finite-amplitude ultrasonic waves in aluminum," *Applied Physics Letters*, vol. 3, no. 5, pp. 77–78, 1963.
- [17] J. Melchor, *Mechanics of Nonlinear Ultrasound in Tissue*, University of Granada, 2016.
- [18] L. K. Zarembo and V. A. Krasil'nikov, "Nonlinear phenomena in the propagation of elastic waves in solids," *Soviet Physics—Uspekhi*, vol. 13, no. 6, pp. 778–797, 1971.
- [19] R. A. Guyer, J. Ten Cate, and P. Johnson, "Hysteresis and the dynamic elasticity of consolidated granular materials," *Physical Review Letters*, vol. 82, no. 16, pp. 3280–3283, 1999.
- [20] K. E. A. Van Den Abeele, P. A. Johnson, R. A. Guyer, and K. R. McCall, "On the quasi-analytic treatment of hysteretic nonlinear response in elastic wave propagation," *The Journal of the Acoustical Society of America*, vol. 101, no. 4, pp. 1885–1898, 1997.
- [21] J. Rivière, P. Shokouhi, R. A. Guyer, and P. A. Johnson, "A set of measures for the systematic classification of the nonlinear elastic behavior of disparate rocks," *Journal of Geophysical Research: Solid Earth*, vol. 120, no. 3, pp. 1587–1604, 2015.

- [22] K. E. A. Van Den Abeele, P. A. Johnson, and A. Sutin, "Nonlinear elastic wave spectroscopy (NEWS) techniques to discern material damage, Part I: Nonlinear wave modulation spectroscopy (NWMS)," *Research in Nondestructive Evaluation*, vol. 12, no. 1, pp. 17–30, 2000.
- [23] K. E. A. Van Den Abeele, J. Carmeliet, J. A. Ten Cate, and P. A. Johnson, "Nonlinear elastic wave spectroscopy (NEWS) techniques to discern material damage, Part II: Single-mode nonlinear resonance acoustic spectroscopy," *Research in Non-destructive Evaluation*, vol. 12, no. 1, pp. 31–42, 2000.
- [24] L. D. Landau and E. M. Lifshitz, *Theory of Elasticity*, Pergamon Press, Oxford, UK, 1986.
- [25] G. Rus, "Nature of acoustic nonlinear radiation stress," *Applied Physics Letters*, vol. 105, no. 12, Article ID 121904, 2014.

Research Article

Steering Control Method for an Underactuated Unicycle Robot Based on Dynamic Model

Hongzhe Jin , Yang Zhang, Hui Zhang, Zhangxing Liu, Yubin Liu ,
Yanhe Zhu , and Jie Zhao 

State Key Laboratory of Robotics and Systems, School of Mechatronics Engineering, Harbin Institute of Technology, Harbin, Heilongjiang 150080, China

Correspondence should be addressed to Hongzhe Jin; hongzhejin@hit.edu.cn, Yubin Liu; liuyubin@hit.edu.cn, and Yanhe Zhu; yhzhu@hit.edu.cn

Received 27 July 2018; Revised 17 October 2018; Accepted 29 October 2018; Published 18 November 2018

Academic Editor: Guillermo Rus

Copyright © 2018 Hongzhe Jin et al. This is an open access article distributed under the Creative Commons Attribution License, which permits unrestricted use, distribution, and reproduction in any medium, provided the original work is properly cited.

This paper proposes a lateral balancing structure based on precession effect of double-gyroscopes and its associated control strategy of the steering for an underactuated unicycle robot. Double-gyroscopes are symmetrically designed on the top of the unicycle robot and utilized to adjust the lateral balance of system. Such design can inhibit the disturbance of the gyroscope system to the pitch angle and is beneficial to maintain the lateral balance in the case of large roll angle fluctuations. Based on the analysis of the dynamics model, the gyroscope precession effects will be caused by the angular velocity of the bottom wheel and the roll angular velocity, i.e., resulting in a torque in the direction of the yaw. Then, a rapid response control strategy is proposed to use the torque to control the steering. Simulation results demonstrate the rationality of the lateral balance structure and the feasibility of the steering control method.

1. Introduction

Mobile robots, consisting of sensors and automatically mobile vehicle, are more flexible than other robots. So they are fitted to be used at inaccessible and harmful for people working environment. As one kind of mobile robot, unicycle robots are more flexible due to the single point contact of wheel of robot and ground. Therefore, the unicycle robot has the potential of free movement and moving at narrow spaces.

In most studies of unicycle robot, lateral balance has been emphasized with attention. According to the lateral balance methods, the unicycle robot can be classified into horizontal flywheel [1–6], vertical flywheel [7–13], high-speed gyros named Gyrover [14–19] and gyro precession with two gyroscopes [20, 21]. However, most of researches focus on balance control and neglect control of steering. If unicycle robot has steering control, it could realize target tracking and avoid obstacles. Some researchers already started to develop steering control method of the unicycle robot. Y. Isomi and S. Majima proposed a method to control unicycle robot's yaw without direct force for changing the yaw [22, 23]. They

derived the dynamics equation of unicycle robot and showed the yaw rate depends on the angular velocity of wheel and the roll angle. Through combining the solved equation of equilibrium state and Kanayama's tracking control method, it was proposed that the unicycle robot can track a target trajectory by this control method. In their simulation, it was confirmed that their control method can help unicycle robot obtain desired yaw rate. Gong Daoxiong and Li Xinghui also present the unicycle robot's yaw rate depending on the roll angle and the angular velocity of the wheel [24]. Through dynamics equation they proposed the theory. Then, they set the roll angle and angular velocity of the wheel to show the rate of the yaw direction achieved in simulation. Zhu Xiao Qing et al. added a horizontal flywheel between vertical flywheel and wheel of the unicycle robot [16, 25]. This unicycle robot uses the horizontal flywheel to control yaw angle with LQR controller.

The existing steering control methods for unicycle robot are mainly divided into two categories. One method appended a horizontal flywheel mechanism for yaw angle control. However, the appended horizontal flywheel not only

increases the weight of the unicycle robot but also makes the mechanism of unicycle robot complex. For the dynamics and control of the unicycle robot, appended horizontal flywheel will increase the complexity of its dynamic model and disturb the pitch and roll angles because of dynamics coupling. Another method used the dynamics coupling between the roll and yaw angles of the unicycle robot to realize steering control. Nevertheless, roll angle of the unicycle robot is too tiny for steady remaining and to reach a quick response in steering control.

This paper proposes a steering control method by regulating the roll angular velocity. According to the gyro precession effect, if a gyroscope has a spinning velocity and gets a precession angular velocity, there will be a gyroscopic torque by the right-hand rule. The steering control method in this paper regards the bottom wheel as a gyro and the roll angular velocity of the unicycle robot is regarded as the precession of the gyro. This can produce a precession torque in the direction of yaw. With a fixed bottom wheel speed, the yaw angle can be regulated by controlling the roll angular velocity of the unicycle robot.

The differences between the proposed and existing steering control methods for underactuated unicycle robot are as follows. (1) Existing steering control method is based on the vertical flywheel unicycle robot and the steering control method mentioned in the paper is based on precession effect of double-gyroscopes unicycle robot. (2) Existing underactuated steering control method realized steering by controlling the roll angle and the steering control method mentioned in the paper, by controlling the rolling angular velocity, more appropriate according to the dynamic analysis. Also, both of the control methods are simulated and compared in Section 5.

The rest of the paper is organized as follows. In Section 2, equations proving the motion of the unicycle robot are derived. Section 3 analyses the dynamics of pitch, roll, and yaw, respectively. Section 4 shows the control strategies of static and steering. In Section 5, the control strategies are proved by simulation and compared with the existing method. Conclusion and future work are presented on Section 6.

2. Model

2.1. Unicycle Robot. Figure 1 shows the model of unicycle robot. This unicycle robot's lateral balance is based on gyro precession. This type of unicycle robot has an excellent controllability on its roll angle. It is helpful for controlling angular velocity of roll.

The robot is consisting of two gyroscopes, a gyro precession, a frame, and a bottom wheel. The two gyroscopes have the same spinning velocity but their direction is opposite. Also we use one motor to control 2 of gyro precession to keep 2 of gyro precession the same at angular velocity and opposite at direction. It can inhibit the torque causing by gyro precession at pitch angle.

Figure 2 shows the coordinate system used to describe the posture of unicycle robot. The posture of the robot is given in

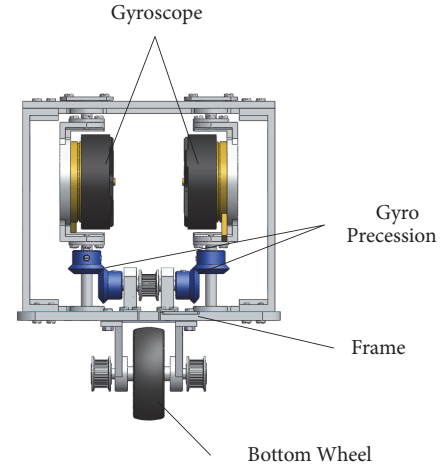


FIGURE 1: 3D model of the unicycle robot.

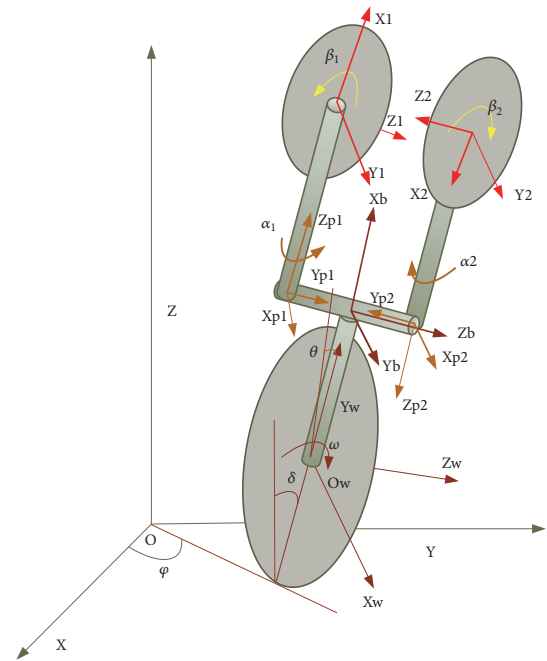


FIGURE 2: Structure map of the unicycle robot.

terms of the roll angle δ , the pitch angle θ , and the yaw angle φ . Table 1 shows the parameters of the unicycle robot.

2.2. Equations of Motion. The dynamic equations of the wheel are derived by the Euler-Lagrange formulation. The Euler-Lagrange equation is

$$\frac{d}{dt} \left(\frac{\partial L}{\partial \dot{q}} \right) - \frac{\partial L}{\partial q} = Q \quad (1)$$

The L in Euler-Lagrange equation is the Lagrangian function. It is defined as

$$L = K - U, \quad (2)$$

TABLE 1: Parameters of the unicycle robot.

Symbol	Description
M_w	Mass of the wheel
M_b	Mass of the frame
M_{p1}, M_{p2}	Mass of precession frame for left and right
M_1, M_2	Mass of gyroscopes for left and right
R_w	Radius of the wheel
L_b	Distance of frame's centre of gravity from centre of wheel
L_{p1}, L_{p2}	Distance of precession frame's centre of gravity from frame's centre of gravity for left and right
L_1, L_2	Distance of gyro's centre of gravity from precession frame's centre of gravity for left and right
I_{Wx}, I_{Wy}, I_{Wz}	Moments of inertia of the wheel's centre of gravity about the X,Y,Z axes, respectively
I_{bx}, I_{by}, I_{bz}	Moments of inertia of frame about the X,Y,Z axes, respectively
$I_{p1x}, I_{p1y}, I_{p1z}$ $I_{p2x}, I_{p2y}, I_{p2z}$	Moments of inertia of precession frame's centre of gravity about the X,Y,Z axes, respectively for left and right
I_{1x}, I_{1y}, I_{1z} I_{2x}, I_{2y}, I_{2z}	Moments of inertia of gyroscopes' centre of gravity about the X,Y,Z axes, respectively for left and right
φ	Yaw angle of the robot
δ	Roll angle of the robot
θ	Pitch angle of the body
ω	Rotating angle of the bottom wheel
α_1, α_2	Precession angle of precession frame for left and right
β_1, β_2	Spinning angle of gyroscopes for left and right
τ_w	Torque of the bottom wheel
τ_α	Torque of precession system
τ_β	Torque of gyroscope system

where K is the kinetic energy of the unicycle robot. It can be represented as

$$K = K_w + K_b + K_{p1} + K_{p2} + K_1 + K_2, \quad (3)$$

where $K_w, K_b, K_{p1}, K_{p2}, K_1, K_2$ are kinetic energy of wheel center and frame's centre of gravity, respectively. K_{p1}, K_{p2}, K_1, K_2 are kinetic energy of precession frame's centre of gravity for left and right. K_1, K_2 are kinetic energy of gyro's centre for left and right.

U is the potential energy of the unicycle robot. From Figure 2, U can be represented as

$$U = U_w + U_b + U_{p1} + U_{p2} + U_1 + U_2. \quad (4)$$

U_w is potential energy of wheel centre. U_b is potential energy of frame's centre of gravity. U_{p1} and U_{p2} are potential energy of precession frame's centre of gravity for left and right. U_1 and U_2 are potential energy of gyroscopes' centre for left and right.

Q and q are the generalized forces and generalized coordinates, respectively. For the system, q is selected as

$$q = (\varphi, \delta, \theta, \omega, \alpha, \beta)^T. \quad (5)$$

Q is given by

$$Q = (0, 0, 0, \tau_w, \tau_\alpha, \tau_\beta)^T. \quad (6)$$

In order to simplify the dynamic equations, cx and sx mean $\cos(x)$ and $\sin(x)$, respectively. Using the Euler-Lagrange equation, the dynamic equation of the system can be given by

$$M(q) \ddot{q} + N(\dot{q}, q) = Q, \quad (7)$$

where $M(q) \in \mathbb{R}^{6 \times 6}$ and $N(\dot{q}, q) \in \mathbb{R}^{6 \times 1}$ are the inertia matrix and nonlinear term, respectively.

$$\vec{M}(\vec{q}) = \begin{pmatrix} m_{11} & m_{12} & m_{13} & m_{14} & 0 & m_{16} \\ m_{21} & m_{22} & m_{23} & 0 & 0 & m_{26} \\ m_{31} & m_{32} & m_{33} & m_{34} & 0 & 0 \\ m_{41} & 0 & m_{43} & m_{44} & 0 & 0 \\ 0 & 0 & 0 & 0 & m_{55} & 0 \\ m_{61} & m_{62} & 0 & 0 & 0 & m_{66} \end{pmatrix} \quad (8)$$

$$\vec{N} = (n_1 \ n_2 \ n_3 \ n_4 \ n_5 \ n_6)^T \quad (9)$$

The dynamic equations of the unicycle robot are far too lengthy to be shown here due to space limitations. Therefore, the reader is referred to in the Appendix. The dynamic equations are complex for control design and they have strong coupling. In order to derive the control strategy of static and steering, we need to simplify the model. According to the steady motion characters of unicycle robot, the dynamic equations of the system are decoupled and simplified to three parts. They are pitch dynamics, roll dynamics, and yaw dynamics, respectively.

3. Analysis on the Dynamics

3.1. Dynamic Model for Pitch Axis. The robot frame and the precession system can be seen as a single body, and the pitch dynamic of the system can be regarded as a wheeled inverted pendulum system. Both of roll angle and yaw angle change are small and can be neglected. The dynamic equations for pitch are derived from Lagrange's equation as follows:

$$\frac{d}{dt} \left(\frac{\partial L}{\partial \dot{q}_1} \right) - \frac{\partial L}{\partial q_1} = Q_1, \quad (10)$$

where $q_1 = (\theta, \omega)^T$ and $Q_1 = (0, \tau_\omega)^T$. According to (10), the state equation for pitch is as follows:

$$\begin{bmatrix} m_{33} & m_{34} \\ m_{43} & m_{44} \end{bmatrix} \begin{bmatrix} \ddot{\theta} \\ \dot{\omega} \end{bmatrix} - \begin{bmatrix} n_3 \\ n_4 \end{bmatrix} = \begin{bmatrix} 0 \\ \tau_\omega \end{bmatrix}. \quad (11)$$

The coefficients of $4s\alpha c\alpha I_{1x} - 4s\alpha c\alpha I_{1z}$ and $c\theta s\alpha I_{1z}$ are tinier than others. The coefficient of $2s^2\alpha I_{1x} + 2c^2\alpha I_{1z}$ is far less than ℓ_{10} and ℓ_1 . The coefficient of $\ell_{11} + 2s^2\alpha I_{1x} + 2c^2\alpha I_{1z}$ is far less than ℓ_2 . These coefficients are ignored. So the simplified dynamic equations about pitch angle are as follows:

$$\ell_{10}\ddot{\theta} + c\theta\ell_2\ddot{\omega} - (M_bgL_b + 2M_{p1}gL + 2M_1gL)s\theta = 0 \quad (12)$$

$$c\theta\ell_2\ddot{\theta} + \ell_1\ddot{\omega} - \dot{\theta}^2s\theta\ell_2 = \tau_\omega. \quad (13)$$

From (12) and (13), the dynamic equations are as follows:

$$\ddot{\theta} = \frac{B \cos \theta \tau_\omega + B^2 \cos \theta \sin \theta \dot{\theta}^2 - CD \sin \theta}{B^2 \cos^2 \theta - AD} \quad (14)$$

$$\ddot{\omega} = \frac{A\tau_\omega + AB \sin \theta \dot{\theta}^2 - BC \cos \theta \sin \theta}{B^2 \cos^2 \theta - AD}, \quad (15)$$

where coefficients are

$$\begin{aligned} A &= \ell_{10} \\ B &= \ell_2 \\ C &= M_bgL_b + 2M_{p1}gL + 2M_1gL \\ D &= \ell_1 \end{aligned} \quad (16)$$

τ_ω represents the torque of the bottom wheel. C is the gravity component of unicycle robot for pitch. In order to balance of pitch, the torque of the bottom wheel τ_ω must relate to pitch angle and pitch angular velocity which control the change of pitch angle stable. When the pitch angle tends to zero, the bottom wheel can keep stable. According to the analysis of the dynamics of pitch axis, the design of detailed control strategy is in next section.

3.2. Dynamic Model for Roll Axis. The robot's frame and the bottom wheel can be seen as a single body, and the roll dynamic of the system can be regarded as a gyroscopic precession system. Both changes of pitch angle and yaw angle

are small and can be neglected. The dynamic equations for roll are derived from Lagrange's equation as follows:

$$\frac{d}{dt} \left(\frac{\partial L}{\partial \dot{q}_2} \right) - \frac{\partial L}{\partial q_2} = Q_2, \quad (17)$$

where $q_2 = (\delta, \alpha, \beta)^T$ and $Q_2 = (0, \tau_\alpha, \tau_\beta)^T$. According to (17), the state equation for roll is as follows:

$$\begin{bmatrix} m_{22} & 0 & m_{26} \\ 0 & m_{55} & 0 \\ m_{26} & 0 & m_{66} \end{bmatrix} \begin{bmatrix} \ddot{\delta} \\ \ddot{\alpha} \\ \ddot{\beta} \end{bmatrix} - \begin{bmatrix} n_2 \\ n_5 \\ n_6 \end{bmatrix} = \begin{bmatrix} 0 \\ \tau_\alpha \\ \tau_\beta \end{bmatrix}. \quad (18)$$

The coefficients of $4s\alpha c\alpha I_{1x} - 4s\alpha c\alpha I_{1z}$ are tinier than others. The coefficient of $2s^2\alpha I_{1x} + 2c^2\alpha I_{1z}$ is far less than $\ell_5 + \ell_6 + 2\ell_2$. The spinning velocity of gyroscopes is constant value, so $\dot{\beta} = 0$ and $\tau_\beta \approx 0$. These coefficients are ignored. So the simplified dynamic equations about roll angle are as follows:

$$\begin{aligned} (\ell_5 + \ell_6 + 2\ell_2)\ddot{\delta} + 2\dot{\beta}\dot{\alpha}c\alpha I_{1z} - (M_w g R_W + M_b g L_b \\ + M_b g R_W + 2M_{p1}gL + 2M_{p1}gR_W + 2M_1gL \\ + 2M_1gR_W)s\delta = 0 \end{aligned} \quad (19)$$

$$(I_{1x} + I_{p1z})\ddot{\alpha} - \frac{1}{2}\delta^2(4s\alpha c\alpha I_{1z}) - 2\dot{\delta}\dot{\beta}c\alpha I_{1z} = \tau_\alpha \quad (20)$$

$$2s\alpha I_{1z}\ddot{\delta} + 2\dot{\delta}\dot{\alpha}c\alpha I_{1z} = 0. \quad (21)$$

τ_α represents the torque of the precession system. $\dot{\beta}\dot{\alpha}$ represents gyroscopic precession moment. The coefficient of $s\delta$ represents gravity component of roll. According to (19), the gyroscopic moment provides torque to resist unicycle robot's gravity component of roll. Besides, the unicycle robot gets an angular acceleration of roll. But gyroscopic moment's coefficient includes cosine precession angle. It means torque of gyroscopic moment is smaller as precession angle is larger. According to the analysis on the dynamics of roll axis, controlling angular velocity of precession is better than torque of the precession system, and the design of detailed control strategy is in next section.

3.3. Dynamic Model for Yaw Axis. For the yaw dynamic of the system, assume the change of the pitch is small and can be neglected. The roll angle is small so that $\sin \delta$ and $\cos \delta$ can be approximated to zero and one, respectively. The bottom wheel and gyroscopes get a constant speed. The dynamic equation for yaw is derived from Lagrange's equation as follows:

$$\frac{d}{dt} \left(\frac{\partial L}{\partial \dot{q}_3} \right) - \frac{\partial L}{\partial q_3} = Q_3, \quad (22)$$

where $q_3 = \varphi$ and $Q_3 = 0$. According to (22), the state equation for yaw is as follows:

$$m_{11}\ddot{\varphi} - n_1 = 0. \quad (23)$$

The coefficients of $-4s\alpha c\alpha I_{1x} - 4s\alpha c\alpha I_{1z}$, I_{1x} are tinier than others. So the simplified dynamic equation about yaw angle is as follows:

$$(\ell_8 + \ell_7) \ddot{\phi} + \dot{\omega} \delta (-\ell_1 + \ell_2) = 0. \quad (24)$$

In the equation, $\dot{\omega} \delta$ is the gyroscopic precession moment of bottom wheel and the unicycle robot's roll angle. According to the equation, influence factor for yaw angle includes the angular velocity of bottom wheel and the angular velocity of roll. The angular velocity of bottom wheel should hold on a constant value for balancing of pitch angle. Therefore, the steering control strategy is designed about the angular velocity of roll, and the design of detailed control strategy is in next section.

Due to the yaw angle coupling to pitch angle and precession angle, the analysis of these 2 angles is necessary in the steering control method. When angular velocities of yaw and the bottom wheel keep stable, the angular velocity of roll will stable to zero and the roll angle is small for being ignored. The dynamic equation for pitch angle is derived as follows:

$$\frac{d}{dt} \left(\frac{\partial L}{\partial \dot{q}_4} \right) - \frac{\partial L}{\partial q_4} = Q_4, \quad (25)$$

where $q_4 = \theta$ and $Q_4 = 0$. According to (25), the state equation for pitch is as follows:

$$m_{33} \ddot{\theta} - n_3 = 0. \quad (26)$$

The coefficients of $4s\alpha c\alpha I_{1x} - 4s\alpha c\alpha I_{1z}$ and $c\theta s\alpha I_{1z}$ are tinier than others. The coefficient of $2s^2\alpha I_{1x} + 2c^2\alpha I_{1z}$ is far less than ℓ_{10} . These coefficients can be ignored. So the simplified dynamic equation is as follows:

$$\begin{aligned} & \ell_{10} \ddot{\theta} \\ & - \frac{1}{2} \dot{\phi}^2 (-2c\theta s\theta \ell_7 + 2c\theta s\theta \ell_8 + 2c\theta s\theta \ell_9 - 4c\theta s\theta I_{1x}) \\ & - s\theta (M_b g L_b + 2M_{p1} g L + 2M_1 g L) = 0. \end{aligned} \quad (27)$$

$\dot{\phi}^2$ is the centripetal force for yaw angle's circle. When the unicycle robot has a yaw angular velocity and the change of pitch angle is stable, the dynamic equation is as follows:

$$\theta = \arccos \frac{(M_b g L_b + 2M_{p1} g L + 2M_1 g L)}{\dot{\phi}^2 (\ell_7 - \ell_8 - \ell_9 + 2I_{1x})} \quad (28)$$

It means centripetal force for yaw angle's circle also affects pitch angle. When the unicycle robot has a constant yaw angular velocity, the pitch angle is stable at a constant.

Similarly, when the angular velocities of yaw and the bottom wheel keep stable, the angular velocity of roll will stable to zero and the roll angle is small for being ignored. Also the change of pitch is stable. The dynamic equation for precession angle is derived as follows:

$$\frac{d}{dt} \left(\frac{\partial L}{\partial \dot{q}_5} \right) - \frac{\partial L}{\partial q_5} = Q_5, \quad (29)$$

where $q_5 = \alpha$ and $Q_5 = \tau_\alpha$. According to (29), the state equation for precession is as follows:

$$m_{33} \ddot{\alpha} - n_5 = \tau_\alpha. \quad (30)$$

So the simplified dynamic equation is as follows:

$$\begin{aligned} & (I_{1x} + I_{p1z}) \ddot{\alpha} - \frac{1}{2} \dot{\phi}^2 (-4s\alpha c\alpha c^2 \theta I_{1x} + 4s\alpha c\alpha s^2 \theta I_{1z}) \\ & - 2\dot{\phi} \dot{s} \theta c\alpha I_{1z} = \tau_\alpha \end{aligned} \quad (31)$$

$\dot{\phi}^2$ is the centripetal force for yaw angle's circle. When the unicycle robot has a yaw angle velocity and the change of precession angle is stable and the torque of precession is stable at zero, the dynamic equation is as follows:

$$\alpha = \arcsin \frac{\dot{\phi} \dot{s} \theta I_{1z}}{\dot{\phi}^2 (c^2 \theta I_{1x} - s^2 \theta I_{1z})} \quad (32)$$

It means centripetal force for yaw angle's circle also affects precession angle. When the unicycle robot has a constant yaw angle velocity, the precession angle is stable at a constant.

4. The Control Strategies Design

For traditional unicycle robots, their controllers are generally separated at lateral and longitudinal and ignored the yaw angle. However, the above dynamic analysis proved that angular velocity of the yaw affects both of lateral balance and longitudinal balance. Also, yaw angle can be controlled by angular velocity of the roll. In this section, there are two control strategies. First is designed for static balance control from the simplified dynamics of the pitch (14), (15) and the roll (19), (20), and (21). Another is steering control, according to the simplified dynamics of the yaw (24).

4.1. Static Balance Control. Based on the dynamic analysis of the previous section, the unicycle robot's pitch angle is balanced by the torque of the bottom wheel and roll angle is balanced by the precession system. The torque of the bottom wheel is to regulate the pitch angle θ and the angular velocity of wheel $\dot{\omega}$. The spinning velocity of gyroscopes keeps a constant value, and angular velocity controller of precession is adaptive for the balance of roll angle according to the analysis of previous section.

The input of bottom wheel is as follows:

$$\tau_\omega = k_{p\theta} e_\theta + k_{D\theta} \dot{e}_\theta + k_{p\dot{\omega}} e_{\dot{\omega}} + k_{I\dot{\omega}} \bar{e}_{\dot{\omega}}, \quad (33)$$

where $k_{p\theta}$, $k_{D\theta}$, $k_{p\dot{\omega}}$, $k_{I\dot{\omega}}$ are controller gains. e_θ is the difference between the real-time pitch angle θ and the set angle θ_r . It is given as

$$e_\theta = \theta - \theta_r. \quad (34)$$

$e_{\dot{\omega}}$ is the difference between the real-time angular velocity of wheel $\dot{\omega}$ and the set angular velocity $\dot{\omega}_r$. Its integration is $\bar{e}_{\dot{\omega}}$. It is given as

$$\bar{e}_{\dot{\omega}} = \dot{\omega} - \dot{\omega}_r. \quad (35)$$

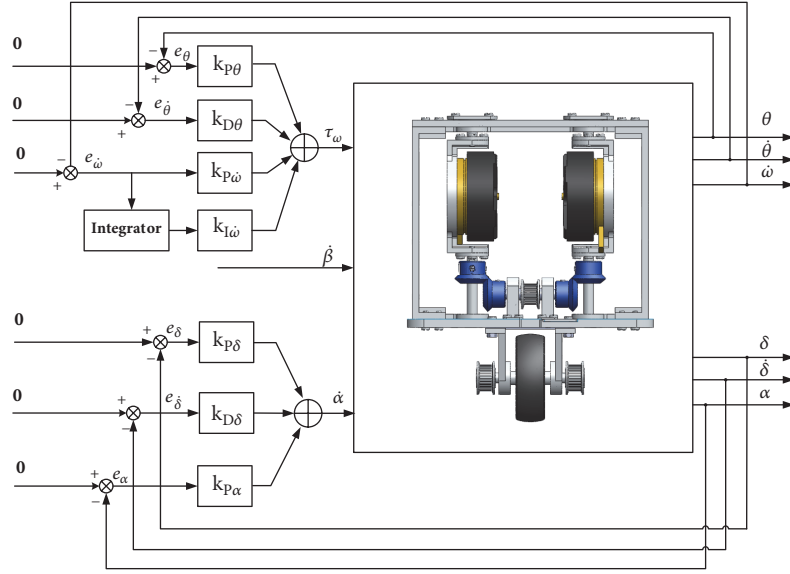


FIGURE 3: The control diagram of static balance control.

The torque of the bottom wheel τ_ω includes PD controller of the pitch angle θ and PI controller of the angular velocity of wheel $\dot{\omega}$. The set values θ_r , $\dot{\theta}_r$, and $\dot{\omega}_r$ are 0 to keep unicycle static for longitudinal.

The input of angular velocity of precession is as follows:

$$\dot{\alpha} = k_{P\delta}e_\delta + k_{D\delta}\dot{e}_\delta + k_{P\alpha}e_\alpha, \quad (36)$$

where $k_{P\delta}$, $k_{D\delta}$, $k_{P\alpha}$ are controller gains. e_δ is the difference between the real-time roll angle δ and the set angle δ_r . It is given as

$$e_\delta = \delta - \delta_r, \quad (37)$$

e_α is the difference between the real-time precession angle α and the set angle α_r . It is given as

$$e_\alpha = \alpha - \alpha_r, \quad (38)$$

The angular velocity of precession $\dot{\alpha}$ includes PD controller of the roll angle δ and P controller of the precession angle α . According to the dynamic analysis of roll angle, the torque of precession system has a coefficient $\cos \alpha$. It means the torque of gyro precession system is smaller as precession angle increasing. So a P controller was designed to return the precession angle to zero. And the set values δ_r , $\dot{\delta}_r$, and α_r are 0 to keep unicycle static for lateral. The detailed control block diagram is shown in Figure 3.

4.2. Steering Control. Based on the dynamic analysis of the previous section, the unicycle robot's yaw angle is related to the angular velocities of roll and bottom wheel. In order to enhance the reaction of steering and the stability of the controller, fast responsive control strategy is opted to steering control.

The input of precession angular velocity is as follows:

$$\dot{\alpha} = k_{P\delta}e_\delta + k_{D\delta}\dot{e}_\delta + k_{P\alpha}e_\alpha, \quad (39)$$

where $k_{P\delta}$, $k_{D\delta}$, $k_{P\alpha}$, e_δ , \dot{e}_δ , e_α are defined as static balance control. The differences are $\dot{\delta}_r$ and δ_r . It is given as

$$\dot{\delta}_r = k_{D\varphi}\dot{e}_\varphi \quad (40)$$

where $k_{D\varphi}$ is coefficient of fast responsive control strategy for steering control. \dot{e}_φ is the difference between the real-time yaw angular velocity $\dot{\varphi}$ and the set yaw angular velocity $\dot{\varphi}_r$. It is given as

$$\dot{e}_\varphi = \dot{\varphi} - \dot{\varphi}_r \quad (41)$$

Also, according to the dynamic analysis of yaw, it is not only related to the angular velocity of roll, but also to the angular velocity of bottom wheel. In the process of steering control, the bottom wheel gets an angular velocity and the set angular velocity $\dot{\omega}$ is constant value. The detailed control block diagram is shown in Figure 4.

5. Simulation

In this section, the controllers will be tested by dynamics simulation and all the data and codes of the simulations are available online (see <https://github.com/ZhangYang157/01-Codes-and-Data-for-Steering-Control-Method-for-an-Under-actuated-Unicycle-Robot-Based-on-Dynamic-.git>) and are included in the supplementary materials (available here). The simulation video for the proposed steering control method is available online (see <https://github.com/ZhangYang157/02-supplementary-material-file-for-simulation-video.git>). A three-dimensional simulation model of unicycle robot is built in the ADAMS environment. It is shown in Figure 5. The simulation model includes 5 parts. They are ground, gyroscopes, precession, frame, and bottom wheel. Ground is fixed in space. Static friction coefficient between bottom wheel and ground is 0.8 and dynamic friction coefficient is 0.4. According to the control strategies design, the input of

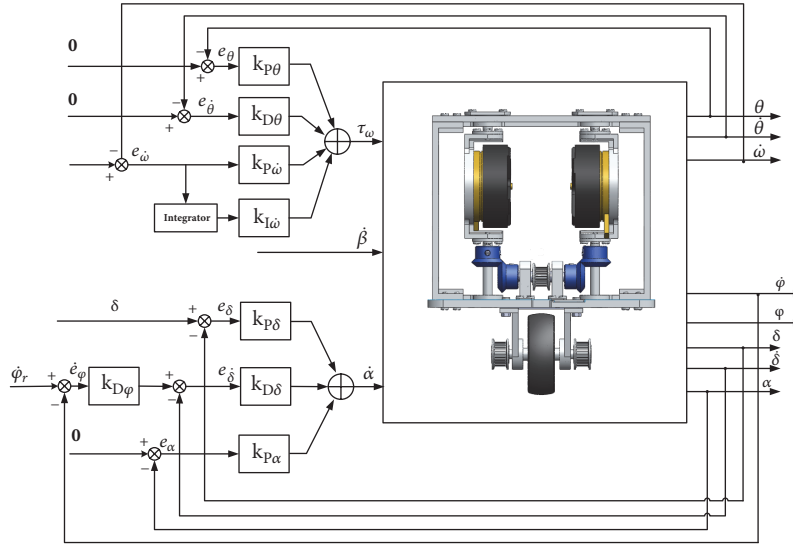


FIGURE 4: The control diagram of steering control.

TABLE 2: Static control parameters value of the static control strategy in simulation.

Parameters	ω_β	$k_{p\theta}$	$k_{D\theta}$	$k_{p\dot{\omega}}$	$k_{I\dot{\omega}}$	$k_{p\delta}$	$k_{D\delta}$	$k_{p\alpha}$
Value	3000rpm	12	0.3	0.03	0.02	15	1.2	1.5

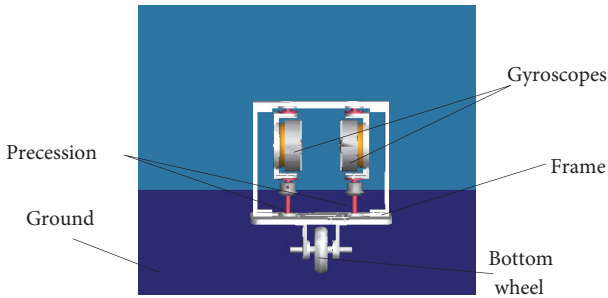


FIGURE 5: Simulation model in ADAMS.

the bottom wheel is the torque τ_ω . The input of precession is angular velocity of precession $\dot{\alpha}$ and the angular velocity of gyro β is constant value. The sampling time is 10 ms. In this section, there are two experiments. Firstly, static balance equilibrium is controlling the unicycle robot stable in place with an interference force. Secondly, steering control method of the unicycle robot is setting the roll angular velocity and giving the angular velocity of bottom wheel a constant value.

5.1. Simulation of Static Equilibrium. For the initial state of the simulation, the unicycle robot has a minimal inclination angle for roll and pitch. In the simulation time of 5s, there is a lateral interference force of 10 N (duration is 0.01s). Using the controller of static balance control, Table 2 shows the control parameters value of the static control strategy in simulation. Simulation is generated in 8 seconds. Figure 6 shows the graphs of roll and pitch angle in static balance simulation. The unicycle robot gets to stability at start. In time 5s, the roll angle

and pitch angle accordingly vary with the lateral interference force. With the static balance control strategy, the unicycle robot was back to stable.

5.2. Simulation of Steering Control. Based on the static balance equilibrium, the steering control adds an angular velocity of the bottom wheel $\dot{\omega}_r$, fast responsive control strategy for steering. Table 3 shows the control parameters value of the steering control strategy in simulation. The set bottom wheel angular velocity $\dot{\omega}_r$ is $50^\circ/s$ and the coefficient of fast responsive control strategy $k_{D\phi}$ is 1.1. Before steering control, the robot is controlled to balance with a given angular velocity of the bottom wheel $\dot{\omega}_r$ and the set angular velocity $\dot{\phi}_r$ is zero. When the angular velocity of bottom wheel is stable to $50^\circ/s$, the set angular velocity $\dot{\phi}_r$ is given.

The simulation experiment also compares the existing under-actuated steering control strategies. As Y. Isomi, S. Majima [22, 23], Gong Daoxiong and Li Xinghui [24] proposed steering control method for unicycle robot; the steering is controlled by the roll angle with the constant speed of bottom wheel. Comparative analysis of the 2 different steering control methods by simulation experiment is next.

The set angular velocity $\dot{\phi}_r$ is ramp and the slope is $0.6^\circ/s^2$ until $\dot{\phi}_r$ is $3^\circ/s$. In order to increase input stability of $\dot{\phi}_r$, there is a low pass filter to the set angular velocity $\dot{\phi}_r$ before input. Figure 7 shows the set yaw angular velocity of previous filter, the set yaw angular velocity of after filter, the practical yaw angular velocity, the practical yaw angular velocity of existing method, the set yaw angle after filter, the practical yaw angle, and practical yaw angle of existing method. The practical angular velocity of yaw is accurate following the set angular

TABLE 3: Parameters value of the steering control strategy in simulation.

Parameters	$\dot{\omega}_r$	$k_{p\theta}$	$k_{D\theta}$	$k_{p\dot{\omega}}$	$k_{I\dot{\omega}}$	$k_{p\delta}$	$k_{D\delta}$	$k_{p\alpha}$	$k_{D\phi}$
Value	50°/s	14	0.5	0.05	0.02	15	1.2	1.5	1.1

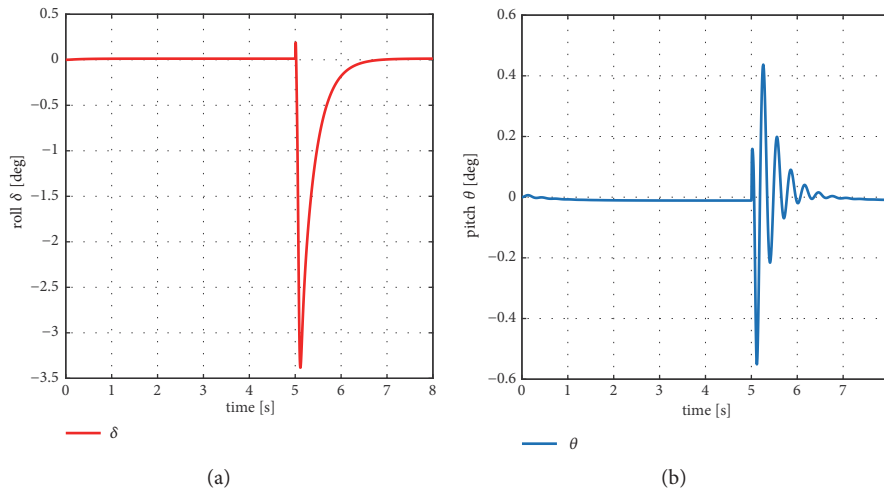


FIGURE 6: The roll and pitch angle in static equilibrium simulation. (a) The graph of roll angle. (b) The graph of pitch angle.

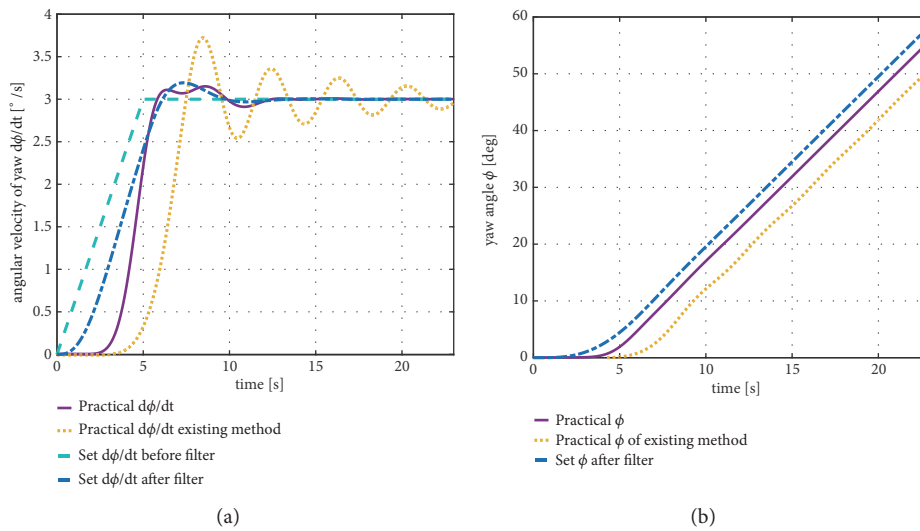


FIGURE 7: The yaw angular velocity and the yaw angle in simulation of yaw angle control. (a) The graph of the set yaw angular velocity previous filter, the set yaw angular velocity after filter, the practical yaw angular velocity, and the practical yaw angular velocity of existing method. (b) The graph of set yaw angle after filter, yaw angle, and practical yaw angle of existing method.

velocity of yaw with a bit of delay at the acceleration. The angle of yaw is increased steadily. Using the coupling of the unicycle robot, the yaw angle is controlled without directly torque for steering. By comparing with existing method, the yaw angle control method proposed in this paper is faster response to yaw angle control command and closer to set yaw angle and yaw angular velocity curves.

Figure 8 shows the graphs of practical roll angle, the practical roll angle of existing method, the practical roll angular velocity, and the practical roll angular velocity of

existing method. The angular velocity of roll and roll angle get a big fluctuation since the fast responsive control strategy of steering. When the practical angular velocity of yaw steadied at a constant value, the angular velocity of roll becomes stable again. By comparing with existing method, the control method proposed in this paper has relatively large amplitude, but it is stable to the steady state for roll angle and roll angular velocity faster.

Figure 9 shows the graphs of practical pitch angle, the practical pitch angle of existing method, the practical pitch

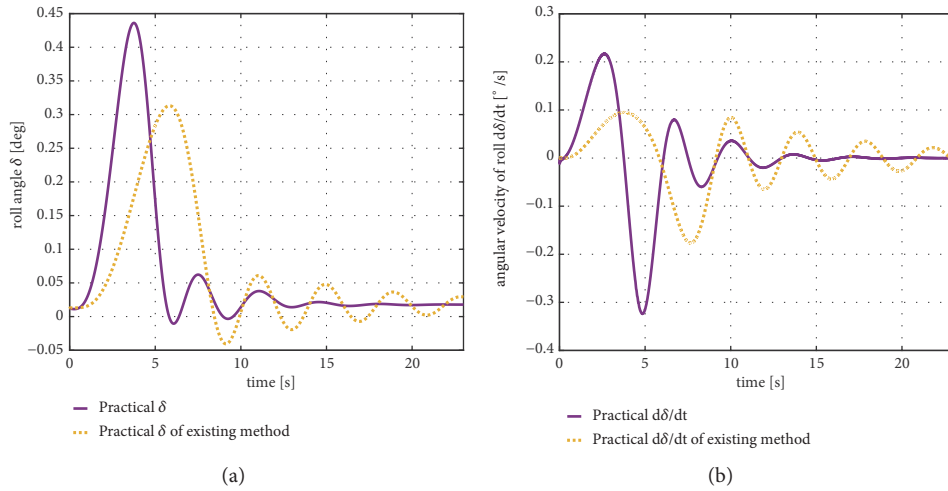


FIGURE 8: The roll angle and the roll angular velocity in simulation of yaw angle control. (a) The graph of practical roll angle and practical roll angle of existing method. (b) The graph of practical roll angular velocity and practical roll angular velocity of existing method.

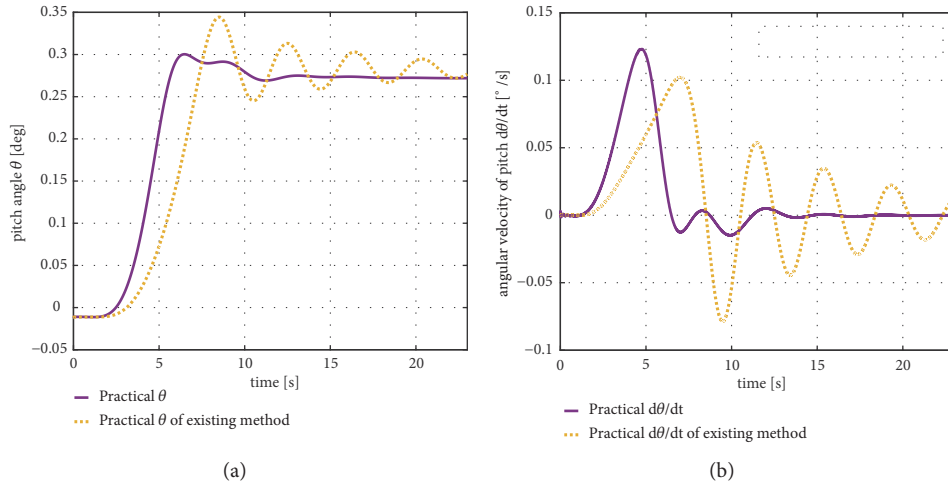


FIGURE 9: The pitch angle and the pitch angular velocity in simulation of yaw angle control. (a) The graph of practical pitch angle and practical pitch angle of existing method. (b) The graph of practical pitch angular velocity and practical pitch angular velocity of existing method.

angular velocity, and the practical pitch angular velocity of existing method. The angular velocity of pitch gets a big fluctuation due to the fast responsive control strategy of steering. When the angular velocity of yaw is going to stabilize, the angular velocity of pitch is stable to zero and the pitch angle is stable to a value due to effect of centripetal force as (28). By comparing with existing method, the control method proposed in this paper is more quickly stable to the steady state for pitch angle and relatively large amplitude for pitch angular velocity.

Figure 10 shows the change of practical precession angle, the practical precession angle of existing method, the practical precession angular velocity, and the practical precession angular velocity of existing method. Through controlling the precession angular velocity, the unicycle robot gets to balance with a short while. The angular velocity of precession is the input for balance of roll angle. When the steering control is

going to stabilize, the angular velocity of precession becomes stable to zero and the precession angle is stable to a value due to effect of centripetal force as (32). By comparing with existing method, the control method proposed in this paper is more quickly stable to the steady state for precession angle and relatively small amplitude for precession angular velocity.

Figure 11 shows the angular velocity of bottom wheel $\dot{\omega}$. At the beginning, the angular velocity of bottom wheel $\dot{\omega}$ becomes stable at $50^\circ/s$. $\dot{\omega}$ has a big fluctuation during the angular velocity of yaw $\dot{\phi}$ causing a change. When the angular velocity of yaw $\dot{\phi}$ is steady, $\dot{\omega}$ is stable at $50^\circ/s$ again. The curve “practical $d\omega/dt$ of existing method” shows the angular velocity of bottom wheel $\dot{\omega}$ for the yaw angle control method by roll angle. Both of the angular velocities of bottom wheel are stable at $50^\circ/s$, but the curve of existing method has higher frequency of oscillation than the control method mentioned in the paper.

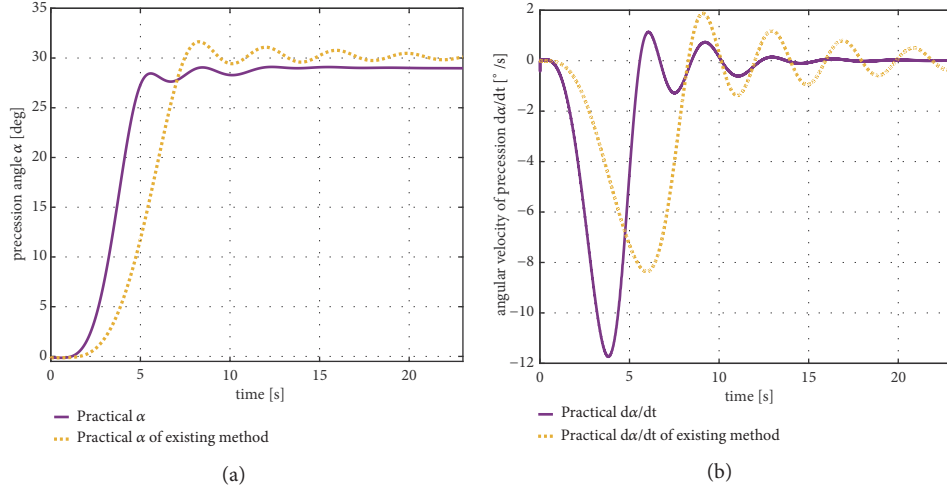


FIGURE 10: The precession angle and the precession angular velocity in simulation of yaw angle control. (a) The graph of practical precession angle and practical precession angle of existing method. (b) The graph of practical precession angular velocity and practical precession angular velocity existing method.

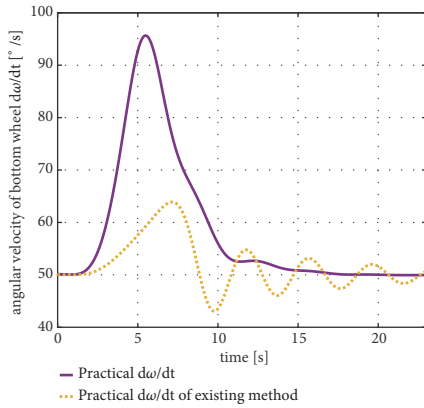


FIGURE 11: The angular velocity of bottom wheel in yaw angle control simulation.

6. Conclusion

This paper has presented a steering control method for the under-actuated unicycle robot which using precession effect of double-gyroscopes for lateral balance. The proposed method uses the coupling to control the roll angular velocity for steering. The steering control method is proposed through analyzing the dynamic model of the unicycle robot and the fast responsive control strategy is designed with a constant bottom wheel speed. The simulation results demonstrated that the control strategy is effective for steering control. Compared with the existing steering control method, the method mentioned in this paper responds faster to steering commands and tracks the set yaw angle more accurately.

Future works focus on the construction of the experimental platform and the improvement of the performance of the steering control method. More comparative experiments with the existing methods will also be conducted. Meanwhile, the

proposed control method will be applied to the autonomous navigation of multiunicycle robots.

Appendix

$$\begin{aligned}
 m_{11} &= s^2 \delta \ell_1 + c^2 \delta \ell_8 + s^2 \delta c^2 \theta \ell_9 + 2s \delta c \theta s \delta \ell_2 \\
 &\quad + c^2 \delta c^2 \theta \ell_7 + c^2 \delta s^2 \theta \ell_8 + s^2 \theta \ell_9 - 4s \delta c \theta c \delta \ell_4 \\
 &\quad + 2(c \delta c^2 \theta c^2 \alpha + s^2 \delta s^2 \alpha + c^2 \delta c^2 \theta) I_{1x} \\
 &\quad + 2c^2 \delta s^2 \theta s^2 \alpha I_{1z} + 2s^2 \delta c^2 \alpha I_{1z}; \\
 m_{12} &= m_{21} = \theta c \delta \ell_2 - c \delta c \theta s \theta \ell_3 + 2s \theta s \delta \ell_4 \\
 &\quad + 2c \delta s \theta c \theta c^2 \alpha I_{1x} + 2s \theta c \theta c \delta s^2 \alpha I_{1z}; \\
 m_{13} &= m_{31} = -s \delta \ell_{10} - c \theta s \delta \ell_2 + 2c \theta c \delta \ell_4 \\
 &\quad - 2s \delta s^2 \alpha I_{1x} - 2s \delta c^2 \alpha I_{1z}; \\
 m_{14} &= m_{41} = -s \delta \ell_1 - s \delta c \theta \ell_2 - 2s^2 \alpha I_{1x} - 2c^2 \alpha I_{1z}; \\
 m_{16} &= m_{61} = 2c \delta s \theta s \alpha I_{1z}; \\
 m_{22} &= \ell_5 + c^2 \theta \ell_6 + 2c \theta \ell_2 + s^2 \theta \ell_7 + 2(c^2 \theta c^2 \alpha + s^2 \theta) \\
 &\quad \cdot I_{1x} + 2c^2 \theta s^2 \alpha I_{1z}; \\
 m_{23} &= m_{32} = -2s \theta \ell_4 - 2c \delta s \theta c \theta I_{1x}; \\
 m_{26} &= m_{62} = 2c \theta s \alpha I_{1z}; \\
 m_{33} &= \ell_{10} + 2s^2 \alpha I_{1x} + 2c^2 \alpha I_{1z}; \\
 m_{34} &= m_{43} = c \theta \ell_2 + \ell_{11} + 2s^2 \alpha I_{1x} + 2c^2 \alpha I_{1z}; \\
 m_{44} &= \ell_1 + 2s^2 \alpha I_{1x} + 2c^2 \alpha I_{1z};
 \end{aligned}$$

TABLE 4: The coefficients in dynamic equations.

Coefficients	Values
ℓ_1	$(M_w R_W^2 + I_{wz} + M_b R_W^2 + I_{bz} + 2R_W^2 (M_{p1} + M_1) + 2I_{p1x})$
ℓ_2	$M_b R_W L_b + 2R_W L_b (M_{p1} + M_1)$
ℓ_3	$I_{bx} - I_{by} - 2I_{p1x} + 2I_{p1z} - M_b L_b^2 - 2 \left(M_{p1} \left(\frac{L_1}{2} \right)^2 + M_1 L_1^2 \right) - 2L_b^2 (M_{p1} + M_1)$
ℓ_4	$L_{p1} \left(M_{p1} \frac{L_1}{2} + M_1 L_1 \right)$
ℓ_5	$M_w R_W^2 + I_{wy} + M_b R_W^2 + 2L_{p1}^2 (M_{p1} + M_1) + 2R_W^2 (M_{p1} + M_1)$
ℓ_6	$M_b L_b^2 + I_{by} + 2 \left(M_{p1} \left(\frac{L_1}{2} \right)^2 + M_1 L_1^2 \right) + 2L_b^2 (M_{p1} + M_1) + 2I_{p1x}$
ℓ_7	$I_{bx} + 2I_{p1z}$
ℓ_8	$(I_{wx} + 2L_{p1}^2 (M_{p1} + M_1))$
ℓ_9	$\left(M_b L_b^2 + 2 \left(M_{p1} \left(\frac{L_1}{2} \right)^2 + M_1 L_1^2 \right) + 2L_b^2 (M_{p1} + M_1) \right)$
ℓ_{10}	$\left(M_b L_b^2 + I_{bz} + 2L_b^2 (M_{p1} + M_1) + 2I_{p1x} + 2 \left(M_{p1} \left(\frac{L_1}{2} \right)^2 + M_1 L_1^2 \right) \right)$
ℓ_{11}	$I_{bz} + 2I_{p1x}$

$$\begin{aligned}
 m_{55} &= I_{1x} + I_{p1z}; & + 4c^2 \delta s^2 \theta s \alpha \alpha I_{1z} - 4s^2 \delta s \alpha \alpha I_{1z} + \theta^2 (s \theta s \delta \ell_2 \\
 m_{66} &= 2I_{1x}; & - 2s \theta c \delta \ell_4) + \theta \dot{\alpha} (-4s \delta s \alpha \alpha I_{1x} + 4s \delta s \alpha \alpha I_{1z}) \\
 n_1 &= \dot{\omega} \delta (-c \delta \ell_1 - c \delta c \theta \ell_2 + 2c \delta c \theta \ell_2) + \dot{\omega} \dot{\theta} (s \delta s \theta \ell_2) & - 2\dot{\beta} \delta s \delta s \theta s \alpha I_{1z} + 2\dot{\beta} \dot{\theta} c \delta c \theta s \alpha I_{1z} \\
 &+ \dot{\omega} \dot{\alpha} (-4s \alpha \alpha I_{1x} + 4s \alpha \alpha I_{1z}) + \delta^2 (-s \theta s \delta \ell_2 & + 2\dot{\beta} \dot{\alpha} c \delta s \theta c \alpha I_{1z}; \\
 &+ s \delta c \theta s \theta \ell_3 + 2s \theta c \delta \ell_4 - 2s \delta s \theta c \theta c^2 \alpha I_{1x} & \\
 &- 2s \theta c \theta s \delta s^2 \alpha I_{1z}) + \dot{\delta} \dot{\theta} (c \theta c \delta \ell_2 + c \delta s \theta s \theta \ell_3 & \\
 &- c \delta c \theta c \theta \ell_3 + 2c \theta s \delta \ell_4 + 2c \delta c \theta c \theta c^2 \alpha I_{1x} & \\
 &- 2c \delta s \theta s \theta c^2 \alpha I_{1x} + 2c \theta c \theta c \delta s^2 \alpha I_{1z} & \\
 &- 2s \theta s \theta c \delta s^2 \alpha I_{1z} - c \delta \ell_{10} - c \theta c \delta \ell_2 - 2c \delta s^2 \alpha I_{1x} & \\
 &- 2c \theta s \delta \ell_4 - 2c \delta c^2 \alpha I_{1z}) + \dot{\delta} \dot{\alpha} (-4c \delta s \theta c \theta s \alpha \alpha I_{1x} & \\
 &+ 4s \theta c \theta c \delta s \alpha \alpha I_{1z}) + \dot{\phi} \dot{\delta} (2s \delta c \delta \ell_1 - 2s \delta c \delta \ell_8 & \\
 &+ 2s \delta c \delta c^2 \theta \ell_9 + 4s \delta c \theta c \delta \ell_2 - 2s \delta c \delta c^2 \theta \ell_7 & \\
 &- 2s \delta c \delta s^2 \theta \ell_8 - 4c \delta c \theta c \delta \ell_4 + 4s \delta c \theta s \delta \ell_4 & \\
 &+ 2(-s \delta c^2 \theta c^2 \alpha + 2s \delta c \delta s^2 \alpha - 2s \delta c \delta c^2 \theta) I_{1x} & \\
 &- 4s \delta c \delta s^2 \theta s^2 \alpha I_{1z} + 4s \delta c \delta c^2 \alpha I_{1z}) & \\
 &+ \dot{\phi} \dot{\theta} (-2s^2 \delta s \theta c \theta \ell_9 - 2s \delta s \theta s \delta \ell_2 - 2s \theta c \theta c^2 \delta \ell_7 & \\
 &+ 2s \theta c \theta c^2 \delta \ell_8 + 2s \theta c \theta \ell_9 + 4s \delta s \theta c \delta \ell_4 & \\
 &+ 2(-2c \delta s \theta c \theta c^2 \alpha - 2c^2 \delta s \theta c \theta) I_{1x} & \\
 &+ 4c^2 \delta s \theta c \theta s^2 \alpha I_{1z}) & \\
 &+ \dot{\phi} \dot{\alpha} (2(-2c \delta c^2 \theta s \alpha \alpha + 2s^2 \delta s \alpha \alpha) I_{1x} & \\
 &+ 4c^2 \theta s \alpha \alpha I_{1z}) & \\
 &- 2\dot{\beta} \dot{\theta} s \theta s \alpha I_{1z} + 2\dot{\beta} \dot{\alpha} c \theta c \alpha I_{1z} - \frac{1}{2} \dot{\phi}^2 (2s \delta c \delta \ell_1
 \end{aligned}$$

$$\begin{aligned}
& -2s\delta c\delta\ell_8 + 2s\delta c\delta c^2\theta\ell_9 + 4s\delta c\delta c\theta\ell_2 \\
& -2s\delta c\delta s^2\theta\ell_8 - 4c\delta c\theta c\delta\ell_4 + 4s\delta c\theta s\delta\ell_4 \\
& + 2(-s\delta c^2\theta c^2\alpha + 2s\delta c\delta s^2\alpha - 2s\delta c\delta c^2\theta)I_{1x} \\
& - 4s\delta c\delta s^2\theta s^2\alpha I_{1z} + 4s\delta c\delta c^2\alpha I_{1z}) \\
& + 2\dot{\phi}\dot{\beta}s\delta s\theta\alpha I_{1z} - M_w g R_W s\delta + M_b g(-s\delta c\theta L_b \\
& - R_W s\delta) + 2M_{p1}g(-s\delta c\theta L - R_W s\delta) \\
& + 2M_1g(-s\delta c\theta L - R_W s\delta); \\
n_3 = & \dot{\phi}\dot{\delta}(-c\delta\ell_{10} - c\theta c\delta\ell_2 - 2c\theta s\delta\ell_4 - 2c\delta s^2\alpha I_{1x} \\
& - 2c\delta c^2\alpha I_{1z} - c\theta c\delta\ell_2 - c\delta s\theta s\theta\ell_3 + c\delta c\theta c\theta\ell_3 \\
& - 2c\theta s\delta\ell_4 - 2c\delta c\theta c\theta c^2\alpha I_{1x} + 2c\delta s\theta s\theta c^2\alpha I_{1x} \\
& - 2c\theta c\theta c\delta s^2\alpha I_{1z} + 2s\theta s\theta c\delta s^2\alpha I_{1z}) \\
& + \dot{\phi}\dot{\theta}(+s\theta s\delta\ell_2 - 2s\theta c\delta\ell_4 - s\theta s\delta\ell_2 + 2s\theta c\delta\ell_4) \\
& + \dot{\phi}\dot{\alpha}(-4s\delta s\alpha c\alpha I_{1x} + 4s\delta s\alpha c\alpha I_{1z}) \\
& + \dot{\theta}\dot{\alpha}(4s\alpha c\alpha I_{1x} - 4s\alpha c\alpha I_{1z}) + \dot{\omega}\dot{\theta}(-s\theta\ell_2 + s\theta\ell_2) \\
& + \dot{\omega}\dot{\alpha}(4s\alpha c\alpha I_{1x} - 4s\alpha c\alpha I_{1z}) + \delta\dot{\theta}(-2c\theta\ell_4 \\
& - 2c\delta c\theta c\theta I_{1x} + 2c\delta s\theta s\theta I_{1x} + 2c\theta\ell_4 + 2c\delta c\theta c\theta I_{1x} \\
& - 2c\delta s\theta s\theta I_{1x}) + \delta^2(2s\delta s\theta c\theta I_{1x} + c\theta s\theta\ell_6 + s\theta\ell_2 \\
& - c\theta s\theta\ell_7 - (-2c\theta s\theta c^2\alpha + 2c\theta s\theta)I_{1x} \\
& + 2c\theta s\theta s^2\alpha I_{1z}) - \frac{1}{2}\dot{\phi}^2(-2c\theta s\theta s^2\delta\ell_9 - 2s\delta s\theta s\delta\ell_2 \\
& - 2c^2\delta c\theta s\theta\ell_7 + 2c^2\delta c\theta s\theta\ell_8 + 2c\theta s\theta\ell_9 \\
& + 4s\delta s\theta c\delta\ell_4 + 2(-2c\theta s\theta c\delta c^2\alpha - 2c\theta s\theta c^2\delta)I_{1x} \\
& + 4c\theta s\theta c^2\delta s^2\alpha I_{1z}) + 2\delta\dot{\beta}s\theta s\alpha I_{1z} \\
& - 2\dot{\phi}\dot{\beta}c\delta c\theta s\alpha I_{1z} + M_b g(-c\delta s\theta L_b) \\
& + 2M_{p1}g(-c\delta s\theta L) + 2M_1g(-c\delta s\theta L); \\
n_4 = & \dot{\omega}\dot{\alpha}(4s\alpha c\alpha I_{1x} - 4s\alpha c\alpha I_{1z}) + \dot{\phi}\dot{\delta}(-c\delta\ell_1 \\
& - c\delta c\theta\ell_2) + \dot{\phi}\dot{\theta}(s\delta s\theta\ell_2) + \dot{\phi}\dot{\alpha}(-4s\alpha c\alpha I_{1x} \\
& + 4s\alpha c\alpha I_{1z}) + \dot{\theta}^2(-s\theta\ell_2) + \dot{\theta}\dot{\alpha}(4s\alpha c\alpha I_{1x} \\
& - 4s\alpha c\alpha I_{1z}); \\
n_5 = & -\dot{\phi}\dot{\delta}(-4c\delta s\theta c\theta s\alpha c\alpha I_{1x} + 4s\theta c\theta c\delta s\alpha c\alpha I_{1z}) \\
& - \frac{1}{2}\dot{\delta}^2(4c^2\theta s\alpha c\alpha I_{1z}) - \frac{1}{2} \\
& \cdot \dot{\phi}^2(2(-2s\alpha c\alpha c\delta c^2\theta + 2s\alpha c\alpha s^2\delta)I_{1x} \\
& + 4s\alpha c\alpha c^2\delta s^2\theta I_{1z} - 4s\alpha c\alpha s^2\delta I_{1z}) \\
& - \dot{\phi}\dot{\theta}(-4s\alpha c\alpha s\delta I_{1x} + 4s\alpha c\alpha s\delta I_{1z}) - \frac{1}{2} \\
& \cdot \dot{\theta}^2(4s\alpha c\alpha I_{1x} - 4s\alpha c\alpha I_{1z}) - \theta\dot{\omega}(4s\alpha c\alpha I_{1x} \\
& - 4s\alpha c\alpha I_{1z}) - 2\delta\dot{\beta}c\theta c\alpha I_{1z} - 2\dot{\phi}\dot{\beta}c\delta s\theta c\alpha I_{1z}; \\
n_6 = & -2\delta\dot{\theta}s\theta s\alpha I_{1z} + 2\delta\dot{\alpha}c\theta c\alpha I_{1z} - 2\dot{\phi}\dot{\delta}s\delta s\theta s\alpha I_{1z} \\
& + 2\dot{\phi}\dot{\theta}c\delta c\theta s\alpha I_{1z} + 2\dot{\phi}\dot{\alpha}c\delta s\theta c\alpha I_{1z};
\end{aligned} \tag{A.2}$$

The coefficients ℓ_1, \dots and ℓ_{12} in the above equations are defined in Table 4.

Data Availability

All the data and codes of the simulations are available online at <https://github.com/ZhangYang157/01-Codes-and-Data-for-Steering-Control-Method-for-an-Under-actuated-Unicycle-Robot-Based-on-Dynamic-.git>.

Conflicts of Interest

The authors declare that they have no conflicts of interest.

Acknowledgments

This work was supported in part by National Key R&D Program of China under Grant 2017YFF0108000, in part by the National Natural Science Foundation of China under Grant 61473102, in part by the Major Research Plan of the National Natural Science Foundation of China under Grant 91648201, and in part by the Joint Research Fund (UI713201) between the National Natural Science Foundation of China (NSFC) and Shen Zhen.

Supplementary Materials

The data and codes of the simulation for our study are offered by using the zipped file “01-Codes and Data for Steering Control Method for an Under-actuated Unicycle Robot Based on Dynamic Model.zip”. The file “read me.txt” in the zipped file describes each data and codes. The supplementary material file of simulation video is contained at the zipped file “02-supplementary material file for simulation video.zip”. The video is available online. The details can read the file “read me.txt” in the zipped file. (*Supplementary Materials*)

References

- [1] A. Schoonwinkel, *Design and test of a computer-stabilized unicycle [Ph.D.dissertation]*, Stanford University, 1987.

- [2] D. W. Vos and A. H. von Flotow, "Dynamics and nonlinear adaptive control of an autonomous unicycle: Theory and experiment," in *Proceedings of the 29th IEEE Conference on Decision and Control Part 6 (of 6)*, pp. 182–187, December 1990.
- [3] D. W. Vos, *Nonlinear control of an autonomous unicycle robot: practical issues [Ph.D. thesis]*, MIT, 1991.
- [4] Z. Sheng and K. Yamafuji, "Study on the Stability and Motion Control of a Unicycle (Part I: Dynamics of a Human Riding a Unicycle and Its Modeling by Link Mechanisms)," *JSME international journal. Ser. C, Dynamics, control, robotics, design and manufacturing*, vol. 38, no. 2, pp. 249–259, 1995.
- [5] Z. Sheng and K. Yamafuji, "Postural stability of a human riding a unicycle and its emulation by a robot," *IEEE Transactions on Robotics and Automation*, vol. 13, no. 5, pp. 709–720, 1997.
- [6] Y. Naveh, P. Z. Bar-Yoseph, and Y. Halevi, "Nonlinear modeling and control of a unicycle," *Dynamics and Control. An International Journal*, vol. 9, no. 4, pp. 279–296, 1999.
- [7] H. Jin, J. Hwang, and J. Lee, "A Balancing Control Strategy for a One-Wheel Pendulum Robot Based on Dynamic Model Decomposition: Simulations and Experiments," *IEEE/ASME Transactions on Mechatronics*, vol. 16, no. 4, pp. 763–768, 2011.
- [8] J. Zhao, M. Xiong, and H. Jin, "Dynamics and a convenient control design approach for a unicycle robot," in *Proceedings of the 2010 IEEE International Conference on Information and Automation, ICIA 2010*, pp. 706–711, China, June 2010.
- [9] MURATA Company, <http://www.murata.com>.
- [10] S. I. Han and J. M. Lee, "Balancing and velocity control of a unicycle robot based on the dynamic model," *IEEE Transactions on Industrial Electronics*, vol. 62, no. 1, pp. 405–413, 2015.
- [11] J. Lee, S. Han, and J. Lee, "Decoupled dynamic control for pitch and roll axes of the unicycle robot," *IEEE Transactions on Industrial Electronics*, vol. 60, no. 9, pp. 3814–3822, 2013.
- [12] M.-T. Ho, Y. Rizal, and Y.-L. Chen, "Balance control of a unicycle robot," in *Proceedings of the 2014 IEEE 23rd International Symposium on Industrial Electronics, ISIE 2014*, pp. 1186–1191, Turkey, June 2014.
- [13] D. Van Bui and Y. Fujimoto, "3D modeling and nonlinear control using algorithmic differentiation for mono-wheel robot," in *Proceedings of the 14th IEEE International Workshop on Advanced Motion Control, AMC 2016*, pp. 558–564, New Zealand, April 2016.
- [14] H. B. Brown Jr. and Y. Xu, "Single-wheel, gyroscopically stabilized robot," in *Proceedings of the 1996 13th IEEE International Conference on Robotics and Automation. Part 1 (of 4)*, pp. 3658–3663, April 1996.
- [15] T. Saleh, Y. H. Hann, Z. Zhen, A. Al Mamun, and V. Prahlad, "Design of a gyroscopically stabilized single-wheeled robot," in *Proceedings of the 2004 IEEE Conference on Robotics, Automation and Mechatronics*, pp. 904–908, Singapore, December 2004.
- [16] Y. Ou and Y. Xu, "Gyroscopically stabilized robot: Balance and tracking," *International Journal of Advanced Robotic Systems*, vol. 1, no. 1, pp. 23–32, 2004.
- [17] Z. Zhu, M. P. Naing, and A. Al-Mamun, "A 3-D simulator using ADAMS for design of an autonomous gyroscopically stabilized single wheel robot," in *Proceedings of the 2009 IEEE International Conference on Systems, Man and Cybernetics, SMC 2009*, pp. 4455–4460, USA, October 2009.
- [18] S.-D. Lee and S. Jung, "Balancing control of a single-wheel robot considering power-efficiency and gyroscopic instability suppression," in *Proceedings of the 15th International Conference on Control, Automation and Systems, ICCAS 2015*, pp. 570–573, Republic of Korea, October 2015.
- [19] M. S. Ha and S. Jung, "Neural network control for balancing performance of a single-wheel transportation vehicle," in *Proceedings of the International Joint Conference on Neural Networks, IJCNN 2015*, Ireland, July 2015.
- [20] M. Dao and K. Liu, "Gain-Scheduled Stabilization Control of a Unicycle Robot," *JSME International Journal Series C Mechanical Systems, Machine Elements and Manufacturing*, vol. 48, no. 4, pp. 649–656, 2005.
- [21] H. Jin, T. Wang, F. Yu, Y. Zhu, J. Zhao, and J. Lee, "Unicycle Robot Stabilized by the Effect of Gyroscopic Precession and Its Control Realization Based on Centrifugal Force Compensation," *IEEE/ASME Transactions on Mechatronics*, vol. 21, no. 6, pp. 2737–2745, 2016.
- [22] S. Majima, T. Kasai, and T. Kadohara, "A design of a control method for changing yaw direction of an underactuated unicycle robot," in *Proceedings of the 2006 IEEE Region 10 Conference, TENCON 2006*, China, November 2006.
- [23] Y. Isomi and S. Majima, "Tracking control method for an underactuated unicycle robot using an equilibrium state," in *Proceedings of the 2009 IEEE International Conference on Control and Automation, ICCA 2009*, pp. 1844–1849, New Zealand, December 2009.
- [24] D. Gong and X. Li, "Dynamics modeling and controller design for a self-balancing unicycle robot," in *Proceedings of the 32nd Chinese Control Conference, CCC 2013*, pp. 3205–3209, China, July 2013.
- [25] X.-Q. Zhu, X.-G. Ruan, R.-Y. Sun, X. Wang, and R.-Y. Wei, "Single-wheel robots with yaw ability," *Beijing Gongye Daxue Xuebao/Journal of Beijing University of Technology*, vol. 40, no. 7, pp. 1099–1104, 2014.

Research Article

Extended Poroelasticity: An Analytical Solution and Its Application to p-Wave Propagation in Cervical Tissues

Roberto Palma ¹ and Antonio M. Callejas²

¹Department of Mechanical Engineering and Construction, Universitat Jaume I, Castellón de la Plana, Spain

²Structural Mechanics and Hydraulic Engineering, University of Granada, Granada, Spain

Correspondence should be addressed to Roberto Palma; rpalma@uji.es

Received 14 September 2018; Accepted 17 October 2018; Published 29 October 2018

Guest Editor: Akhtar A. Khan

Copyright © 2018 Roberto Palma and Antonio M. Callejas. This is an open access article distributed under the Creative Commons Attribution License, which permits unrestricted use, distribution, and reproduction in any medium, provided the original work is properly cited.

This work presents a semianalytical solution based on Laplace transform to study the behaviour of poroelastic materials in the context of the Extended Nonequilibrium Thermodynamics. In this framework, the fluid phase incorporates a relaxation time and, consequently, a frequency-dependence appears. This rheological behaviour could explain the frequency-dependence experimentally observed in biological tissues, which has traditionally attributed to the solid phase of tissues. In particular, the analytical solution is applied to two cases, heaviside and sinusoidal inputs, of a semi-infinite domain, which is filled with a material such as the human cervix. From the results, it is observed that the frequency-dependence of the fluid phase could be relevant to high relaxation times while for null relaxation times the classical poroelastic theory is recovered. Finally, the present analytical solution could be used to validate future computational codes and experimental settings.

1. Introduction

Nowadays, understanding mechanical behaviour of the human cervix is a challenge for theoretical, computational, and experimental communities since it could be used to develop functional anticipation diagnostic tools, which will be applied to reduce the main cause of infant mortality: preterm birth, according to [1]. Notice that the understanding of cervical tissues is considered one of the most pressing problems in obstetrics [2].

According to [3], the human cervix is composed of a distribution of cells embedded in an extracellular matrix of fibrillar collagen, which can be considered as the solid phase and represent 20-30% of the tissue and water with dissolved salts (fluid phase). The latter phase is the responsible for the cervix incompressibility [4].

There exist many models to study dynamic responses of tissues in specialised literature. However, most of them are contradictory since they are based on phenomenological equations, which lack robustness. In particular, measured values in cervix tissues differ several orders of magnitude for

medium and high frequencies [5]. In this connection, there are several viscoelastic approaches to properly characterise the human cervix: a linear viscoelastic model was proposed in [6], an in-homogenous model in [7], and several approaches by the Rus' group; see [8–10].

Despite the fact that the cervix is composed of solid and fluid, all the previous works are only focused on the solid contribution. On the contrary, the Extended Nonequilibrium Thermodynamics (ENET) [11] incorporates a viscous-like term to the fluid phase, which could explain the frequency-dependence of the cervix. For instance, R. Palma et al. have developed analytical and numerical solutions to study the *second sound* in thermoelasticity (see [12, 13]), which can be considered as a viscothermal effect. Also, ENET is applied in [14] to study the Debye relaxation: a viscoelectric effect.

On this ground, this paper presents a poroelastic formulation based on the ENET to study the frequency-dependence of cervix tissues due to the fluid phase, and it could be considered the main novelty of the present work. Then, the formulation is expressed in one-dimension in order to obtain a dynamical solution by a semianalytical approach based

on Laplace transform. Finally, two numerical examples are developed to highlight the importance of the fluid-relaxation in the response of the cervix.

The present work assumes small strains and linear elasticity for the solid phase. For the fluid, constant properties are considered and the effects of temperature are neglected.

2. Three-Dimensional Governing Equations

Consider an arbitrary domain Ω and boundary Γ for which the governing equations are composed of equilibrium and constitutive equations and of the boundary conditions.

With regard to the equilibrium equation and since the domain contains solid and fluid constituents, two equations must be enforced: linear momentum and mass conservation. Mathematically, they are expressed in local form as follows:

$$\begin{aligned} \rho \ddot{\mathbf{u}} &= \nabla \cdot \boldsymbol{\sigma}^\top + \mathbf{f}, \\ c_{pu} \dot{\epsilon} + c_{pp} \dot{p} &= -\nabla \cdot \mathbf{d} + D, \end{aligned} \quad (1)$$

where ρ , $\ddot{\mathbf{u}}$, and \mathbf{f} denote mass density (including solid and fluid), acceleration, and body forces, respectively; $\boldsymbol{\sigma} = \boldsymbol{\sigma}^\top$ is the Cauchy stress tensor; \mathbf{d} and D denote the rate of change in fluid mass through the boundary and the production of fluid from an external source, respectively. Finally, ϵ , p , c_{pu} , and c_{pp} denote volumetric strain, fluid pressure, and two constants closely related to the porosity and fluid bulk modulus, respectively.

Obviously, two constitutive equations, solid and fluid phases, are required to model poroelasticity; these equations read

$$\begin{aligned} \boldsymbol{\sigma} &= \mathbf{C} : \boldsymbol{\epsilon} - c_{up} p \mathbf{I}, \\ \tau \dot{\mathbf{d}} + \mathbf{d} &= -\mathbf{K} \cdot \nabla p. \end{aligned} \quad (2)$$

At this point, it is necessary to define all terms in (2):

- (i) \mathbf{C} denotes the elastic fourth order tensor, which is composed of matrix \mathbf{C}_{mt} and of fibre \mathbf{C}_{fb} (both solid phases) by the rule of mixture:

$$\begin{aligned} \mathbf{C} &= \xi \mathbf{C}_{mt} + (1 - \xi) \mathbf{C}_{fb}, \\ \text{with : } \begin{cases} \mathbf{C}_{mt} = 2\mu_{mt} \mathbf{I} + \lambda_{mt} \mathbf{I} \otimes \mathbf{I}, \\ \mathbf{C}_{fb} = 2\mu_{fb} \mathbf{I} + \lambda_{fb} \mathbf{I} \otimes \mathbf{I}, \end{cases} \end{aligned} \quad (3)$$

where $\xi = 0.88$ is the percentage of matrix, \mathbf{I} denotes the fourth-order identity tensor, and μ , λ are the Lamé parameters for matrix and fibre constituents, respectively.

- (ii) $\boldsymbol{\epsilon} = (1/2)(\nabla \otimes \mathbf{u} + \mathbf{u} \otimes \nabla) = \nabla^s \mathbf{u}$ is the small strain second order tensor and ∇^s denotes the symmetric part of the gradient of displacements.
- (iii) $\mathbf{K} = (1/\nu_f) \boldsymbol{\kappa}$ denotes solid permeability and it is closely related to the fluid viscosity ν_f .

- (iv) τ is the relaxation times, which is introduced by the assumption of a mixed entropy; see [15]. This empirical parameter is responsible for viscosity in the fluid phase and, consequently, for the frequency-dependence. Notice that the classical poroelasticity theory is recovered by imposing $\tau = 0$.

Finally, the Dirichlet and Neumann boundary conditions for the extended poroelastic problem read

$$\begin{aligned} \mathbf{u} &= \bar{\mathbf{u}}, \\ \boldsymbol{\sigma}^\top \cdot \mathbf{n} &= \mathbf{t}, \\ p &= \bar{p}, \\ \mathbf{d} \cdot \mathbf{n} &= d_c, \end{aligned} \quad (4)$$

where $\bar{\mathbf{u}}$ and \bar{p} denote prescribed displacements and pressure, respectively, and \mathbf{t} and d_c prescribed traction and fluid flux on the boundary with outward normal \mathbf{n} .

3. Analytical Solution

This section presents a one-dimensional, semianalytical, and dynamical solution for a half-space filled with a poroelastic material. For this purpose, the three-dimension extended poroelastic equations reported in Section 2 are rewritten along the x -axis in order to apply the state space technique; see [16]. The three-dimensional Euclidean coordinates become

$$\mathbf{x} \equiv (x, 0, 0, t) \implies \begin{cases} \mathbf{u}(\mathbf{x}, t) \equiv u(x, t), \\ p = p(x, t), \end{cases} \quad (5)$$

and the components of strain tensor are reduced to

$$\{\boldsymbol{\epsilon}\} \implies \begin{cases} \epsilon_1 = \frac{\partial u(x, t)}{\partial x} = \epsilon, \\ \epsilon_2 = \epsilon_3 = \epsilon_4 = \epsilon_5 = \epsilon_6 = 0, \end{cases} \quad (6)$$

and, finally, the constitutive equation of (2) (upper) becomes

$$\begin{aligned} \sigma_1 &= C_{11} \epsilon_1 - c_{up} p \longrightarrow \sigma = C \epsilon - c_{up} p, \\ \sigma_2 &= \sigma_3 = \sigma_4 = \sigma_5 = \sigma_6 = 0. \end{aligned} \quad (7)$$

In absence of body forces $\mathbf{f} = \mathbf{0}$ and mass sources $D = 0$, the equilibrium equations of (1) are reduced to

$$\begin{aligned} \frac{\partial \sigma}{\partial x} &= \rho \ddot{u}_x \implies \\ \frac{\partial^2 \sigma}{\partial x^2} &= \rho \frac{\partial \ddot{u}_x}{\partial x} = \rho \ddot{\epsilon}, \\ K \frac{\partial^2 p}{\partial x^2} &= \left(\frac{\partial}{\partial t} + \tau \frac{\partial^2}{\partial t^2} \right) (c_{pu} \dot{\epsilon} + c_{pp} \dot{p}), \end{aligned} \quad (8)$$

Now, equations (6), (7), and (8) are rewritten in the Laplace domain by applying the transformation $\bar{f}(s) = \int_0^\infty f(t)e^{-st} dt$:

$$\begin{aligned}\bar{\sigma} &= C\bar{\epsilon} - c_{up}\bar{p}, \\ \frac{\partial^2 \bar{\sigma}}{\partial x^2} &= s^2 \rho \bar{\epsilon}, \\ K \frac{\partial^2 \bar{p}}{\partial x^2} &= (s + \tau s^2)(c_{pu}\bar{\epsilon} + c_{pp}\bar{p}).\end{aligned}\quad (9)$$

These equations can be expressed in compact form by introducing the coefficients L_1, L_2, M_1 , and M_2 :

$$\begin{aligned}L_1 &= \left(\frac{c_{pu}c_{up} + Cc_{pp}}{KC} \right) (s + \tau s^2), \\ L_2 &= \left(\frac{c_{pu}}{KC} \right) (s + \tau s^2), \\ M_1 &= \frac{c_{up}\rho s^2}{C}, \\ M_2 &= \frac{s^2 \rho}{C},\end{aligned}\quad (10)$$

to give

$$\begin{aligned}\frac{\partial^2 \bar{p}}{\partial x^2} &= L_1 \bar{p} + L_2 \bar{\sigma}, \\ \frac{\partial^2 \bar{\sigma}}{\partial x^2} &= M_1 \bar{p} + M_2 \bar{\sigma},\end{aligned}\quad (11)$$

and the closed solution of this system of two couple equations can be expressed as follows:

$$\begin{Bmatrix} \bar{p}(x, s) \\ \bar{\sigma}(x, s) \end{Bmatrix} = \exp\left(\sqrt{\begin{bmatrix} L_1 & L_2 \\ M_1 & M_2 \end{bmatrix} x}\right) \begin{Bmatrix} \bar{p}(0, s) = \bar{p}_0 \\ \bar{\sigma}(0, s) = \bar{\sigma}_0 \end{Bmatrix}. \quad (12)$$

The solution of this system is obtained by applying the Cayley-Hamilton theorem [16] to give

$$\begin{Bmatrix} \bar{p}(x, s) \\ \bar{\sigma}(x, s) \end{Bmatrix} = \begin{bmatrix} L_{11} & L_{12} \\ L_{21} & L_{22} \end{bmatrix} \begin{Bmatrix} \bar{p}_0 \\ \bar{\sigma}_0 \end{Bmatrix}, \quad (13)$$

where \bar{p}_0 and $\bar{\sigma}_0$ are the boundary conditions and the coefficient and are explicitly given by

$$\begin{aligned}L_{11} &= \frac{e^{-\sqrt{\eta_2}x}(\eta_1 - L_1) - e^{-\sqrt{\eta_1}x}(\eta_2 - L_1)}{\eta_1 - \eta_2}, \\ L_{22} &= \frac{e^{-\sqrt{\eta_1}x}(\eta_2 - M_2) - e^{-\sqrt{\eta_2}x}(\eta_1 - M_2)}{\eta_2 - \eta_1}, \\ L_{12} &= \frac{L_2(e^{-\sqrt{\eta_1}x} - e^{-\sqrt{\eta_2}x})}{\eta_1 - \eta_2}, \\ L_{21} &= \frac{M_1(e^{-\sqrt{\eta_1}x} - e^{-\sqrt{\eta_2}x})}{\eta_1 - \eta_2},\end{aligned}\quad (14)$$

where η_1 and η_2 are the solutions of the following characteristic equations:

$$\begin{aligned}\eta_1 + \eta_2 &= L_1 + M_2, \\ \eta_1 \eta_2 &= L_1 M_2 - L_2 M_1.\end{aligned}\quad (15)$$

Finally, the semianalytical solution is attained by imposing boundary conditions and by inverting the Laplace transform using Riemann-sum approximations, as in [12].

4. Results

This section presents two analytical solutions, called cases, in order to highlight the main features of the present formulation. For this purpose, the material properties are obtained from the literature (see Table 1), and they are real measured variables of the human cervix. In particular, Lamé parameters for fibre and matrix phases are obtained from [8, 9], bulk modulus of fluid from [17], solid permeability from [18], and fluid viscosity from [19]. Finally, the coefficient $c_{up} = 0.75$ obeys the composition of the cervix, namely, 80-70% of fluid phase; see [20].

4.1. Case I. For case I, the boundary conditions are assumed to be a heaviside unit step function $H(t)$:

$$\begin{aligned}\bar{p}_0 &= \frac{p_0}{s}, \\ \bar{\sigma}_0 &= 0.\end{aligned}\quad (16)$$

Introducing (16) in (12) and taking into account (14), the solutions for \bar{p} and $\bar{\sigma}$ in the Laplace domain read

$$\begin{aligned}\bar{p} &= \frac{p_0 \left[(\eta_1 - L_1) e^{-\sqrt{\eta_2}x} - (\eta_2 - L_1) e^{-\sqrt{\eta_1}x} \right]}{s(\eta_1 - \eta_2)}, \\ \bar{\sigma} &= \frac{p_0 M_1 (e^{-\sqrt{\eta_1}x} - e^{-\sqrt{\eta_2}x})}{s(\eta_1 - \eta_2)}.\end{aligned}\quad (17)$$

Furthermore, the mechanical displacement and the flux can be obtained taking into account

$$\begin{aligned}\bar{d} &= -K \frac{\partial \bar{p}}{\partial x}, \\ \frac{\partial^2 \bar{\sigma}}{\partial x^2} &= s^3 \rho \bar{u} \implies \\ \bar{u} &= \frac{1}{s^3 \rho} \frac{\partial^2 \bar{\sigma}}{\partial x^2},\end{aligned}\quad (18)$$

TABLE 1: Material properties of the human cervix.

Magnitude	Value	Units
ρ	1000	[kg/m ³]
ρ_f	1000	[kg/m ³]
c_{up}	0.75	[-]
ν_f	1.2×10^{-3}	[Pa·s]
μ_{fb}	6.45×10^7	[Pa]
λ_{fb}	1.47×10^8	[Pa]
μ_{mt}	7.47×10^3	[Pa]
λ_{mt}	1.7×10^9	[Pa]
B_f	2.2×10^9	[Pa]
κ	7.2×10^{-14}	[m ²]

to give

$$\begin{aligned} \bar{d} &= \frac{Kp_0 \left[(\eta_1 - L_1) \sqrt{\eta_2} e^{-\sqrt{\eta_2}x} - (\eta_2 - L_1) \sqrt{\eta_1} e^{-\sqrt{\eta_1}x} \right]}{s(\eta_1 - \eta_2)}, \quad (19) \\ \bar{u} &= \frac{p_0 M_1 (\eta_1 e^{-\sqrt{\eta_1}x} - \eta_2 e^{-\sqrt{\eta_2}x})}{\rho s^4 (\eta_1 - \eta_2)}. \end{aligned}$$

Consider a one-dimensional and semi-infinite domain, which is filled with a material as that of cervix. At $t = 0$, a fluid pressure of heaviside type is applied and, then, the evolution of all variables of (17) and (18) is numerically studied. In particular, Figure 1 shows the time evolution of p (left column), u (middle column), and σ (right column) for three different relaxation times: $\tau = 0.5, 0, 1, 0$ [s] (each one in a row). In addition, each figure contains three different curves at three time instants $t = 0.3, 0.5, 1$ [s].

For $\tau \neq 0$ [s] (extended poroelasticity) a hyperbolic behaviour is attained in the evolution of p and, consequently, in u . It is observed in the wave front, which is moving at each time instant. On the contrary, for the case $\tau = 0$ a parabolic behaviour is observed, absence of wave front, and the classical poroelastic theory is recovered. In this sense, the extended poroelasticity removes the paradox of infinite velocity, which lacks physical meaning: in nature, there are no infinity velocities.

Since the problem is coupled, the stresses for $\tau \neq 0$ [s] show a viscous-like behaviour that could explain the frequency-dependence experimentally observed in cervical tissues. On the contrary, for $\tau = 0$ [s], a linear behaviour is observed and, therefore, it is concluded that the classical poroelasticity can not be used to model the human cervix.

4.2. *Case II.* For case II, a sinusoidal function $p_0 \sin(\omega t)$ of frequency ω is prescribed:

$$\begin{aligned} \bar{p}_0 &= p_0 \frac{\omega}{s^2 + \omega^2}, \\ \bar{\sigma}_0 &= 0. \end{aligned} \quad (20)$$

Following a procedure similar to that of case I, the solutions for \bar{p} and $\bar{\sigma}$ in the Laplace domain are

$$\begin{aligned} \bar{p} &= \frac{p_0 \omega \left[(\eta_1 - L_1) e^{-\sqrt{\eta_2}x} - (\eta_2 - L_1) e^{-\sqrt{\eta_1}x} \right]}{(s^2 + \omega^2)(\eta_1 - \eta_2)}, \quad (21) \\ \bar{\sigma} &= \frac{p_0 M_1 \omega (e^{-\sqrt{\eta_1}x} - e^{-\sqrt{\eta_2}x})}{(s^2 + \omega^2)(\eta_1 - \eta_2)}, \end{aligned}$$

and the mechanical displacement and the flux are given by

$$\begin{aligned} \bar{d} &= \frac{Kp_0 \omega \left[(\eta_1 - L_1) \sqrt{\eta_2} e^{-\sqrt{\eta_2}x} - (\eta_2 - L_1) \sqrt{\eta_1} e^{-\sqrt{\eta_1}x} \right]}{(s^2 + \omega^2)(\eta_1 - \eta_2)}, \quad (22) \\ \bar{u} &= \frac{p_0 M_1 \omega (e^{-\sqrt{\eta_1}x} - e^{-\sqrt{\eta_2}x})}{\rho s^3 (s^2 + \omega^2)(\eta_1 - \eta_2)}. \end{aligned}$$

Consider the same semi-infinite domain as that in case I. Now, a fluid pressure of sinusoidal type is applied at $t = 0$ and all variables of (21) and (22) are shown in Figure 2. Again, the same conclusion as those in case I can be observed for this sinusoidal input. Nevertheless, the curves are smoother due to the nature of the sinusoidal signal. Therefore, these solutions are more amenable for future computational validations since it is not necessary to use regularisation schemes.

5. Conclusions

This work has presented a theoretical approach based on Nonequilibrium Thermodynamics to study the behaviour of poroelastic materials taking into account the frequency-dependence of the fluid phase. In this connection, the main novelty of the present work is the incorporation of relaxation times for the fluid phase to perform a material constitution applied to biological tissues. Then, the three-dimensional governing equations are reduced to one dimension in order to obtain a semianalytical and dynamical solution based on Laplace transform. In particular, the solution is applied to simulate a semi-infinite domain, which is filled with a material such as the human cervix, and it is observed that the frequency-dependence also could be due to the fluid phase.

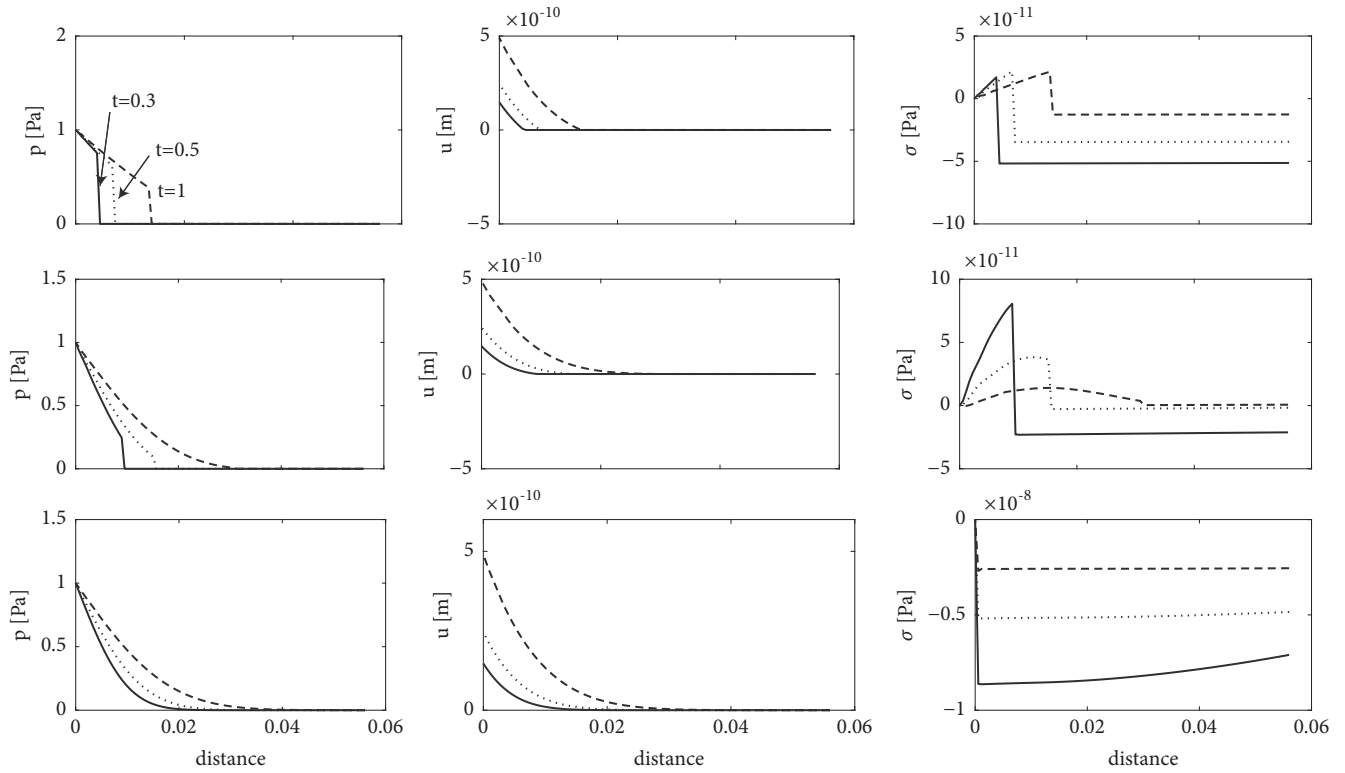


FIGURE 1: Case I. Fluid pressure (left column), mechanical displacement (middle), and mechanical stress (right) versus distance for three relaxation times: $\tau = 0.5$ (top row), $\tau = 0.1$ (middle) and $\tau = 0$ [s] (bottom). Each figure shows three different curves at three time instants: $t = 0.3, 0.5, 1$ [s].

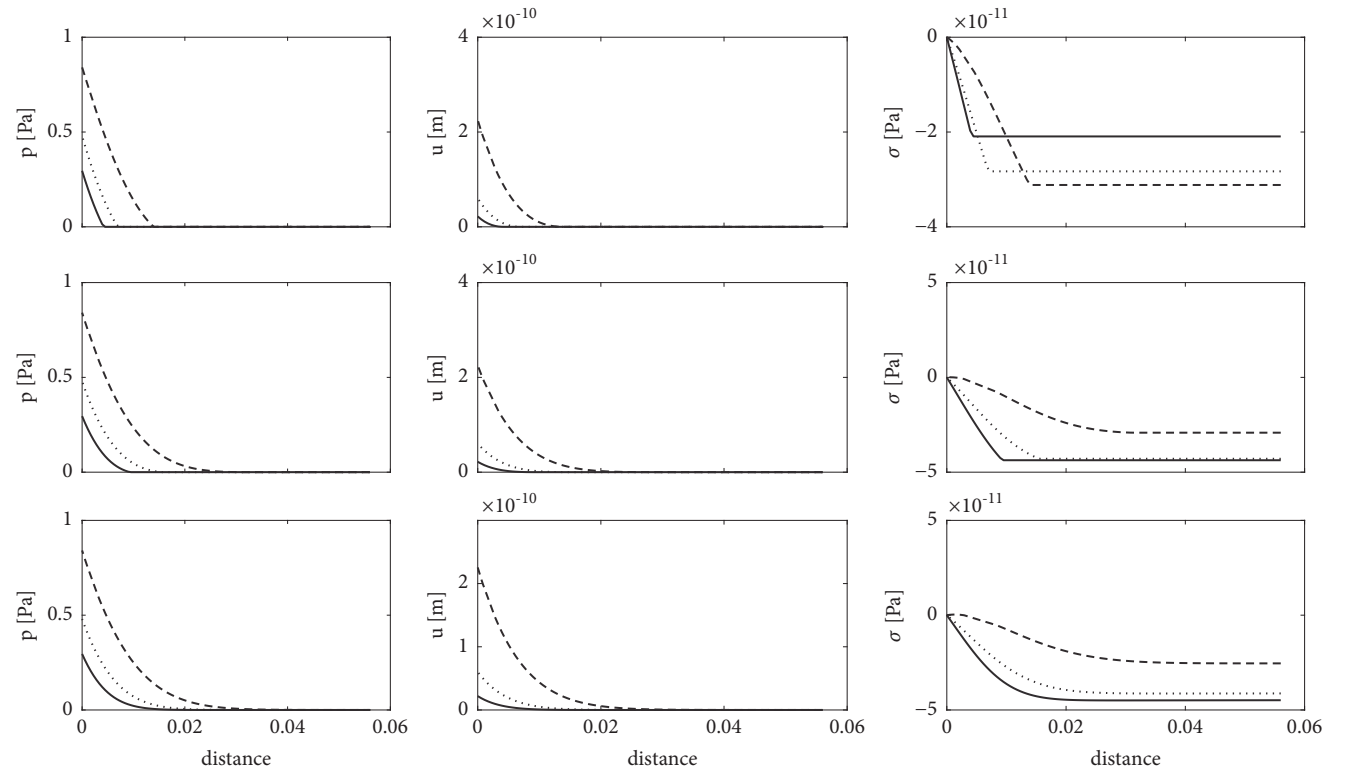


FIGURE 2: Case II. Fluid pressure (left column), mechanical displacement (middle), and mechanical stress (right) versus distance for three relaxation times: $\tau = 0.5$ (top row), $\tau = 0.1$ (middle), and $\tau = 0$ [s] (bottom). Each figure shows three different curves at three time instants: $t = 0.3, 0.5, 1$ [s].

Data Availability

The data used to support the findings of this study are available from the corresponding author upon request.

Conflicts of Interest

The authors declare that they have no conflicts of interest.

Acknowledgments

This research was supported by the Ministry of Education DPI2017-83859- R, DPI2014-51870- R, DPI2010-17065, and UNGR15-CE- 3664, Ministry of Health DTS15/00093, and PI16/00339, PI-0107-2017, PIN-0030-2017, and Junta de Andalucía P11-CTS- 8089 projects.

References

- [1] M. House and S. Socrate, "The cervix as a biomechanical structure," *Ultrasound in Obstetrics & Gynecology*, vol. 28, no. 6, pp. 745–749, 2006.
- [2] N. Uldbjerg, G. Ekman, A. Malmström, B. Sporrang, U. Ulmsten, and L. Wingerup, "Biochemical and morphological changes of human cervix after local application of prostaglandin e2 in pregnancy," *The Lancet*, vol. 31, pp. 267–268, 1981.
- [3] M. Winkler and W. Rath, "Changes in the cervical extracellular matrix during pregnancy and parturition," *Journal of Perinatal Medicine*, vol. 27, no. 1, pp. 45–60, 1999.
- [4] S. Weiss, T. Jaermann, P. Schmid et al., "Three-dimensional fiber architecture of the nonpregnant human uterus determined ex vivo using magnetic resonance diffusion tensor imaging," *Anatomical Record - Part A Discoveries in Molecular, Cellular, and Evolutionary Biology*, vol. 288, no. 1, pp. 84–90, 2006.
- [5] E. Turgay, S. Salcudean, and R. Rohling, "Identifying the mechanical properties of tissue by ultrasound strain imaging," *Ultrasound in Medicine & Biology*, vol. 32, no. 2, pp. 221–235, 2006.
- [6] J. M. Pereira, J. M. Mansour, and B. R. Davis, "Dynamic measurement of the viscoelastic properties of skin," *Journal of Biomechanics*, vol. 24, no. 2, pp. 157–162, 1991.
- [7] E. A. Barannik, A. Girnyk, V. Tovstiyak, A. I. Marusenko, S. Y. Emelianov, and A. P. Sarvazyan, "Doppler ultrasound detection of shear waves remotely induced in tissue phantoms and tissue in vitro," *Ultrasonics*, vol. 40, no. 1–8, pp. 849–852, 2002.
- [8] L. Peralta, G. Rus, N. Bochud, and F. S. Molina, "Assessing viscoelasticity of shear wave propagation in cervical tissue by multiscale computational simulation," *Journal of Biomechanics*, vol. 48, no. 9, pp. 1549–1556, 2015.
- [9] L. Peralta, G. Rus, N. Bochud, and F. S. Molina, "Mechanical assessment of cervical remodelling in pregnancy: Insight from a synthetic model," *Journal of Biomechanics*, vol. 48, no. 9, pp. 1557–1565, 2015.
- [10] A. Callejas, A. Gomez, J. Melchor et al., "Performance Study of a Torsional Wave Sensor and Cervical Tissue Characterization," *Sensors*, vol. 17, no. 9, p. 2078, 2017.
- [11] D. Jou, J. Casas-Vázquez, and G. Lebon, *Extended Irreversible Thermodynamics*, Springer-Verlag, Berlin, Heidelberg, Germany, 1996.
- [12] R. Palma, J. L. Pérez-Aparicio, and R. L. Taylor, "Non-linear finite element formulation applied to thermoelectric materials under hyperbolic heat conduction model," *Computer Methods Applied Mechanics and Engineering*, vol. 213–216, pp. 93–103, 2012.
- [13] R. Palma, E. Moliner, and J. L. Pérez-Aparicio, "Elasto-thermoelectric beam formulation for modeling thermoelectric devices," *Finite Elements in Analysis and Design*, vol. 129, pp. 32–41, 2017.
- [14] R. Palma, J. L. Perez-Aparicio, and R. L. Taylor, "Dissipative finite element formulation applied to piezoelectric materials with Debye memory," *IEEE/ASME Transactions on Mechatronics*, 2018.
- [15] G. Lebon, T. Desaive, and P. Dauby, "A unified extended thermodynamic description of diffusion, thermo-diffusion, suspensions, and porous media," *Transaction of the ASME*, vol. 73, no. 1, pp. 16–20, 2006.
- [16] H. M. Youssef and E. A. Al-Lehaibi, "State-space approach of two-temperature generalized thermoelasticity of one-dimensional problem," *International Journal of Solids and Structures*, vol. 44, no. 5, pp. 1550–1562, 2007.
- [17] J. B. Pendry and J. Li, "An acoustic metafluid: Realizing a broadband acoustic cloak," *New Journal of Physics*, vol. 10, 2008.
- [18] F. J. O'Brien, B. A. Harley, M. A. Waller, I. V. Yannas, L. J. Gibson, and P. J. Prendergast, "The effect of pore size on permeability and cell attachment in collagen scaffolds for tissue engineering," *Technology and Health Care*, vol. 15, no. 1, pp. 3–17, 2007.
- [19] L. Colla, L. Fedele, M. Scattolini, and S. Bobbo, "Water-based Fe 2O 3 nanofluid characterization: Thermal conductivity and viscosity measurements and correlation," *Advances in Mechanical Engineering*, vol. 2012, 2012.
- [20] P. Fratzl, "Collagen: structure and mechanics, an introduction," *Collagen: Structure and Mechanics*, pp. 1–13, 2008.

Research Article

Estimating the Relative Stiffness between a Hepatic Lesion and the Liver Parenchyma through Biomechanical Simulations of the Breathing Process

S. Martínez-Sanchis ¹, M. J. Rupérez,¹ E. Nadal ¹, E. Pareja,² S. Brugger,³
D. Borzacchiello ⁴, R. López-Andújar,⁵ and C. Monserrat⁶

¹Centro de Investigación en Ingeniería Mecánica y de Materiales, Universitat Politècnica de València, Camino de Vera s/n, 46022 Valencia, Spain

²Servicio de Cirugía General, Hospital Universitario Dr. Peset Alexandre de València, Av. Gaspar Aguilar, 90, 46017 Valencia, Spain

³Servicio de Radiodiagnóstico, Hospital Universitari i Politècnic La Fe de València, Bulevar Sur s/n, 46026 Valencia, Spain

⁴Equipe Matériaux, Procédés et Technologie des Composites, Centrale Nantes, 1 rue de la Noe, 44321 Nantes Cedex 3, France

⁵Unidad de Cirugía Hepatobiliopancreática, Hospital Universitari i Politècnic La Fe de València, Bulevar Sur s/n, 46026 Valencia, Spain

⁶Departamento de Sistemas Informáticos y Computación, Universitat Politècnica de València, Camino de Vera s/n, 46022 Valencia, Spain

Correspondence should be addressed to S. Martínez-Sanchis; sanmars1@upv.es

Received 21 August 2018; Accepted 18 October 2018; Published 25 October 2018

Academic Editor: Guillermo Rus

Copyright © 2018 S. Martínez-Sanchis et al. This is an open access article distributed under the Creative Commons Attribution License, which permits unrestricted use, distribution, and reproduction in any medium, provided the original work is properly cited.

In this paper, a method to in vivo estimate the relative stiffness between a hepatic lesion and the liver parenchyma is presented. This method is based on the finite element simulation of the deformation that the liver undergoes during the breathing process. Boundary conditions are obtained through a registration algorithm known as Coherent Point Drift (CPD), which compares the liver form in two phases of the breathing process. Finally, the relative stiffness of the tumour with respect to the liver parenchyma is calculated by means of a Genetic Algorithm, which does a blind search of this parameter. The relative stiffness together with the clinical information of the patient can be used to establish the type of hepatic lesion. The developed methodology was first applied to a test case, i.e., to a control case where the parameters were known, in order to verify its validity. After that, the method was applied to two real cases and low errors were obtained.

1. Introduction

There are four main types of cells in the liver: hepatocytes (or parenchymal cells), Kupffer cells, endothelial cells, and stellate cells, which can receive stimulations to produce fibrous tissue [1]. A fibrous liver is less deformable and has less tissue with good function. The blood passes with difficulty and, therefore, is more prone to diseases. [2]. There are different diseases that can attack the liver, such as cirrhosis and hepatitis, and these attacks can be related to the type of cells. For example, hepatocellular carcinoma (HCC), which is the most common type of liver cancer, is produced by

hepatocytes, the main type of cells in the liver. Some diseases can result in other more serious illnesses, such as cirrhosis or hepatic tumour. These attacks are localized in a region, and a main goal in clinical application is delimiting these regions in situ for their treatment.

Traditionally, biopsy was the most effective test to identify damage in the liver. However, nowadays, there are also analytic tests, known as liver function tests (LFTs or LFs), which are analyses of blood to extract additional information about the state of liver. There are different types of test, but among these, the liver transaminases tests, i.e., aspartate transaminase (AST or SGOT) and alanine transaminase

(ALT or SGPT), are the most important since they are used as biomarkers of a liver injury. Other important biomarkers, such as NAFLD (nonalcoholic fatty liver disease) fibrosis score, FIB-4 index, and BARD score, or combination of these, are used in the clinical setting [3]. However, these analytic tests do not predict the degree of the disease and the localization of the damaged tissue, which is very important for a good diagnosis [2, 4]. The localization of the damaged tissue can be proved through medical image. Computer Tomography (CT) and Magnetic Resonance (MR) are the most commonly used medical images, especially when there is suspicion of a hepatic tumour [5].

Characterizing the liver through the study of its mechanical properties can help to establish the degree of the illness. Particularly, in HCC, the stiffness of the tumour tissue is greater than the rigidity of the normal tissue, which influences the progression of the illness and the probability of normal cells transformation into malignant cells [6, 7]. Thus, the difference of stiffness between the tissue of a tumour and the tissue of the parenchyma can be used as a biomarker. Nowadays, ultrasound elastography (USE) is the most used methodology to measure tissue stiffness. USE is an ultrasound-based technique for measuring liver stiffness according to the velocity of the elastic wave propagation across the tissue [8]. Theoretically, elastography can assess the stiffness of tumours. Several authors have studied the utility of elastography for the characterization of liver tumours ([9–12] and others). For focal liver lesions, elastography is still an open investigation, because this method cannot distinguish between benign and malignant lesions, although there are studies with promising results. For example, in Ma et al. [11], the sensitivity and specificity for differentiation of malign from benign lesions were 85% and 84%, respectively. Also, in Guo et al. [12], the sensitivity and specificity were 83.3% and 77.9%, respectively. However, other studies, such as those presented by Heide et al. [9] and Frulio et al. [10], showed that this differentiation was not so significant. Therefore, the results are not conclusive, and more research or an alternative methodology is necessary.

Currently, there are different USE techniques, which depend on the measured physical quantity [13, 14]. That is, the displacement parallel to the normal stress is measured in strain imaging technique. However, the shear wave speed is measured in shear wave imaging technique [15]. In general, these techniques present some limitations; for example, tissue attenuation decreases the ultrasound signal as a function of depth; for this reason, assessment of deeper tissue or organs is limited. Other limitation is that fluid and fat also attenuate the propagation of the external stimulus applied at the skin surface as what happens with FibroScan™ (Echosens, Paris, France). For this reason, USE techniques are not recommended for people with abdominal ascites (accumulation of liquid, produced generally by cirrhosis) or obesity [16, 17]. In these cases, other methods, such as image techniques (CT or MR), are required. Concretely, clinical applications of USE in liver are limited because, in general, USE is susceptible to internal source of stress, i.e., cardiac and breathing. For this reason, in the case of the liver, it is better to measure the stiffness in the right lobe (far of the heart) because the throbbing of the heart can result in

erroneous measurements. Therefore, the measurement of the stiffness of tumours, which are located near the heart, is also limited [18, 19]. The last limitation is that, previously, the patients need to be coached in breathing (to stop breathing at the end of end-exhale state or end-inhale state) because the deep breathing can increase the errors in the stiffness measurements [20].

On the other hand, recently, Magnetic Resonance Elastography (MRE) has appeared as a novel noninvasive imaging technique to describe the biomechanical behaviour of soft tissues *in vivo*, reducing the limitations of the traditional USE method. For example, MRE can be applied in patients with ascites or obesity. These patients have problems with using the traditional USE method, as indicated in [21]. The largest amount of clinical studies in MRE have been based on the evaluation of chronic illness in the parenchymal liver [22]. Thomson et al. [23] affirm that MRE has been used clinically in the liver for diagnoses and for establishing the liver stage of fibrosis, and they showed that the MRE may be able to differentiate HCC tumour grade. However, the MRE method has some limitations. The iron-overload state is the most important, because this overload may result in the MRI signal being too low for shear wave detection on a MRE sequence. Other limitation of MRE is a possible error of diagnosis of parenchymal organ fibrosis confounding the causes that produce an increase tissue stiffness [22]. For example, in the liver, the causes of elevated stiffness include acute inflammation, biliary obstruction, passive hepatic congestion from cardiac failure, and hepatic venous obstruction. Although MRE proves capable of differentiating benign from malignant tumours in a variety of organ systems, an overlap of the causes of stiffness in the liver can be a limiting factor, and prospective studies involving larger numbers of patients are required for validation.

The purpose of this work is to present a novel methodology for the patient-specific estimation of the relative stiffness between a hepatic lesion and the liver parenchyma. The methodology proposed uses a finite element (FE) simulation of the liver deformation during a natural process such as human breathing. This FE model is based on two CT images of the patient's abdomen, corresponding to two stages: end-exhale and end-inhale. The patients of this study had a hepatic tumour whose relative stiffness regarding the liver parenchyma was estimated. Genetic Algorithms were used to find this relative stiffness using a constitutive model to characterize the mechanical behaviour of these tissues. An iterative process was designed, so the simulation of the deformation of the liver in breathing was performed varying the elastic constants of the model. The shape of the tumour volume in the FE simulation was compared with the shape of the tumour volume in the experimentally deformed liver (i.e., the volume in inhalation) until the overlap of these two volumes was maximum, thus measuring the relative stiffness between tumour and liver parenchyma.

The presented methodology reduces some of the limitations that the elastography techniques present. For example, in the case of USE, the attenuation of the ultrasound signal as a function of the tissue depth allows the assessment of deeper tissue or organs. In the case of the MRE, the iron-overload state, which may result in the MRI signal being too low for

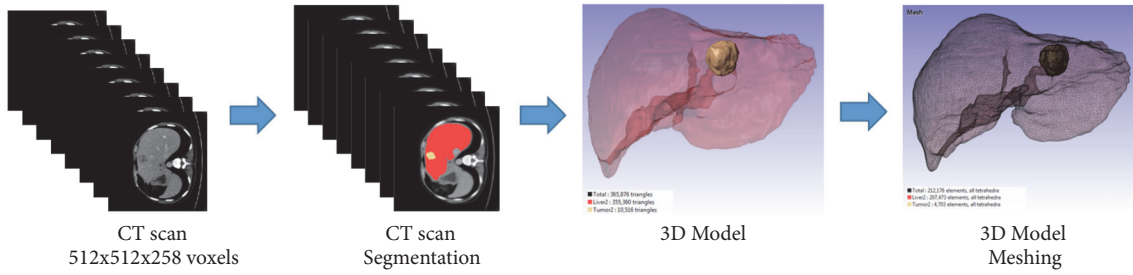


FIGURE 1: Scheme of the generation of the model FE meshes.

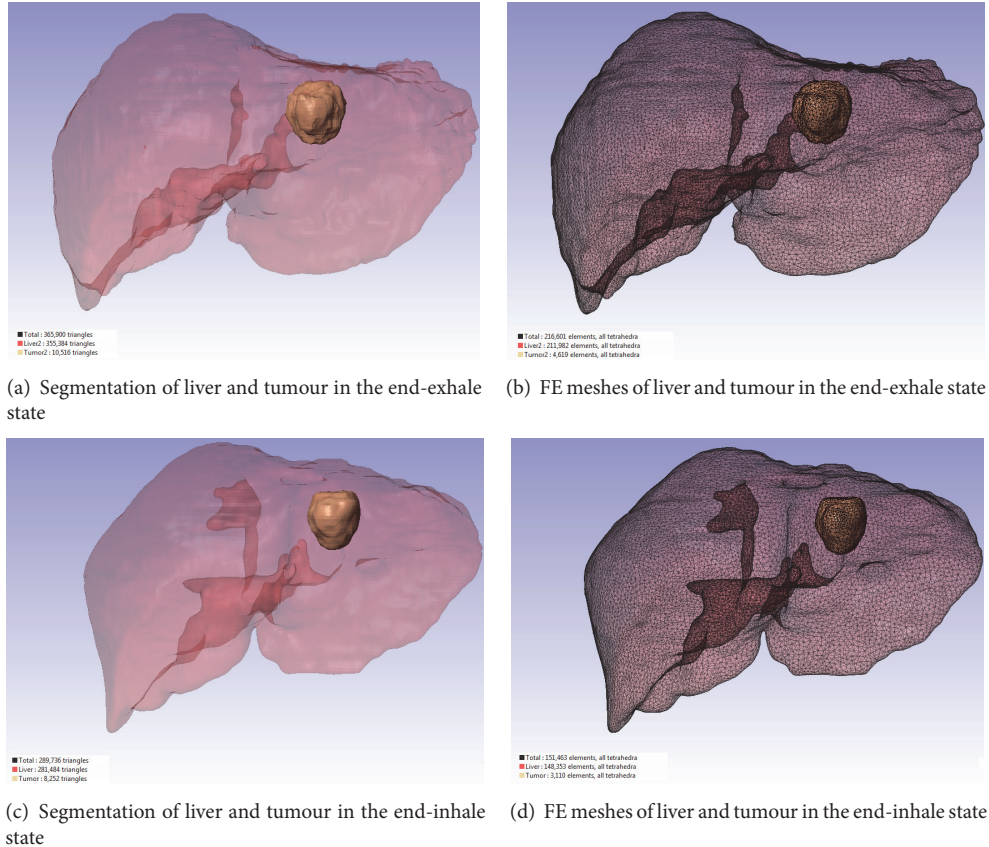


FIGURE 2: Model and mesh of liver and tumour in the end-exhale state and in the end-inhale state.

shear wave detection on a MRE sequence, is not a problem in this methodology.

2. Materials and Methods

CT images of the abdomen and pelvis of two anonymous patients, who had an internal tumour in the liver, were supplied by the Unidad de Cirugía Hepatobiliopancreática y Trasplante Hepático of Hospital Universitari i Politènic La Fe de València (CT images used to support the findings of this study have not been made available because they are property of this hospital). Two CT images were acquired from each patient, corresponding to two different states of the liver deformation related to position of diaphragm in breathing: end-exhale and end-inhale. Each patient's abdomen was

scanned with Philips Diamond Select Brilliance CT 64-slice. The scan parameters were 120 kVp and 86 mA s. CT images of the liver were acquired in DICOM format with a size of 512x512x258 voxels, with a voxel size of 0.64x0.64x1.5 mm.

The software Simpleware (version 4.2; Synopsys, Inc., Mountain View, California, USA) was used to process these two series of images in order to obtain the FE meshes of the models. First, liver and tumour were segmented and the two 3D geometrical models were generated (one for the end-inhale state and other for the end-exhale state). Afterwards, a smoothing Gaussian filter was used to obtain continuous surfaces for both models. Finally, the two FE meshes corresponding to each state were generated (Figure 1). The element type used for each tissue, liver, and tumour, was the linear tetrahedron. Figure 2 shows the models and FE meshes in

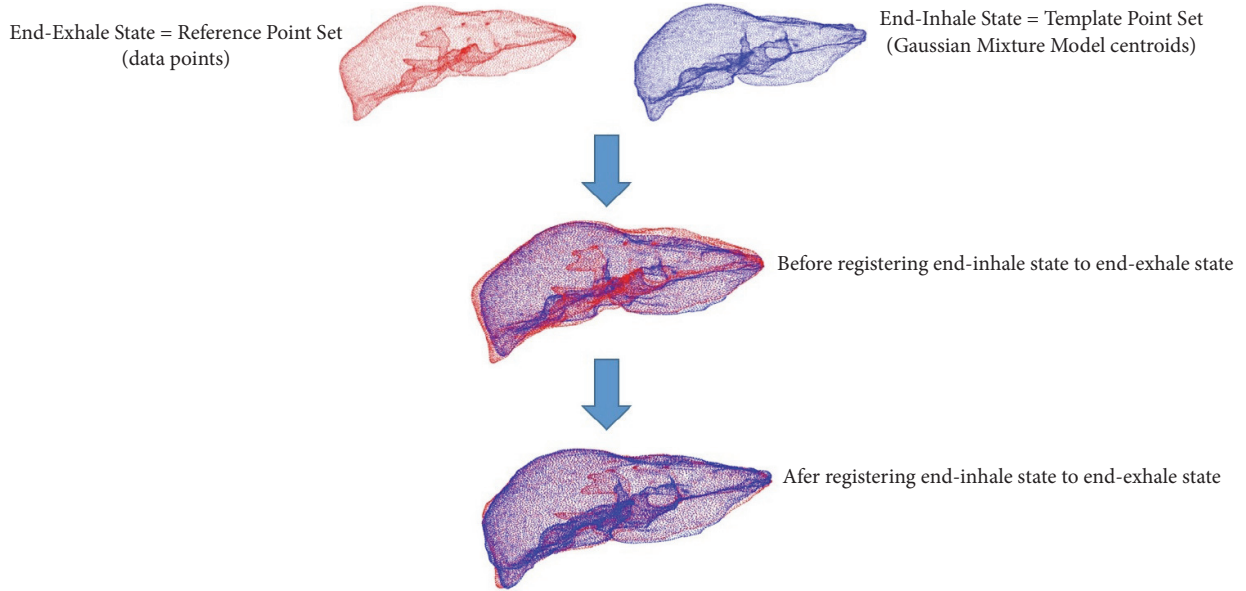


FIGURE 3: External nodes from the nondeformed state (in red) and from the deformed state (in blue) of a liver.

both states, end-exhale and end-inhale, for the same patient.

After constructing the FE meshes of the models, it was necessary to define the boundary conditions of the problem and a suitable constitutive model for liver and tumour in order to perform the simulation of their deformation in breathing.

2.1. Boundary Conditions. FE modelling allows simulating the mechanical response of the tissues of an organ by means of the relationship between a displacement and/or a force field applied to the organ and a constitutive model of the organ tissues. For that, it is necessary to establish the boundary conditions (BC) of the problem to be tackled, in this case, the BC corresponding to the simulation of the liver deformation in breathing. To obtain the BC of the problem, we propose the use of point set registration, whose main goal is to find correspondences between two sets of points and obtain the transformation that maps one of the sets to the other. There are two types of transformation: rigid and nonrigid. The second type is used in medical registration and it allows translation, rotation, scaling (included anisotropic scaling), and skews. There are different registering algorithms, but a lot of them have a high computational complexity and are limited to rigid registrations. For this reason, in this study, the Coherent Point Drift (CPD) algorithm [24] was used. CPD considers the alignment between both sets of points as a probability density estimation problem, where the first point set (Gaussian Mixture Model centroids) is fitted to the second point set (data points). CPD forces the centroids to move coherently preserving the topological structure through a transformation function, which is defined as the initial position plus a displacement function, ν :

$$T(\mathbf{Y}, \nu) = \mathbf{Y} + \nu(\mathbf{Y}) \quad (1)$$

where \mathbf{Y} is the first point set (Gaussian Mixture Model centroids). In the work of Myronenko and Song [24], the mean squared distance between the corresponding points after registration was used as error measure, which rises with the deformation level. In this study, the maximum error obtained was about 2%, and the authors concluded that CPD shows robust and accurate performance, especially in cases with noise, outliers, and missing points.

In this work, CPD was used to align the nodes of the external surface of the liver mesh at exhalation considered as the initial state to the external nodes of the liver surface at inhalation; thus the displacements to be applied to the nodes of the liver mesh (Dirichlet conditions) were obtained. This point set registration algorithm allowed mapping the end-exhale FE mesh to the end-inhale FE mesh, creating a displacement field that defined the transition between both states and provided the boundary conditions of the problem. The displacements obtained from the liver registration (Figure 3) were used as the boundary conditions and applied to the liver at the end-exhale state for the FE simulations of the breathing process. Once the boundary conditions were established, the final location of the tumour in the FE-simulated deformed state (end-inhale) would allow the estimation of the relative stiffness between the tumour and the liver parenchyma.

2.2. Constitutive Model. Nonlinear constitutive models, which are described by a specific strain energy function (W), are used to define the biomechanical behaviour of the liver tissue. There are a lot of types of constitutive laws to describe the mechanical behaviour of the liver in the literature, for example, polynomial hyperelastic models, exponential and logarithmic hyperelastic models, and combined models. In this study, a first-order Ogden model was chosen to represent the mechanical behaviour of the liver and the

tumour based on the results from Martínez-Martínez et al. [25] and Untaroiu and Lu [26]. For this model, the strain energy potential for the Ogden model [27], W_O , is defined as

$$W_O = \frac{\mu}{\alpha} (\bar{\lambda}_1^\alpha + \bar{\lambda}_2^\alpha + \bar{\lambda}_3^\alpha - 3) + \frac{K_O}{2} (J - 1)^2 \quad (2)$$

where N denotes the order of the model; μ_i and α_i stand for the material elastic parameters; $\bar{\lambda}_1$, $\bar{\lambda}_2$, and $\bar{\lambda}_3$ denote the deviatoric stretches; K_O is the initial bulk modulus; and J is the determinant of the elastic deformation gradient.

One limitation of this study is that the liver is prestressed inside the body at the end-exhale state. Establishing the nondeformed state of the liver inside the body is an unsolved problem of great difficulty due to the fact that all the interactions of the liver with the rest of the organs and fluids should be known in order to apply an algorithm to determine this nondeformed state. Therefore, a first approximation, the end-exhale state, was considered as a nondeformed state in our methodology. Anisotropy is considered another important factor. Most of the biological soft tissues have properties highly anisotropic, such as the cartilage or the muscular tissue, and the liver is not an exception. However, liver tissue is considered as isotropic in a large majority of studies [28, 29], as a good approximation to model its behaviour. Therefore, the mechanical behaviour of the liver parenchyma and the tumour tissue was considered isotropic.

The elastic constants of the first-order Ogden constitutive model of the tumour, μ_T and α_T , were related to the elastic constants first-order Ogden constitutive model of the liver parenchyma, μ_L and α_L , as (3) and (4) show.

$$\mu_T = k_{rel} \mu_L \quad (3)$$

$$\alpha_T = \alpha_L \quad (4)$$

The purpose of this work was to find the relative stiffness factor between tumour and liver parenchyma using the first-order Ogden model, k_{rel} . Small strains are not considered in this work. However, this model must verify that, for small strains, the material elastic parameters (μ and α) are related to the modulus of rigidity (G) as (5) shows.

$$\mu_1 \alpha_1 = 2G \quad (5)$$

For this study, the elastic constants of the liver parenchyma were fixed to $\mu_1^L = 364.74$ Pa and $\alpha_1^L = 16.19$ [25]. Therefore

$$\mu_T = k_{rel} \mu_L = 364.74 k_{rel} \quad (6)$$

$$\alpha_T = \alpha_L = 16.19. \quad (7)$$

The bulk modulus K_O was fixed to 10^4 Pa based on the results measured by Hostettler et al. [30] for the bulk modulus of the human liver in vivo.

2.3. Iterative Process and Cost Function. In this study, a FE simulation of the deformation from end-exhale state to the target deformation, end-inhale, state was included within an

iterative optimization routine based on Genetic Algorithms, which is aimed at finding the relative stiffness that defines the biomechanical behaviour of the tumour with respect to the liver parenchyma. The computation of the optimal values of the relative stiffness is based on an iterative process that is performed in two steps: the first step consists in estimating the error committed by a selected value of the stiffness factor, and the second one consists in recomputing this value to reduce the above-mentioned error. This iterative process is carried out by minimising an error function that is dependent on this relative stiffness factor called cost function. In this work, a metaheuristic method called Genetic Algorithms (GAs) [31] was chosen for the global optimization of the relative stiffness factor of the biomechanical model based on the result from a previous research, where the performance of gradient descent algorithms was compared with the performance of several evolutionary algorithms Martínez-Martínez et al. [32]. GAs belong to the family of evolutionary computation algorithms, which are inspired in biological evolution [33, 34]. GAs mimic the natural evolution of a population by allowing solutions (parents) to reproduce new ones (children) and competing for survival in the following generations. After generations, the population progresses toward an optimal solution.

2.3.1. Geometric Similarity Function. In this work, a modified version of the Geometric Similarity Function (GSF) presented by Martínez-Martínez et al. [32] was chosen as a cost function in order to find the optimal stiffness factor. This modified version is shown in

$$GSF = \ln((1 - JC) MHD) \quad (8)$$

where JC stands for the Jaccard coefficient and MHD stands for the modified Hausdorff distance. JC [35] measures the overlap between two volumes A and B providing values between 0, no overlap, and 1, total overlap, through

$$JC = \frac{|A \cap B|}{|A \cup B|}. \quad (9)$$

On the other hand, MHD [36] measures the maximum of the minimum distances between any pair of points belonging to the border of two different overlapping volumes through

$$MHD = \max(\bar{d}_B(i), \bar{d}_A(i)) \quad (10)$$

where $\bar{d}_X(i)$ is the distance between the voxel i and the closest voxel of a volume X .

The idea underlying the choice of this function is the comparison of the total deformed shape of two volumes as a whole, representing the deformed shape of an organ. A previous study about several coefficients carried out by Lago et al. [37], which could be used to measure the error committed in the comparison of a deformed state of a body with a reference state of that body, proved that JC and MHD coefficients performed better than other classic comparisons. Furthermore, it was proved that a combination of both coefficients provided more information about the error committed in the comparison than using them

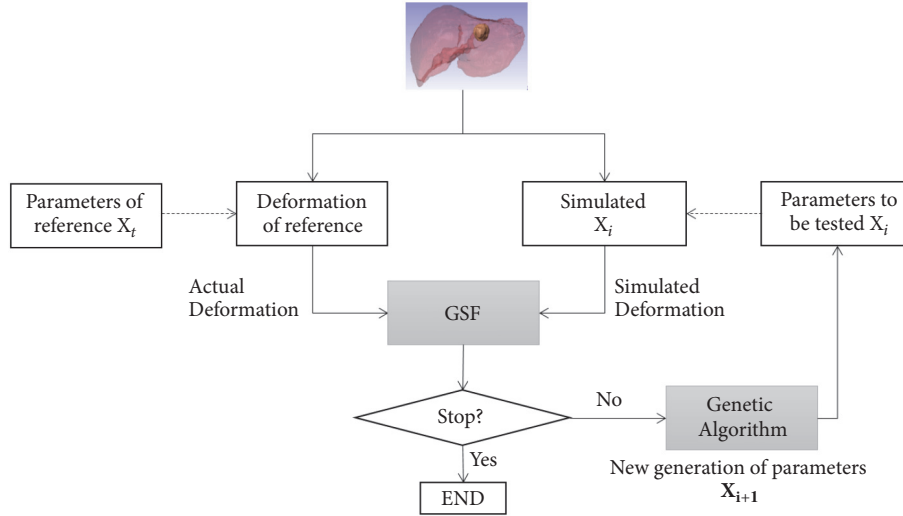


FIGURE 4: Schematic of the process in the test case.

separately. Therefore, GSF was computed as a combination of both coefficients, so when overlap is maximum ($JC = 1$) and Hausdorff distance is minimum ($MHD = 0$), GSF tends to zero. The natural logarithm of the combination of both coefficients was chosen in order to distinguish values close to zero with more precision. It is important to notice that these coefficients, Jaccard coefficient and modified Hausdorff distance, which are commonly used in medical image analysis, make comparisons of volumes. This means that the FE meshes to be compared are voxelized before the comparison. In this work, GSF provided the error in the comparison between the deformed shape of the two tumour volumes, one corresponding to the tumour in the actual deformed state (end-inhale) and the other corresponding to the tumour in simulation of this situation using the biomechanical model with the proposed elastic parameters and relative stiffness provided by the GA algorithm. The smaller the committed error, the lower the GSF value.

2.3.2. Genetic Algorithm. In this work, GAs were used to find the patient-specific relative stiffness factor between tumour and liver parenchyma within certain bounds. The choice of these bounds were based on values provided in the literature. These bounds were normalized (between 0 and 1) to allow the optimization to converge faster avoiding the cost function to take skewed shapes.

Firstly, GAs randomly generated an initial population in the first generation which contained 50 individual candidate solutions. GAs create a new population, with 50 individuals, from the population of the previous generation (30 individuals are created through crossover and the remaining 20 through mutation). The two of the individual solutions in the current generation that have the best GSF values are chosen as elite and replicated to the next generation. The terminating condition in this case was achieved when the cost function value of the best solution was below a given threshold.

The entire method was implemented in a MATLAB script (version: MATLAB TAH 2018a, MathWorks, Inc.), which

TABLE 1: Lower and upper bounds of the search intervals for the optimization of the relative stiffness factor of the test sample.

Case	Interval
Test Case	$1 \leq k_{rel} \leq 50$

communicates with the free FE software FEBio (version 2.7).

3. Results

3.1. Test Case. To begin with, the feasibility of the proposed methodology was proved using a test case. In this case, the constitutive model of liver parenchyma and tumour was obtained fixing to 10 the relative stiffness between both tissues ($k_{rel} = 10$) and using the elastic parameters proposed in Section 2.2. GAs were used to find this factor choosing the bounds shown in Table 1 for its searching. The algorithm performed a blind search of it. The final result was obtained choosing the best GSF value among the values obtained in the iterative process.

Figure 4 shows a schematic of the methodology applied for the test case. This approach is based on getting a reference deformed state for the liver and the tumour, which is compared with each deformed state simulated through GA and evaluated by means of a cost function (GSF). The reference deformed state was obtained from the model of the liver at the end-exhale state using a reference relative stiffness k_{rel} and the liver and tumour properties provided in Section 2.2, in addition to the model the displacements obtained with CPD algorithm as boundary conditions. The shape of the tumour in the deformed state of reference was compared with the shape of the tumour in each simulation obtained for each generation of parameters. This process was iterative, and when the minimal value of GSF was obtained, the relative stiffness was selected.

TABLE 2: Optimal values of the relative stiffness between tumour and liver estimated by GAs (k_{rel}) together with Jaccard coefficient (JC), modified Hausdorff distance (MHD), and Geometric Similarity Function (GSF) values for test case.

Case	k_{rel}	JC	MHD (mm)	GSF
Test Case	10.003	0.99983	0.5493	-9.2906

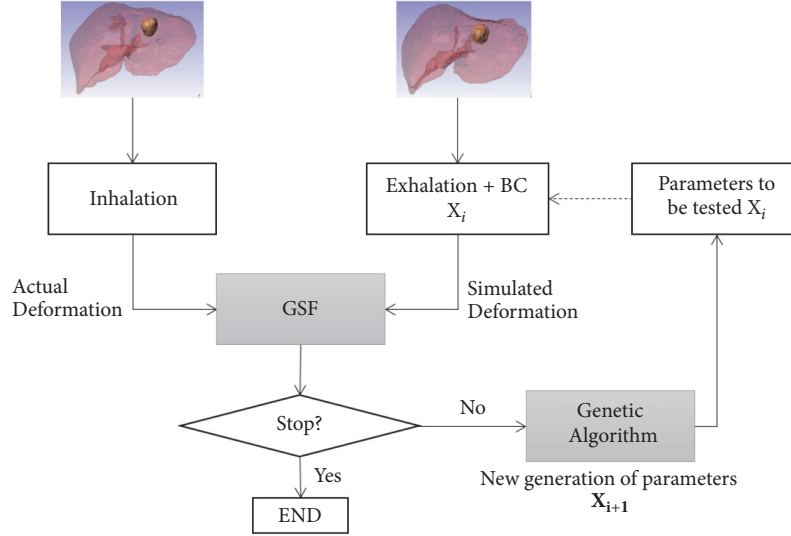


FIGURE 5: Schematic of the process in both real samples.

The optimal value of the relative stiffness factor obtained by GAs for the test case is shown in Table 2. The test case provided an overlap greater than 99%. The relative stiffness factor obtained was 10.003, and theoretically this value should be 10, so the relative error committed in the estimation of this factor was only 0.03%. This way, the capability of the algorithm to perform the estimation of the relative stiffness factor was proved.

3.2. Real Cases. After that, the methodology was applied to two real cases. Figure 5 shows a scheme of the methodology used for the real cases. In this kind of cases, the two states of the liver, end-inhale state and end-exhale state, were compared through GA to find the relative stiffness factor between tumour and liver parenchyma. In the same way as before, the final result was obtained choosing the best GSF value among the obtained values in the iterative process. For these cases, the liver at the end-inhale state was the deformed reference state and each simulation was performed from the model of the liver at the end-exhale state to which the boundary conditions obtained with the CPD algorithm were applied. These BC were the displacements of the nodes of the external surface of the liver. It is important to highlight that, in this case, the value of k_{rel} was unknown, and, therefore, the committed error could only be evaluated studying the values of JC and MHD (overlap and distance between borders) in the comparison of the two tumour shapes.

For this part, the bounds shown in Table 3 were chosen for this search.

The relative stiffness factor provided by GAs for each of the actual samples is shown in Table 4.

TABLE 3: Lower and upper bounds of the search intervals for the optimization of the relative stiffness factor of the actual livers for the Ogden model.

Case	Interval
Liver 1	$1 \leq k_{rel} \leq 50$
Liver 2	$1 \leq k_{rel} \leq 50$

For these cases, the value of the overlap (JC coefficient) was about 85.7% for Liver 1 and a value of about 92.2% was obtained for Liver 2. The Hausdorff distances were 1.43 mm for Liver 1 and 1.29 mm for Liver 2, and the relative stiffness was 31.19 and 41.502 for Liver 1 and Liver 2, respectively.

4. Discussion

The method proposed in this document has been proved by means of a test case, where the relative stiffness was known and the algorithm made a blind research of it. In this case, the error was very low, only 0.03%. Moreover, the overlap between the tumour volume in the reference state and the tumour in the simulated state was very high, JC coefficient was 99.98%, and HMD was 0.55 mm. Taking into account the fact that the voxel size was 0.64x0.64x1.5 mm, these values showed that the methodology achieves good results and can be used to estimate the relative stiffness between the tumour and the liver parenchyma. This methodology had already been applied to establish the elastic constants of a constitutive model for the cornea [38] and for the breast [39]. However, this is the first time that this methodology is applied

TABLE 4: Optimal values of the relative stiffness between tumour and liver estimated by GAs (k_{rel}) together with Jaccard coefficient (JC), modified Hausdorff distance (MHD), and Geometric Similarity Function (GSF) values for each real sample.

Case	k_{rel}	JC	MHD (mm)	GSF
Liver 1	31.186	0.85744	1.4342	-1.5874
Liver 2	41.502	0.92189	1.2886	-2.2996

to estimate the relative stiffness between tumour and liver parenchyma.

Regarding the real cases, the overlap between the tumour in the actual deformed state and in the simulated state is smaller than for the test case, but still acceptable. As the values of the relative stiffness for the real cases were unknown, the committed error can be analysed looking at the values of JC and MHD for the test case, which guarantees an error of 0.03%. For Liver 1, the overlap obtained in the comparison of the shape of the tumour volume was of 85% with a maximum distance between borders (MHD) of 1.4 mm, and for Liver 2 the overlap obtained was 92% and the distance between borders was 1.3 mm, indicating higher errors than for the test case, but still acceptable. The difference with the test case and the difference between both results in the real cases could be due to the material model used, but it could mainly be due to the quality of the segmentation. In other words, in the test case, the reference state of the liver was obtained from the same state used for performing the simulation (the liver at end-exhale). Hence, the segmentation error did not affect the search. However, for the real cases, two different states were used, end-inhale state as the reference state, and end-exhale state as the initial state for performing the simulation. Thus, two processes of segmentation were necessary. For this reason, the error committed in the segmentation processes could have affected the comparison between the tumour in the actual deformed state and the tumour in the simulated configuration.

It is important to notice that the estimated relative stiffness is not the real relative stiffness because the end-exhale state of the liver was considered as a nondeformed state. As previously commented, this is an approximation that allows us to establish a suitable parameter to measure relative stiffness that can be used as a biomarker of a hepatic lesion, since liver is prestressed inside the body. It is also important to notice that the relative stiffness was obtained because Dirichlet BC were applied to the problem. However, the Ogden parameters μ_L and μ_T could also be obtained if the forces that the liver undergoes in the breathing process would be applied, as it was performed for the mechanical characterization of the cornea in vivo [38] or for the estimation of the elastic constants of the breast [39]. However, the in vivo measurement of these forces is still a challenge due to the difficult access to the internal organs. This makes it very difficult to establish boundary conditions and loads for the simulation process of liver deformation during the breathing process. Therefore, the presented work can be considered a small step in the in vivo estimation of the patient-specific stiffness of liver and tumour. In these cases, the results about the relative stiffness can be supported with other type of test, such as analytic tests or elastography in order to determine

the state of the liver parenchyma since relative stiffness is a relative parameter. Although, the latter has limitations, it can be used as a test to verify the results.

Keeping in mind that there are differences of relative stiffness between patients, it is interesting to use the relative stiffness between tumour and liver parenchyma as a biomarker, since these differences can arise due to different causes: the type of tumour (metastasis or hepatocarcinoma), the ground pathology (i.e., if liver is healthy or has cirrhosis), the patient having received chemotherapy previously, or the age of the patient (if the patient is older, he/she has more fibrosis). In our case, Liver 1 had suffered metastasis, and due to chemotherapy it was showing calcifications. However, Liver 2 had suffered a portal embolization, and this liver was showing cirrhosis and hepatocarcinoma. Therefore, the different nature of the tumours and liver parenchyma is reflected in the different relative stiffness obtained. It is important to notice that some authors have studied the stiffness as biomarker of tumours, but these studies have been on breast [40], prostate [41], or ovarian cancer cells [42]. For example, Hoyt et al. [41] showed that increasing tumour aggressiveness is associated with increased collagen in the healthy tissue, and this statement was supported by Fenner et al. [40]) and Xu et al. [42]. This result shows that stiffness may be used as biomarker to evaluate the relative metastasis in different types of cancer, because the stiffness can distinguish malignant cells from benign cells and the aggressivity of the cancer cells.

Finally, it is important to highlight the methodology used to establish the BC of the problem. Establishing Dirichlet BC by CPD is a novel methodology that can be very useful for other models and applications in which the access to the organs is invasive, but displacements from two different deformed states must be obtained from medical images.

5. Conclusion

This paper has presented a computational method to obtain the patient-specific relative stiffness between tumour and liver parenchyma; this relative stiffness can be used together with the pathological information as a biomarker of the type of tumour. The method allows the measurements of the relative stiffness of tumours regarding liver parenchyma by means of the use of medical images. Two CT images of the liver in two different states of deformation are needed to estimate this relative stiffness factor, which is computed by an iterative algorithm based on the FE simulation of the human breathing. To establish the boundary conditions of the FE problem, a registration algorithm provides the displacements to be applied to reach the end-inhale state from the end-exhale state. This methodology tries to overlap

the limitations that other methods present, for example, the limitations in ultrasound elastography. The method could also be used to model the behaviour of the tumour during image-guided interventions (as biopsy or radiation therapy) improving tumour targeting accuracy, reducing the margins of the irradiated tissue, or reducing the treatment duration, if the elastic constants of the liver parenchyma are known. Furthermore, this methodology could be applied to other organs, for example, lungs or prostate.

As future research, this work will expand the number of cases to be studied. The main idea is getting a database large enough to definitively verify the feasibility of the proposed methodology. Moreover, the presented methodology will be applied to other organs, such as breast and prostate.

Data Availability

The data used to support the findings of this study have not been made available because they are property of Hospital Universitari i Politècnic La Fe de València.

Ethical Approval

The studies reported in this paper were approved by the ethics committee of the Hospital Universitari i Politècnic La Fe de València and were performed in accordance with the ethical standards of the responsible committee on human experimentation (institutional and national) and with the Helsinki Declaration of 1975, as revised in 2008.

Disclosure

This methodology was presented in VI European Congress on Computational Methods in Applied Sciences and Engineering, VipIMAGE 2017, in Porto (Portugal) [43].

Conflicts of Interest

The authors declare that they have no conflicts of interest.

Acknowledgments

This work has been funded by the Spanish Ministry of Economy and Competitiveness (MINECO) through research projects DPI2013-40859-R and TIN2014-52033-R, both also supported by European FEDER funds.

References

- [1] Z. Kimiec, "Cooperation of liver cells in health and disease," *Advances in Anatomy, Embryology and Cell Biology*, vol. 161, pp. 1–151, 2001.
- [2] A. Cequera and M. C. García de León Méndez, "Biomarkers for liver fibrosis: Advances, advantages and disadvantages," *Revista de Gastroenterología de México (English Edition)*, vol. 79, no. 3, pp. 187–199, 2014.
- [3] E. Vilar-Gomez and N. Chalasani, "Non-invasive assessment of non-alcoholic fatty liver disease: Clinical prediction rules and blood-based biomarkers," *Journal of Hepatology*, vol. 68, no. 2, pp. 305–315, 2018.
- [4] E. G. Giannini, R. Testa, and V. Savarino, "Liver enzyme alteration: a guide for clinicians," *Canadian Medical Association Journal*, vol. 172, no. 3, pp. 367–379, 2005.
- [5] M. R. Oliva and S. Saini, "Liver cancer imaging: Role of CT, MRI, US and PET," *Cancer Imaging*, vol. 4, pp. S42–S46, 2004.
- [6] J. K. Mouw, Y. Yui, L. Damiano et al., "Tissue mechanics modulate microRNA-dependent PTEN expression to regulate malignant progression," *Nature Medicine*, vol. 20, no. 4, pp. 360–367, 2014.
- [7] M. J. Paszek, N. Zahir, K. R. Johnson et al., "Tensional homeostasis and the malignant phenotype," *Cancer Cell*, vol. 8, no. 3, pp. 241–254, 2005.
- [8] Y.-H. Kuo, S.-N. Lu, C.-H. Hung et al., "Liver stiffness measurement in the risk assessment of hepatocellular carcinoma for patients with chronic hepatitis," *Hepatology International*, vol. 4, no. 4, pp. 700–706, 2010.
- [9] R. Heide, D. Strobel, T. Bernatik, and R. S. Goertz, "Characterization of focal liver lesions (FLL) with acoustic radiation force impulse (ARFI) elastometry," *Ultraschall in der Medizin / European Journal of Ultrasound (UiM/EJU)*, vol. 31, no. 4, pp. 405–409, 2010.
- [10] N. Frulio, H. Laumonier, T. Carteret et al., "Evaluation of liver tumors using acoustic radiation force impulse elastography and correlation with histologic data," *Journal of Ultrasound in Medicine*, vol. 32, no. 1, pp. 121–130, 2013.
- [11] X. Ma, W. Zhan, B. Zhang et al., "Elastography for the differentiation of benign and malignant liver lesions: A meta-analysis," *Tumor Biology*, vol. 35, no. 5, pp. 4489–4497, 2014.
- [12] L. Guo, S. Wang, H. Xu et al., "Differentiation of benign and malignant focal liver lesions: value of virtual touch tissue quantification of acoustic radiation force impulse elastography," *Medical Oncology*, vol. 32, no. 3, 2015.
- [13] C. F. Dietrich, J. Bamber, A. Berzigotti et al., "EFSUMB Guidelines and Recommendations on the Clinical Use of Liver Ultrasound Elastography, Update 2017 (Long Version)," *Ultraschall in der Medizin / European Journal of Ultrasound (UiM/EJU)*, vol. 38, no. 4, pp. e16–e47, 2017.
- [14] G. Ferraioli, C. Filice, L. Castera et al., "WFUMB guidelines and recommendations for clinical use of ultrasound elastography: Part 3: Liver," *Ultrasound in Medicine & Biology*, vol. 41, no. 5, pp. 1161–1179, 2015.
- [15] R. M. S. Sigris, J. Liau, A. E. Kaffas, M. C. Chammas, and J. K. Willmann, "Ultrasound elastography: Review of techniques and clinical applications," *Theranostics*, vol. 7, no. 5, pp. 1303–1329, 2017.
- [16] D. Cosgrove, F. Piscaglia, and J. Bamber, "EFSUMB guidelines and recommendations on the clinical use of ultrasound elastography. Part 2: clinical applications," *Ultraschall in der Medizin / European Journal of Ultrasound (UiM/EJU)*, vol. 34, no. 3, pp. 238–253, 2013.
- [17] M. L. Palmeri and K. R. Nightingale, "What challenges must be overcome before ultrasound elasticity imaging is ready for the clinic?" *Imaging in Medicine*, vol. 3, no. 4, pp. 433–444, 2011.
- [18] A. E. Samir, M. Dhyani, A. Vij et al., "Shear-Wave elastography for the estimation of liver fibrosis in chronic liver disease: Determining accuracy and ideal site for measurement," *Radiology*, vol. 274, no. 3, pp. 888–896, 2015.
- [19] T. Toshima, K. Shirabe, K. Takeishi et al., "New method for assessing liver fibrosis based on acoustic radiation force impulse: a special reference to the difference between right and left liver," *Journal of Gastroenterology*, vol. 46, no. 5, pp. 705–711, 2011.

- [20] R. G. Barr, G. Ferraioli, M. L. Palmeri et al., "Elastography assessment of liver fibrosis: Society of radiologists in ultrasound consensus conference statement," *Radiology*, vol. 276, no. 3, pp. 845–861, 2015.
- [21] S. K. Venkatesh, M. Yin, and R. L. Ehman, "Magnetic resonance elastography of liver: technique, analysis, and clinical applications," *Journal of Magnetic Resonance Imaging*, vol. 37, no. 3, pp. 544–555, 2013.
- [22] G. Low, S. A. Kruse, and D. J. Lomas, "General review of magnetic resonance elastography," *World Journal of Radiology*, vol. 8, no. 1, p. 59, 2016.
- [23] S. M. Thompson, J. Wang, V. S. Chandan et al., "MR elastography of hepatocellular carcinoma: Correlation of tumor stiffness with histopathology features—Preliminary findings," *Magnetic Resonance Imaging*, vol. 37, pp. 41–45, 2017.
- [24] A. Myronenko and X. Song, "Point set registration: coherent point drifts," *IEEE Transactions on Pattern Analysis and Machine Intelligence*, vol. 32, no. 12, pp. 2262–2275, 2010.
- [25] F. Martínez-Martínez, M. A. Lago, M. J. Rupérez, and C. Monserrat, "Analysis of several biomechanical models for the simulation of lamb liver behaviour using similarity coefficients from medical image," *Computer Methods in Biomechanics and Biomedical Engineering*, vol. 16, no. 7, pp. 747–757, 2013.
- [26] C. D. Untaroiu and Y.-C. Lu, "Material characterization of liver parenchyma using specimen-specific finite element models," *Journal of the Mechanical Behavior of Biomedical Materials*, vol. 26, pp. 11–22, 2013.
- [27] R. W. Ogden, "Large deformation isotropic elasticity: on the correlation of theory and experiment for incompressible rubberlike solids," *Proceedings of the Royal Society of London A: Mathematical A*, vol. 326, no. 1567, pp. 565–584, 1972.
- [28] C. Chui, E. Kobayashi, X. Chen, T. Hisada, and I. Sakuma, "Transversely isotropic properties of porcine liver tissue: Experiments and constitutive modelling," *Medical & Biological Engineering & Computing*, vol. 45, no. 1, pp. 99–106, 2007.
- [29] S. Marchesseau, S. Chatelin, and H. Delingette, "Nonlinear Biomechanical Model of the Liver," *Biomechanics of Living Organs: Hyperelastic Constitutive Laws for Finite Element Modeling*, pp. 243–265, 2017.
- [30] A. Hostettler, D. George, Y. Rémond, S. A. Nicolau, L. Soler, and J. Marescaux, "Bulk modulus and volume variation measurement of the liver and the kidneys in vivo using abdominal kinetics during free breathing," *Computer Methods and Programs in Biomedicine*, vol. 100, no. 2, pp. 149–157, 2010.
- [31] S. Chatterjee, M. Laudato, and L. A. Lynch, "Genetic algorithms and their statistical applications: an introduction," *Computational Statistics & Data Analysis*, vol. 22, no. 6, pp. 633–654, 1996.
- [32] F. Martínez-Martínez, M. J. Rupérez, J. D. Martín-Guerrero et al., "Estimation of the elastic parameters of human liver biomechanical models by means of medical images and evolutionary computation," *Computer Methods and Programs in Biomedicine*, vol. 111, no. 3, pp. 537–549, 2013.
- [33] D. B. Fogel, *Evolutionary Computation: Toward a New Philosophy of Machine Intelligence*, IEEE Press, Piscataway, NJ, USA, 1995.
- [34] K. A. de Jong, *Evolutionary Computation: a Unified Approach*, MIT Press, Cambridge, Mass, USA, 2006.
- [35] P. Jaccard, "Etude comparative de la distribution florale dans une portion des Alpes et des Jura," *Bulletin de la Société vaudoise des sciences naturelles*, vol. 37, pp. 547–579, 1901.
- [36] M.-P. Dubuisson and A. K. Jain, "A modified Hausdorff distance for object matching," in *Proceedings of the 12th IAPR International Conference on Pattern Recognition, Conference A: Computer Vision & Image Processing*, vol. 1, pp. 566–568, IEEE, Jerusalem, Israel, 1994.
- [37] M. A. Lago, F. Martínez-Martínez, M. J. Rupérez, J. D. Martín-Guerrero, C. Monserrat, and M. Alcaniz, "A study about coefficients to estimate the error in biomechanical models used to virtually simulate the organ behaviors," in *Proceedings of the International Conference on Medicine Meets Virtual Reality*, vol. 137, pp. 250–256, 2012.
- [38] M. Lago, M. Rupérez, F. Martínez-Martínez et al., "A new methodology for the in vivo estimation of the elastic constants that characterize the patient-specific biomechanical behavior of the human cornea," *Journal of Biomechanics*, vol. 48, no. 1, pp. 38–43, 2015.
- [39] M. A. Lago, M. J. Rupérez, F. Martínez-Martínez, S. Martínez-Sanchis, P. R. Bakic, and C. Monserrat, "Methodology based on genetic heuristics for in-vivo characterizing the patient-specific biomechanical behavior of the breast tissues," *Expert Systems with Applications*, vol. 42, no. 21, pp. 7942–7950, 2015.
- [40] J. Fenner, A. C. Stacer, F. Winterroth, T. D. Johnson, K. E. Luker, and G. D. Luker, "Macroscopic stiffness of breast tumors predicts metastasis," *Scientific Reports*, vol. 4, 2014.
- [41] K. Hoyt, B. Castaneda, M. Zhang et al., "Tissue elasticity properties as biomarkers for prostate cancer," *Cancer Biomarkers*, vol. 4, no. 4-5, pp. 213–225, 2008.
- [42] W. Xu, R. Mezencev, B. Kim, L. Wang, J. McDonald, and T. Sulchek, "Cell stiffness is a biomarker of the metastatic potential of ovarian cancer cells," *PLoS ONE*, vol. 7, no. 10, Article ID e46609, 2012.
- [43] S. Martínez-Sanchis, M. J. Rupérez, E. Nadal et al., "Estimating the Patient-Specific Relative Stiffness Between a Hepatic Lesion and the Liver Parenchyma," in *VipIMAGE 2017*, vol. 27 of *Lecture Notes in Computational Vision and Biomechanics*, pp. 485–494, Springer International Publishing, Cham, 2018.

Research Article

Influence of the Temporomandibular Joint in the Estimation of Bone Density in the Mandible through a Bone Remodelling Model

Maria S. Commisso ¹, Joaquín Ojeda,² Juana Mayo,² and Javier Martínez-Reina ²

¹Université de Lyon, ECAM de Lyon, LabECAM, 69005 Lyon, France

²Department of Mechanical Engineering, Universidad de Sevilla, Camino de los Descubrimientos s/n, 41092 Sevilla, Spain

Correspondence should be addressed to Maria S. Commisso; m.commisso@ecam.fr

Received 25 July 2018; Accepted 2 October 2018; Published 21 October 2018

Academic Editor: Guillermo Rus

Copyright © 2018 Maria S. Commisso et al. This is an open access article distributed under the Creative Commons Attribution License, which permits unrestricted use, distribution, and reproduction in any medium, provided the original work is properly cited.

The temporomandibular joint (TMJ) plays a key role in the distribution of stresses in the mandible during mastication and consequently in the distribution of bone density, due to the interconnection between both variables through bone remodelling. Two finite element models of the mandible were compared to study the influence of the redistribution of stresses produced by the joint: (1) a model without TMJ, but with simplified boundary conditions to replace the joint, as done in previous models; (2) a more realistic model including the articular disc and some ligaments present in the TMJ. The stresses and strains in both models were compared through the strain energy density, used in many bone remodelling models as a measure of the mechanical stimulus. An anisotropic bone remodelling model was used to simulate the behaviour of mandible bone and to estimate its density distribution. The results showed that the TMJ strongly affects the stress distribution, the mechanical stimulus, and eventually the bone density, and not only locally in the condyle, but also in the whole mandible. It is concluded that it is utterly important to include a detailed model of the TMJ to estimate more correctly the stresses in the mandible during mastication and, from them, the bone density and anisotropy distribution.

1. Introduction

Bone density and stresses (or strains) are intimately related to each other. That is the reason why bone remodelling models (BRMs) have been widely used to predict the density distribution in bones [1–4]. Bone apparent density can be more easily estimated through computer tomography (CT). However, some BRMs can additionally estimate bone anisotropy, not accessible through CT and thus provide a closer estimation of bone elastic properties. BRMs have been traditionally used to study the proximal femur (see Doblaré and García [5], Fernandes et al. [6], among many others). In the case of the jaw, many authors have used models of a mandible section to study bone around dental implants [7, 8]. Only a few have estimated bone density in the whole mandible from the stresses produced by mastication loads [3, 4], but the temporomandibular joint (TMJ) was not included in

those models. Instead, equivalent boundary conditions were used to simulate, in a very simplistic way, the constraints imposed by the joint. This has important effects on the stress distribution of the whole mandible, as discussed in the present work.

The main component of the TMJ is the articular disc, which eases the relative movement between the condyle of the mandible and the temporal bone. The articular disc absorbs and distributes the joint reaction force over a larger contact area than a direct contact between bones would achieve and reduces the friction of the bone-on-bone contact, to prevent the damage of the articulating surfaces [9]. That redistribution of loads has an effect on the stresses and strains which is not only local but affects the whole mandible. Several studies have proposed different viscoelastic models to characterize the mechanical behaviour of the disc and to analyse its effect on the masticatory tasks [10–14].

In one of those works [14], a FE model of the mandible including the TMJ was used to simulate a masticatory cycle, applying the loads exerted by the jaw opening and jaw closing muscles during the cycle. In that study, the activity of the lateral pterygoid, which is hardly accessible with electromyography and has been a subject of discussion in other computational simulations [11, 12], was adjusted through inverse analysis to reproduce the movement of the jaw during mastication. That work [14] analysed the evolution of stresses and strains in the mandible during the masticatory cycle, which are used in the present work to study the remodelling response in the mandible bone.

The main objective of the present work is to study how the change in stress distributions affects the remodelling response of the mandible bone. Particularly, the study shows the important effect of the TMJ on the stress distribution during the masticatory cycle. This will be done by comparing the bone density distribution estimated with two models: with and without TMJ. In the last case, the joint constraints were modelled with simplified boundary conditions, restraining certain movements of the condyle, as done in a previous study [3]. In contrast, the new model includes the TMJ and simulates the contact between the articular disc and the articulating surfaces, as well as some ligaments that constrain the relative movements between the jaw and the temporal bone.

2. Materials and Methods

2.1. Finite Element Model. A finite element (FE) model of the mandible, called $\mathcal{M}1$ and built in a previous work [3], was compared with a more recent model, named $\mathcal{M}2$ and described in detail in Commisso et al. [14]. Both were built using Abaqus FEA[®]. The difference between them is that $\mathcal{M}2$ includes a detailed model of the TMJ: ligaments, articular disc, and temporal bone. By contrast, in $\mathcal{M}1$ certain displacements were constrained on the condylar surface to simulate the conditions imposed by the TMJ [3]. The inclusion of the TMJ entailed some improvements. First, the disc-condyle and disc-temporal bone contacts were modelled, resulting in a better approximation of the local boundary conditions. Second, the implementation of dynamic loads with $\mathcal{M}1$ is not easy, for example, to simulate a masticatory cycle in which the boundary conditions vary with time. On the contrary, $\mathcal{M}2$ allows the simulation of a masticatory cycle in a straightforward manner.

Both $\mathcal{M}1$ and $\mathcal{M}2$ model comprise 77,490 eight-node linear brick elements (named C3D8 in Abaqus FEA element library) for the mandible. In addition, $\mathcal{M}2$ model comprises 965 elements for each articular disc and 1,788 elements for the ligaments of each side, all of them of type C3D8H (eight-node linear brick, hybrid with constant pressure). In $\mathcal{M}2$, the temporal bones were modelled as rigid surfaces, using 1,324 type M3D4 elements for each side.

2.2. Material Models. The articular disc was modelled with a quasi-linear viscoelastic (QLV) model, where the uniaxial stress response to a step stretch is factorized as

$$\sigma(t, \lambda) = \bar{G}(t) T^e(\lambda) \quad (1)$$

thus, separating the dependence of time and deformation [15]. \bar{G} is the reduced relaxation function defined with a 4-term Prony series:

$$\bar{G}(t) = g_\infty + \sum_{i=1}^4 g_i e^{-t/\tau_i} \quad (2)$$

$$\text{normalized such that } g_\infty + \sum_{i=1}^4 g_i = 1$$

The elastic response function, T^e , is the instantaneous stress produced by a uniaxial step stretch. The strain energy function, Ψ , proposed by Humphrey and Yin [16] was used to define T^e .

$$\Psi = \frac{1}{D} (J - 1)^2 + A e^{B(I_1 - 3)} \quad (3)$$

where D , A , and B are material constants and I_1 is the first invariant of the left Cauchy-Green tensor. The first term was added to model quasi-incompressibility, so that D must be chosen small enough. This function was previously applied to the articular disc [17] and provides the following elastic response function in the incompressible case:

$$T^{(e)}(\lambda) = 2ABe^{B(\lambda^2 + 2/\lambda - 3)} \left(\lambda^2 - \frac{1}{\lambda} \right) \quad (4)$$

The QLV model was easily implemented in Abaqus FEA by defining a hyperelastic behaviour given by (3) and using a viscoelastic behaviour with a time domain definition given by the Prony series (2). The following constants were taken from a previous experimental work [17]: $g_1 = 0.28$, $g_2 = 0.37$, $g_3 = 0.27$, $g_4 = 0.08$; $\tau_1 = 0.01$ s, $\tau_2 = 0.1$ s, $\tau_3 = 1.0$ s, $\tau_4 = 10$ s; $A = 0.16$ MPa, $B = 4.18$, and $D = 0.01$ MPa⁻¹. The ligaments of the TMJ were also modelled as in [13], following the approach of Gardiner and Weiss [18]. A friction coefficient of $\mu = 0.015$ was assumed for the contact between the disc and the bony parts [19].

2.3. Bone Remodelling Models. The BRM used here to simulate the behaviour of the mandible bone (termed later as ABRM) was proposed by Doblaré and García [5] and is an extension of the isotropic model developed by Beaupré et al. [1] to include anisotropy. It relates density, anisotropy, and mechanical properties of bone with the loads the tissue is daily subjected to. The basic aspects of the models are explained next: first the isotropic BRM [1] and next the anisotropic model [5], focusing on the modifications made to the isotropic BRM. However, consulting the original papers is advised for further comprehension of both.

2.3.1. Isotropic Bone Remodelling Model (IBRM). In the IBRM Beaupré et al. [1] defined a daily mechanical stimulus based on the strain energy density (SED) accumulated in each point of the tissue during the daily activity. This stimulus considers the contribution of each load i of the normal activity. At the continuum level, it is given by

$$\psi = \left(\sum_{\text{day}} n_i \bar{\sigma}_i^m \right)^{1/m} \quad (5)$$

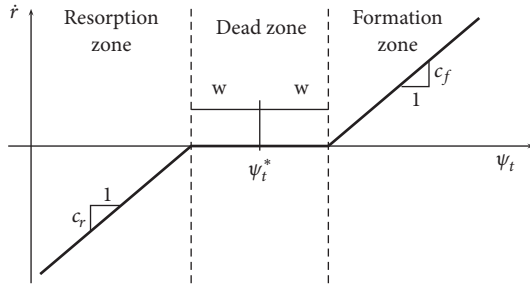


FIGURE 1: Remodelling response as a function of the daily stress stimulus at the tissue level.

where m is an empirical constant, adjusted to 4 by Whalen and Carter [20], n_i is the daily number of cycles of load i , and $\bar{\sigma}_i$ is an effective stress at the continuum level, defined as $\bar{\sigma}_i = \sqrt{2EU_i}$, where E is Young's modulus and U_i is the SED corresponding to load i at a given point. The stimulus that controls the bone remodelling response is the daily stress stimulus measured at the tissue level, ψ_t , which is related to the stimulus at the continuum level, ψ , through porosity p using the relation:

$$\psi_t = \left(\frac{1}{p}\right)^2 \psi = \left(\frac{\hat{\rho}}{\rho}\right)^2 \psi \quad (6)$$

where ρ is the bone apparent density and $\hat{\rho}$ is the density of bone matrix, which is assumed to be fully mineralized in this model and, thus, $\hat{\rho} = 2 \text{ g/cm}^3$ constant.

The remodelling response is measured in terms of the bone resorption/apposition rate, $\dot{\rho}$. This rate provides the volume of bone matrix resorbed/formed per day and per unit surface available for bone resorption/formation. It is given by the mechanostat theory [21], as a function of ψ_t and a reference stimulus, ψ_t^* , close to which no net remodelling response is observed (see Figure 1). Bone density change rate is

$$\dot{\rho} = \dot{\rho} S_v \hat{\rho} \quad (7)$$

where the specific surface, S_v , is the free bone surface (where bone resorption/formation occurs) per unit volume and was correlated with porosity by Martin [22]. Finally, Young's modulus and Poisson's ratio are related to the apparent density by the following correlations [23]:

$$E \text{ (MPa)} = \begin{cases} 2014\rho^{2.5} & \text{if } \rho \leq 1.2 \text{ g/cm}^3 \\ 1763\rho^{3.2} & \text{if } \rho > 1.2 \text{ g/cm}^3 \end{cases} \quad (8a)$$

$$\nu = \begin{cases} 0.2 & \text{if } \rho \leq 1.2 \text{ g/cm}^3 \\ 0.32 & \text{if } \rho > 1.2 \text{ g/cm}^3 \end{cases} \quad (8b)$$

2.3.2. Anisotropic Bone Remodelling Model (ABRM). This ABRM, proposed by Doblaré and García [5], is an extension of the IBRM to the anisotropic case. The anisotropy is

measured with the fabric tensor $\widehat{\mathbf{H}}$, normalized such that $\det(\widehat{\mathbf{H}}) = 1$. Then, a tensor \mathbf{H} is defined to consider jointly the porosity and the orientation of the pores, which is measured by $\widehat{\mathbf{H}}$:

$$\mathbf{H}(\rho, \widehat{\mathbf{H}}) = \left(\frac{\rho^{\beta(\rho)} B(\rho)}{\hat{\rho}^{\beta(\hat{\rho})} B(\hat{\rho})} \right)^{1/4} \widehat{\mathbf{H}}^{1/2} \quad (9)$$

where $B(\rho)$ and $\beta(\rho)$ represent, respectively, the constant and exponent in the correlation (8a), which depend on ρ (e.g. $\beta(\hat{\rho}) = 3.2$, $B(\hat{\rho}) = 1763$).

The ABRM establishes the strain tensor, $\boldsymbol{\varepsilon}$, as the mechanical variable that drives bone remodelling. The tensorial mechanical stimulus is given by

$$\mathbf{Y} = 2 \left[2\widehat{G} \text{sym}[(\mathbf{H}\boldsymbol{\varepsilon}\mathbf{H})(\mathbf{H}\boldsymbol{\varepsilon})] + \widehat{\lambda} \text{tr}(\mathbf{H}^2\boldsymbol{\varepsilon}) \text{sym}(\mathbf{H}\boldsymbol{\varepsilon}) \right] \quad (10)$$

with \widehat{G} and $\widehat{\lambda}$ the Lamé constants corresponding to bone with density $\hat{\rho}$ and obtained from (8a) and (8b). To weigh the relative influence of the spherical and deviatoric parts of the stimulus, a new stimulus tensor, \mathbf{J} , is defined as

$$\mathbf{J} = \frac{(1-\omega)}{3} \text{tr}(\mathbf{Y}) \mathbf{1} + \omega \text{dev}(\mathbf{Y}) \quad (11)$$

where the parameter $\omega \in [0, 1]$ must be chosen *a priori*. If $\omega = 0$, the model is purely isotropic and if $\omega = 1$, $\mathbf{J} = \text{dev}(\mathbf{Y})$ and the spherical part of the stimulus has no influence on the bone response.

Doblaré and García [5] defined two functions, g^r and g^f , to establish the resorption and formation criteria, respectively. These functions were dependent on the stimulus tensor, \mathbf{J} , the reference stimulus, ψ_t^* , and the width of the dead zone, $2w$ (see Figure 1), and define the domains of the stimulus \mathbf{J} for which formation, resorption, or no net remodelling response (dead zone) take place, analogously to the domains defined in Figure 1 for ψ_t :

$$g^r(\mathbf{J}, \psi_t^*, w) \leq 0$$

$$g^f(\mathbf{J}, \psi_t^*, w) > 0$$

formation

$$g^r(\mathbf{J}, \psi_t^*, w) \leq 0$$

$$g^f(\mathbf{J}, \psi_t^*, w) \leq 0$$

dead zone

$$g^r(\mathbf{J}, \psi_t^*, w) > 0$$

$$g^f(\mathbf{J}, \psi_t^*, w) \leq 0$$

resorption

(12)

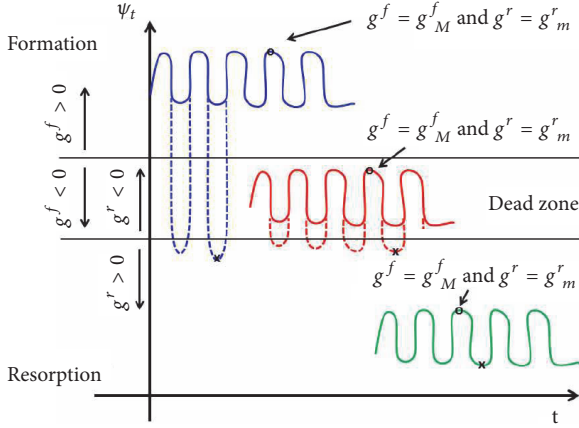


FIGURE 2: The evolution of stimulus in three individuals are represented in solid line. The peaks correspond to the maximums of g^f and minimums of g^r . Dashed lines: alternative activities with the same peaks but different valleys.

The remodelling response \dot{r} is given by the active remodelling criterion, that is, the condition in (12) which is currently accomplished:

$$\dot{r} = \begin{cases} c_f \frac{g^f}{\rho^{2-\beta(\rho)/2}} & \text{in formation} \\ 0 & \text{in the dead zone} \\ -c_r \frac{g^r}{\rho^{2-\beta(\rho)/2}} & \text{in resorption} \end{cases} \quad (13)$$

where c_r and c_f are, respectively, the slopes of the resorption and formation ramps (Figure 1). Finally, this remodelling response, \dot{r} , is used to calculate $\dot{\mathbf{H}}$, which leads to the variation of density and anisotropy.

$$\dot{\mathbf{H}} = \frac{3\beta k \dot{r} S_v}{4tr(\mathbf{H}^{-1}\mathbf{J}^{-3}\hat{\boldsymbol{\omega}})} \frac{\hat{\rho}}{\rho} \mathbf{J}^{-3}\hat{\boldsymbol{\omega}} \quad \text{in resorption} \quad (14)$$

$$\dot{\mathbf{H}} = \frac{3\beta k \dot{r} S_v}{4tr(\mathbf{H}^{-1}\mathbf{J}\hat{\boldsymbol{\omega}})} \frac{\hat{\rho}}{\rho} \mathbf{J}\hat{\boldsymbol{\omega}} \quad \text{in formation}$$

2.3.3. Modified Anisotropic Bone Remodelling Model (MABRM). ABRM was modified by Ojeda [24] to consider cyclic loads more appropriately. In cyclic loads like those shown in Figure 2 the remodelling response would depend, according to Carter et al. [25], on the typical peak of stimulus and the number of cycles performed during the daily activity. As far as the authors know, all the BRMs proposed in the literature treat cyclic loads in a simplified way: by solely considering one instant of the cycle, usually when the applied forces are maximum. Thus, a pseudo-static elastic problem is solved at this instant to calculate the stresses, the mechanical stimulus, and the remodelling response in every point of the bone. However, in a chewing cycle, the peaks of stimulus can be out of phase; that is, each point of the mandible can reach its peak of stimulus at a different instant of the chewing cycle. That way, the simulation of

a single instant would overlook the peaks of stimulus in some points of the bone. For instance, in the previous study implementing $\mathcal{M}1$ [3] it was assumed that the whole mandible was subjected to the higher stresses (and stimulus) at the instant of centric occlusion (CO); but that might not be the instant of maximum stimulus for the area near the mandibular foramen, where the depressor muscles are attached. The stresses in this area are relatively low at CO, but they are higher when the mandible is being pulled by the depressor muscles to open the mouth. Cases like that must be analysed with MABRM that considers appropriately the variation of stimulus through the cycle.

Let us consider three individuals (I1, I2, and I3) whose daily activities produce evolutions of the stimulus like those shown in Figure 2. I1 (in blue) carries out an intense exercise inducing net bone formation. I3 (in green) performs an activity of low intensity leading to net bone resorption. Finally, I2 (in red) performs an activity of moderate intensity which does not produce a net change of bone mass (dead zone). In cyclic loads peaks of stimulus coincide in time with maximums of the function g^f , named here g_M^f , and with minimums of g^r , named g_m^r . (They only coincide in time, because g_M^f and g_m^r have different values, in general.) Similarly, valleys of stimulus coincide in time with minimums of the formation function, g_m^f , and with maximums of the resorption function, g_M^r . According to Carter et al. [25] the remodelling response depends only on the peaks of stimulus. Thus, the activities plotted in dashed lines for I1 and I2 would lead to the same remodelling response as those plotted in solid lines.

In MABRM the whole cycle is simulated to calculate the evolution of g^f and g^r . With those evolutions, g_M^f and g_m^r are calculated in every point of the model to apply the remodelling criterion (15) that places the peaks in one of the three regions: formation, resorption, or dead zone.

$$\begin{aligned} &g_M^f > 0 \\ &\text{and } g_m^r \leq 0 \\ &\quad \text{formation} \\ &g_M^f \leq 0 \\ &\text{and } g_m^r \leq 0 \\ &\quad \text{dead zone} \\ &g_M^f \leq 0 \\ &\text{and } g_m^r > 0 \\ &\quad \text{resorption} \end{aligned} \quad (15)$$

Finally, the bone resorption/apposition rate is obtained as in (13):

$$\dot{r} = \begin{cases} c_f \frac{g_M^f}{\rho^{2-\beta(\rho)/2}} & \text{in formation} \\ 0 & \text{in the dead zone} \\ -c_r \frac{g_m^r}{\rho^{2-\beta(\rho)/2}} & \text{in resorption} \end{cases} \quad (16)$$

and $\dot{\mathbf{H}}$ is evaluated using (14).

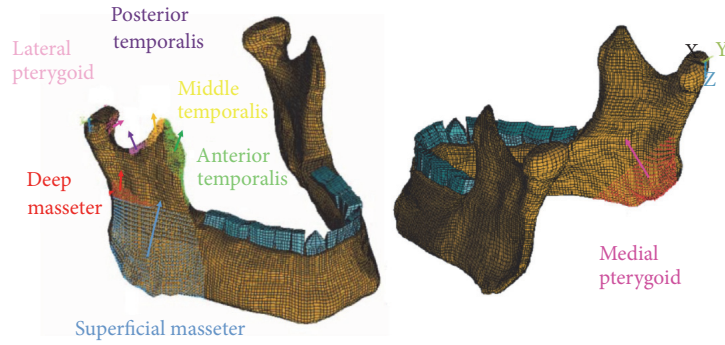


FIGURE 3: Insertion and schematic orientation of different portions of the closing muscles used in models M1 and M2.

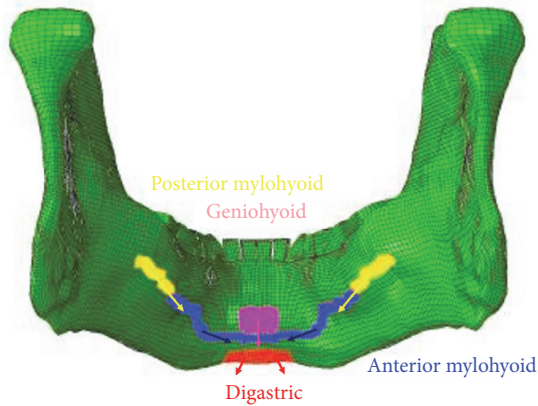


FIGURE 4: Insertion and schematic orientation of different portions of the opening muscles used in model M2.

2.4. Loads. A complete mastication cycle with the right molars (RM) was simulated. In $\mathcal{M}2$, the viscoelastic nature of the articular disc could cause differences between the first and subsequent cycles in a mastication sequence. However, the fast stress relaxation occurring in the disc allowed analysing only the first cycle as representative of the whole sequence, as concluded in [14]. The model is symmetric and therefore the stresses produced by mastication with the left molars were obtained from RM by applying a symmetry operation.

The closing and opening phases of the cycle were simulated by applying the muscle activation patterns given by Hylander [26], except for the lateral pterygoid. The activity of this muscle is difficult to measure and has been widely debated in the literature, with no agreement in the activation pattern the muscle has during the mastication cycle. In a recent work, we have adjusted that activity with an inverse procedure [14]. This activation pattern was used here and can be seen in Figure 5, along with the activities of the rest of masticatory muscles. These activities were multiplied by the maximum forces of each muscle, F_0^M , the peak of activity, a_{max} , and the direction cosines shown in Table 1, to get the components of the muscular forces. The muscle forces were imposed as external loads, distributed over the insertion area of each muscle as can be seen in Figure 3 for the closing muscles and Figure 4 for the opening muscles. In the figures,

the areas highlighted in different colours correspond to various groups of nodes where the different muscles are inserted. Also, an arrow indicates the approximate orientation of each muscle.

Those direction cosines give the orientation of muscle fibres (in average as some muscles have a fan shape) relative to the mandible and corresponding to the instant of centric occlusion (CO). However, that relative orientation may vary with mouth opening and needed to be updated throughout the cycle, in the following way. For each muscle the origin and insertion were distinguished, the latter being its attachment to the mandible. First, the origin of each muscle was estimated using the position of the insertion point in the mandible, the direction cosines at CO, and the length shown in Table 1. The origins are located in the skull and were thus assumed fixed during the simulation, so that the updated direction cosines were easily calculated from the position of those fixed origins and the position of the mandible (more details can be found in [14]).

The instant of CO is indicated in Figure 5 with a red vertical arrow (around $t = 0.19\text{ s}$). This is approximately the instant of maximum mastication force and was the only instant analysed with $\mathcal{M}1$ in the previous work of Reina et al. [3]. As stated above, $\mathcal{M}1$ was not adequate to simulate a mastication cycle, given that the displacement constraints used in that model were only valid for the instant of CO. Therefore, $\mathcal{M}1$ simulated the masticatory activity as a static load with the forces exerted by the closing muscles applied in the highlighted areas of Figure 3 and their corresponding magnitudes given in Figure 5 at CO. In contrast, $\mathcal{M}2$ was able to simulate a mastication cycle with the complete record of muscular activity. Inertial forces were very small and thus neglected, leading to a pseudostatic simulation of the cycle.

2.5. Displacement Boundary Conditions. The boundary conditions applied to simulate CO in each model are depicted in Figure 6. At CO, the mouth is closed and the condyles are at their back position, in contact with the articular eminence of the temporal bone. In $\mathcal{M}1$ this contact was not considered as such, but it was simplified by constraining the displacements of the articular surface of the condyle. The pressure in this contact is different for each side, being usually smaller in the ipsilateral (working) side [30, 31], where food thickness interposes between both dental arches, thus separating the

TABLE 1: Forces exerted by masticatory muscles. Only the orientation of the forces of the right side are given (symmetry with respect to the sagittal plane was assumed). The magnitude of the muscle force peak in CO for the ipsilateral (I) and contralateral (C) sides are also provided. The +x-axis is directed anteriorly, the +y-axis rightward, and the +z-axis downward. CP: closing phase, OP: opening phase. 1: length with the mouth closed [27]. 2: Koriotoh et al. [28] for the jaw closing muscles. 3: van Eijden et al. [27] for the jaw opening muscles. 4: Nelson [29] for the jaw closing muscles. 5: proportional to the values adopted by Hannam et al. [12] for the jaw opening muscles.

Muscle	Portion	Length (mm) ¹	$\cos-x^{2,3}$	$\cos-y^{2,3}$	$\cos-z^{2,3}$	Activity peak $a_{max}^{4,5}$			$F_0^M (N)^{2,3}$
						I	C	C	
Masseter	Superficial	48.0	0.419	0.207	-0.885	0.56	0.56	0.20	190.4
	Deep	25.7	-0.358	0.546	-0.758	0.56	0.56	0.20	81.6
Temporalis	Anterior	51.9	0.044	0.149	-0.988	0.65	0.65	0.51	158.0
	Middle	52.7	-0.5	0.221	-0.837	0.60	0.60	0.53	95.6
	Posterior	52.9	-0.855	0.208	-0.474	0.54	0.54	0.54	75.6
Medial pterygoid		42.7	0.372	-0.486	-0.791	0.97	0.97	0.47	174.8
Lateral pterygoid (CP)	Inferior	32.6	0.757	-0.63	0.174	0.50	0.50	0.36	66.9
Lateral pterygoid (OP)	Inferior	32.6	0.757	-0.63	0.174	0.10	0.10	0.10	66.9
	Superior	31.3	0.645	-0.761	-0.074	0.039	0.039	0.026	28.8
	Anterior belly digastric	43.2	0.053	0.815	-0.576	5E-4	5E-4	5E-4	40.0
Geniohyoid		40.0	-0.995	0.103	0.018	2.6E-4	2.6E-4	2.6E-4	38.8
Mylohyoid	Anterior	23.0	-0.176	-0.831	0.528	1.6E-4	1.6E-4	1.6E-4	63.6
	Posterior	42.6	-0.223	-0.616	0.756	4.7E-4	4.7E-4	4.7E-4	21.2

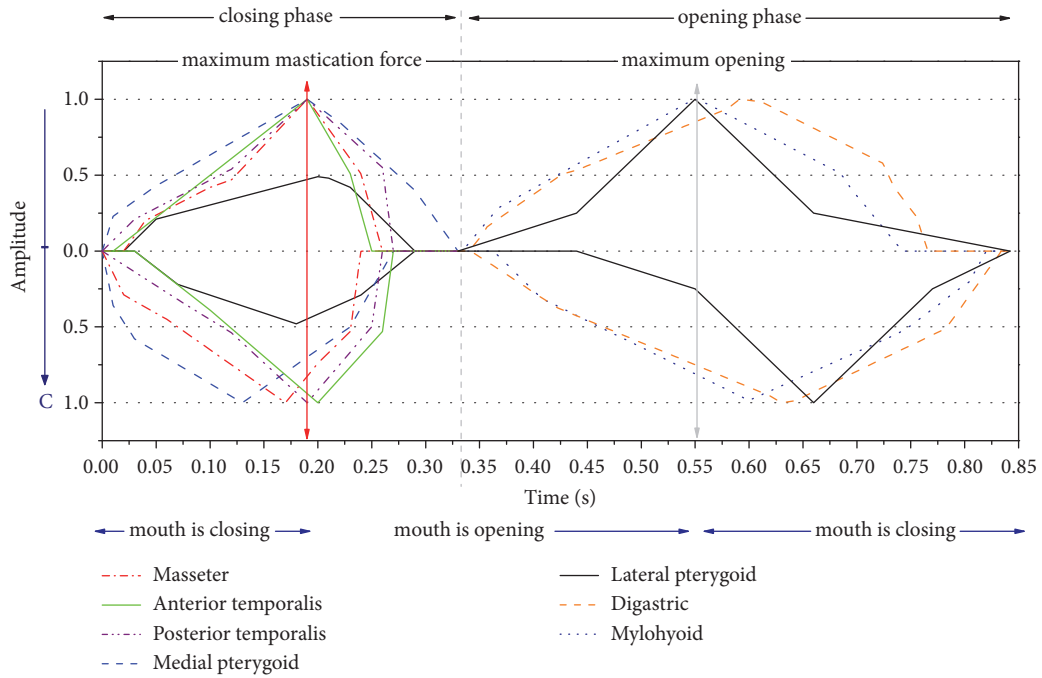


FIGURE 5: Activation pattern of the jaw closing and opening muscles during unilateral mastication. The ipsilateral (I) muscles are above, in the upper y-axis, while the contralateral (C) ones are represented in the inferior y-axis. The amplitudes are normalized to the corresponding peak of muscle force, given in Commisso et al. [14]. The closing and opening phases are named after those muscles which are active during the corresponding phase (jaw opening or jaw closing muscles) and not after the direction of the movement, which is shown down in the figure. The instant of CO is indicated with a red vertical arrow.

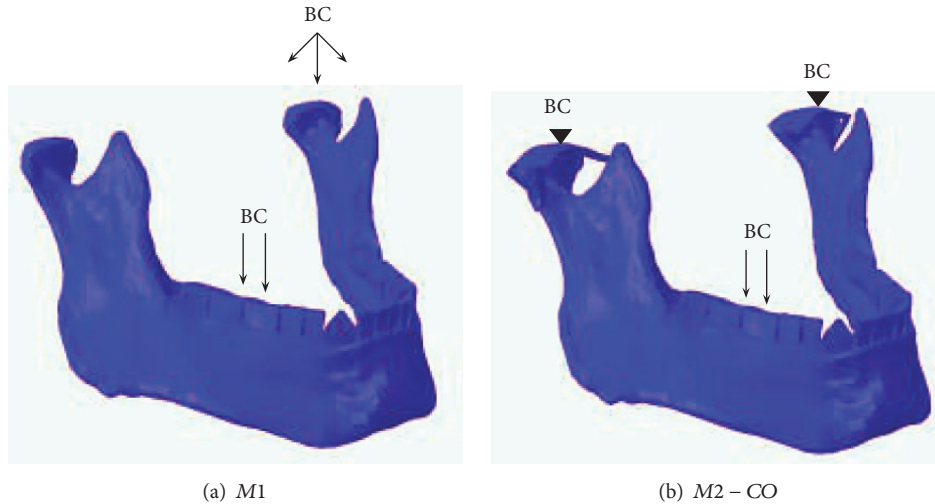


FIGURE 6: Boundary conditions applied at the instant of CO in a mastication with the right molars: (a) in $\mathcal{M}1$ and (b) in $\mathcal{M}2$. The triangle represents a rigid fixation of temporal bone (contact pairs temporal bone-disc and disc-condyle are defined in the TMJ), while the arrows indicate the direction in which the corresponding displacements are constrained.

articular surfaces. So, for instance, in the simulation of RM with $\mathcal{M}1$ the articular surface of the left condyle was fixed and the right condyle was assumed to move freely (Figure 6). It must be noted that this is a strong simplification of the real situation in which the ipsilateral joint bears a lower reaction force, though not null [30, 31].

The new models aimed to avoid this simplification by modelling the contact at the joints. In $\mathcal{M}2$, temporal bones

were fixed, condyles were constrained by the contact interaction with the articular disc, and, in turn, articular discs were constrained by the contact interaction with temporal bones. This way reaction forces arose naturally from the contact at the joints, with a lower value in the ipsilateral condyle. Additionally, the ligaments of the joint limit the movement of the mandible by preventing condyles from being pulled apart from the articular eminence. Figure 7 shows the finite

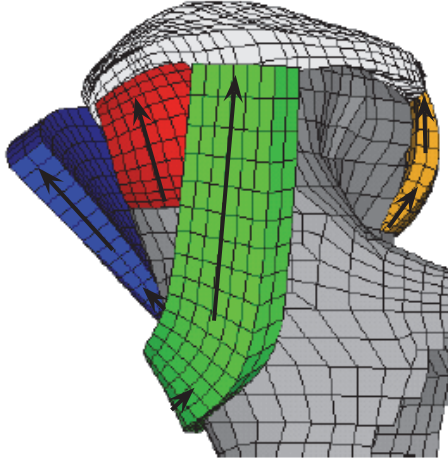


FIGURE 7: Finite element model of the articular disc and ligaments in the TMJ. The direction of the collagen fibers in the ligaments is indicated with arrows.

element model of the collateral and temporomandibular ligaments and the posterior part of the articular capsule. Additionally, the direction of the collagen fibers are indicated with arrows (more details on the joint model can be found in Commisso et al. [14]).

On the other hand, the tooth-food contact was not modelled. Instead, the vertical displacements were constrained in the occlusal face of ipsilateral molars (e.g., right molars in RM) in order to simulate grinding forces as reaction forces [3].

2.6. Description of the Performed Simulations. Three simulations, summarized in Table 2, were performed. *M1* was the same performed in a previous study [3], using model $\mathcal{M}1$ (without TMJ), in a static problem and applying the muscle forces at the instant of CO (red vertical arrow in Figure 5).

Simulation *M2 - CO* uses the model $\mathcal{M}2$, including the TMJ, to perform a pseudostatic analysis of the instant of CO. Since the articular disc has a viscoelastic behaviour, the time variable was important, but the analysis *M2 - CO* was simplified to ignore the temporal evolution of muscle forces. Instead, these muscle forces were varied from 0 to the values at CO in a ramp-like manner of length $t = 0.2\text{ s}$, small enough to focus just on the instant of CO, but long enough to be considered a pseudostatic analysis and not to introduce spurious stresses due to the application of instantaneous loads in viscoelastic models.

Simulation *M2 - cycle* uses the model $\mathcal{M}2$ as well, but now to perform a pseudostatic analysis of the whole masticatory cycle. Muscle forces were varied following the pattern depicted in Figure 5.

The effect of the simplification of the loads could be assessed through comparison of the stresses obtained in *M2 - CO* and those obtained in *M2 - cycle* at CO. The differences were negligible and, thus, the simplification was validated. Nonetheless, the interest of *M2 - cycle* mostly lies in simulating the whole masticatory cycle and specifically the

opening phase during which some points of the mandible could reach its peak of stimulus.

As stated before, the vertical displacements of the occlusal face of ipsilateral molars were constrained to simulate grinding forces as reaction forces. This was made in simulations *M1* and *M2 - CO*, while in *M2 - cycle* vertical displacements were constrained only during the closing phase and released during the opening phase. A summary of the performed simulations is given in Table 2.

2.7. Simulation of the Bone Remodelling Response. In the previous work [3] (simulation *M1*) and in other similar works, the simulations started from a bone with uniform density ($\rho_0 = 0.5\text{ g/cm}^3$ in that particular case) and initially isotropic. The final bone density and anisotropy distribution were estimated by simulating the daily masticatory activity until a remodelling equilibrium was achieved, with no further changes in bone density. (It could also be checked that the convergence of density implied the convergence of anisotropy.)

In simulations with model $\mathcal{M}2$ it was not advisable to start from a low uniform density ($\rho_0 = 0.5\text{ g/cm}^3$). In such case, numerical problems arise from the disc-condyle contact, due to the low stiffness of both materials. Moreover, the computing cost of simulating the large number of days needed to achieve the remodelling equilibrium is excessive in the more complex model $\mathcal{M}2$. For these reasons, simulations *M2 - CO* and *M2 - cycle* started from the bone density and anisotropy distribution obtained in simulation *M1* at the remodelling equilibrium. The simulation of the masticatory cycle with $\mathcal{M}2$ produced a redistribution of stresses, caused by the TMJ, thus leading to a change in the density distribution until a new remodelling equilibrium was achieved. The density distribution obtained at the new equilibrium was compared with that obtained in *M1* to analyse the effect of the TMJ.

The masticatory pattern assumed here was an alternating unilateral molar chewing followed by 75% of the population [32]: chewing with the right molars (RM) followed by chewing with the left molars (LM), thus, defining the sequence: RM, LM, RM, LM, . . . , until the remodelling equilibrium was achieved. A total of $n_i = 500$ (see (5)) daily masticatory cycles (250 RM + 250 LM) were assumed, like in Reina et al. [3]. The convergence of the density distribution was checked by computing the following parameter:

$$CV (\%) = \frac{\int_V |\rho_{j+1} - \rho_j| dV}{\int_V \rho_j dV} \cdot 100 \quad (17)$$

where ρ_j represents the density of a given point at day j . The remodelling equilibrium was assumed to occur when $CV < 1\%$.

3. Results

3.1. Comparison of Simulations *M1* and *M2 - CO*. The strain energy density (SED) distribution obtained in *M1* and *M2 - CO* at the remodelling equilibrium is compared in Figure 8. A detail of this distribution in the ramus and the body of the mandible (cross-sections 1-1' and 2-2') can be seen in Figures

TABLE 2: Summary of the performed simulations.

Simulation	Starting point	Description	BRM used	TMJ	Muscular activity	Boundary conditions
<i>M1</i>	$\rho_0 = 0.5 \text{ g/cm}^3$, uniform and isotropic	Static. Instant of CO. Sequence: RM- LM-RM-LM...	ABRM	NO	At CO (red vertical arrow of Figure 5)	Articular surface of contralateral condyle fixed. Vertical displacement of occlusal face of ipsilateral molars constrained.
<i>M2 – CO</i>	Remodelling equilibrium obtained with <i>M1</i>	Pseudostatic. Instant of CO. Sequence: RM- LM-RM-LM...	ABRM	YES	At CO (red vertical arrow of Figure 5)	Temporal bone fixed. Contacts: temporal bones-discs and discs-condyles. Vertical displacement of occlusal face of ipsilateral molars constrained.
<i>M2 – cycle</i>	Remodelling equilibrium obtained with <i>M1</i>	Pseudostatic. Complete cycle. Sequence: RM- LM-RM-LM...	MABRM	YES	Complete record of Figure 5	Temporal bone fixed. Contacts: temporal bones-discs and discs-condyles. Vertical displacement of occlusal face of ipsilateral molars constrained in the closing phase and released in the opening phase.

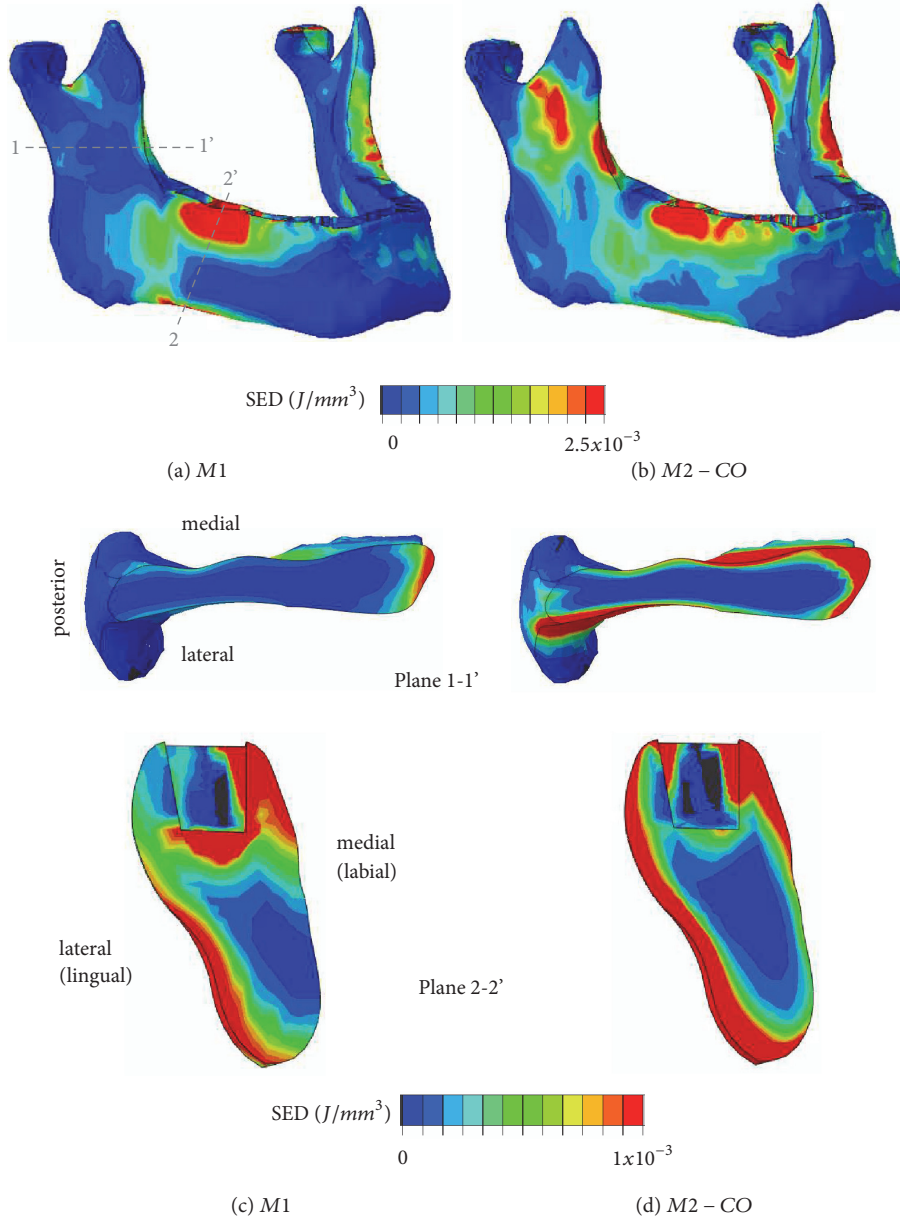


FIGURE 8: Distribution of SED at the instant of CO in M1 and M2 – CO, for the whole mandible (a, b) and at the cross-sections 1-1' and 2-2' (c, d). Plane 1-1 cuts the ramus and plane 2-2 is a cross-section located approximately at the second molar.

8(c) and 8(d). SED is shown because it is closely related to bone density distribution, given that the mechanical stimulus is defined in terms of SED.

Starting from a uniform density distribution ($\rho_0 = 0.5 \text{ g/cm}^3$) and an initially isotropic bone, around 300 days of mastication were needed to achieve the remodelling equilibrium state in M1. Starting from that state, SED changed noticeably in M2 – CO, inducing changes in density distribution. For that reason, 10 further days of mastication were needed to achieve a new remodelling equilibrium state ($CV < 1\%$). The new density distribution is compared with that of M1 in Figure 9. A detail of both density distributions at a premolar section is compared with a CT scan of the real mandible in Figure 10.

Mastication forces at the instant of CO could be estimated from reaction forces at the nodes of the occlusal faces of the first and second right molars, where the displacements were constrained. The maximum mastication force was 501 N in M1 and a little lower, 458 N, in M2 – CO.

3.2. Comparison of Simulations M2 – CO and M2 – cycle. Comparison of simulations M2 – CO and M2 – cycle allows analysing the effect of MABRM and to check whether the variation of the mechanical stimulus through the masticatory cycle affects the remodelling response of the mandible. The difference of bone density between both simulations was hardly noticeable and, therefore, instead of showing

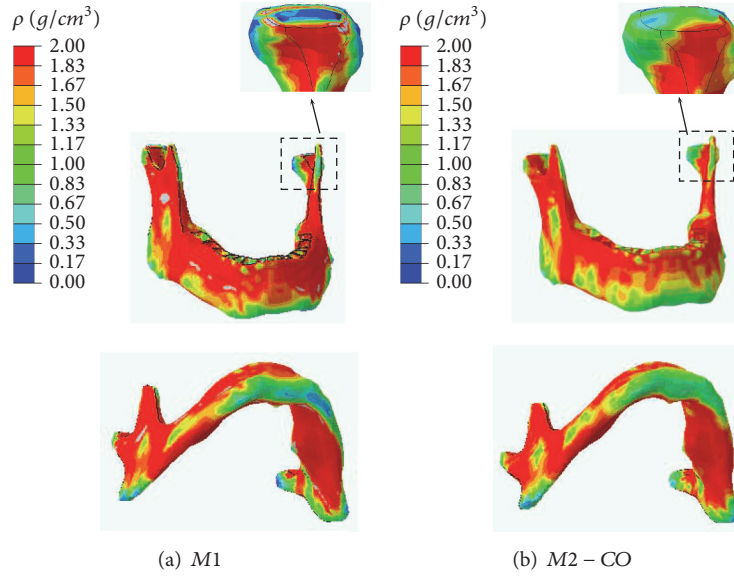


FIGURE 9: Bone density distribution at the remodelling equilibrium in (a) $M1$ and (b) $M2 - CO$.

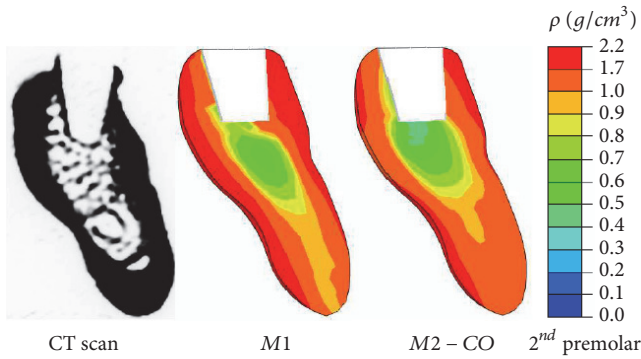


FIGURE 10: Detail of the bone density distribution obtained at the second premolar region compared with a CT scan of the real mandible.

its distribution for $M2 - cycle$, the following variable was represented in Figure 11:

$$\Delta\rho^{M2} = \rho_{M2-cycle} - \rho_{M2-CO} \quad (18)$$

where $\rho_{M2-cycle}$ and ρ_{M2-CO} represent the density of a certain point at the remodelling equilibrium in simulations $M2 - cycle$ and $M2 - CO$, respectively.

4. Discussion

The comparison of simulations $M1$ and $M2 - CO$ revealed significant differences in all aspects: SED, bone density distribution and mastication forces.

SED is more uniformly distributed in $M2 - CO$ and not so concentrated in the ipsilateral molar region, as it was in $M1$ (Figure 8). The cross-sections in Figures 8(c) and 8(d) also revealed great differences. In the ramus (plane 1-1'), $M2 - CO$ estimates a continuous layer of high SED surrounding the

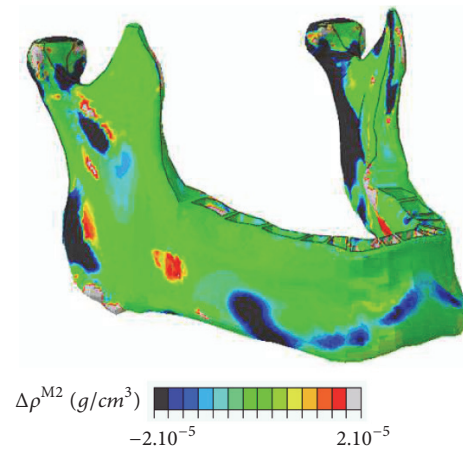


FIGURE 11: Distribution of $\Delta\rho^{M2}$, difference in density estimation between simulations $M2 - cycle$ and $M2 - CO$.

central part of the section, not seen in $M1$. In the molar region (plane 2-2'), the inner area of low SED is larger in $M2 - CO$ and, again, there is a continuous layer of high SED enclosing the section. This is not seen in $M1$, due to a small portion of the inferior medial surface which has a very low SED.

Given that SED is directly related to the mechanical stimulus, the differences of SED can explain the different estimated density. A significant change is seen at the condyles, where bone density is more uniformly distributed in $M2 - CO$, due to the TMJ and the redistribution of loads it produces. Constraining displacements, as done in $M1$, always produce a stress concentration in the FE solution, which leads to a discontinuous bone density across elements (see detail of the condyle in Figure 9(a)). In the rest of the mandible, the TMJ induces smaller changes, but they are still worth a mention, for example, in the chin. Here, the area of density close to

1 g/cm^3 (green in Figure 9) spreads in $M2-CO$, reducing the area of maximum density (2 g/cm^3), but, more importantly, reducing the area of minimum density (0.3 g/cm^3), in light blue. In conclusion, the simulations that use $\mathcal{M}2$ tend to close the so-called cortical shell, a continuous layer of intermediate to dense bone that surrounds the real mandible.

If numerical results are compared with CT scan at the premolar region (Figure 10), bone density distribution obtained with $M2-CO$ is, again, closer to the actual one. It is true that $M2-CO$ produces less cortical bone of high density (in red) than $M1$, but, it corrects an important problem seen in the old model: the cortical shell was missing at the inferior side of the canine region, where a portion of very light bone ($\sim 0.5 \text{ g/cm}^3$) was obtained. This tubular structure of dense bone surrounding an inner central area of bone of low density is usual in the diaphysis of long bones and is also seen in the mandible, to resist bending and torsion loads that mastication produces [3].

Mastication force was obtained as the resultant reaction force in the occlusal face of molars, in both $M1$ and $M2-CO$. Despite the applied muscle forces being the same, mastication force was almost 10% higher in $M1$ (501 N) than in $M2-CO$ (458 N). Both values were within the range measured in experimental studies, 430 – 650 N [33, 34].

The difference found between $M1$ and $M2-CO$ shows that the TMJ, modelled in $\mathcal{M}2$, does not only redistribute the stresses in the condyle, but also reduce the stresses in the alveolar region around molars. The same conclusion can be drawn by comparing the distribution of SED (Figure 8). With TMJ ($\mathcal{M}2$) SED is more uniformly distributed, and not only in the condyles, as could be expected, but also in the ramus and the body of the mandible. In the model without TMJ ($\mathcal{M}1$) SED was mainly concentrated around the molar region of the ipsilateral side.

In this regard, the flexibility of the articular disc might play an important role to redistribute the stresses, as well as the stress relaxation that the disc experiences, which increases that flexibility. For that reason, in $M2-CO$ it was important to apply loads at a rate close to the real one. In this sense, a ramp of length $t = 0.2\text{s}$ seemed adequate as it produced very similar results compared to the more realistic simulation $M2-cycle$.

$M2-CO$ also improves the estimation of density in the alveolar region right below teeth, which is clearly noticeable in the premolar section (Figure 10). $M1$ produces a bone of intermediate density in that area, unlike $M2-CO$, which predicts the actual light bone that can be seen in the CT scan.

The influence of analysing only the instant of CO or the whole masticatory cycle was studied through the comparison of the bone density distributions obtained in $M2-CO$ and $M2-cycle$. This comparison revealed very little differences (Figure 11), which were explained by the low mechanical stimulus the mandible was bearing during the opening phase. This stimulus was much lower than that produced during the closing phase for two reasons: (1) jaw opening muscles exert forces of lower magnitude than jaw closing muscles and (2) during the closing phase the displacements were constrained in the molars, giving rise to the mastication force. The mechanical stimulus was particularly high at CO, when the activity of closing muscles is maximum. Consequently,

most of the mandible reaches its peak of stimulus at CO and bone formation is driven in simulation $M2-cycle$ by the stress state at that instant, which is the one captured in $M2-CO$. There was a very small area in the lingual side of the chin, close to the insertion of opening muscles, where the peaks of stimulus were reached during the opening phase. Nonetheless, these peaks were similar to those obtained at CO and they did not lead to significant differences in the estimated bone density. In conclusion, the simulation of the whole mastication cycle did not yield relevant differences with respect to previous analysis in which only the instant of CO was studied. In other words, the simplification of the analysis to focus just on CO was justified from the perspective of the remodelling response of the mandible.

This fact does not mean that the modification introduced in MABRM to study cyclic loads is irrelevant on a general basis. It was in the case of mastication, but not in the case of the femur during gait, for example, where the peaks of stimulus were reached in different phases of the cycle for different locations in the femur [24]. In this particular case, it was shown that MABRM led to important differences from the bone remodelling perspective.

Some limitations of the model are discussed next. First, the articular disc was assumed as isotropic. Actually, it is an anisotropic material, composed of an extracellular matrix reinforced with collagen fibres. These fibres run in antero-posterior direction in the central portion of the disc and in mediolateral direction, in both the anterior and posterior regions [35]. In any case, fibres run mostly perpendicular to the thickness. In the load cases simulated in this work the disc was mainly subjected to compression in vertical direction (across its thickness). With such loads, fibres would be stretched, so contributing to the stiffness of the tissue. For that reason, they should be taken into account in the disc constitutive model, but they were not. Nonetheless, compression along thickness was the type of load applied in the experiments where the constitutive model was adjusted [13]. Therefore, the stiffness of the fibres was indirectly included in the material model. In any case, the anisotropy should be explicitly considered (by using a fibre reinforced material model) if the type of load varied during the mastication cycle.

Another limitation of the study was the omission of the articular cartilage that covers the surface of articulating bones. The articular cartilage helps to reduce the stresses in the condyle [36]. The mechanical properties of this layer has not been established appropriately, but it is generally accepted that it is more flexible than the articular disc [10]. For this reason, it is thought to have an effect on the redistribution of stresses over the condyle that needs to be addressed in future works. Other limitations are the simplified definition of the teeth-food contact and not considering the pennation angle of muscles, though this was simplified by using the average direction of muscle fibres and taking into account that pennation angle is close to zero in all the muscles involved.

Overcoming these limitations is the aim of the short-term future research, but another interesting topic to be addressed is to analyse the influence of pathologic conditions of the articular disc in the reaction forces and stress distribution of the mandible. It is known that bruxism may cause damage on

the disc [37], likely altering its viscoelastic properties. Since the influence of the TMJ has been shown to be important on the stress distribution, this alteration of viscoelastic properties could, in turn, affect the bone density distribution within the mandible, specially if damage is not symmetrical. As a matter of fact, another interesting topic, not yet addressed in the literature, is to study the effect of other types of mastication patterns, such as unilateral, on bone density distribution.

5. Conclusions

A FE model of the mandible including the TMJ was used to simulate the mastication process. The most relevant features of the joint were modelled. A viscohyperelastic model fitted from experimental tests was used to simulate the behaviour of the TMJ articular disc. In contrast to previous similar studies, mandible bone was considered a deformable material, which, additionally, is able to remodel and change its mechanical properties to adapt itself to the mechanical environment. The model presented here allows analysing the influence of the joint on the stresses produced in bone during the masticatory cycle and the effect of those stresses on the bone remodelling response.

By comparing the FE models with and without TMJ it was concluded that the joint plays an important role by redistributing the stresses and strains and not only over the condyles but also throughout the whole mandible.

Regarding bone remodelling, it was observed that the joint has also an important effect on the bone density distribution predicted by the model. If the joint was modelled, the estimated density was closer to the actual one, specially below the teeth and in the chin. Here, a cortical shell confining a central area of trabecular bone was seen in the whole body of the mandible, unlike the model without TMJ, which failed to close the cortical shell in the premolar and incisive region.

Furthermore, considering the complete mastication cycle instead of only the instant of centric occlusion had a small effect in the estimation of density and could be disregarded. This is an important conclusion, as it simplifies this type of studies of bone remodelling in the mandible. In other words, the analysis of the whole cycle does not seem necessary in this case from the remodelling perspective, as it was in other cyclic loads, such as gait cycle, where it had a strong influence on femoral bone remodelling [24].

Data Availability

The data used to support the findings of this study are available from the corresponding author upon request.

Conflicts of Interest

The authors declare that they have no conflicts of interest.

Acknowledgments

Funding was provided by *Ministerio de Industria, Economía y Competitividad* for the research project DPI2016-80796-P entitled *Diseño de un banco de pruebas para la optimización*

de la cinemática y la cinética 3D en la práctica del ciclismo for which this article has been prepared.

References

- [1] G. Beaupré, T. Orr, and D. Carter, "An approach for time-dependent bone modelling and remodelling - theoretical development," *Journal of Orthopaedic Research*, vol. 8, no. 5, pp. 651–661, 1990.
- [2] M. Doblaré and J. M. García, "Application of an anisotropic bone-remodelling model based on a damage-repair theory to the analysis of the proximal femur before and after total hip replacement," *Journal of Biomechanics*, vol. 34, no. 9, pp. 1157–1170, 2001.
- [3] J. M. Reina, J. M. García-Aznar, J. Domínguez, and M. Doblaré, "Numerical estimation of bone density and elastic constants distribution in a human mandible," *Journal of Biomechanics*, vol. 40, no. 4, pp. 828–836, 2007.
- [4] M. A. Pérez, P. Fornells, M. Doblaré, and J. M. García-Aznar, "Comparative analysis of bone remodelling models with respect to computerised tomography-based finite element models of bone," *Computer Methods in Biomechanics and Biomedical Engineering*, vol. 13, no. 1, pp. 71–80, 2010.
- [5] M. Doblaré and J. M. García, "Anisotropic bone remodelling model based on a continuum damage-repair theory," *Journal of Biomechanics*, vol. 35, no. 1, pp. 1–17, 2002.
- [6] P. Fernandes, H. Rodrigues, and C. Jacobs, "A model of bone adaptation using a global optimisation criterion based on the trajectorial theory of Wolff," *Computer Methods in Biomechanics and Biomedical Engineering*, vol. 2, no. 2, pp. 125–138, 1999.
- [7] J. Ojeda, J. Martínez-Reina, J. García-Aznar, J. Domínguez, and M. Doblaré, "Numerical simulation of bone remodelling around dental implants," *Proceedings of the Institution of Mechanical Engineers, Part H: Journal of Engineering in Medicine*, vol. 225, no. 9, pp. 897–906, 2011.
- [8] C. Field, Q. Li, W. Li, M. Thompson, and M. Swain, "A comparative mechanical and bone remodelling study of all-ceramic posterior inlay and onlay fixed partial dentures," *Journal of Dentistry*, vol. 40, no. 1, pp. 48–56, 2012.
- [9] J. W. Osborn, "The disc of the human temporomandibular joint: design, function and failure," *Journal of Oral Rehabilitation*, vol. 12, no. 4, pp. 279–293, 1985.
- [10] M. Beek, J. H. Koolstra, L. J. Van Ruijven, and T. M. G. J. Van Eijden, "Three-dimensional finite element analysis of the cartilaginous structures in the human temporomandibular joint," *Journal of Dental Research*, vol. 80, no. 10, pp. 1913–1918, 2001.
- [11] J. H. Koolstra and T. M. G. J. Van Eijden, "Consequences of viscoelastic behavior in the human temporomandibular joint disc," *Journal of Dental Research*, vol. 86, no. 12, pp. 1198–1202, 2007.
- [12] A. G. Hannam, I. Stavness, J. E. Lloyd, and S. Fels, "A dynamic model of jaw and hyoid biomechanics during chewing," *Journal of Biomechanics*, vol. 41, no. 5, pp. 1069–1076, 2008.
- [13] M. S. Commisso, J. Martínez-Reina, and J. Mayo, "A study of the temporomandibular joint during bruxism," *International Journal of Oral Science*, vol. 6, no. 2, pp. 116–123, 2014.
- [14] M. S. Commisso, J. Martínez-Reina, J. Ojeda, and J. Mayo, "Finite element analysis of the human mastication cycle," *Journal of the Mechanical Behavior of Biomedical Materials*, vol. 41, pp. 23–35, 2015.

- [15] Y. Fung, *Biomechanics: Mechanical Properties of Living Tissues*, Springer-Verlag, New York, NY, USA, 1993.
- [16] J. Humphrey and F. Yin, "On constitutive relations and finite deformations on passive cardiac tissue: I a pseudostatic energy function," *Journal of Biomechanical Engineering*, pp. 109–298, 1987.
- [17] M. S. Commisso, J. Martínez-Reina, J. Mayo, and J. Domínguez, "Numerical simulation of a relaxation test designed to fit a quasi-linear viscoelastic model for temporomandibular joint discs," *Proceedings of the Institution of Mechanical Engineers, Part H: Journal of Engineering in Medicine*, vol. 227, no. 2, pp. 190–199, 2013.
- [18] J. C. Gardiner and J. A. Weiss, "Subject-specific finite element analysis of the human medial collateral ligament during valgus knee loading," *Journal of Orthopaedic Research*, vol. 21, no. 6, pp. 1098–1106, 2003.
- [19] E. Tanaka, N. Kawai, M. Tanaka et al., "The frictional coefficient of the temporomandibular joint and its dependency on the magnitude and duration of joint loading," *Journal of Dental Research*, vol. 83, no. 5, pp. 404–407, 2004.
- [20] R. T. Whalen, D. R. Carter, and C. R. Steele, "Influence of physical activity on the regulation of bone density," *Journal of Biomechanics*, vol. 21, no. 10, pp. 825–837, 1988.
- [21] H. Frost, "The mechanostat: a proposed pathogenetic mechanism of osteoporoses and the bone mass effects of mechanical and nonmechanical agents," *Bone Miner*, vol. 2, pp. 73–85, 1987.
- [22] R. B. Martin, "Porosity and Specific Surface of Bone," *CRC Critical Reviews in Biomedical Engineering*, vol. 10, no. 3, pp. 179–222, 1984.
- [23] C. Jacobs, *Numerical Simulation of Bone Adaptation to Mechanical Loading [Ph.D. thesis]*, Stanford University, Stanford, Calif, USA, 1994.
- [24] J. Ojeda, *Application of Multibody System Technique to Human Locomotor System [Ph.D. thesis]*, University of Seville, Spain, 2012.
- [25] D. Carter, D. Fyhrie, and R. Whalen, "Trabecular bone density and loading history: Regulation of connective tissue biology by mechanical energy," *Journal of Biomechanics*, vol. 20, no. 8, pp. 785–794, 1987.
- [26] W. Hylander, "The temporomandibular joint: a biologic basis for clinical practice," in *chap Functional Anatomy*, pp. 60–92, W.B. Saunders Co., Philadelphia, Pa, USA, 1992.
- [27] T. M. G. J. Van Eijden, J. A. M. Korfage, and P. Brugman, "Architecture of the human jaw-closing and jaw-opening muscles," *Anatomical Record*, vol. 248, no. 3, pp. 464–474, 1997.
- [28] T. W. P. Koriath, D. P. Romilly, and A. G. Hannam, "Three-dimensional finite element stress analysis of the dentate human mandible," *American Journal of Physical Anthropology*, vol. 88, no. 1, pp. 69–96, 1992.
- [29] G. Nelson, *Three Dimensional Computer Modeling of Human Mandibular Biomechanics [Ph.D. thesis]*, University of British Columbia, Columbia, 1986.
- [30] F. Mongini, G. Preti, P. M. Calderale, and G. Barberi, "Experimental strain analysis on the mandibular condyle under various conditions," *Medical & Biological Engineering & Computing*, vol. 19, no. 5, pp. 521–523, 1981.
- [31] T. Kuboki, Y. Azuma, M. G. Orsini, Y. Takenami, and A. Yamashita, "Effect of sustained unilateral clenching on the temporomandibular joint space," *Oral Surgery, Oral Medicine, Oral Pathology, Oral Radiology*, vol. 82, no. 6, pp. 616–624, 1996.
- [32] A. Manns and G. Daz, *Sistema Estomatogntico*, Sociedad Grfica Almagro Ltda., Santiago de Chile, 1988.
- [33] A. Van Der Bilt, A. Tekamp, H. Van Der Glas, and J. Abbink, "Bite force and electromyography during maximum unilateral and bilateral clenching," *European Journal of Oral Sciences*, vol. 116, no. 3, pp. 217–222, 2008.
- [34] H. Pottipalli and S. Patil, "Assessment of maximum voluntary bite force in adults with normal occlusion and different types of malocclusions," *The Journal of Contemporary Dental Practice*, vol. 13, no. 4, pp. 534–538, 2013.
- [35] M. S. Detamore and K. A. Athanasiou, "Structure and function of the temporomandibular joint disc: Implications for tissue engineering," *Journal of Oral and Maxillofacial Surgery*, vol. 61, no. 4, pp. 494–506, 2003.
- [36] K. Hu, R. Qiguo, J. Fang, and J. J. Mao, "Effects of condylar fibrocartilage on the biomechanical loading of the human temporomandibular joint in a three-dimensional, nonlinear finite element model," *Medical Engineering & Physics*, vol. 25, no. 2, pp. 107–113, 2003.
- [37] G. J. Lavigne, N. Huynh, T. Kato et al., "Genesis of sleep bruxism: motor and autonomic-cardiac interactions," *Archives of Oral Biolog*, vol. 52, no. 4, pp. 381–384, 2007.